EPSRC - CMAC Future Manufacturing Research Hub

UNIVERSITY OF STRATHCLYDE

Strathclyde Institute of Pharmacy and Biomedical Sciences

Measurement, Optimisation and Control of Particle Properties in Pharmaceutical Manufacturing Processes

Submitted in accordance with the requirements for the degree of

Doctor of Philosophy

Frederik J. S. Dörr

2019

Author:	Frederik J. S. Dörr [a,b]
Registration No:	201562518
Email:	frederik.doerr@strath.ac.uk
Primary Supervisor:	Prof Alastair J. Florence [a,b]
Secondary Supervisor:	Dr Iain D. H. Oswald [a,b]
Internal Reviewer:	Dr Daniel Markl [a,b]
External Reviewer:	Prof Andrew E. Bayly [c]
Submission Date:	November 30, 2019

Affiliation:
[a] EPSRC CMAC Future Manufacturing Research Hub, Technology and Innovation Centre, 99 George Street, Glasgow, G1 1RD, UK.
[b] Strathclyde Institute of Pharmacy & Biomedical Sciences (SIPBS), University of Strathclyde, Glasgow, G4 0RE, UK.
[c] School of Chemical and Process Engineering, University of Leeds, Leeds, LS2 9JT, UK.

Declaration of Authors Rights

This thesis is the result of the author's original research. It has been composed by the author and has not been previously submitted for examination which has led to the award of a degree.

Glasgow (U.K.), May 19, 2020 _____

Frederik J. S. Dörr

Abstract

The understanding and optimisation of particle properties connected to their structure and morphology is a common objective for particle engineering applications either to improve material-handling in the manufacturing process or to influence Critical Quality Attributes (CQAs) linked to product performance. This work aims to demonstrate experimental means to support a rational development approach for pharmaceutical particulate systems with a specific focus on droplet drying platforms such as spray drying.

Micro-X-ray tomography (micro-XRT) is widely applied in areas such as geo- and biomedical sciences to enable a three dimensional investigation of the specimens. Chapter 4 elaborates on practical aspects of micro-XRT for a quantitative analysis of pharmaceutical solid products with an emphasis on implemented image processing and analysis methodologies. Potential applications of micro-XRT in the pharmaceutical manufacturing process can range from the characterisation of single crystals to fully formulated oral dosage forms. Extracted quantitative information can be utilised to directly inform product design and production for process development or optimisation. The non-destructive nature of the micro-XRT analysis can be further

employed to investigate structure-performance relationships which might provide valuable insights for modelling approaches.

Chapter 5 further demonstrates the applicability of micro-XRT for the analysis of ibuprofen capsules as a multi-particulate system each with a population of approximately 300 pellets. The in-depth analysis of collected micro-XRT image data allowed the extraction of more than 200 features quantifying aspects of the pellets' size, shape, porosity, surface and orientation. Employed feature selection and machine learning methods enabled the detection of broken pellets within a classification model. The classification model has an accuracy of more than 99.55% and a minimum precision of 86.20% validated with a test dataset of 886 pellets from three capsules.

The combination of single droplet drying (SDD) experiments with a subsequent micro-XRT analysis was used for a quantitative investigation of the particle design space and is described in Chapter 6. The implemented platform was applied to investigate the solidification of formulated metformin hydrochloride particles using D-mannitol and hydroxypropyl methylcellulose within a selected, pragmatic particle design space. The results indicate a significant impact of hydroxypropyl methylcellulose reducing liquid evaporation rates and particle drying kinetics. The morphology and internal structure of the formulated particles after drying are dominated by a crystalline core of D-mannitol partially suppressed with increasing hydroxypropyl methylcellulose additions. The characterisation of formulated metformin hydrochloride particles with increasing polymer content demonstrated the importance of an early-stage quantitative assessment of formulation-related particle properties.

A reliable and rational spray drying development approach needs to assess parameters of the compound system as well as of the process itself in order to define a well-controlled and robust operational design space. Chapter 7 presents strategies for process implementation to produce peptide-based formulations via spray drying demonstrated using s-glucagon as a model peptide. The process implementation was supported by an initial characterisation of the lab-scale spray dryer assessing a range of relevant independent process variables including drying temperature and feed rate. The platform response was captured with available and in-house developed Process Analytical Technology. A B-290 Mini-Spray Dryer was used to verify the development approach and to implement the pre-designed spray drying process. Information on the particle formation mechanism observed in SDD experiments were utilised to interpret the characteristics

of the spray dried material.

Contents

Declaration ii

Abstract iv

Contents vii

List of Figures xi

List of Tables xvi

List of Abbreviations xviii

1 Introduction 1

1.1 Liquid Evaporation and Particle Formation during Drying 2

1.1.1 Droplet Drying Stages 3

1.1.2 Mass- and Heat-transfer during Liquid Evaporation 5

1.1.3 Solid Phase Formation 9

1.1.4 Particle Properties 13

1.2 Single Droplet Drying Experiments using Acoustic Levitation 17

1.2.1 Single Droplet Drying Experiments - Introduction 17

1.2.2 Single Droplet Drying Experiments - Acoustic Levitation 18

1.2.3 Single Droplet Drying Experiments - Spray Drying Process Development 20

1.3 Spray Drying 20

1.3.1 Process Model 21

1.3.2 Process Parameters 24

1.3.3 Process Analytical Technology 25

1.3.4 Product Characterisation 26

1.4 X-ray Tomography 29
1.4.1 XRT - image acquisition (scanning) 29
1.4.2 XRT - image reconstruction 31
1.4.3 XRT - image artefacts 32
1.4.4 XRT - Visualisation and Analysis 33

2 Aims and Objective **35**
2.1 Aims 35
2.2 Objectives 36

3 Acoustic Levitation Platforms **39**
3.1 Single-Axis Acoustic Levitator (SAL) 39
3.2 Multi-emitter Single-axis Acoustic Levitator (MSAL) 40
3.3 Imaging Techniques 41
3.3.1 Digital Imaging 41
3.3.2 Infrared Thermography Imaging 42

4 XRT Characterisation of Pharmaceutical Solid Products **44**
4.1 Introduction 45
4.2 Materials and Methods 46
4.3 Results and Discussion 47
4.3.1 XRT Sample Preparation Strategies 48
4.3.2 Image Acquisition and Reconstruction 50
4.3.3 Image Processing - 3D Volume Builder 52
4.3.4 Image Processing - Image Segmentation 57
4.3.5 Image Analysis - Feature Extraction 59
4.3.6 Application of micro-XRT for the Analysis of Solid Pharmaceutical Products 66
4.3.7 Coupled micro-XRT and ToF-SIMS analysis for chemical mapping . . 75
4.4 Conclusions 78

5 XRT Image Analysis and Machine Learning for the Characterisation of Multi-Particulates **80**

5.1 Introduction . . . 82
5.2 Materials and methods . . . 84
5.2.1 Commercial ibuprofen capsule . . . 84
5.2.2 X-ray tomography . . . 84
5.2.3 3D Image Processing and Single Particle Analysis . . . 85
5.2.4 Feature-based Particle Classification: ReliefF and SVM . . . 86
5.3 Results and Discussion . . . 88
5.3.1 Capsule - Full Sample Analysis . . . 89
5.3.2 Capsule - Pellet Segmentation . . . 91
5.3.3 Capsule - Pellet Characterisation . . . 93
5.3.4 Capsule - Pellets Classification . . . 95
5.4 Conclusions . . . 102

6 Investigation of the Particle Design Space of Novel Pharmaceutical Formulations 104
6.1 Introduction . . . 105
6.2 Materials and methods . . . 107
6.2.1 Chemicals / Samples . . . 107
6.2.2 Single Axis - Acoustic Levitator . . . 108
6.2.3 X-ray Tomography and XRT Image Analysis . . . 110
6.3 Results and Discussion . . . 113
6.3.1 Solidification and Skin Formation of HPMC K100LV and formulated Systems of MET . . . 113
6.3.2 Particle Morphology Characterisation using XRT . . . 120
6.4 Conclusions . . . 126

7 Peptide Isolation via Spray Drying 129
7.1 Introduction . . . 131
7.2 Materials and methods . . . 133
7.2.1 Chemicals . . . 133
7.2.2 Single droplet drying experiments . . . 135
7.2.3 Spray drying . . . 136
7.2.4 Spray dried powder characterisation . . . 139

7.3 Results and discussion . . . 142
7.3.1 Single droplet drying experiments . . . 142
7.3.2 Spray drying - process implementation . . . 143
7.3.3 Spray drying - product characterisation . . . 153
7.4 Conclusions . . . 160

8 Conclusion and Future Experimental Work **163**
8.1 Future Work . . . 164

Bibliography **167**

9 Appendix **A1**
A1 Appendix - XRT Characterisation of Pharmaceutical Solid Products (Chapter 4) A1
A1.1 Micro-XRT Data Acquisition Details . . . A1
A1.2 ToF-SIMS Characterisation . . . A2
A2 Appendix - XRT Image Analysis and Machine Learning for the Characterisation of Multi-Particulates (Chapter 5) . . . A3
A2.1 Micro-XRT Data Acquisition Details . . . A3
A2.2 Voxel-based arithmetic Operations . . . A3
A2.3 Micro-XRT Sensitivity Analysis Details . . . A4
A2.4 ReliefF Feature Selection Results . . . A12
A2.5 Data Analysis . . . A16
A3 Appendix - Investigation of the Particle Design Space of Novel Pharmaceutical Formulations (Chapter 6) . . . A19
A3.1 Estimation of polymer diffusion coefficient using Stokes-Einstein equation . . . A20
A4 Appendix - Peptide Isolation via Spray Drying (Chapter 7) . . . A22
A4.1 Formulas . . . A22
A4.2 Tables . . . A24
A4.3 Figures . . . A28

List of Figures

1.1 Equilibrium moisture curve indicating bound and unbound moisture at increasing moisture content of the solids. . . . 3
1.2 Drying stages for droplet evaporation below the liquid boiling temperature. . . 4
1.3 Solubility Phase Diagram. . . . 12
1.4 Particle morphologies obtained from evaporating droplets. . . . 13
1.5 Droplet drying systems often used for characterising evaporation and particle formation. . . . 17
1.6 Single-axis acoustic levitation and acoustic streaming. . . . 19
1.8 Mass- and heat-balance of lab-scale spray dryer in open loop configuration. . . 23
1.9 Generic steps during a micro-XRT characterisation. . . . 30
1.10 Visualisation of X-ray attenuation through photoelectric effect and X-ray scattering. . . . 31

3.1 Experimental setup of the Single-Axis Acoustic Levitator. . . . 40
3.2 Multi-emitter acoustic levitator setup with integrated imaging system. . . . 41
3.3 Processing of recorded droplet images during liquid evaporation. . . . 42
3.4 Processing of thermal images during droplet evaporation. . . . 43

4.1 SkyScan 2211 with cone-beam arrangement. . . . 47
4.2 Overview of micro-XRT data acquisition and processing workflow. . . . 48
4.3 Examples for sample presentation and micro-XRT image acquisition. . . . 49
4.4 Optimising image acquisition and reconstruction. . . . 51
4.5 Implemented 3DVB image data processing routine. . . . 53
4.6 Impact of changing parameters for morphological operations on micro-XRT image data. . . . 56

4.7 Micro-XRT image analysis subroutine for the extraction of structure-based object size descriptors. . . . 60
4.8 Micro-XRT image analysis subroutine for the extraction of structure-based object shape descriptors. . . . 62
4.9 Micro-XRT image analysis subroutine for the extraction of object porosity descriptors. . . . 64
4.10 Overview of micro-XRT samples with applications covering a wide range of the pharmaceutical downstream manufacturing pipeline. . . . 66
4.11 Particles from SDD experiments characterised with micro-XRT. . . . 70
4.12 Micro-XRT characterisation of a physical mixture of MET crystals and PVP polymer particles. . . . 72
4.13 Surface-rendered micro-XRT visualisation of 3D printed HPMC-PCM tablets with increasing internal density. . . . 74
4.14 Micro-XRT coupled with ToF-SIMS for the analysis of particles with a two-compound crystalline structure. . . . 76
4.15 Pixel intensity-assignment for a qualitative assessment of the chemical distribution across the particle volume. . . . 78

5.1 Graphical abstract Chapter 5. . . . 81
5.2 Image processing sequence to separate connected particle volumes. . . . 86
5.3 3D-to-2D image transformation to isolate translation- and rotation-invariant 2D cross-sections. . . . 87
5.4 Full workflow combining micro-XRT analysis and machine learning methodologies. . . . 89
5.5 *Global* sample analysis (a) detecting internal capsule void space, pellet solid phase volume and intra-pellet porosity. . . . 91
5.6 The segmentation of all "touching" pellets was achieved after applying a marker-supported watershed transformation. . . . 92
5.7 Normalised number density distributions (q0) of four selected features describing the pellet populations. . . . 94
5.8 Selected features for a classification of *non-broken* and *broken* pellets. . . . 97

5.9 SVM models with RBF kernels for the feature-based classification of 886 pellets in DTT. . . . 99
5.10 Individual *non-broken* and *broken* pellets with feature combinations associated to support vectors of the TC-SVM classification model. . . . 101

6.1 Graphical abstract Chapter 6. . . . 105
6.2 Experimental Setup with acoustic levitator and an enclosure. Image analysis allows the extraction of information on the droplet volume and surface temperature. . . . 109
6.3 XRT image processing to extract quantitative descriptors for particle size, shape, porosity and surface buckling. . . . 112
6.4 Drying curves for de-ionized water and aqueous HPMC K100LV solution. . . . 114
6.5 Drying curves for formulations of MET and MAN with increasing additions of HPMC K100LV. . . . 117
6.6 Solidification kinetics of formulation of MET and MAN with varying additions of HPMC K100LV. . . . 119
6.7 Visualisation of the investigated particle design space for solids obtained from single droplet evaporation experiments. . . . 122
6.8 XRT reveals the internal structure and morphology of particles collected from single droplet evaporation experiments. . . . 123
6.9 Selected 2D cross-sections of formulated MET particles with MAN and increasing additions of HPMC K100LV. . . . 124
6.10 Ratios of particle solid phase volume, particle porosity volume, and particle concave surface volume for MS_0 - MS_4. . . . 125

7.1 Graphical abstract Chapter 7. . . . 131
7.2 Molecular Structure of D-(+)-Trehalose dihydrate. . . . 134
7.3 Acoutic Levitation Setup (MSAL) used to investigate particle formation of peptide-based systems from single droplet drying experiments. . . . 136
7.4 Experimental setup of the lab-scale spray dryer in open loop configuration. . . . 137
7.5 Visualisation of the data integration approach with details on the process parameters monitored and recorded during each spray drying experiment. . . . 138

7.6 Molecular Structure of Thioflavin T. 140
7.7 Particle morphologies of TRE, GLUC and a formulation of GLUC:TRE as collected from the MSAL system and analysed using XRT. 143
7.8 B290 spray dryer system characterisation. 146
7.9 Psychrometric chart with the theoretically derived stickiness curve. 148
7.10 Mass change of spray dried TRE and GLUC samples utilising vacuum drying as a secondary drying step. 153
7.11 SEM micrographs of spray dried powder samples. 155
7.12 Selected LD-PSDs for spray dried samples of TRE and GLUC samples. 156
7.13 Results of the employed HPLC potency assay assessing feed stability. 160

A1 Determination of ToF-SIMS spatial resolution using a 20/80 edge-resolution analysis. A2
A2 Box plots of the top 30 features with the highest variability during a quantitative sensitivity analysis. A6
A3 Qualitative visualisation of the impact of the collected micro-XRT image quality and critical image processing parameters on the binarized object volume. . . A7
A4 Plotmatrix of the training dataset (DTR) with selected feature combinations. . . A16
A5 2^{nd} order polynomial fit to calculate the diffusion coefficient of MAN in water. . A19
A6 Lock-point detection during SDD experiments. A20
A7 Changes in the calculated solution viscosity and diffusion coefficient of HPMC K100LV during liquid evaporation until LP. A21
A8 Implementation of the BME680 sensor recording temperature, pressure and relative humidity of the exhaust gas. A28
A9 Example for the B290 system characterisation. A28
A10 Water adsorption isotherm of amorphous TRE at 25 °C. A29
A11 Reported glass transition temperature (T_g) values of TRE samples with changing moisture content [354, 379, 377, 378]. A30
A12 HPLC analysis with sample pre-filtration was used in order to allow a semi-quantitative assessment of the peptide fibrillation. A30
A13 Details of the HPLC potency assay as described in Section 7.2.4.3. . . . . A31

A14 Details of the HPLC impurity assay as described in Section 7.2.4.3. . . . . A31
A15 Drying curves of TRE, GLUC and a formulation of GLUC:TRE recorded during SDD experiments on the MSAL. A32
A16 XRPD data of spray dried TRE and GLUC powders. A33
A17 DSC data of spray dried TRE powders. A34
A18 TG-MS data of spray dried TRE powders. A34
A19 TG-MS data of spray dried GLUC powders. A35
A20 ThT assay for kinetic assessment of freeze-dried GLUC reference powder regarding feed stability and fibrils growth kinetics. A36
A21 Tht Assay of spray dried GLUC powders in 0.05M HCl. A37
A22 Small scale GLUC samples of 5 mg/mL with increasing ethanol solvent ratios. . A38
A23 *High performance* cyclones after spray drying experiments. A39
A24 SEM images of spray dried TRE and GLUC samples. A40

List of Tables

1.1 Potential applications of PAT in spray drying. 27

1.2 Overview of selected offline characterisation techniques for spray dried products. 28

4.1 Overview of implemented image filter (3DVB_2). 54

4.2 Overview of implemented image binarization methods (3DVB_3). 55

4.3 Overview of structural features used to describe the object size. 61

4.4 Overview of structural features describing to object shape. 63

4.5 Overview of structural features used to describe the object porosity. 64

4.6 Overview of structural features used to describe the object surface. 65

4.7 Overview of structural features used to describe the object surface. 65

4.8 Overview of prepared solution for SDD experiments. 67

4.9 Comparison of estimated tablet solid phase volume from weighed tablet mass and micro-XRT. 75

5.1 Quantification of capsule volume distribution and individual measurements. . . 90

6.1 Preparation schemata for solutions of metformin hydrochloride. 108

6.2 Calculated density of HPMC K100LV and its molecular diffusion coefficient in water. 115

6.3 Maximum mass flux ($\dot{m}_{max}$) and heating rate ($\dot{T}_{max}$) during droplet drying experiments. 120

6.4 Overview of extracted shape descriptors from formulated MET particle systems. 126

7.1 Results for the performed TRE spray drying experiments. 150

7.2 Results for the performed GLUC spray drying experiments. 152

7.3 Product characterisation of spray dried TRE and GLUC samples. 158

A1 Data acquisition settings for scanned pharmaceutical micro-XRT samples. . . . A1
A2 Micro-XRT data acquisition settings for scanned ibuprofen capsules. A3
A3 Overview of sampling points for a sensitivity analysis. A4
A4 Relative changes in the porosity volume distribution for selected samples during a sensitivity analysis and the contribution related to the local thickness. A5
A5 Sensitivity analysis ranking of 132 structural features exhibiting values above a 10% variability threshold. A8
A6 ReliefF feature ranking of 74 extracted structural features linked to pellet size, shape, surface and orientation attributes. A12
A7 Thermal emissivity correction factors for solid phase of HPMC K100LV (HPMC_10) and formulations of MET with MAN and HPMC K100LV (MS_0 - MS_4). . . A19
A8 Values for the calculation of the cyclone's cut-off size. A23
A9 Reported published spray drying conditions for the production of peptide- or protein-based powders. A24
A11 Overview of all spray drying experiments performed as part of a study for platform characterisation and process implementation. A25
A12 Spray drying experiments of TRE and GLUC. A26
A13 Spray Drying TRE: Evaluation of BME sensor data. A27

List of Abbreviations

Acronym	
3DVB	*3D Volume Builder* routine
DSC	Differential scanning calorimetry
FBP	Filtered back projection
FT-IR	Fourier transformation infra-red spectroscopy
HPLC	High performance liquid chromatograph
IEV	Translation- and rotation-invariant cross-section
IR	Infra-red
LD	Laser diffraction
MSAL	Multi-emitter single-axis acoustic levitator
OC-SVM	One-class support vector machine
OSH	Optimal separating hyperplane
PDE	Partial derivatives equations
PSD	Particle size distribution
RBF	Radial basis function
ROI	Region-of-interest
RT	Room temperature
SDD	Single droplet drying
SEM	Scanning electron microscopy
TC-SVM	Two-class support vector machine
TG-MS	Thermogravimetric analysis with mass spectrometry
V	Single Pellet
V_CP	Pellet population
V_CP_Poros	Pellet population porosity

V_CP_ROI	Pellet population region-of-interest
V_CS	Capsule shell
V_CS_InV	Capsule shell internal volume
V_CS_Poros	Capsule shell void
V_CS_ROI	Capsule shell region-of-interest
V_ROI	Single pellet ROI
XRPD	Powder X-ray diffraction
XRT	X-ray tomography

Chemicals

ACN	Acetonitrile
CBZ	Carbamazepine
GLUC	s-Glucagon
GLY	Glycine
HPMC	Hydroxypropyl methylcellulose
INA	Isonicotinamide
LAC	Lactose
MAN	D-mannitol
MET	Metformin hydrochloride
PCM	Paracetamol
PVP	Polyvinylpyrrolidone
ThT	Thioflavin T
TRE	Trehalose
TRE-h	Trehalose dihydrate

Symbol		Unit
c	Solute concentration	$mg \cdot mL^{-1}$
d	Diameter	m (μm)
d_a	Aerodynamic particle diameter	m (μm)
D_s	Solute diffusion coefficient (liquid phase)	$m^2 \cdot s^{-1}$
D_v	Solvent diffusion coefficient (gas phase)	$m^2 \cdot s^{-1}$

e	Eccentricity	
E	Surface enrichment of the solute	
FR	Feed rate (subscripts: S - set, R - recorded, C - calculated)	$mL \cdot min^{-1}$
h	Specific enthalpy	$J \cdot kg^{-1}$
Δh_{vap}	Latent heat of vaporisation	$J \cdot kg^{-1}$
K	Gordon-Taylor fit constant	
Nu	Nusselt number	
p	Pressure (subscripts: S - set, R - recorded, C - calculated)	Pa
p_0	Atmospheric pressure	Pa
Pe	Péclet number	
RH	Relative humidity (subscripts: S - set, R - recorded, C - calculated)	%RH
RM	Residual moisture	wt%
Sh	Sherwood number	
SH	Specific humidity (subscripts: S - set, R - recorded, C - calculated)	$g \cdot kg^{-1}$
T	Inlet temperature (subscripts: S - set, R - recorded, C - calculated)	°C
T_d	Dehydration temperature	°C (K)
T_g	Glass transition temperature	°C (K)
T_m	Melting temperature	°C (K)
w	Mass fraction	wt%
Y_∞	Solvent concentration gas phase (bulk)	
Y_s	Solvent concentration gas phase (droplet surface)	
Greek Letters		
ε	Emissivity thermal radiation ($\varepsilon = [0,1]$)	
κ	Evaporation rate	$m^2 \cdot s^{-1}$
μ	Attenuation coefficient	m^{-1}
$\mu^{\cdot}$	Effective attenuation coefficient	m^{-1}
μ_c	Chemical potential	$J \cdot mol^{-1}$
ρ_g	Density gas phase	$kg \cdot m^{-3}$
ρ_l	Density liquid phase	$kg \cdot m^{-3}$

1 Introduction - Pharmaceutical Multi-Particle Systems

Pharmaceutical multi-particle systems consist of a population of individual discrete particles which in combination affect on the overall drug product performance. (Micro-) particles are used within pharmaceutical products designed for oral administration (e.g. powders, granules, pellets and mini-tablets), as aerosols for inhalation into the lung, to be delivered to the nose or even to be injected transdermally through the skin. The drug product design and aspects of the manufacturing process largely depend on the physical properties of the active pharmaceutical ingredient (API) and other pharmaceutical additives (excipients) which define the overall drug composition i.e. its formulation. Approaches to optimise the particle performance focus on a targeted manipulation of specific particle properties to improve manufacturability and to ensure desirable therapeutic objectives whilst minimising any potential side effects. Physical properties (e.g. size, shape, internal structure) are commonly part of these particle quality attributes defining the final product performance and are linked to pharmaceutical specifications such as purity, uniformity, dissolution, stability, appearance, and mechanical durability. Complex therapeutic requirements of modern pharmaceutical products led to advanced particle forms designed e.g. to ensure product stability during re-distribution and storage or to meet specific requirements for the drug bioavailability after administration to the patient. Often, many process variables and factors related to the chemical composition are involved to successfully optimise (micro-) particles with complex structures, which therefore requires a deeper understanding of the particle formation process [1].

This chapter aims to give an introduction to relevant aspects around the investigation and production of pharmaceutical multi-particle systems with a specific focus on droplet drying platforms such as spray drying and on micro-X-ray Tomography (micro-XRT) as an advanced particle characterisation technique. Section 1.1 serves as a basis covering the current theory used

to describe the particle formation during droplet drying and its impact on the properties of the final particles. The evaporation process is governed by heat- and mass-transfer phenomena described in Section 1.1.2. Mechanisms of solid phase formation including amorphous solidification and crystallisation are introduced in Section 1.1.3. The particles can be distinguished by their size, shape, porosity and solid state attributes (Section 1.1.2). Single droplet drying (SDD) experiments performed within an acoustic levitation system can be employed to investigate particle formation processes and Section 1.2 highlights areas where this research has previously been applied effectively to inform and / or improve manufacturing processes. Section 1.3 gives an overview of spray drying as a platform for the production of particulate solids. The use of micro-XRT as described in Section 1.4 enables a further characterisation of structural properties for (multi-) particulate systems and a wider range of other solid pharmaceutical (intermediate) products. Image processing and analysis strategies enable the extraction of quantitative information.

1.1 Liquid Evaporation and Particle Formation during Drying

Drying is an essential step in the manufacturing of pharmaceuticals, which provides a unique route for particle and formulation engineering applications [2]. Drying is the process of liquid removal from an object through evaporation or freezing and sublimation to recover a dry solid product. The driving force for the mass-transfer during the drying process is the difference in the vapour pressure between moisture in the object and in the surrounding gas phase. In case of hygroscopic materials, liquids can be present as bound and unbound moisture [3]. An example for a moisture sorption isotherm of a hygroscopic material is visualised in Fig. 1.1. Bound moisture is liquid in a solid with a vapour pressure that is less than that of pure liquid at the same temperature. Bound moisture includes water taken up by capillary forces or adsorbed on the solid surface due to chemical attraction forces on a molecular level. In contrast, non-hygroscopic materials contain only unbound moisture. Unbound moisture exerts the equilibrium vapour pressure equal to that of pure liquid at a given temperature. As shown in Fig. 1.1, free moisture is defined in respect to the surrounding air humidity and refers to all moisture that can be evaporated within that environment.

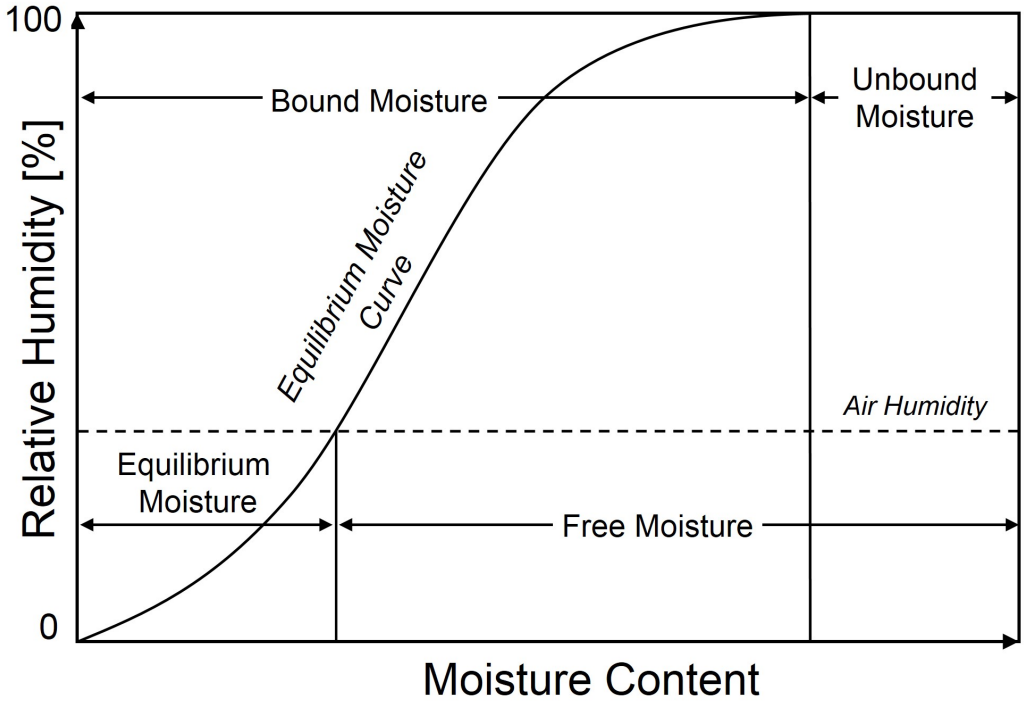

Figure 1.1: Equilibrium moisture curve indicating bound and unbound moisture at increasing moisture content of the solids (adpated from Masters [3])

1.1.1 Droplet Drying Stages

Droplets of a solution or a suspension dispersed in a drying gas experience different stages with changes in local temperature and mass. Developing a mechanistic understanding of the droplet drying process requires an accurate description of mechanisms dominating droplet evaporation and solidification. Droplet drying processes operating below the liquid boiling point can be sub-divided in four main characteristic stages which are shown in Fig. 1.2.

Stage A Droplets which are exposed to the drying gas are heated and liquid evaporation initiates. The droplet temperature converges close to the so-called wet bulb temperature of the solvent. The wet bulb temperature is characterised through effects of evaporative cooling and therefore is equal (saturated air) or lower (undersaturated air) than the temperature of the drying gas. The wet bulb temperature is a function of the drying gas temperature and the amount of water/solvent vapours in the gas phase.

Stage B In the second stage, the droplet reaches the constant rate period where evaporation is at a quasi-equilibrium. Unbound moisture is readily available at the droplet surface. The

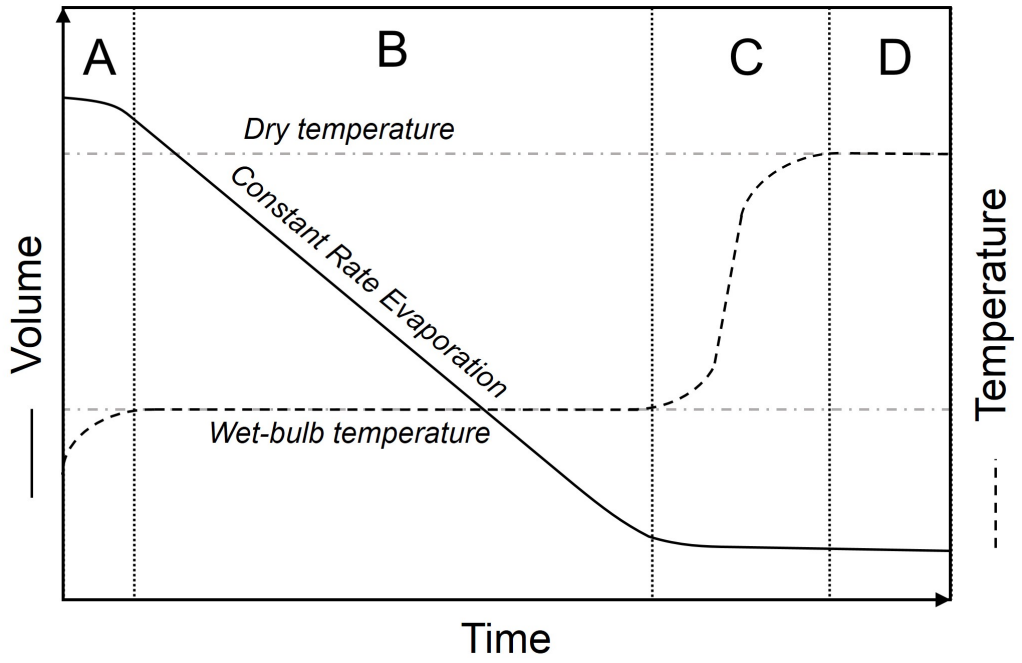

Figure 1.2: Drying stages for droplet evaporation below the liquid boiling temperature: A) Equilibration of heat- and mass-transfer, B) constant rate period, C) skin formation and reduced evaporation and D) reaching a dried particle state (figure adapted from Handscomb et al. [4]).

kinetics of liquid evaporation during this stage are limited by the heat-transfer to the droplet surface. The droplet temperature remains close to the wet bulb temperature. The solute concentration constantly increases with decreasing liquid volume, which itself can lead to a reduced liquid evaporation rate [5, 6, 7].

Stage C The droplet evaporation kinetics drastically change upon the formation of a solid phase crust on the droplet surface. This point is referred to as the lock point (LP) and often marks the begin of the falling rate period, however, various exceptions have been reported where changes in the drying rate do not directly correlate with a solid phase crust formation [8, 9, 10]. From solution, the precipitation of a solid phase can be observed after reaching a saturated state. Once a solid skin is formed, liquid evaporation is significantly reduced, which leads to an increase in the droplet/particle temperature. In this stage the system switches from a heat-transfer to a mass-transfer limited regime indicating that further drying is pre-dominantly influenced by the mass-transfer kinetics of residual free moisture through the solid crust.

Stage D The evaporation of liquid moisture is further reduced and the particle reaches a temperature equivalent to the ambient dry bulb temperature. The generated solid reaches its equilibrium moisture content or the evaporation of remaining liquid is hindered due to limitations of the mass-transfer through the solid phase crust.

The kinetics of these droplet drying stages are subject to selected process conditions and can deviate significantly. Additional stages can be introduced to describe drying of multi-solvent mixtures [11] or where the drying temperature exceeds the boiling point of the solvent [6, 4]. After solid phase formation at LP, the particle morphology and local solid micro-structure can have an impact on drying during stages C and D.

1.1.2 Mass- and Heat-transfer during Liquid Evaporation

The evaporation process within droplet drying platforms can be described by mechanisms of mass- and heat-transfer, which are introduced in Section 1.1.2.1 and Section 1.1.2.2, respectively. Mass-transfer can occur as diffusive and/or convective mass-transfer. Heat is transported via conduction, convection or radiation. Often multiple mechanisms of heat- and mass-transfer are involved during droplet evaporation [12]. This may require the deconvolution of observed heat- and mass-transfer kinetics to accurately describe the full complexity of the droplet evaporation process.

1.1.2.1 Mass-transfer

Changes of the droplet mass undergoing liquid evaporation are directly linked to changes in its volume (V_d) assuming constant liquid density (ρ_l). The evaporative mass-transfer ($\dot{m}_{vap}$) from the droplet surface to the gaseous bulk phase is defined as its time-derivative (Equation 1.1). For spherical droplets, the mass-transfer kinetics during the droplet drying process can be more specifically expressed through the time-derivative of the droplet radius ($\frac{dr_s}{dt}$) receding during liquid evaporation.

$$-\dot{m}_{vap} = \frac{d}{dt}\rho_l V_d = 4\pi \cdot r_s^2 \cdot \rho_l \cdot \frac{dr_s}{dt} \tag{1.1}$$

For ideal systems, $\frac{dr_s}{dt}$ can be calculated using information of the mass transfer coefficient (k_m), liquid molar mass (M_l), ideal gas constant (R), ρ_l and the arithmetic mean temperature (T_{av}) as

shown in Equation 1.2 [12]. The driver of the liquid evaporation is the difference in the liquid's partial vapour pressure between the surface ($p_{\mathrm{v},s}$) and the bulk of the gas phase ($p_{\mathrm{v},\infty}$).

$$\frac{dr_s}{dt} = -k_m \frac{M_l}{R\rho_l T_{av}}(p_{\mathrm{v},s} - p_{\mathrm{v},\infty}) \tag{1.2}$$

The liquid evaporation at the wet-bulb temperature is controlled by the energy flux in the form of heat required for liquid vaporization at the gas interface. In cases where the evaporation kinetics reach the constant rate period (Fig. 1.2, Stage B) and convection can be excluded, the volume changes of a spherical droplet evaporating over time (t) in an infinite, uniform, stagnant gas can be described using the d2-law in Equation 1.3, a mechanistic one-dimensional approach derived from Fick's second law of diffusion, to determine the time dependent droplet diameter ($d_s(t)$) from its initial diameter ($d_{s,0}$) and at a constant rate of evaporation (κ) [13].

$$d^2(t) = d_0^2 - \kappa t \tag{1.3}$$

With κ containing all of the system specific parameters:

$$\kappa = 8D_v \frac{\rho_g}{\rho_l}(Y_s(T) - Y_\infty) \tag{1.4}$$

D_v = diffusion coefficient of solvent in gas phase

Y_∞ = solvent concentration in gas phase

$Y_s(T)$ = temperature dependent solvent concentration on the droplet surface

ρ_g = density of gas phase

Mass transfer kinetics of the solvent from the droplet surface can significantly increase under convection. Convective mass transfer describes the transport of matter between a boundary surface and a moving fluid or between two immiscible moving fluids. Convective mass transfer can be divided in natural convection, i.e. caused by local changes in density within the fluid due to a temperature or concentration gradient, and forced convection, under the influence of an external force. The impact and extent of convective mass transfer has to be addressed to accurately describe the evaporation of droplets. The Sherwood number (Sh) is the ratio between convective and diffusive mass-transfer as shown in Equation 1.5. Sh is commonly employed

to express the extent of forced convection during droplet evaporation. For spherical droplets the characteristic length (L) corresponds to the droplet diameter ($2r_s$). For spherical droplets evaporating in stagnant air without convective mass transfer Sh yields a value of 2.

$$Sh = \frac{k_m \cdot L}{D_v} = \frac{k_m \cdot 2r_s}{D_v} \tag{1.5}$$

1.1.2.2 Heat-transfer

The process of liquid evaporation during droplet drying consumes heat for solvent vaporization ($\dot{m}_{vap} L_{vap}$ with L_{vap} = latent heat of evaporation) and creates a local heat sink with a temperature gradient between the droplet surface and the surrounding gas phase. The total heat flux ($\dot{Q}_g$) from the gas phase to the droplet is described by Equation 1.6 and corresponds to the heat for solvent vaporization and potential heat entering the droplet ($\dot{Q}_l$). $\dot{Q}_l$ can be determined from Equation 1.7 and depends on the droplet volume ($\frac{4}{3}\pi r_s^3$), ρ_l, the specific heat capacity of the liquid phase ($C_{p,l}$) and the temperature change of the liquid droplet ($\frac{\mathrm{d}T_d}{\mathrm{d}t}$). Heat transfer mechanisms between the droplet surface and its environment can be divided in substance-bound transfer mechanisms via conduction and/or convection and the substance-unbound transfer mechanism of thermal radiation.

$$\dot{Q}_g = \dot{Q}_l + \dot{m}_{vap} L_{vap} \tag{1.6}$$

$$\dot{Q}_l = \frac{4}{3}\pi r_s^3 \rho_l C_{p,l} \frac{\mathrm{d}T_d}{\mathrm{d}t} \tag{1.7}$$

Conductive heat transfer occurs on a molecular level where internal energy is transferred from more energetic to less energetic molecules along the local temperature gradient. The energy transfer in form of heat drives towards a thermal equilibrium between all bodies. The rate of conductive heat transfer is substance dependent and can consist of vibrations and collisions of molecules or free electrons diffusion. Fourier's law is shown in Equation 1.8 and describes the conductive heat flux density ($\dot{q}_{cond}$) between two regions as a function of the local temperature gradient (∇T) and the material's thermal conductivity (k_h). Integrated over the total heat exchange area (A), $\dot{q}$ yields the absolute conductive heat flux ($\dot{Q}_{cond}$).

$$\dot{q}_{cond} = -k_h \nabla T = \frac{d\dot{Q}_{cond}}{dA} \tag{1.8}$$

Convective heat transfer is promoted by fluid motion, which transports thermal energy of a liquid or gas. Convective heat transfer between the droplet surface and the moving gas phase involves a combination of diffusion and bulk motion of molecules. The fluid velocity is low in direct proximity of the droplet surface and diffusion dominates. Convective heat transfer can occur naturally, due to differences in the density within the liquid related to local temperature gradients, or under forced conditions induced by an external force such as a mechanical device like a pump or an agitator with no dependency of fluid motion to density gradients. Newton's law of cooling shown in Equation 1.9 is a re-statement of Fourier's law (Equation 1.8) and describes convective heat transfer employing the heat transfer coefficient (h) to determine the convective heat flux ($\dot{q}_{cov}$) between two regions with a temperature gradient (ΔT) over a film thickness (δ) where heat diffusion is dominant.

$$\dot{q}_{cov} = -h(\Delta T) = -k_h \frac{\Delta T}{\delta} \tag{1.9}$$

Radiative heat is transferred in the form of electromagnetic waves which are emitted by molecules as a result of thermal agitation and can pass through vacuum (substance-unbound) and regions of low temperature. Where the electromagnetic waves interact with matter, they are transmitted, reflected or absorbed. Absorbed electromagnetic radiation is transformed to internal energy including thermal energy. The electromagnetic waves can cover a wide band of wavelengths. Heat flow by radiation is most significant for wavelengths between 0.1 and 100 µm. The infrared (IR) spectrum is included in this range and covers wavelengths from 780 nm up to 1 mm. For thermal imaging with IR cameras, wavelengths from 0.8 - 20 µm are commonly analysed for a non-contact measurement of surface temperatures. The emissivity (ε) of objects depends on its material and describes its ability to emit thermal radiation in comparison to an ideal black body ($\varepsilon = 1$). The emissivity is used in IR imaging to correct the measured surface temperature values of real bodies. The radiative heat flux ($\dot{q}_{rad}$) from a ideal black body with the surface temperature T_{BB} can be calculated using the Stefan-Boltzmann law for radiant heat transfer in Equation 1.10 with the Stefan-Boltzmann constant $\sigma_S = 5.67 \cdot 10^{-8} W \cdot m^{-2} \cdot K^{-4}$ and ε to correct for the material's emissivity (grey bodies).

$$\dot{q}_{rad} = \sigma_S \cdot T_{BB}^4 = \sigma_S \cdot \varepsilon \cdot T^4 \tag{1.10}$$

Heat transfer is commonly described based on conductive and potential convective heat transfer. Here, the Nusselt number (*Nu*) can be used to express the ratio between both as shown in Equation 1.11. For spherical droplets the characteristic length (L) corresponds to the droplet diameter ($2r_s$). For spherical droplets evaporating in stagnant air without convective heat transfer *Nu* yields a value of 2.

$$Nu = \frac{h \cdot L}{k_h} = \frac{h \cdot 2r_s}{k_h} \tag{1.11}$$

As it is the case for mass-transfer (Section 1.1.2.1), forced convection can significantly increase the overall heat transfer to droplets. Information on the potential impact of forced convection on the heat-transfer kinetics need to be assessed to accurately describe droplet evaporation experiments [12].

1.1.3 Solid Phase Formation

The process of solid phase formation occurs during the transformation of a solution droplet into a dried particle. The emerging solid phase can consist of amorphous matter and/or structured crystal nuclei. Crystallisation is a fundamentally different process of particle formation connected to an emerging structured solid phase. Often both mechanisms of solid phase formation can be observed during the solidification process, especially for complex multi-component formulations.

1.1.3.1 Amorphous solid skin formation

The amorphous state lacks the long-range order that characterises crystalline matter, but has short-range order at the atomic length scale. The glass transition of an amorphous solid at the glass transition temperature (T_g) is characterised by the system's high level of entropy and free energy. Elevated temperatures above the glass transition temperature cause an increase in free volume and molecular mobility significantly lowering the material viscosity and increasing its heat capacity [14]. Below the glass transition temperature, the solid is (kinetically) stabilized in its glassy state as molecular mobility is dramatically reduced, although remaining molecular

mobility can not be fully neglected. Enthalpic relaxation effects of amorphous solids have been observed up to 50 K below the glass transition temperature [15, 16]. Amorphous formulations in the pharmaceutical industry have shown distinct performance characteristics and are a popular formulation approach for poorly water-soluble drug candidates (BCSII) [17, 18].

Solid skin formation at LP is often reported in the context of solidification of droplets from solution during evaporation. Amorphous skin formation occurs on the liquid-gas interface when the local concentration exceeds a critical concentration level. Theoretical explanation to describe the formation of a solid skin are often based on Péclet number considerations [1]. The dimensionless Péclet number (*Pe*) presented in Equation 1.12 describes the relation between the diffusion of the solute (D_s) and the receding droplet surface related to the liquid evaporation rate (κ).

$$Pe = \frac{\kappa}{8 \cdot D_s} \tag{1.12}$$

Pe is linked to the radial solute concentration profile in evaporating droplets and can be used as an indicator for the extent of surface enrichment of the solute (E). Equation 1.13 allows an estimation of E under steady-state evaporation in accordance with the d2-law (Equation 1.3) and for *Pe* values below 20 [19, 20] and corresponds to the ratio of the solute surface concentration (c_s) and its mean concentration (c_m) in the droplet.

$$E = \frac{c_s}{c_m} = 1 + \frac{Pe}{5} + \frac{Pe^2}{100} + \frac{Pe^3}{4000} \tag{1.13}$$

Slow solvent evaporation rates and a fast solute diffusion in the droplet gives a $Pe < 1$, which corresponds to a flat radial solute concentration profile ($c_s \simeq c_m$). In contrast, fast solvent evaporation rates and slow solute diffusion gives high *Pe* numbers ($Pe \gg 1$) resulting in an enrichment of the solute towards the droplet surface ($c_s \gg c_m$). High concentrations towards the droplet surface can lead to shell formation and result in large hollow particles.

1.1.3.2 Crystallisation and precipitation of crystalline matter

Crystallisation is the process describing the formation of an ordered solid phase from a vapour, solution or melt [21, 22]. The first-order phase transition of the crystalline matter at the melting point (T_m) is a discontinuous, highly endothermic event. Energy at the melting point is con-

sumed to reach the entropy level of the liquid state. Crystallisation from solution involves the formation of crystalline solids after exceeding the solute's thermodynamically defined solubility limit at a given temperature and pressure above which nucleation and growth can occur. The extent of the supersaturation (S) provides the driving force for crystallisation corresponding to a non-equilibrium thermodynamic state. Therefore, the driving force of the system ($\Delta\mu_c$) can be expressed as the difference between the chemical potential ($\Delta\mu_c$) in its current, non-equilibrium state (μ_c) and the equilibrium state ($\mu_{c,eq}$).

$$lnS = \frac{\Delta\mu_c}{RT} = ln\left(\frac{a}{a_{c,eq}}\right) = ln\left(\frac{\gamma c}{\gamma_{c,eq}c_{c,eq}}\right) \tag{1.14}$$

with

$$\Delta\mu_c = \mu_c - \mu_{c,eq} \tag{1.15}$$

where c is the solute concentration, a is the activity, γ is the activity coefficient, and $_{c,eq}$ marks the property at saturation [23]. For practical applications and assuming an ideal solution with an activity coefficient of 1, levels of supersaturation are expressed as the ratio of the solute concentration to its saturation concentration at the equilibrium state (solubility line, c_{eq}):

$$S = \frac{c}{c_{eq}} \tag{1.16}$$

Evaporative crystallisation is the isothermal process of reaching a supersaturated concentration through solvent removal as indicated in Fig. 1.3. Nucleation is expected to occur after crossing the metastable zone width (MSZW). The extent of the MSZW depends a wide range of system parameters including supersaturation kinetics, solvent choice and hydrodynamics [24, 25]. Important for small evaporating droplets, the MSZW has to be considered as a volume-dependent stochastic property rather than a volume-independent deterministic one [26]. In general, the chances of crystal nucleation tend to increase for droplets with high initial solute concentrations and fast crystallisation kinetics [20].

Primary nucleation is the formation of crystalline nuclei which emerge and grow from a clear solution. Primary nucleation can be further sub-categorised as homogeneous and heterogeneous nucleation. Homogeneous nucleation is defined as crystal formation excluding the impact of

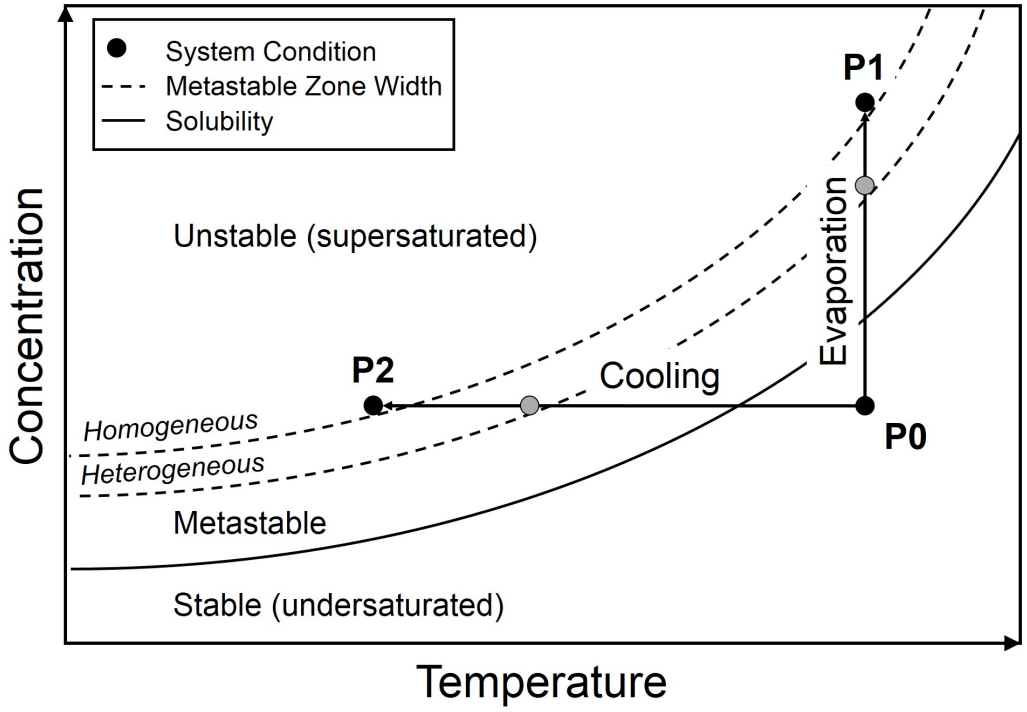

Figure 1.3: Solubility Phase Diagram: (**P0**) solution in under-saturated, stable state. Solvent evaporation and/or cooling can lead to levels of supersaturation where primary nucleation can occur at conditions indicated by **P1** and **P2**, respectively.

foreign materials (heteronuclei) on the nucleation i.e. through the presence of dust particles or walls of the crystallising environment. The presence of heteronuclei in a supersaturated solution reduces the energy barrier and therefore, the MSZW of heterogeneous nucleation is smaller than that for homogeneous nucleation as indicated in Fig. 1.3.

Secondary nucleation relates to the formation of nuclei in the presence of crystals from the same material. Secondary nucleation can be induced deliberately through the use of supersaturated seed-solutions, but are often linked to local hydrodynamics (e.g. fluid shear) and particle collisions leading to attrition. Secondary nucleation is commonly a dominating nucleation phenomenon in industrial crystallisations processes using stirred tank reactors [27], but is usually neglected in describing crystal formation in droplet drying platforms such as spray drying [28].

Polymorphs are different crystalline structures of the same chemical compound [29]. The polymorphic forms can potentially be found in any crystalline material and can exhibit significant differences in the crystal properties related to differences in packing and lattice energy. This can lead to distinct characteristics related to solid state stability [30], melting point [31], hygroscopicity [32, 30], compressibility [33, 34] and solubility [35, 30, 36].

1.1.4 Particle Properties

The droplet evaporation process yields particulates with distinct properties impacted by both, formulation and process parameters. Charlesworth and Marshall [37] reported changing particle morphologies observed during SDD experiments of aqueous solutions with varying initial solute concentrations and drying temperatures, demonstrating the value of droplet drying experiments to investigate the correlation between the droplet drying process and the final particle morphology. The structural properties of the final particle and its local solid phase composition are further directly linked to performance attributes including mechanical strength, flowability or dissolution rate. Potential pathways for the particle formation process from droplet drying platforms such as spray drying, leading to distinct final particle morphologies, are visualised in Fig. 1.4.

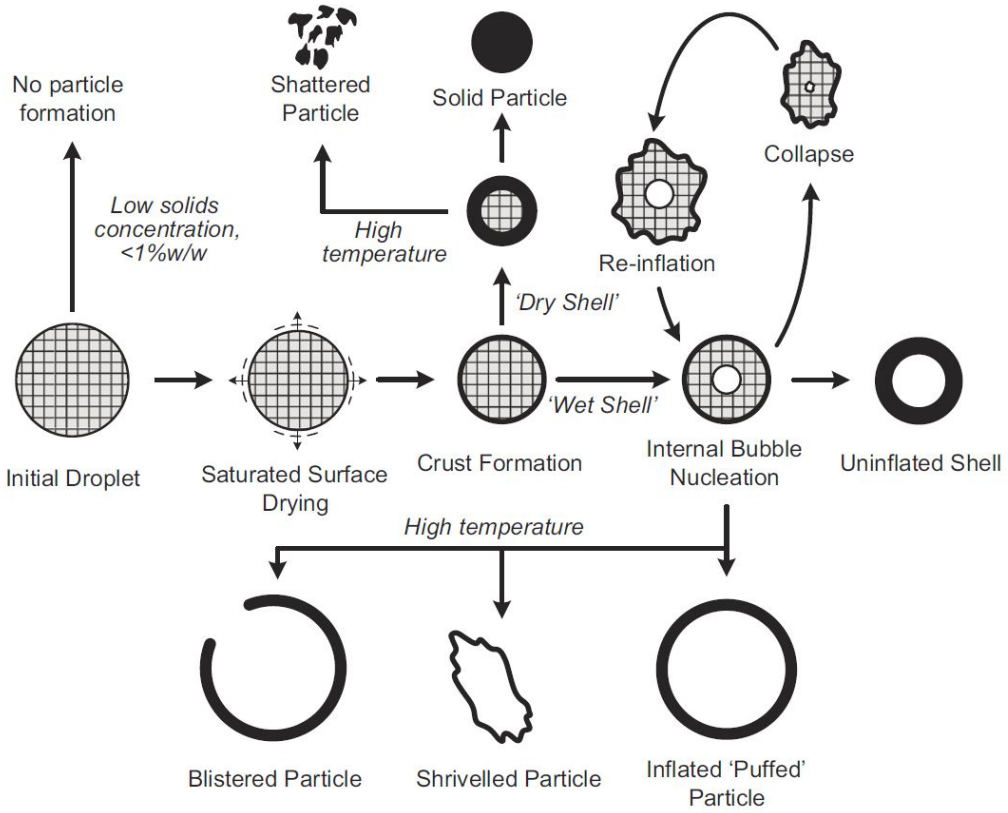

Figure 1.4: Particle morphologies obtained from evaporating droplets are influenced by formulation and process parameter. The final particles can exhibit differences in size, shape and internal micro-structure (from Handscomb [38]).

The final particle morphology is influenced by mechanisms of crystal and/or amorphous solid

phase formation as described in Section 1.1.3. Once an initial solid crust forms at LP, the drying kinetics change and further solid phase growth or nucleation occur in parallel to the drying process, with remaining moisture diffusing to the particle surface. Drying mechanisms and kinetics then strongly depend on the droplet/particle microstructure. Walton and Mumford [39] defined three distinct types of dried particle morphologies: skin forming, crystalline and agglomerate. Particles of each category exhibit characteristic drying behaviours. Low drying gas temperatures below the moisture boiling point often generate solid, dense, dried particles [40]. Aerated feeds might lead to the nucleation of internal bubbles or voids and yield an uninflated, hollow shell morphology [40]. Amorphous skin forming materials include large macro-molecules [41, 42]. After crust formation, these polymeric surface layers might permit further solvent diffusion and collapse over the further course of the evaporation. Sub-microcrystalline skins, which commonly comprise of crystals significantly smaller than the corresponding overall skin thickness and exhibit a dominant skin-forming behaviour, tend to be more rigid and often form cracks on the particle surface, which then enable further drying. Drying at elevated temperatures above the solvent boiling point tends to cause inflated, blistered or broken/shattered particles due to large internal solvent vapour pressures [43].

1.1.4.1 Particle Size

The size or size distribution (PSD) is a central property in the characterisation of individual particles or powders. The size is an important quality attribute since it can have an impact on the manufacturability as well as the performance of the solids within the production process or during their final application [44, 45, 46]. For pharmaceutical applications, control of the PSD is important during downstream processing e.g. filtration [47] or tablet compression [48, 46], but also due to its direct impact on the dissolution kinetics [49]. In general, smaller particles are preferred for fast dissolution profiles maximising the surface-to-volume ratio whilst larger particles are preferred during manufacturing and product handling. In spray dried powders designed for pulmonary drug delivery, particle sizes below 5 μm are targeted to reach the lungs airways for maximum therapeutic effectiveness. Commonly, the aerodynamic particle diameter (d_a) is optimised to improve the particle performance more accurately [50]. d_a is defined according to the particle's settling velocity and, therefore, it also takes into account effects of particle porosity and shape properties. Often, particle sizes are reported as a measure of width

(sieving), chord length (FBRM) or equivalent sphere diameter (laser diffraction), but may be expressed in alternative ways depending on the method employed for the measurement. Imaging techniques combined with image analysis drastically increase the possibilities of expressing and quantifying particle sizes [51, 52].

1.1.4.2 Particle Shape

The particle shape is another important quality attribute of (multi-)particulate systems linked to their manufacturability and performance. Optimising particle shapes can improve powder handling / flowability [53, 45], filtration [54, 55] and compaction [48]. Modifications of the particle shape for spray dried material have been further studied extensively for inhalation products. Here, the small particle sizes lead to dominant effects of Van-der-Waal forces, which can be reduced producing shrinkled particles with strong surface buckling for improved dispersibility of the powder [56, 57]. Particle morphologies are often investigated qualitatively employing imaging techniques e.g SEM or optical microscopy. However, the particle morphology can also be assessed (semi-)quantitatively using shape descriptors, for instance through aspect ratios, sphericity, or surface buckling [51, 58, 52, 7]. The particle morphology is a complex function of process conditions and formulation parameters. Particles from droplet drying experiments can further consist of multiple sub-particles of crystalline solids with specific shape properties defining the overall morphology of the aggregate. The crystal habit of these primary crystalline solids depends on the molecular packing in the crystal lattice and the growth kinetics of individual crystal faces during crystallisation.

1.1.4.3 Particle Porosity

Porosity is the ratio of the total pore volume within the apparent volume of individual particles. Pore volumes can be sub-categorized in open and closed porosities, which refers to the distinction between void space accessible from the particle surface and enclosed/encapsulated pores, respectively. Open and closed porosity can both have a significant effect on key particle performance attributes such as mechanical stability [59], compressibility [60], aerodynamic properties [61] and/or disintegration/dissolution profiles [62]. Spray dried particles with a solid foam structure are deliberately produced to achieve high levels of particle porosity [20]. A prominent example are PulmoSpheres^{TM} designed for pulmonary drug delivery and are utilised as carrier

or composite particles [63, 64]. The particle porosity is often measured as part of the bulk density of a powder, which captures internal particle porosity volumes and intra-particle void space [65]. Information on the bulk density are particularly important to link volume fill and weight fill methods during manufacturing. Particle porosity can be quantified using a broad range of characterisation techniques including helium pycnometry, mercury porosimetry and micro-XRT. Some of these techniques are size sensitive, are limited to bulk information and/or are complementary to each-other. A detailed comparison of techniques used to characterise pore structures of pharmaceutical products and their limitations is given by Markl et al. [66].

1.1.4.4 Particle Solid State

The solid state describes the molecular packing of the particle's solid phase, which can be categorized in crystalline (high/long range order) or amorphous (low/short-range order) domains as introduced in more detail in Section 1.1.3. Understanding the accessible solid state landscape can help to design drug products with tailored performance characteristics. Often, the thermodynamically most stable crystal form is chosen for production to avoid uncontrolled transformations to alternative crystal structures [21]. However, polymorphic forms might provide unique advantages in their performance as elaborated in Section 1.1.3.2. In this case, spray drying was able to provide a reliable route for the production of meta-stable polymorphic forms which were difficult to isolate on other unit operations [67]. The amorphous solid state form is thermodynamically less stable than its crystalline counterpart. Despite the resulting stability risks potentially leading to re-crystallisation events, the amorphous solid state has been targeted to achieve fast dissolution rates and high concentrations, especially as a formulation approach for drug candidates with low water-solubility (BSCII). Due to its rapid drying and solidification, spray drying is a popular route for the production of amorphous material [17, 18]. The solid state attributes of particles and multi-particle powders are routinely analysed to meet product specifications of solid state uniformity and stability. Unforeseen changes in the solid state can have severe implications in product efficacy and patient safety. The polymorphism of ritonavir is a prominent example to highlight the importance of solid state stability. In this case, a lower energy, more stable polymorph (form II) with reduced solubility appeared during the production compromising drug bioavailability, which led to a retraction of the oral capsule formulation from the market [68].

1.2 Single Droplet Drying Experiments using Acoustic Levitation

1.2.1 Single Droplet Drying Experiments - Introduction

Ranz and Marshall were the first to investigate droplet drying from solution and primary particle suspensions to gain information on heat- and mass-transfer kinetics [5]. Since then, droplet drying experiments have been used as a valuable method to obtain information about shrinkage behaviour [69], skin formation [70] and the buckling phenomena [71] of evaporating droplet systems undergoing drying. Fig. 1.5 shows four techniques which are commonly utilised to study the evaporation and particle formation process of droplets under controlled conditions: mono-disperse droplet drying towers [72, 73, 74, 75], sessile droplets [76, 77, 41, 78], filament method [5, 40, 79, 80, 81, 82, 83] and acoustic levitation [84, 85, 86, 87, 88, 7, 89]. Compared to the mono-disperse droplet drying tower, all other techniques are used for single droplet drying (SDD) experiments focused on the monitoring and the characterisation of individual droplets.

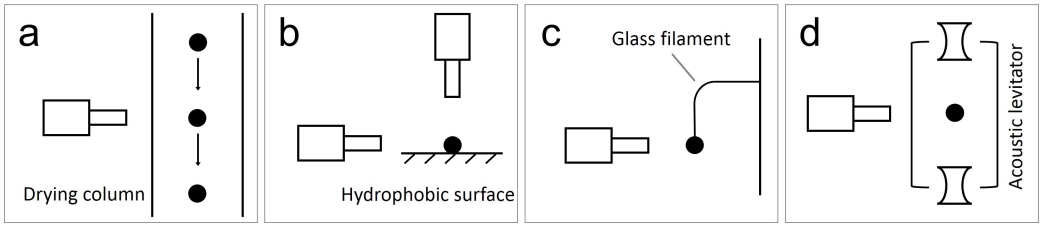

Figure 1.5: Droplet drying systems often used for characterising evaporation and particle formation: (a) mono-disperse droplet drying towers (b) sessile droplets, (c) filament method and (d) acoustic levitation.

Mono-disperse droplet drying towers (Fig. 1.5 a) are a spray drying characterisation platform in which a well-defined, mono-disperse droplet chain is dried after being dispersed in a drying gas within a drying column. The maximum droplet sizes are often limited to achieve full drying within the column during free-fall. Mono-disperse droplet drying towers allow fast solidification and represent well the drying conditions in a spray dryer. However, instead of monitoring individual, single droplets, the camera is moved along the drying column to monitor the drying state at defined distances from the dispenser.

Sessile droplets (Fig. 1.5 b) is a SDD technique, where individual droplets are monitored while undergoing drying, after being dispensed on a hydrophobic (heated) surface. Heated surfaces with temperatures significantly above the liquid's boiling point induce the Leidenfrost effect

producing a vapour layer between the droplet and the surface. Despite its utility to enable SDD experiments, this technique is criticised due to its differences in the flow and temperature field compared to droplets drying in a spray dryer.

The glass filament method (Fig. 1.5 c) is among the most used platforms to perform SDD experiments. Individual droplets are suspended from filaments in a controlled environment. Droplet drying and solidification can be observed with imaging techniques, but the droplet weight can also be monitored connecting the filament to a micro-balance [81]. Others have replaced the glass filament with a thermocouple to acquire local temperature information of the droplet [40]. Limitations of this technique are the heat conduction between the droplet and the filament as well as potential risks related to heterogeneous crystal nucleation elaborated in Section 1.1.3.2.

Compared to the other platforms, acoustic levitation (Fig. 1.5 d) enables contact-less SDD experiments within a controlled drying environment. A detailed description of this technique and its previous application for spray drying process development are provided in the following sections.

1.2.2 Single Droplet Drying Experiments - Acoustic Levitation

Compared with other levitation techniques (magnetic levitation and electrostatic levitation), acoustic levitation has no specific restrictions on the levitated particles, such as their electric or magnetic properties. Therefore, acoustic levitation can be used to levitate a broad range of aqueous and organic solutions. The technique of levitating spheres in a standing acoustic wave was first described as early as 1934 [90]. Acoustic levitation uses ultrasound to create a pressure field typically between two transducers or a single transducer and a reflector that can be utilised to levitate small liquid droplets or particles. Pressure nodes within the standing acoustic wave hold the levitated object in place. A schematic of an acoustic levitator is shown in Fig. 1.6a. The distance between the two transducers has to be an integral multiple of the half wavelength of the ultrasonic wave (λ) to create a standing acoustic wave. The pressure nodes and anti-nodes are separated by a half a wavelength ($\lambda/2$). Levitated samples are positioned slightly below the pressure node due to gravity and the vertical displacement is proportional to the sample size and density [91]. Thus, the droplet/particle will rise within the acoustic field over the course of a SDD experiment. Acoustic levitation was successfully utilised to levitate metals with densities

of up to 22.6 g·cm^{-3} such as iridium and liquid mercury [92]. For liquids, the force field leads to a deformation of the droplets to an oblate spheroid, which is related to differences between radial (Fig. 1.6a, F_r) and axial forces (Fig. 1.6a, F_z). The extent of the droplet deformation is related to the applied sound pressure and excessive acoustic pressure levels can even result in a rupturing of the droplets. The force field of radial and axial forces prevents the levitated sample from leaving the local pressure node and ensures stable positioning [93].

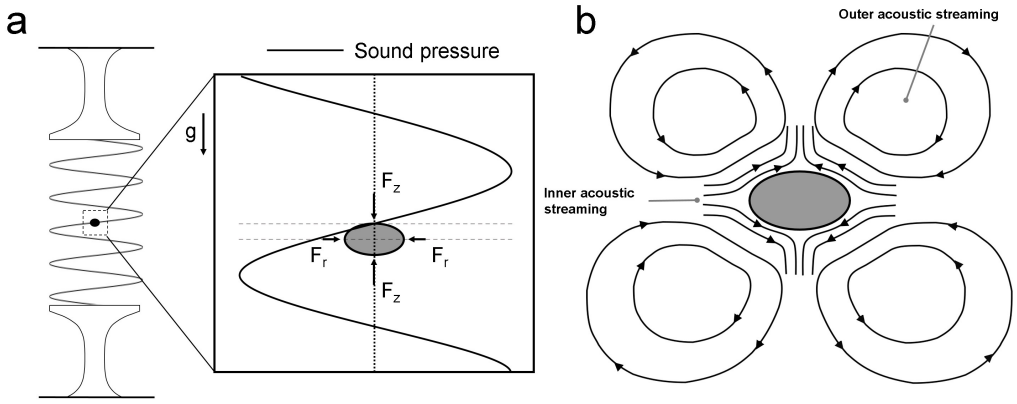

Figure 1.6: (a) Single-axis acoustic levitation in a two-transducer system with a standing acoustic wave for single droplet drying experiments. Differences between radial (F_r) and axial forces (F_z) lead to a deformation of the droplet into an oblate spheroid. (b) Forced convection on the droplet surface due to acoustic streaming (adapted from Tuckermann et al. [94] and Yarin et al. [95])

The absorption of high amplitude acoustic oscillations induces a movement of the gas phase around the levitated sample commonly referred to as acoustic streaming. Inner acoustic streaming is found at the surface of a droplet (near-boundary streaming [96]) creating an acoustic boundary layer, whilst the outer acoustic streaming describes larger toroidal vortices induced through the inner acoustic streaming. The effect of acoustic streaming is shown schematically in Fig. 1.6b. Acoustic streaming causes forced convection at the droplet surface, which can become the primary driving force for evaporation and, therefore, the drying process can significantly differ from purely diffusion-based evaporation in stagnant air as described by the d2-law (Section 1.1.2.1) [95, 97].

Image analysis methods are often used to monitor and record the droplet evaporation process in acoustic levitation experiments. Imaging techniques have been utilised previously by various groups to extract relevant information from the droplet including size and shape descriptors and detect the formation of emerging solids [95, 93, 98, 99]. Furthermore, infra-red thermography

can be used to measure the droplet surface temperature [99, 93]. This gives additional insights into the conditions during heat- and mass-transfer at the droplet/particle surface.

1.2.3 Single Droplet Drying Experiments - Spray Drying Process Development

In a spray dryer, individual droplets are generated during liquid atomization from a continuous liquid feed. These droplets represent small micro-systems undergoing liquid evaporation, solidification and drying as part of a population of droplets dispersed into the drying gas. SDD experiments can be used to gain a better understanding of the solidification process during droplet drying whilst minimising material and time consumption [12, 100, 101, 102, 103, 104]. Information from SDD experiments have further potential to inform spray drying models used for process development and have been used to systematically investigate the drying of carbohydrate-rich formulations linking drying behaviour to inactivation kinetics of enzymes and probiotics in spray drying processes [105]. DRYNETICS^{TM} is a proprietary method offered as a service by GEA Process Engineering (Soeborg, Denmark) exploiting SDD experiments in an acoustic levitator to inform spray drying applications [106, 107, 108]. Spray drying process models create the link between SDD experiments and process implementation/scale-up. However, there is an ongoing need to develop a better understanding of the droplet drying process to be able to effectively translate experimental results from the SDD experiments to spray drying applications. Current research employing SDD experiments in an acoustic levitator focuses on the understanding of particle morphology development [87, 88, 7], local chemical composition and phase segregation[109, 87], peptide aggregation and inactivation during drying [104] or drying kinetics of particle suspensions [102, 103].

1.3 Spray Drying

Spray drying is a classical unit operation in the pharmaceutical, food and chemical industry to transform a solution or suspension into a dry powder of solid particulates [3]. Spray drying is an inherently continuous process and has been employed for the production of a wide range of (bio-) materials as a rapid isolation and drying process. In the pharmaceutical industry, it gained particular interest in the 1990s for the production of inhalable powders acting as a carrier platform for biomolecules, most notably recombinant human insulin [110].

Fig. 1.7 shows a simplified process flow diagram of a laboratory scale co-current spray dryer.

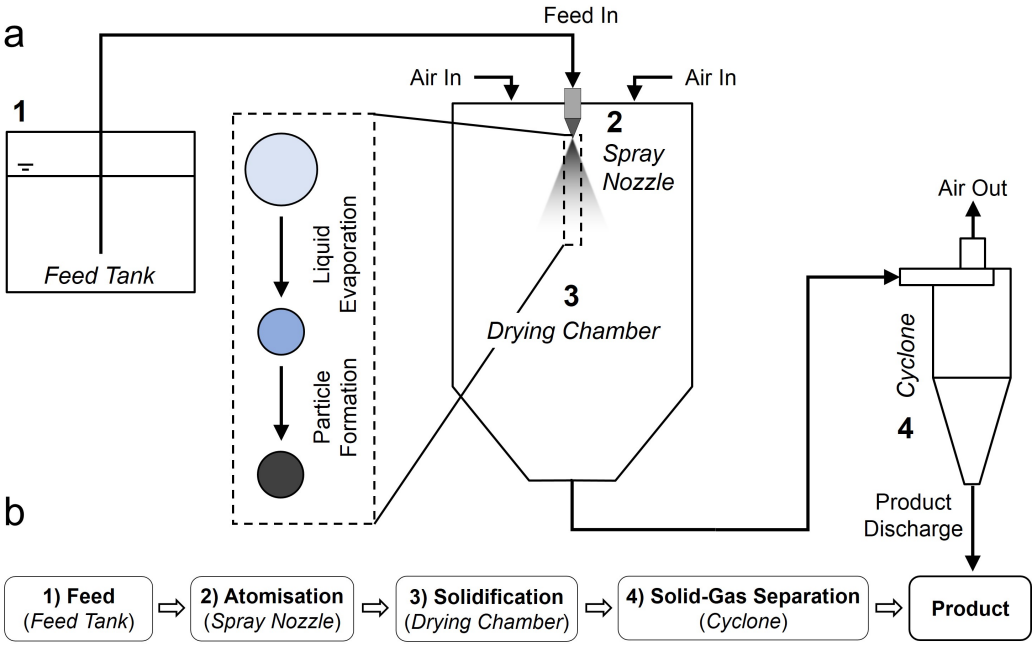

Figure 1.7: (a) Basic co-current spray dryer design: (1) liquid feed, (2) feed atomisation into droplets, (3) droplet drying and solidification and (4) solid-gas separation. (b) Fundamental steps during spray drying.

A liquid feed (1) is continuously pumped into the process. The spraying nozzle (2) atomises the liquid into a population of fine droplets dispersed within the hot drying gas. The particle formation process inside the drying chamber (3) is complex and involves simultaneous transfer of heat, mass and momentum between the droplet population and a partially turbulent drying gas. For solutions, the droplet drying stages can be categorized in phases of pure liquid evaporation and droplet solidification after crust formation as previously discussed in Section 1.1.4. The particles are then transported with the gaseous stream to a solid-gas separation unit (4), commonly in the form of a cyclone, where the product is discharged or collected. For particle engineering applications, spray drying offers opportunities to generate (formulated) particle systems with unique performance attributes e.g. regarding aerodynamic properties for inhalation [111, 112], stability [113], compaction/tabletability [114], flowability [42] or dissolution [20, 115, 116].

1.3.1 Process Model

Process models aim to enable an interpretation and prediction of process and product properties to guide and inform process design aspects [117]. Models have been developed to describe

droplet drying at all levels, from the microscopic scale employing molecular dynamics simulations of single droplets [118, 119] to large, macroscopic models capturing the full spray drying system [120, 121, 122]. Models aiming to describe the full spray dryer can be further distinguished stretching from approaches utilising simple concepts of mass- and heat-balance to extensive simulations of complex three-dimensional flow patterns. The latter one involves the use of computational fluid dynamics (CFD) for the prediction of local droplet drying kinetics [117]. The integration of a droplet drying model is needed wherever a local prediction of droplet drying is desired to distinguish between droplet drying stages with distinct drying kinetics (see Section 1.1.4). Coupled with CFD, these droplet drying models allow a spatially resolved description of the (polydisperse) droplet population along the simulated particle trajectories. These models are computationally expensive and require extensive information on material properties as well as precise experimental data for parameter estimation and model validation. The selection of the appropriate spray drying model is linked directly to the desired merits of the modelling approach itself e.g. to interpret and guide experimental process optimisation with a global mass- and heat-balance [123, 124], to predict particle size distributions and residual moisture levels in spray dried powders using a (semi-) empirical mathematical description of the spray dryer with an integrated droplet drying model [122], or working with droplet dying models linked to CFD simulations to enable a full optimisation of the spray dryer working towards improvements related to equipment engineering or a translation and scale-up between platforms [120, 121].

A typical lab-scale spray dryer used for pharmaceutical research and small-scale production is the B-290 Mini-Spray Dryer (Büchi Labortechnik AG, Switzerland, Fig. 1.8). A mass balance (Equation 1.17) needs to take into account the drying gas ($\dot{m}_{g,in}$), the spray gas ($\dot{m}_{a,in}$) and liquid feed ($\dot{m}_{l,in}$) going into the system as well as mass flows leaving the systems, e.g. produced solid mass flow ($\dot{m}_s$) and exhaust air mass flow ($\dot{m}_{g,out}$). $\dot{m}_{g,out}$ consists of $\dot{m}_{g,in}$, $\dot{m}_{a,in}$ and the evaporated liquid during drying ($\dot{m}_{vap}$). Wall depositions ($\dot{m}_{loss}$) are a common problem in spray drying [125, 126] and have to be included in the overall mass balance reducing the solid mass flow discharged by the cyclone ($\dot{m}_{s,out}$).

$$\dot{m}_{l,in} + \dot{m}_{a,in} + \dot{m}_{g,in} = \dot{m}_s + \dot{m}_{g,out} = \dot{m}_{s,out} + \dot{m}_{loss} + \dot{m}_{a,in} + \dot{m}_{g,in} + \dot{m}_{vap} \tag{1.17}$$

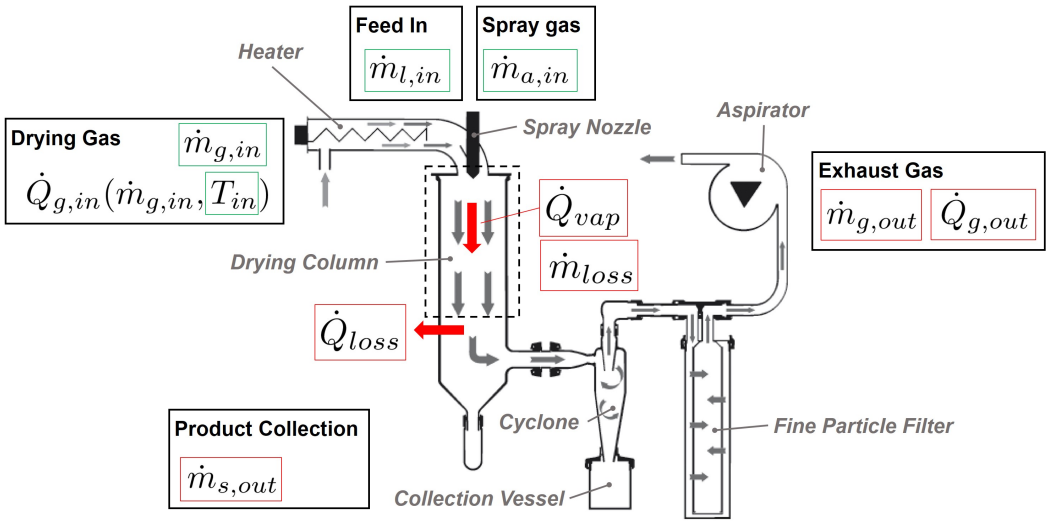

Figure 1.8: Lab-scale spray dryer (Type: B290, Büchi Labortechnik) in open loop configuration. Process parameters which can be directly selected are marked in green and consist of the drying temperature (T_{in}), the aspirator rate controlling the drying gas mass flow ($\dot{m}_{g,in}$), the feed rate ($\dot{m}_{l,in}$) and the spraying gas influencing droplet atomisation ($\dot{m}_{a,in}$). Dependent process variables (marked in red) are the solid mass flow discharged by the cyclone ($\dot{m}_{s,out}$), the exhaust gas mass flow ($\dot{m}_{g,out}$), potential wall depositions ($\dot{m}_{loss}$) and those related to the overall heat balance of the system e.g. evaporative heat consumption ($\dot{Q}_{vap}$), heat loss over the equipment walls ($\dot{Q}_{loss}$) or exhausted heat ($\dot{Q}_{g,out}$). Figure adapted from Operation Manual - Mini Spray Dryer B-290 [127].

A simplified heat balance for the spray dryer is presented in Equation 1.18. The heat of the drying gas ($\dot{Q}_{g,in}$) provides energy for liquid evaporation ($\dot{Q}_{vap}$), however, heat also leaves the system with the exhaust gas ($\dot{Q}_{g,out}$). For a more detailed heat-balance, one also has to take into account additional areas of energy consumption such as heating of $\dot{m}_{l,in}$, $\dot{m}_{s,out}$ and $\dot{m}_{a,in}$. For the B-290 Mini-Spray Dryer, the heat loss over the equipment's glass walls ($\dot{Q}_{loss}$) is significant whilst drying at temperatures above the local environment. A detailed characterisation of the B-290 Mini-Spray Dryer is described in Chapter 7.

$$\dot{Q}_{g,in} = \dot{Q}_{g,out} + \dot{Q}_{vap} + \dot{Q}_{loss} \tag{1.18}$$

The heat balance can be re-written using the specific enthalpy (h) and latent heat of liquid vaporisation (Δh_{vap}).

$$\dot{m}_{g,in} \cdot h_{g,in} = (\dot{m}_{a,in} + \dot{m}_{g,in}) \cdot h_{g,out} + \dot{m}_{vap} \cdot \Delta h_{vap} + \dot{Q}_{loss} \tag{1.19}$$

1.3.2 Process Parameters

The following sections introduce additional aspects of spray drying operation on a lab-scale platform, specifically elaborating on process parameters of the B-290 Mini-Spray Dryer and their effect on the final product properties. Their optimisation often involves a tedious experimental assessment, ideally within a structured Design-of-Experiments (DoE) approach. A firm understanding on the potential impact of individual process parameters helps to reduce experimental efforts. Moreover, Section 1.3.3 reviews the use of process analytical technology (PAT) in spray drying processes and Section 1.3.4 focuses on relevant offline product characterisation methods.

1.3.2.1 Aspirator Rate

The aspirator rate is a measure controlling volume flow of the drying gas ($\dot{m}_{g,in}$) through the spray drying system. Increasing the volume flow of the drying gas intensifies the enthalpy throughput of the spray dryer and reduces drying gas moisture loading (relative humidity), however, also decreases the mean residence time in the system, which shortens the available drying time for droplets/particles suspended in the drying gas. Changes in the relative humidity levels due to a reduction of the aspirator rate can influence the moisture content of the particle products [126].

1.3.2.2 Drying Temperature

The drying temperature (T_{in}) is one of the central parameters describing the drying process and directly influences the droplet drying kinetics. Changes in the drying temperature can impact particle size, shape and porosity attributes, especially when operating above the liquids boiling point [39]. The use of high drying temperatures can damage heat-sensitive materials causing denaturation or decomposition, however, the evaporative cooling effect protects these materials under rapid drying conditions and solids are expected to experience temperatures close to the exhaust gas temperature [3]. The exhaust gas temperature is impacted by the selected drying temperature and can therefore be optimised to design the spray drying process using considerations of the product's T_g and the material's thermal stability.

1.3.2.3 Feed Rate

The feed rate defines the mass flow of the liquid feed ($\dot{m}_{l,in}$) transported to the spray dryer for drying. On lab scale, solutions or suspensions are often fed into the process using a peristaltic pump. The feed rate has to be evaluated as part of a mass- and energy-balance to make successful drying feasible. Higher feed rates cause a raising heat consumption required for liquid vaporization, leading to decreased exhaust gas temperatures, higher relative humidity levels and potentially higher levels of residual moisture. Therefore, the feed rate has a direct effect on the drying efficiency.

1.3.2.4 Atomization

During atomization, the liquid feed is dispersed into a spray of fine droplets. The population of droplets drastically increases the surface area of the liquid feed entering the drying chamber accelerating heat- and mass-transfer kinetics. The atomization step is important for the final product properties and the overall process economy. A narrow droplet size distribution is beneficial to produce powders with homogeneous drying history.

On lab-scale, the drying of large droplets is often not achievable due to the short residence times of the droplets, which are assumed to be less than one second (i.e. estimated average 0.2 - 0.3 s [120]). In this case atomization must be balanced between restrictions for droplet drying kinetics and the desired particle properties. Most commonly, atomization on lab-scale is performed using a two-fluid nozzle, which is based on the dispersive force of a high velocity gas brought into contact with the liquid feed ($\dot{m}_{l,in}$) at the nozzle tip. Increased spray gas volume flows ($\dot{V}_{a,in} \propto \dot{m}_{a,in}$) with accelerated terminal velocities lead to smaller droplet size distributions. The generated droplet size distribution has an impact on the final particle size and the kinetics of the drying process. Typical droplet sizes of the B-290 Mini-Spray Dryer are between 2 and 50 μm [128].

1.3.3 Process Analytical Technology

Process analytical technology (PAT) has been defined by the United States Food and Drug Administration (FDA) and is referred to as technical measures to design, analyse, and control pharmaceutical manufacturing processes through the monitoring of Critical Process Parameters

(CPPs) with an impact on Critical Quality Attributes (CQAs) [129]. In the context of spray drying, CCPs are often linked to those CQAs affected by the temperature history of the product and to those CQAs directly influencing particle properties described in Section 1.1.4. PAT is regularly employed for pilot- or production-scale spray drying processes, but often disregarded for lab-scale. The use of PAT capabilities on lab-scale has the potential to reduce the time required for process development, implementation and optimisation. Linked to a model-predictive control approach, information from PAT can assure more reliable process operation by measuring and addressing potential system variability, for instance in the ambient air humidity [130]. The recorded process data can further be used to validate mechanistic or inform data-driven modelling approaches e.g. for up-scaling.

On lab-scale spray driers, temperature information is regularly recorded to optimise the spray drying process to minimise risks of thermal damage to the product [131], to reduce residual moisture levels [131, 126, 132] or to improve overall process yields and product manufacturability [131, 126, 132]. Process yields might be drastically reduced operating above the material's glass transition temperature [125]. The relative humidity of the drying gas can be measured to gain a better understanding of its capability for additional moisture uptake to increase throughput or improve process economics by maximising the humidity in the exhaust gas [123]. Recently, Raman spectroscopy was used as PAT to monitor the production of a metastable polymorph via spray drying on lab-scale [67]. An overview of potential PAT applications is provided in Table 1.1.

1.3.4 Product Characterisation

Beside the employment of PAT within the process, the control of CQAs can also be achieved using additional offline characterisation techniques. A wide range of offline characterisation techniques can be employed to develop, optimise and control products from lab-scale spray drying experiments. Individual techniques are selected according to the overall research objective and probe different product properties. A selection of commonly utilised characterisation techniques for the offline analysis of spray dried powders is provided in Table 1.2. Often multiple techniques are required to collect conclusive information from the powder samples.

Offline characterisation techniques play a vital role during process and product development. They aim to selectively deliver information on potential quality attributes which cannot be mon-

Table 1.1: Potential applications of PAT in spray drying to directly monitor product CQAs and/or independent process parameters.

Technique	**Description**
Process viscometer	Analysis to measure feed viscosity with a direct impact on droplet atomization [133, 134]. The fluid viscosity is commonly determined due to the shear stress imposed on the fluid by a moving part of the instrument.
Focused beam reflectance measurement	Analysis to detect potential agglomeration indicating problems related to feed (suspension) stability. Consists of a focused, rotating laser beam and measures chord length distributions from backscattered laser light of particles passing through the scanning zone [135, 136].
Process laser diffraction	Analysis of real-time particle size distribution after drying prior to solid-gas separation [137]. Analysis of the diffraction patterns of a laser beam passing through a sample.
Thermocouples / resistance thermometers	Measuring drying and exhaust temperature in the process. The temperature profile throughout the process gives important information about heat input, drying capacity, heat loss (heat dissipation via walls/exhaust) and thermal risks for the product. Enables process control for optimised drying conditions below T_g.
Pressure sensors	Typically measuring local differential/absolute/gauge pressure levels. It can indicate blockage in the process e.g. cross-filter resistance of the fine particle filter. There is a wide range of analogue and digital pressure sensors available.
Gas flow meters	Measuring gas flow of the spraying gas and/or drying gas. It allows a more reliable control of droplet atomisation and evaluation of the heat capacity of the drying gas. There is a wide range of analogue and digital gas flow meters available.
Process near infrared spectroscopy (P-NIR)	P-NIR is used for exhaust gas analysis to monitor solvent concentration/composition in the gas phase. Requires a concentration calibration for reliable quantification. Is based on a spectroscopic analysis of overtones and combinations of bond vibrations in molecules.
Process mass spectroscopy (P-MS)	P-MS is used for exhaust gas analysis to evaluate its molecular composition. High sensitivity for the detection of compounds with low concentrations. Chemical entities are ionised and separated according to their mass-charge ratio prior to detection.

Table 1.2: Overview of selected offline characterisation techniques for spray dried products aiming to investigate particle size and shape properties as well as solid state structure and residual moisture content.

Technique	**Description**
Particle size and shape	
Light-microscopy	Uses visible light and lenses to magnify and visualise small objects (size range: μm to cm). Optical imaging for a qualitative investigation of particle properties related to size, shape and morphology [43]. Image analysis capabilities allow the extraction of quantitative information.
Scanning electron microscopy (SEM)	Scans the surface of objects with a focused beam of electrons (size range: nm to mm). The sample topography (and composition) can be resolved e.g. through the detection of secondary electrons, reflected or back-scattered electrons, characteristic X-rays or transmitted electrons. SEM is an imaging technique for a qualitative investigation of particle properties related to size, shape and morphology [138, 139, 140].
Laser diffraction (LD)	Analysis of the diffraction patterns of a laser beam passing through a sample (size range: $\sim$ 0.2 µm to 3500 µm). Uses Fraunhofer or Mie theory to relate diffraction pattern to particle size information assuming spherical particles [56].
Particle Solid State	
Differential scanning calorimetry (DSC)	Thermoanalytical technique comparing the heat flux required to increase the temperature of a sample and a reference as a function of temperature. DSC can be used to detect (and quantify) phase transitions related to melting/crystallisation temperatures, glass transition temperatures or evaporation/condensation [141, 142].
X-ray powder diffraction (XRPD)	Uses X-rays for the characterization of the long-range solid-state structure in materials [143, 144, 67]. Patterns of scattered X-rays are commonly presented in a diffractogram and peaks can be related to unit cell parameters of crystalline materials in accordance with Bragg's law. Pair Distribution Function (PDF) analysis of high quality XRPD data can be used to extract information on local, short-range order, which is of particular interest for amorphous systems.
Residual Moisture	
Thermogravimetric analysis (TGA)	Thermal analysis method quantifying changes in sample mass as a function of time and temperature. Information allow the detection and quantification of bound and unbound/free moisture [112, 145]. TGA can be coupled with mass spectrometry (TG-MS) to analyse the exhaust gas and relate changes in sample weight to the evaporation and/or decomposition of chemicals with distinct TG-MS pattern.
Karl-Fischer Titration (KF)	Titration method to quantify trace amounts of water in samples. KF relies on a reaction which consumes water. KF offers high accuracy and precision, but is selective for water only [146, 147].
Gravimetric Analysis	Simple quantitative analysis based on mass changes after storing the sample in a humidity- and temperature-controlled environment (loss on drying (LOD) method) [147]. Commonly samples are stored under (partial) vacuum conditions for extended time periods (> 24 hours). The sample mass is monitored until a stable end-weight is reached. This technique requires larger quantities of material (> 30-50 mg) to reduce the impact of weighing errors. A moisture balance is designed to quantify residual moisture using the LOD method under accelerated conditions for selected drying profiles.

itored online, but are critical to ensure the quality of the product. Spectroscopic methods such as Fourier transformation infra-red spectroscopy (FT-IR) spectroscopy or Raman spectroscopy are selectively employed for specific compound systems to gain additional information on solute aggregation and secondary structure [148], local phase separation [149] or solid state form [140]. Physical properties such as size and shape are some of the most commonly assessed quality attributes to characterise multi-particle systems such as spray dried powders. In this regard, recent developments of image based techniques enabled applications for quantitative particle size and shape analysis overcoming limitations of laser diffraction for non-spherical shapes. An additional offline characterisation technique that finds increased applicability for pharmaceutical (particulate) solid products is micro-X-ray tomography (micro-XRT). Micro-XRT allow a full 3D characterisation of the particle structure and potential changes in the solid phase composition introduced in more details in Section 1.4.

1.4 X-ray Tomography

Micro-X-ray tomography (micro-XRT) is a popular non-destructive 3D imaging technique to visualise and investigate the internal structure of a wide range of samples, especially used for bio-medial imaging [150, 151] or applications in geoscience [152, 153, 154, 155]. For pharmaceutical solid products, micro-XRT has been successfully used to characterise various (intermediate) products including particles [156, 7], coated pellets [157, 158], spray dried powders [159] and tablets [160, 161]. Coupled with effective means of quantification through image processing and analysis strategies, micro-XRT has great potential to become a standard technique for the characterisation of pharmaceutical solid products covering the manufacturing process from single particles to fully formulated, final products. This section introduces basic principles of micro-XRT sample characterisation related to raw data acquisition (Fig. 1.9 a, Section 1.4.1) and reconstruction (Fig. 1.9 b, Section 1.4.2). Additionally, Section 1.4.4 reviews advances towards a quantitative analysis of the reconstructed micro-XRT image data to extract desired sample information of local phase composition and/or structure (Fig. 1.9 c).

1.4.1 XRT - image acquisition (scanning)

Transmission micro-XRT is a powerful technique to investigate the morphology and internal micro-structure of a wide variety of solid samples. Micro-XRT is based on differences in the X-

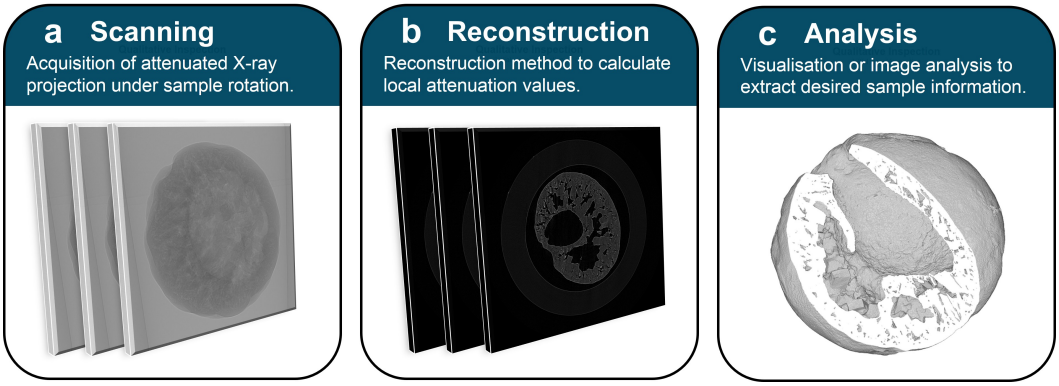

Figure 1.9: Generic steps during a micro-XRT characterisation: (a) raw data acquisition during scanning, (b) image reconstruction and (c) 3D sample visualisation/quantitative analysis.

ray attenuation (μ) of an electromagnetic wave traversing through the sample solid phase. For pure monochromatic beams, the X-ray attenuation follows the Lambert-Beer's law shown in Equation 1.20. The intensity (I) is attenuated in comparison to the incident radiation intensity (I_0) along the beam path between source and detector(x).

$$I = I_0 \cdot \exp(-\mu x) \tag{1.20}$$

In case of lab-based micro-XRT systems, the emitted beam is typically composed of a target-specific, polychromatic X-ray spectra. For such polychromatic beams, the attenuation coefficient varies as a function of each specific energy level, which has to be considered during reconstruction to compensate for beam hardening artefacts (see Section 1.4.3). The effective X-ray attenuation can be influenced by absorption, scattering (elastic or inelastic), diffraction or refraction of photons from the beam. The attenuation depends on the individual atomic electron density of the interacting components and the overall bulk density of the sample region. For low-energetic X-rays (50–100 keV, Fig. 1.10 a), effects of photoelectric absorption dominate over scattering and X-ray attenuation strongly correlates with the atomic number of the elements [162, 153]. Therefore, micro-XRT can be used to investigate local solid phase composition for compounds carrying distinct elements or changing local bulk density, which can be resolved in the two-dimensional projections related to intensity differences of the attenuated beam [153]. Micro-XRT contrast media containing elements with excellent K-edge characteristics are capable of significantly increasing the effective attenuation coefficient due to the photoelectric absorption of X-rays. Micro-XRT contrast media have been applied in various studies for bio-

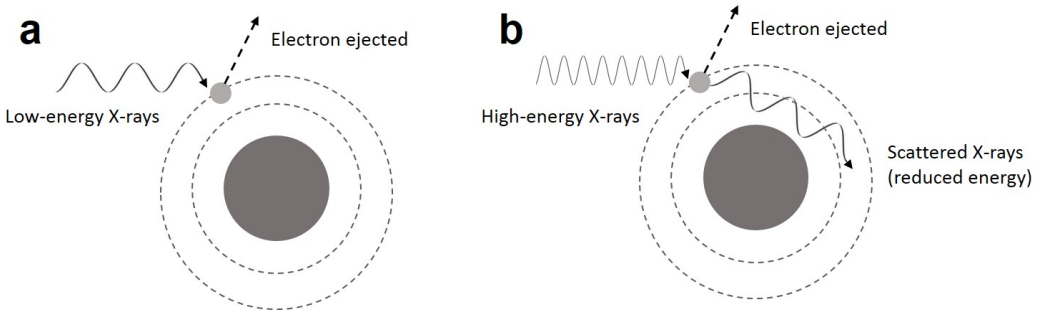

Figure 1.10: Visualisation of X-ray attenuation through (a) photoelectric effect (photoelectric absorption) dominant at low X-ray energies and (b) scattering of high-energy X-rays.

medical research to selectively enhance the phase contrast [163, 164, 165, 166, 167]. A common staining agents for biological micro-XRT samples are iodine-based solutions e.g. Lugol's solution [163].

Time-resolved (4D) micro-XRT applications aim to monitor structural changes over time e.g. during particle dissolution, which can give unique insights into system disintegration [168]. A time-resolved micro-XRT characterisation needs to balance image acquisition times and micro-XRT image data quality within the assessed imaging time-scales. Often the data-acquisition is performed on synchrotron beamlines, which can significantly reduce scanning times [169].

In lab-based micro-XRT systems, the sample object is typically mounted on a rotation stage between the X-ray source and a detector. In cone-beam X-ray tomography systems with geometric magnification (illustrated in Fig. 4.1b), the position of this rotation stage defines the resolution of the collected attenuated X-ray image data, which are projected onto the detector. An additional important development for cone-beam X-ray tomography systems with capabilities to analyse micro-structures at high resolution is the employment of micro-/nano-focused X-ray sources [170]. High resolution micro-XRT is now available in commercial, lab-based X-ray tomography systems [171, 152].

1.4.2 XRT - image reconstruction

The concept of computed axial tomography (CAT or CT) technique was introduced to determine a spatial distribution of attenuation values within a sample from multiple 2D X-ray images [172]. This required the development of reconstruction software allowing the deconvolution of local attenuation values along the X-ray path. The collected, finite number of 2D X-ray projection

images of a scanned object recorded during micro-XRT acquisition can be used to reconstruct cross section images of the sample. Iterative reconstruction can be applied, which involves solving a linear system of equations from the Radon transform. This is computationally expensive and time consuming. For micro-XRT systems with cone beam arrangements, filtered back projection (FBP) reconstruction algorithms are more practical, which was first demonstrated by Feldkamp et al. [173] and are used routinely to generate reconstructed cross-section images utilising parallel computing capabilities of computers and graphics processing units [153].

1.4.3 XRT - image artefacts

The micro-XRT data acquisition or reconstruction algorithm can create image artefacts present in the reconstructed micro-XRT cross-section image data. Strong artefacts can severely alter the micro-XRT cross-section image data and, therefore, may have a significant impact on the quantification of structural descriptors employing image analysis algorithms. Depending on the nature of the artefacts, an optimisation of the acquisition parameters or the employment of image correction algorithms can be used to address image artefacts and reduce their impact on the micro-XRT cross-section image data.

1.4.3.1 Beam hardening

The beam of lab-based micro-XRT systems is typically composed of a target-specific, polychromatic X-ray spectrum. Important for polychromatic beams, the effective attenuation coefficient ($\mu^{\cdot}$) of a given material varies as a function of each specific energy level. In general, $\mu^{\cdot}$ decreases for materials with increasing photon energy and 'harder', higher energetic X-rays penetrate materials more. This leads to changes in the polychromatic spectrum as a function of travel distance through the sample relatively depleted in lower energies. Therefore, a tomographic image reconstruction based on the Lambert-Beer's law leads to beam hardening artefacts for polychromatic X-rays. Beam hardening correction approaches such as a energy-based beam hardening model can be used to improve reconstructed micro-XRT image quality and, hence, downstream image processing and analysis [174].

1.4.3.2 Random Noise

For image acquisition, micro-XRT systems either contain a pixelated, direct flat panel detector or a visible light detector with scintillator. In both systems, the measured image intensity in each pixel is related to the number of photons impacting the pixel over a defined exposure time. Patterns of attenuated X-rays will always be affected by a degree of random variation due to fluctuations inherent in the detection of a finite number of X-ray quanta [175]. These fluctuations in pixel intensity are referred to as random statistical noise. The extent of this type of noise can be addressed during micro-XRT image acquisition by increasing the total number of collected X-ray photons, e.g. using frame averaging to increase the signal-to-noise ratio (SNR). Collected images can further be processed to reduce random noise applying image filters or applying pixel binning during an initial image processing step.

1.4.3.3 Ring Artefacts

Damaged or defective pixels on the detector screen will cause errors in the measured intensity level, which are typically consistent over the scanning process. This will lead to so called "ring artefacts" with ring-shaped lines in the reconstructed image with relatively high or low intensity values. Ring artefacts form vertical lines within the sinogram images during tomographic reconstruction and, therefore, can be identified and corrected during reconstruction [176, 177].

1.4.3.4 Phase contrast

Artefacts as a result of temporal or spatial coherence of the X-ray beam are referred to as "phase contrast". These artefacts are caused by refraction and are observed even with sources emitting polychromatic, incoherent beams [178]. In the micro-XRT images, the phase contrast leads to an edge-enhancement effect, which can be favourable for a visual inspection of the sample [179], but might cause difficulties for subsequent image analysis on grayscale. On lab-based micro-XRT systems, this effect is most pronounced during data acquisition at very high resolution and low sample attenuation. Edge-enhancement effects can be utilised during image processing, e.g. to guide image segmentation, or corrected employing additional processing methods [180, 181].

1.4.4 XRT - Visualisation and Analysis

After reconstruction, micro-XRT image cross-sections can be inspected for a qualitative investigation of internal structure and changes in solid phase related to changing X-ray attenuation. The reconstructed micro-XRT image data can further be utilised to build a model of the sample, which is volume- or surface-rendered for visualisation and permits the user to interactively inspect the collected 3D image data.

Image processing strategies are often applied to micro-XRT image data to remove image noise and artefacts. This can significantly improve sample visualisation. Regularly employed steps during image processing involve image filters and binarisation/thresholding techniques. The analysis of the micro-XRT image data is often achieved using algorithms developed to address a specific research question for the investigated sample system, e.g. to extract quantitative information related to object size [7, 156], shape/morphology [7, 156, 182, 183, 184, 185], porosity [186, 7, 156, 139], local micro-structure [157, 158] or solid phase homogeneity [187, 188]. The application of micro-XRT in combination with image processing and analysis enables the in-depth characterisation of particle systems. The extracted structural descriptors have been used for example for polymorph detection [189] based on differences in the crystal surface roughness, or to gain insights into spray dried hollow particles quantifying the wall thickness and overall porosity to understand the processability and performance characteristics of the bulk powder material [159]. Limitations of micro-XRT are often linked to its achievable maximum resolution with an impact on the subsequent quantification of e.g. micro-porosities, especially for pharmaceutical systems, where there is commonly a low contrast between the organic solid phase and its local voids [190]. The use of image processing and analysis for the evaluation of micro-XRT image data highly benefits from recent advances in computer vision and machine learning methodologies [189, 191, 192].

A framework used for the measurement of particle properties using micro-XRT is presented in detail in Chapter 4. The framework aims for a flexible application of image processing and analysis methodologies to quantify structural descriptors of the object related to its size, shape, surface, porosity and location/orientation. Together with SDD experiments and spray drying, this thesis outlines approaches to better understand particle formation, achieve an in-depth structural characterisation to investigate pharmaceutical particle systems and utilise this information

to guide and control spray drying as a platform for the production of particle powders.

2 Aims and Objective

2.1 Aims

The overall aim of this research project is centred around the practical aspects of measurement, optimisation and control of particle properties with a specific focus on droplet drying platforms such as spray drying. Micro-XRT has great potential as a characterisation technique for a broad range of pharmaceutical products including particulate systems. In this context, the research focuses on developing strategies for robust image processing and analysis to further advance this area of sample characterisation towards a more reliable quantitative characterisation of pharmaceutical products. The investigation of complex structures within these samples can be exploited to inform manufacturing processes and make predictions on the product's functionality or performance downstream and/or after administration to the patient.

Small scale single droplet drying (SDD) experiments in an acoustic levitator allow the rapid assessment of formulation parameters to optimise particle properties. Linked to micro-XRT, SDD experiments deliver valuable information to improve the understanding of droplet drying kinetics and particle formation which affect the final particle morphology and internal microstructure. The combined approach aims to further advance capabilities to describe the correlation of droplet drying history and particle formation to key structural particle properties such as porosity and surface buckling.

Information on the particle formation mechanism are the basis of a rational spray drying process development approach, but further require a firm understanding on the relationship between process parameters and the experienced droplet drying history. The use of process analytical technology (PAT) during spray drying is commonly not considered for lab-scale, but has great potential to support process implementation and inform on local drying conditions. This research aims to explore opportunities to employ low-cost PAT as part of a process data integration framework. Derived (semi-) empirical process models allow a systematic optimisation of

targeted product quality attributes.

2.2 Objectives

The following research objectives were defined to meet the aims of the research project:

Development of a micro-XRT analysis framework for the quantitative analysis of pharmaceutical (multi-) particulate systems (Chapter 4)

A robust micro-XRT analysis framework for the quantitative characterisation of a broad range of pharmaceutical (multi-) particulate samples is part of a flexible micro-XRT workflow covering aspects related to micro-XRT image data acquisition, processing and analysis. This leads to the following key objectives:

- Implement a workflow for the systemic characterisation of pharmaceutical products using micro-XRT.
- Develop a flexible image processing and analysis framework for collected micro-XRT image data.
- Demonstrate the flexibility of the image processing and analysis framework for the application of changing pharmaceutical products.
- Explore means to couple micro-XRT with complementary characterisation techniques e.g. ToF-SIMS for chemical imaging.

Characterisation of multi-particulate capsule formulations using micro-XRT image analysis and machine learning methodology (Chapter 5)

The use of micro-XRT allows a quantitative analysis of structural properties of pharmaceutical products. The developed micro-XRT workflow (outlined in Chapter 4) is applied for the quantitative characterisation of multi-particulate capsule formulations further expanding the scope of the micro-XRT characterisation towards advanced data analysis strategies. Defined key objectives to demonstrate opportunities and limitations of using micro-XRT for the analysis of multi-particulate systems are:

- Implementation of a three-dimensional image segmentation approach for multi-particle systems.

- Extraction of quantitative pellet descriptors linked to size, shape, porosity, surface and orientation.
- Build a classification model for the detection of broken pellets within the population.

Defining a combined approach using single droplet drying experiments and X-ray tomography to investigate the particle design space of novel pharmaceutical formulations (Chapter 6)

The optimisation of particle properties requires an in-depth understanding of the particle formation process and its impact on the final structure. Micro-XRT and acoustic levitation are employed as a combined characterisation platform for the quantitative investigation of particle formation during droplet drying. Key objectives are:

- Assess the use of acoustic levitation and X-ray tomography for particle formulation development.
- Implementation of novel descriptors to quantify the extent of particle surface buckling.
- Investigation of the link between changes of the internal microstructure and the final particle morphology.
- Describe the link between formulation parameters and the final particle structure.

Investigate particle formation and means of process implementation for peptide isolation via spray drying (Chapter 7)

Ultimately, the research aims to inform droplet drying processes such as spray drying. Details of the particle formation mechanism assessed using SDD experiments aim to inform a rational spray drying development approach. Additional process related dependencies need to be evaluated in order to systematically optimise and control particle properties. Here, the research aims to facilitate the implementation of an isolation process for peptides via spray drying. Key objectives are:

- Development and implementation of Process Analytical Technology for exhaust gas analysis to enable a spray dryer characterisation and improve process control.
- Utilise process data during platform characterisation to establish a process model to identify ideal operating space.
- Use a Design-of-Experiment approach to validate the process model and optimise product properties.

- Define and apply offline product characterisation techniques to evaluate key powder attributes related to particle size, shape, agglomeration and peptide fibrillation.

3 Acoustic Levitation Platforms and Image Processing Methods

Single droplet drying experiments (SDD) were performed using acoustic levitation. Two systems were used: a commercial single-axis acoustic levitator (SAL, Materials Development, Inc., Arlington Heights, USA, Section 3.1); and a re-designed multi-emitter single-axis acoustic levitator (MSAL) based on a levitator geometry published by Marzo *et al.* [193] (Section 3.2). The experiments were monitored using high speed and thermal imaging (Section 3.3).

3.1 Single-Axis Acoustic Levitator (SAL)

The SAL was used to study the evaporation of droplets from aqueous and organic solvent-based solutions. Single droplets with volumes between 0.2 and 20 μl were suspended in the central pressure node with a syringe. A custom-build enclosure with heated walls and pre-treated drying gas gave control over temperature (RT – 55 °C) and relative humidity levels ($<$ 2.5 - 45%RH). Nitrogen was used as an inert drying gas. The nitrogen was filtered and heated externally before entering the chamber at 0.4 L/min. The enclosure contained windows to permit the application of high speed and thermal imaging to monitor each SDD experiment. For thermal imaging the windows were made from calcium fluoride, which is transparent in the detected infrared (IR) frequency range.

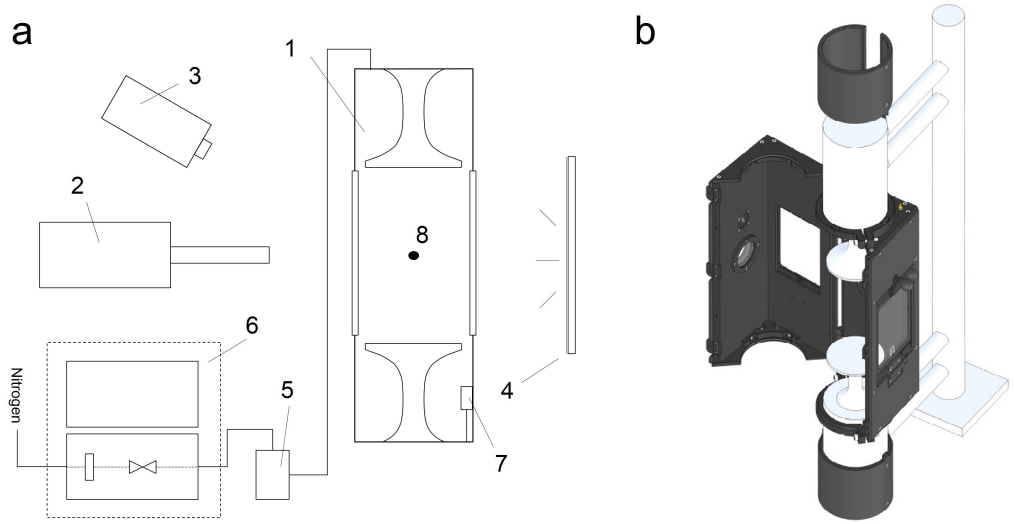

Figure 3.1: (a) Experimental setup of the Single-Axis Acoustic Levitator (SAL) using (a2) high speed and (a3) thermal imaging to monitor each (a8) SDD experiment. (a4) A light shield was employed for back-illumination. (a5 - a6) The drying gas was regulated, heated and humidified with a system from Okalab. Information of the drying gas were captured with (a7) a gas sensor recording local temperature, relative humidity, volatile organic compounds and pressure. (b) The enclosure was custom-build to fit the SAL transducers.

3.2 Multi-emitter Single-axis Acoustic Levitator (MSAL)

The multi-emitter single-axis acoustic levitator (MSAL) is a modular system, which combines the container-less experimental platform of an acoustic levitator with a chamber for temperature/humidity control and integrated data collection capability. The MSAL was developed based on a levitator design from Marzo et al. [193]. Information of the environment including temperature (-40 - 85°C, accuracy ± 1°C), humidity (0 - 100%RH, accuracy ± 3%RH), concentrations of volatile organic compounds (non-calibrated) and local pressure (300 - 1100 hPa, accuracy ± 0.6 hPa) are constantly monitored and recorded using a BME680 gas sensor (Bosch Sensortec GmbH, Germany). The experiments are further monitored and analysed using optical imaging in combination with image analysis software.

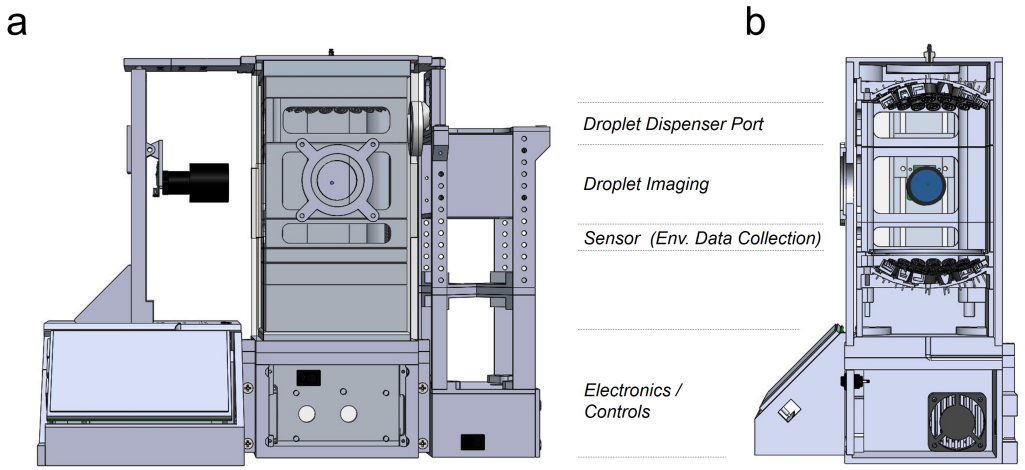

Figure 3.2: Multi-emitter acoustic levitator (MSAL) setup with integrated imaging system to monitor the experiment (a - front view, b - side, full section view). Additional information of the drying gas were captured using an environmental sensor recording local temperature, relative humidity, volatile organic compounds and pressure.

3.3 Imaging Techniques

High speed digital and thermal imaging techniques were used to monitor the SDD experiments in the acoustic levitation systems. Liquid evaporation and solidification were characterised in terms of changes in droplet-volume, detection of the precipitation of solid matter and droplet surface temperatures over the course of each experiment.

3.3.1 Digital Imaging

The Photron FastCam SA1.1 (Photron, Japan) is a high speed camera with a complementary metal–oxide–semiconductor (CMOS) active pixel sensor capable of recording short image sequences with a framerate of up to 5,400 fps at a resolution of 1024 x 1024 pixel and a dynamic range of 16 bit. SDD images had an image pixel size of 6.79 μm/px. Images were taken using back-illumination with a high-power LED light source (Photron LED Light Kit, SAL, Fig. 3.1 a4) or an integrated light screen with low-power LED arrays (MSAL, Fig. 3.2 a right side), respectively. Collected images were processed in MATLAB (R2016a - R2018b, Mathworks, USA), which included noise reduction, binarization and a size analysis as shown in Fig. 3.3. The droplets are characterised by their projected 2D absolute area as well as the major and minor axis of a fitted ellipse.

The droplet volume ($V_{S,O}$) and its surface area ($A_{S,O}$) were calculated using Equation 3.1 and

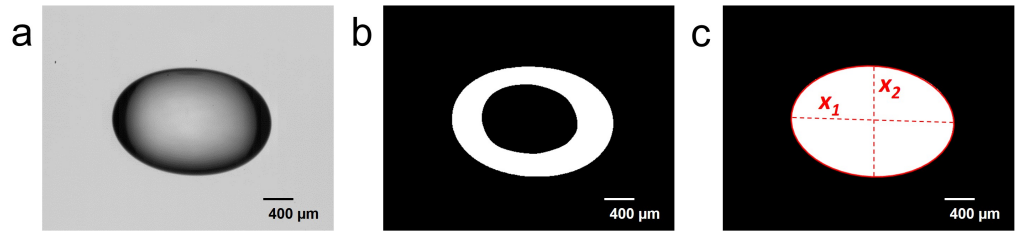

Figure 3.3: Processing of recorded droplet images during liquid evaporation: (a) collected image of a large, deformed liquid droplet, (b) binarised image after noise reduction and (c) droplet ROI with fitted ellipsoid to extracted characteristic lengths for the calculation of droplet volume and surface.

Equation 3.2 for oblate spheroids, respectively [194]. The oblate spheroid is defined by its major (x_1) and minor axis (x_2, axis of symmetry), which were quantified from the recorded 2D images as shown in Fig. 3.3. Equation 3.2 requires information on the eccentricity (e) of the oblate spheroids calculated using Equation 3.3.

$$V_{S,O} = \frac{4}{3}\pi(x_1/2)^2(x_2/2) \tag{3.1}$$

$$A_{S,O} = 2\pi(x_1/2)^2 + \pi\frac{(x_2/2)^2}{e}\ln\left(\frac{1+e}{1-e}\right) \tag{3.2}$$

$$e^2 = 1 - \frac{x_1^2}{x_2^2} \tag{3.3}$$

3.3.2 Infrared Thermography Imaging

The A6702sc (FLIR Systems, Inc.) thermal camera enables the user to record infra-red radiation emitted by objects as a function of their surface temperature(s). The thermal information are saved as calibrated images with an image pixel size of $\backsim$140 μm/px. Thermal information on the droplet surface were extracted automatically from the image data using the FLIR Atlas SDK (FLIR Systems, USA) for MATLAB (R2016a - R2018b, Mathworks, USA). The droplet/-particle detection process is outlined in Fig. 3.4. The droplet was identified within an image processing workflow, which included a background subtraction (Fig. 3.4b) as well as integrated conditionals for droplet/particle position and size to permit a robust object detection (Fig. 3.4c). Surface temperature values were extracted from a center region ($< 3x3$ px $\lesssim 0.18$ mm^2) of the detected object to calculate a local mean.

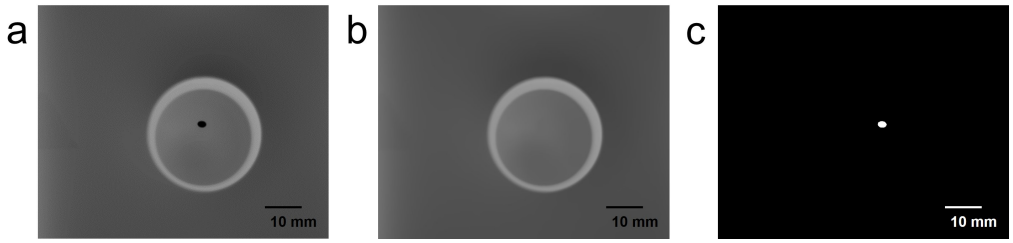

Figure 3.4: Processing of thermal images: The droplet/particle position in (a) the collected raw thermal images was detected after performing a (b) background subtraction. (c) The established logic mask was used to read local temperature values corresponding to the droplet/particle surface.

4 XRT Characterisation of Pharmaceutical Solid Products: Image Acquisition and Analysis Framework

Declaration: *This chapter is the result of a collaboration between Frederik J.S. Doerr[a,b], Eleonora Paladino[a,b,c], Elke Prasad[a,b], Muhammad T. Islam[a,b], John Robertson[a,b] and Alastair J. Florence[a,b].*

Abstract: A Micro-X-ray tomography image acquisition and analysis framework was developed for the quantitative characterisation of solid pharmaceutical products. Sample preparation strategies and acquisition parameters were optimised for organic solid phase samples with low X-ray attenuation. Beside sample visualisation, the use of image processing and analysis strategies for the micro-XRT image data allows an in-depth quantitative sample characterisation. Concepts of image noise reduction, binarization and segmentation are elaborated and used to prepare the micro-XRT image data for the application of feature extraction algorithms. In total, the here presented micro-XRT image analysis framework is capable to assess over 200 features related to the sample size, shape, porosity, surface and location/orientation. The framework was applied to a wide range of pharmaceutical systems from crystals, particles, powders to fully formulated tablets and capsules. Three selected case studies, single particles, a powder mixture and 3D-printed tablets, are used to exemplify the utility of a systematic micro-XRT characterisation workflow in more detail. The extracted information can be used directly to support product and process development throughout the pharmaceutical downstream manufacturing pipeline.

[a] *EPSRC CMAC Future Manufacturing Research Hub, Technology and Innovation Centre, Glasgow, UK*

[b] *Strathclyde Institute of Pharmacy & Biomedical Sciences (SIPBS), University of Strathclyde, Glasgow, UK*

[c] *National Centre of Excellence in Mass Spectrometry Imaging (NiCE-MSI), National Physical Laboratory (NPL), Teddington, Middlesex, UK*

Keywords: Pharmaceutical Products, XRT Characterisation Workflow, Image Analysis Framework, Structural Quantification, Data Mining, Data Fusion

Highlights:

- Micro-XRT workflow for the quantitative characterisation of solid pharmaceutical products.
- Flexible micro-XRT image processing and analysis framework.
- Micro-XRT case studies: singe particles, powders,and 3D printed tablets.
- Coupling micro-XRT with complementary ToF-SIMS chemical imaging.

4.1 Introduction

X-ray tomography (XRT) is an important non-destructive 3D imaging and analysis technique for the characterisation of a wide variety of samples and is frequently employed in areas spanning across material science [195, 196, 197], archaeology [198], biomedical science [150, 166] or geo-science [199, 200, 201, 155]. Beside enabling a qualitative 3D sample visualisation, XRT image processing methodologies have been successful in further exploiting the XRT image data to extract quantitative information of object properties. Specifically, biomedical applications of XRT have seen great advances in areas of medical-XRT image analysis e.g. using machine learning approaches or data fusion to enhance the interpretability of the XRT data to support diagnosis for early detection of breast cancer [202], tuberculosis [192] or the examination of complex bone fractures [203]. Geoscientific applications have employed micro-X-ray tomography (micro-XRT) systems to investigate aspects of size, shape, porosity, surface and orientation e.g. of composite materials [199, 204] or complex (multi-) particle systems [205, 206, 201]. Here, image analysis approaches are under continuous development to improve their capability to extract quantitative structural sample information.

In the pharmaceutical sciences, micro-XRT is of increasing interest as an off-line sample characterisation technique for pharmaceutical products or drug product intermediates. Micro-XRT was used to evaluate properties of (formulated) products including particles [156, 7], coated pellets [157, 158], spray dried powders [159] and tablets [160, 207, 161]. Micro-XRT was also applied to evaluate individually selected product quality attributes, which can be directly re-

lated to the manufacturing process for development and optimisation [208, 161] and to enable a prediction of sample performance [168, 209]. The translation of image analysis strategies from other research areas such as biomedical or geo-scientific applications have great potential to accelerate the adoption of micro-XRT for a quantitative investigation of pharmaceutical systems.

Each micro-XRT analysis consists of a large set of two-dimensional radiographs projected onto the detector under stepwise rotation to obtain three-dimensional information on local X-ray attenuation related to the sample's phase composition. The full set of radiographs is used to reconstruct the three-dimensional object inside the field of view. The reconstructed cross-sections can be further exploited to investigate the three dimensional structure of the scanned object. A transparent and reliable image analysis framework provides means to systemically interrogate the collected micro-XRT image data.

This study outlines strategies for the processing and analysis of micro-XRT image data from pharmaceutical solid samples. Implemented strategies allow the visualisation and quantification of object structure and solid phase composition. Besides sample presentation and raw data acquisition strategies, a central focus of this study was the development of an image analysis framework that can be flexibly applied to collected micro-XRT image data. These methodologies are the basis for a reliable quantitative characterisation of pharmaceutical samples using micro-XRT and are presented as part of a workflow to ease their adoption for pharmaceutical process and product development.

4.2 Materials and Methods

A laboratory micro-XRT system, a Skyscanner 2211 X-ray tomograph (NanoCT, Bruker, Kontich, Belgium, Fig. 4.1a), was used for micro-XRT data collection of the pharmaceutical products investigated in this study, which included single particles, powders and 3D-printed tablets. The commercial system uses a cone-beam arrangement with geometric magnification (Fig. 4.1b). Samples were scanned with an image pixel size between 0.5 μm - 4 μm, frame averaging of 1 - 8 and a rotation step size of 0.1 - 2 °. X-ray acceleration voltage was set to 40 keV. Details of the acquisition parameters for all samples are listed in Table A1 (ESI, page A2). The acquisition parameters were optimised for individual samples to achieve high-resolution

micro-XRT image data whilst minimising the required total scanning times. A reference scan was collected at the end of each run to enable post-alignment and therefore, compensate for potential shifts during the scan.

Image reconstruction included beam hardening correction and ring artefact reduction, which was performed with commercial software using NRecon with InstaRecon (version 1.7.1.6, Bruker, Kontich, Belgium). Visualisation of the image stacks were generated with CTVox (version 3.2.0, Bruker, Kontich, Belgium). The micro-XRT image processing and analysis framework was developed in MATLAB (version 9.5, R2018b).

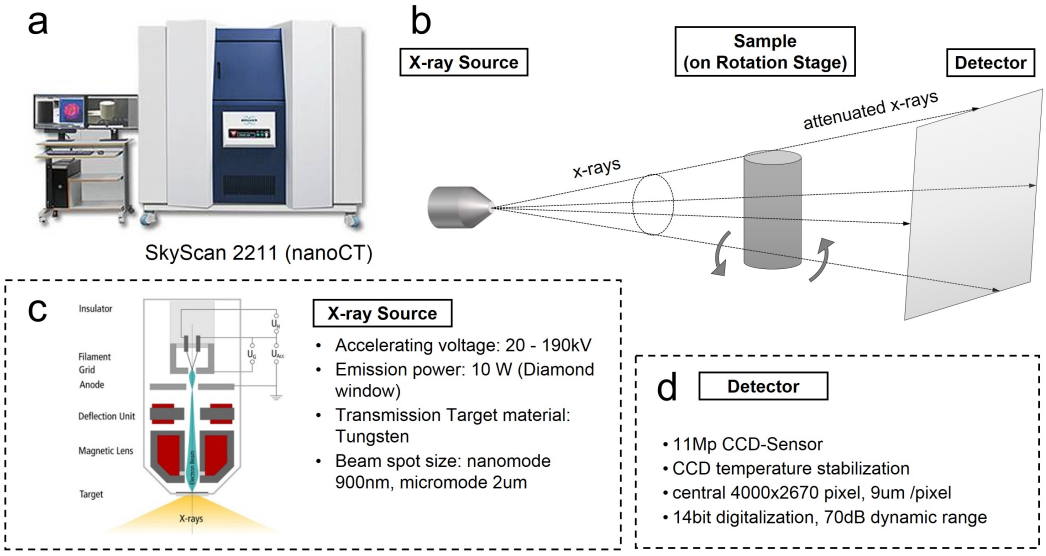

Figure 4.1: (a) A SkyScan 2211 with cone-beam arrangement and (b) geometric magnification is used for micro-XRT image acquisition. The system employs a (c) X-ray source with micro- / nano-focus capabilities. The attenuated X-ray images are projected on (d) CCD detector for high-resolution imaging.

4.3 Results and Discussion

The micro-XRT characterisation of each sample consists of basic steps of XRT data acquisition, XRT image reconstruction and an initial optimisation of image processing parameters for noise reduction (Fig. 4.2, *Stage 1 - 4*). Careful considerations around sample presentation and an optimisation of the data acquisition parameters can significantly improve the interpretability of the collected micro-XRT image data. Generated high quality images ease the application of noise reduction and binarization algorithms, which are essential for a successful qualitative and

quantitative analysis of the scanned specimens. The following outlines implemented strategies for the collection and analysis of pharmaceutical solid products using a commercial micro-XRT system. In this context, this chapter elaborates details of image processing and analysis (Fig. 4.2, *Stage 5 - 6*) for a quantification of structural sample properties from the micro-XRT image data including image segmentation and feature extraction. The presented micro-XRT characterisation workflow has the potential to be applied for a broad range of pharmaceutical solid products directly informing processes along the downstream manufacturing pipeline. Examples demonstrating its applicability for selected case studies of single particles, a powder mixture and 3D-printed tablets are included in Section 4.3.6.

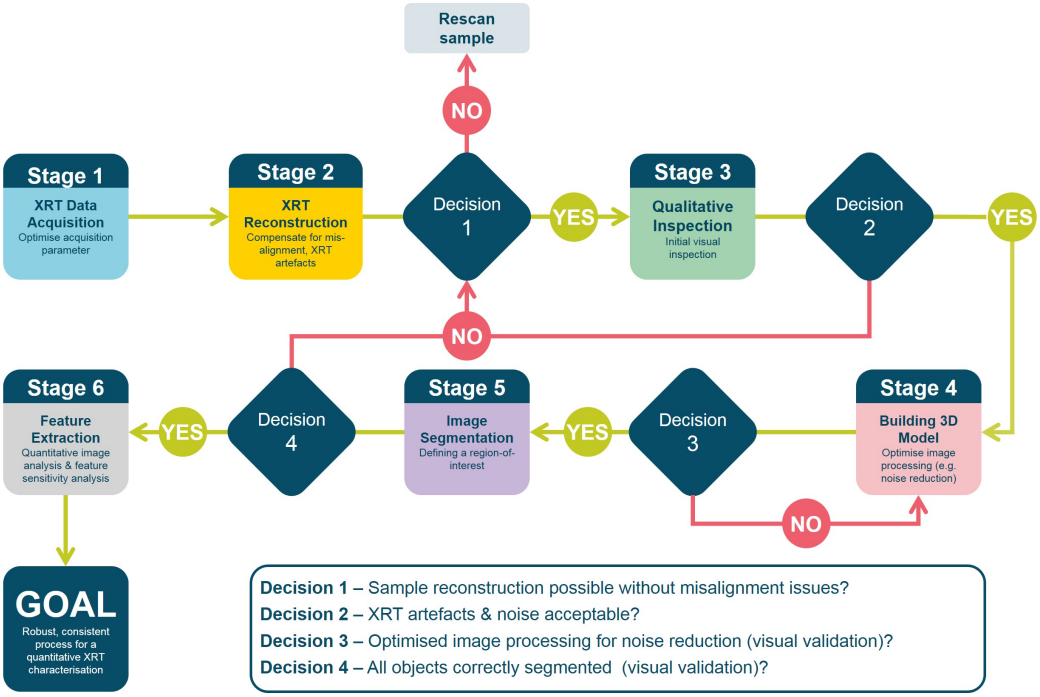

Figure 4.2: Overview of micro-XRT data acquisition and processing workflow aiming to provide qualitative and/or quantitative information of the investigated specimen. Commercial software solutions were used for scanning and data reconstruction. Image data analysis and visualisation was accomplished with costumised solutions.

4.3.1 XRT Sample Preparation Strategies

The aim of micro-XRT sample preparation is to ensure fixation of the sample within the available Field of View (FOV). The sample position should be optimised to fit into a cylindrical volume with minimised radius ensuring maximum geometric magnification in systems with cone-beam arrangements (Fig. 4.1 b). The cylindrical radius typically corresponds to the min-

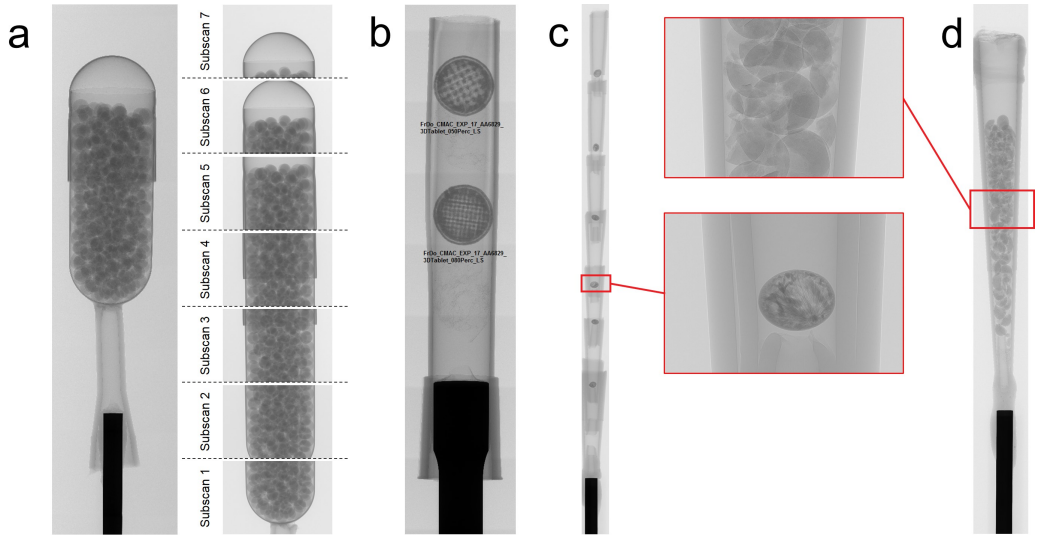

Figure 4.3: Examples for sample presentation and micro-XRT image acquisition: (a, capsule with formulated pellets) Oversized scan of the elongated samples with multiple subscans to cover the full sample length, (b, tablets / c, single particles) stacked samples with individual scans along the vertical length and (d, particle powder) section scan of a powder filled in low X-ray attenuating plastic tip.

imum achievable distance of the sample to source and/or detector under rotation during raw data acquisition. Micro-XRT sample holders try to minimise X-ray attenuation and therefore, ideally should consist of "X-ray transparent" polymeric materials consisting of simple hydrocarbon polymers (alkane-, cycloalkane-, and alkyne-based e.g. Mylar® or Kapton®). Selected examples of mounted pharmaceutical samples within polypropylene tips are shown in Fig. 4.3 and include (a) capsules, (b) tablets, (c) single particles and (d) powders. Elongated samples can be captured with a series of subscans (Fig. 4.3 a, subscan 1 - 7) along the rotational axis to vertically increase the FOV at maximum resolution micro-XRT image data. The subscans are "stitched" together to generate a continuous radiograph capturing the full sample length. Instead of discrete subscans, a helical scan allows the continuous imaging of elongated samples which are vertically translated through the FOV while under rotation. This has the advantage of allowing a more homogeneous X-ray exposure of the volume with each volume element of the sample travelling through the central imaging axis (closest source-detector distance). However, this is at the expense of requiring a dedicated reconstruction method for helical cone-beam tomography [210].

4.3.2 Image Acquisition and Reconstruction (Micro-XRT Workflow *Stage 1 - 3* [Fig. 4.2])

Initially, the micro-XRT image acquisition is optimised selecting values for the image exposure time, applied accelerating voltage and emission current, which all depend on the sample and the selected micro-XRT system arrangement (e.g. detector type, detector pixel size, use of source/detector filters). Pharmaceutical (intermediate) products are often mixtures of low X-ray attenuating, organic compounds. Therefore, the X-ray source accelerating voltage is commonly selected first to maximise the phase contrast using softer, lower energetic X-ray beams (35 kV - 60 kV). The selected X-ray source emission current is limited by the maximum power rating of the X-ray source (here: SkyScan 2211.v1 4W and SkyScan 2211.v2 10W [211]). Finally, the image exposure time is selected in order to avoid overexposure of images and to stay within the linear response range of the detector of approx. 30% - 70% saturation for the CCD detector used in this study [211].

Additionally, the micro-XRT image acquisition consists of parameters for frame averaging (FA) and rotation step size (RS) with an equidistant angular distribution. FA is a method to gain a better signal-to-noise ratio (SNR) in the micro-XRT images by averaging multiple images of the same exposure. FA is of particular importance for pharmaceutical products with low X-ray attenuating organic material. RS determines the angle selection during micro-XRT image acquisition and has an impact on the reconstructed micro-XRT image quality. RS has to be optimised to resolve the main sample features and therefore, the optimum angle selection is specimen-dependent. Fig. 4.4 a shows an example for increasing FA and reduced RS yielding significantly improved image data. Both, selected frame averaging and rotation step size, contribute to the total sample acquisition time. Here, the total acquisition time increases from 00h:02min (TR3, FA 4, RS 0.2°) to 01h:19min (TR0, FA 1, RS 2°). Between TR0 to TR3, the evaluated SNR for the images is reduced from 4.57 (foreground intensity 115.86 $\pm$ 25.35) in TR0 to 1.52 (foreground intensity 61.09 $\pm$ 40.20) in TR3 determined within a logic mask of TR0. Details of the acquisition parameters for TR0 - TR3 are provided in Table A1 (ESI, page A2).

Micro-XRT data acquisition often has to be balanced and optimised between high resolution imaging and extensive scanning times. Beside potential limitations of instrument access time, long scanning times can potentially cause X-ray radiation damage mostly frequently observed

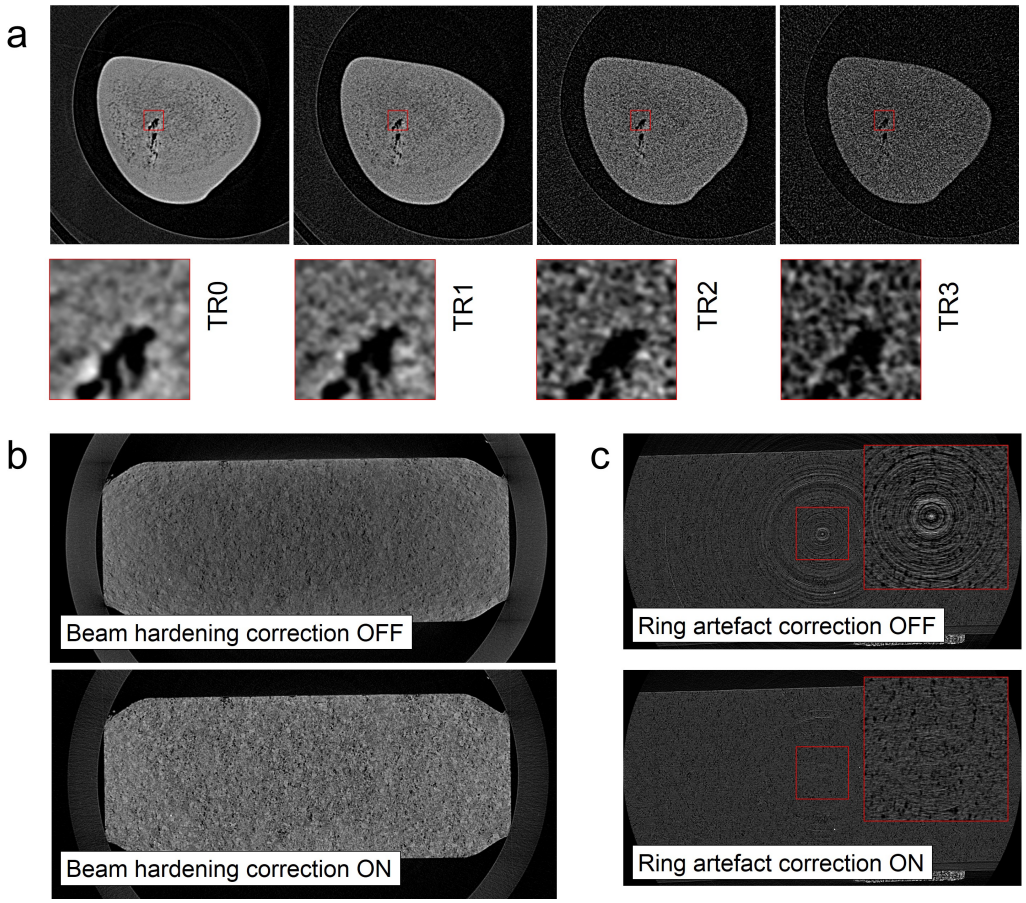

Figure 4.4: Optimising image acquisition and reconstruction: (a, left to right) Changing parameters for frame averaging and rotation step size between TR0 and TR3 leads to an increase in image noise, but allows faster scanning times. (b) Soft X-rays are predominately attenuated and result in a non-uniform intensity distribution in the reconstructed images (beam hardening). The beam hardening effect can be corrected to provide images with higher intensity uniformity. (c) Ring artefact correction significantly improves image quality.

for biological samples e.g. exposed to synchrotron radiation [212] and, furthermore, might lead to a thermal drift of the focal spot resulting in difficulties of image post-alignment [213, 214]. A short scan with equivalent source settings and a duration of approximately one hour was performed prior to high-resolution data acquisition scans to give an appropriate warm-up period of the X-ray source.

During tomographic reconstruction the finite number of collected radiographs (2D X-ray projections) are used to calculate cross-sectional images of the 3-dimensional object. Filtered backprojection (FBP) reconstruction methods are commonly used for micro-XRT systems with cone-beam arrangements, which achieve high reconstructed image quality and fast processing times [173, 153]. Depending on the reconstruction software, potential beam hardening artefacts

(Fig. 4.4 b), ring artefacts (Fig. 4.4 c) and mis-alignment artefacts can be (partially) compensated during reconstruction [215, 174, 177], which is crucial for a successful analysis of the micro-XRT image data.

4.3.3 Image Processing - 3D Volume Builder (Micro-XRT Workflow *Stage 4* [Fig. 4.2])

The reconstructed micro-XRT image data can be used directly for sample visualisation or further processed to reduce remaining image noise and to exploit the micro-XRT image data for a quantitative characterisation. The "3D Volume Builder" (3DVB) is an in-house developed image processing routine for initial noise reduction and binarization incorporated as part of a larger framework for micro-XRT image data analysis designed for the quantitative characterisation of pharmaceutical samples. An overview of the 3DVB routine is provided in Fig. 4.5. 3DVB is designed to create a clean binary image stack of the scanned object, which can be used for a structural analysis or as a logic mask to define the object's region-of-interest (ROI) within the 3D volume. The 3DVB consists of well established methodologies utilised for accelerated parallel processing of individual 2D images including image filtering, binarization and (binary) noise reduction. Additional approaches for 3D noise reduction and 3D ROI methods are used for samples with challenging image data to avoid unwanted image information during 2D parallel-processing. The following sections give more details on each step in the 3DVB routine.

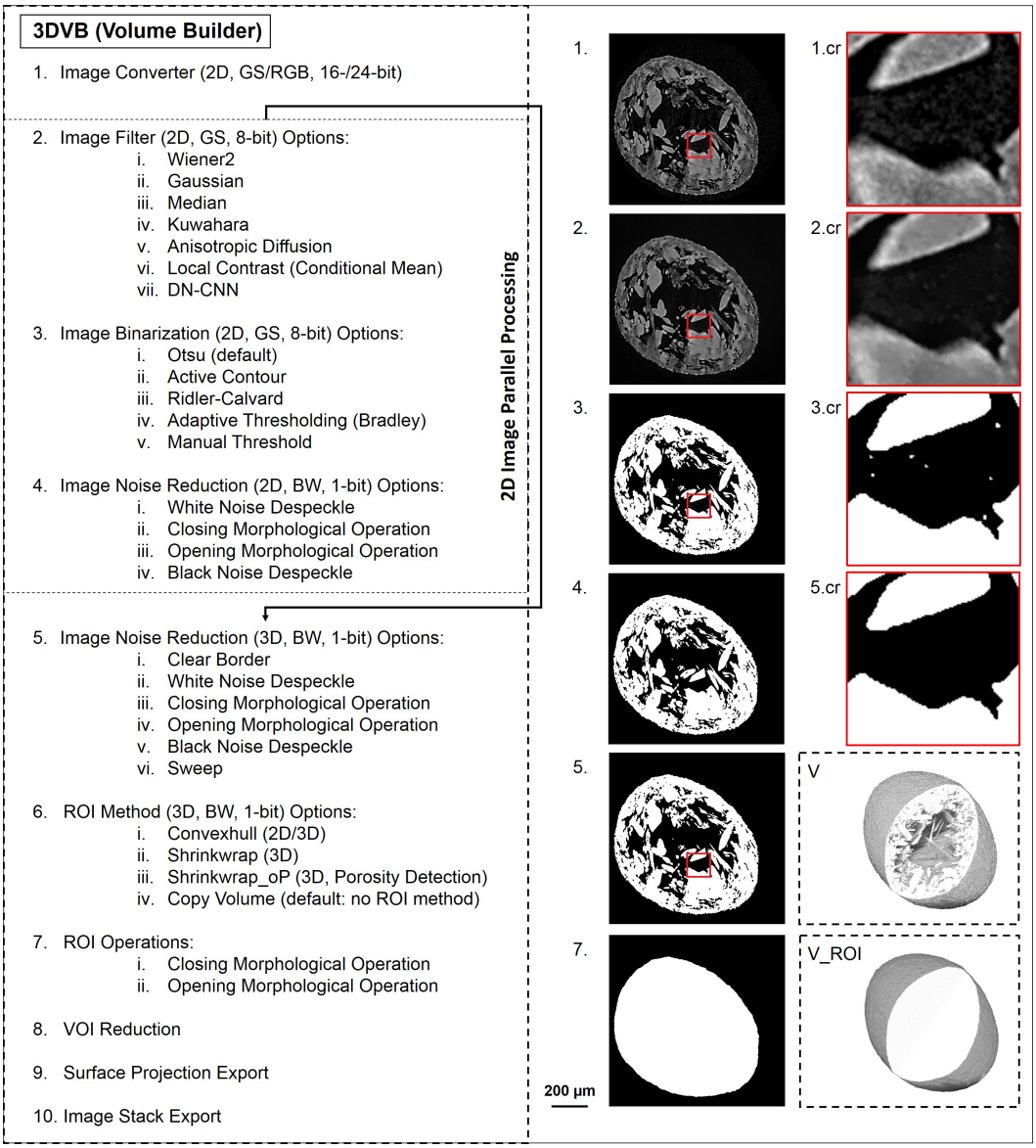

Figure 4.5: Implemented 3DVB image data processing routine to build 3D binary object volumes. (2. - 4.) Parallel processing of 2D reconstructed cross-sections to reduce noise and apply binarisation. (5.) The full image stack is further used for additional 3D noise reduction algorithms and (6. - 7.) to establish an object ROI.

4.3.3.1 Image filter (3DVB.2)

In image processing, filters are employed to suppress high frequencies in images for smoothing or low frequencies for edge enhancement. The image filters typically operate on the basis of a user-defined pixel neighborhood, which is a parameter within 3DVB to adjust the pixel region considered for the filter operation. The neighborhood defines which pixels are included for the local operation in respect to the kernel center. Advanced filter methods are edge-preserving,

aiming to protect valuable image information for downstream image segmentation and feature extraction. An overview of implemented image filtering methods in the 3DVB routine is provided in Table 4.1. The filter selection mostly depends on attributes of the micro-XRT image data and potential requirements for image processing times. In general, edge preserving filters are preferred minimising the risk to introduce image processing artefacts. The Gaussian blur filter can be used to simulate the effects of decreasing image quality as part of a sensitivity analysis assessing the impact of changing micro-XRT image quality on a quantitative characterisation (see application in Chapter 5).

Table 4.1: Overview of implemented image filter (3DVB_2) for random noise reduction on grayscale with MATLAB function names. [a] CMAC, [b] MATLAB Image Processing Toolbox, [c] literature/Mathworks File Exchange.

Name (*Function*)	**Description**	**Application**
Wiener filter[b] (MatF: *wiener2*)	Adaptive noise-removal low-pass filter removing constant power additive noise. Noise detected from m-by-n pixel neighborhood statistics [216].	(+) effective for high-power random noise
Gaussian blur[b] (MatF: *imgaussfilt*)	Low-pass filter attenuating high frequency signals. Smoothing kernel with user-defined standard deviation within a m-by-n pixel neighborhood.	(+) simple (-) no edge preserving
Median filter[b] (MatF: *medfilt2*)	Nonlinear smoothing filter where each pixel takes the median value within a m-by-n pixel neighborhood. Isolated out-of-range noise is suppressed.	(+) effective for speckle noise (-) only moderate edge preserving
Kuwahara[c] (MatF: *kuwahara*)	Non-linear smoothing filter for adaptive noise reduction. The central pixel takes the mean value of the sub-area that is most homogeneous within a m-by-m pixel neighborhood [217].	(+) edge preserving (-) block artefacts
Anisotropic diffusion[c] (MatF: *imdiffusefilt*)	Partial differential equation (PDE)-based, space-variant denoising filter with a threshold function to prevent diffusion across edges (aka Perona–Malik diffusion [218]).	(+) edge preserving (-) slow
Conditional local contrast[b] (MatF: *localcontrast*)	Edge-aware local contrast manipulation of images for contrast enhancement or smoothing. Edge threshold is user defined.	(+) edge preserving (-) user-defined edge condition
DN-CNN[b] (MatF: *denoiseImage, net = 'DnCNN'*)	Noise reduction using a pre-trained image denoising convolutional neural network for Gaussian noise reduction.	(+) pre-trained CNN (DnCNN) (-) low flexibility

4.3.3.2 Image binarization (3DVB.3)

Objects in the reconstructed micro-XRT image data are typically represented by lighter image pixels surrounded by dark background pixels as defined by the image polarity. Here, the pixel intensity corresponds to the local X-ray attenuation with higher attenuation being represented with higher pixel intensities. Image thresholding or binarization describes the process of trans-

forming the reconstructed micro-XRT images with a 8-/16-bit dynamic range to binary, 1-bit ones. This can be achieved by selecting a grayscale value dividing the image histogram in foreground and background regions. An overview of binarization methods incorporated in the 3DVB routine is provided in Table 4.2. For histogram-based global thresholding methods (e.g. Otsu, Ridler), pixel intensity information of the full or a representative subset of the 3D image stack are used to determine a fixed threshold value that is then applied to all images.

Table 4.2: Overview of implemented image binarization methods (3DVB_3) with MATLAB function names. [a] CMAC, [b] MATLAB Image Processing Toolbox, [c] literature/Mathworks File Exchange.

Name (*Function*)	**Description**	**Application**
Otsu[b] (MatF: *imbinarize, method = 'global'*)	Histogram-based thresholding method aiming to minimize intra-class intensity variance [219]. Can be extended to a multi-level thresholding for image intensity discretisation. Particularly effective for histograms with distributions of equal size and variance [220].	(+) automatic thresholding (-) difficult for multi-modal histograms, requires a representative historgram
Ridler[c] (MatF: *ridlercalvard*)	Histogram-based thresholding method which uses class weights to divide the image into foreground and background [221].	(+) automatic thresholding (-) difficult for multi-modal histograms, requires a representative historgram
Manual[a]	User defined, fixed manual threshold value.	(+) robust for images with complex multi-modal GS (-) subjective, user biased

4.3.3.3 Image noise reduction (3DVB.4 & 3DVB.5)

Beside the utilisation of image filter methods applied on 8-/16-bit grayscale images, remaining binary image noise can be removed after binarisation. The simplest method of noise removal is a size-dependent removal of small clusters of pixels/voxels defined as *speckles*. This method is commonly refereed to as despeckling and can be called within 3DVB using a user-defined cut-off size. 3DVB further employs closing and/or opening operations for noise reduction applied on the binary images. Image dilation, erosion, closing, and opening are basic operations in mathematical morphology. All operations use a user-defined structuring element for this image transformation. The structuring element describes a basic shape (e.g. square, circle) and its size. A closing operation consists of an dilation & erosion, which practically removes small holes and connects objects closing small gaps between them. In contrast, the opening operation consists of an erosion & dilation, which removes small foreground clusters and separates volume elements with thin connections between them. An example demonstrating the impact of closing

and opening image transformations with changing structuring element size on a 3D printed pharmaceutical tablet is shown in Fig. 4.6. Changes in the size of the structuring element, defining the extent of the morphological image transformation, can lead to significant changes in the final image. For the 3D printed tablet in Fig. 4.6, an increasing size of the structuring element (Strel) led to considerable changes of local porosities (Fig. 4.6 b) or even overall tablet structure (Fig. 4.6 c). The parameters of these operations have to be carefully optimised to effectively reduce binary image noise whilst avoiding structural changes to the object itself. Morphological operations can be useful to reduce e.g. light ring artefacts or streak artefacts in the reconstructed micro-XRT image data.

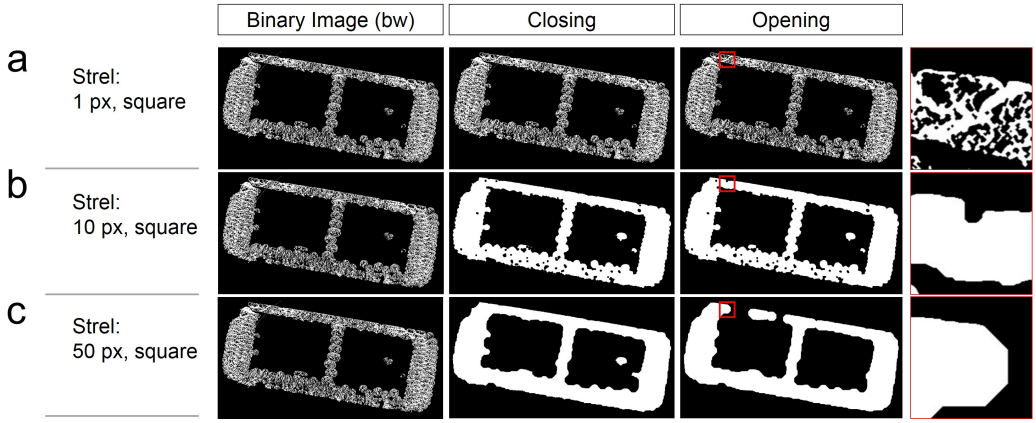

Figure 4.6: Impact of changing parameters for morphological operations on micro-XRT image data of a 3D printed tablet sample with fine primary structures (left). (1) Closing and (2) opening operations can be used to reduce binary image noise. Its parameters for the structuring element (Strel) have to be carefully assessed regarding their impact within the image analysis workflow: (b, Strel 10 px) Small sample attributes are lost including its internal micro-structure. (c, Strel 50 px) The overall object structure is significantly altered.

Within 3DVB, operations for image noise reduction such as despeckling for size-dependent noise removal or morphological image processing operations (closing and/or opening) can be applied to the full 3D image stack, which minimises risks to create single layers with discontinuous foreground structure. Additionally, objects on the image border can be removed using 3DVB-*Clear Border*. This is helpful for separated multi-object samples automatically identifying objects fully contained within the 3D image space. Another effective techniques for noise reduction is the 3DVB-*Sweep* implementation, which can be used to automatically remove all random white (foreground) noise in binary images, which is not connected to the main sample object. The main object is here detected as the largest connected voxel cluster in the 3D image

volume with a pixel/voxel connectivity of 26 i.e. a group of pixels/voxels connected with each other through their 6 faces, 12 edges or 8 corners.

The methodology sequence for noise reduction within the 3DVB routine was designed to give best flexibility for processing micro-XRT image data specifically working with pharmaceutical samples. Parameter optimisation for an effective noise reduction is partially automated, but often have to be user-defined. Therefore, parameter optimisation should be carefully assessed, either qualitatively by expert users or ideally, using an objective assessment approach within a quantitative sensitivity analysis.

4.3.3.4 ROI Method and ROI Operations (3DVB.6 & 3DVB.7)

After noise reduction, the cleaned binary image stack can be utilised within the 3DVB routine to automatically re-define the object ROI. This is crucial for samples with a high extent of internal porosities (open and/or closed) to capture not only the object solid phase, but its total 3D object volume. A Convex-Hull can be applied on the binary 3D image stack to describe convex topographies (3DVB-*Convexhull3D*). More advanced methods, such as the implemented 3DVB-*Skrinkwrap* approach uses morphological closing operations together with a background filter to more accurately capture irregular object topologies. 3DVB-*Skrinkwrap_oP* further includes a feedback loop to distinguish open porosity from concave surface volumes with no connection to the internal object volume, which is useful to establish accurate single particle ROIs (see Chapter 6, [7]) or multi-particle ROIs (see Chapter 5). In contrast to the Convex-Hull method, the 3DVB-*Skrinkwrap* approach requires a user-defined structuring element with a minimum size stretching over expected surface gaps connected to internal object porosity.

4.3.4 Image Processing - Image Segmentation (Micro-XRT Workflow *Stage 5* [Fig. 4.2])

Image segmentation is the process of separating images into multiple partitions (segments, super-pixels). Previously discussed image binarisation/thresholding techniques (Section 4.3.3.2) segment an image into a foreground and a background in order to have a logic mask for the object's solid phase. Here, image segmentation aims to further transform the micro-XRT image data to allow the identification and analysis of image sub-structures e.g. in multi-object or multi-component systems. For multi-object systems, image segmentation aims to further subdivide the image volume to define regions corresponding to each individual object. The

detection of each object and the isolation of the image sub-volume is crucial to perform a characterisation of individual objects e.g. in multi-particle systems. For multi-component systems, image segmentation aims to define regions with differences in their X-ray attenuation related to changes in the local solid phase composition. Explored image segmentation methods for the micro-XRT image data of pharmaceutical products are manual PolyROI segmentation, automated structure-based segmentation algorithms (watershed) or advanced pixel-wise classification approaches (k-means clustering).

Manual image segmentation requires a user-defined ROI commonly generated from interpolated basic geometric shapes (e.g. circle, ellipse, box) or a more complex polygonal region of interest (PolyROI) which is described by a finite number of connected straight line segments forming a closed polygonal chain. Working with PolyROI is time-consuming, but can be flexibly adapted to any sample for a manual ROI creation. The number and length of each straight line segment as well as the position of its endpoints are manually arranged to best capture the desired ROI.

Structure-related segmentation algorithms use information of the objects' local structure to separate individual sub-volumes. Morphological opening operations are a simple solution to enable the separation of two objects. The marker-supported watershed transformation is a more advanced image processing method which uses local thickness information to find and optimise the image segmentation process for object separation [222, 223]. Structure-related segmentation algorithms work best on multi-object samples with well defined object bodies and light "touching" zones (see application in Chapter 5).

Image segmentation can also be performed directly on the pixel-/voxel-level. In applications where a one-dimensional threshold fails to accurately segment the micro-XRT image data (e.g. multi-thresholding, Section 4.3.3.2), additional information of each pixel can be extracted through targeted micro-XRT image transformations (e.g. filtering, Section 4.3.3.1). A k-means clustering algorithm can subsequently be applied aiming for a pixel-wise classification of the input image into a user-defined, finite number of clusters. The classification is based on vector quantization with each cluster minimising the distance distribution around its centroid. The (unsupervised) k-means clustering algorithm is often used for data mining applications [224, 225, 226, 227] and is here applied as part of multi-dimensional image segmentation approach (see application in Section 4.3.6.2).

Image segmentation problems of multi-object systems or samples with multi-component mix-

tures are often complex. The selection of the optimal segmentation method is depending on the nature of the sample such as its structure and dynamic range resolution of its solid phase components. Details on additional methods for practical applications of micro-XRT image segmentation are discussed in more detail by Wildenschild and Sheppard [153].

4.3.5 Image Analysis - Feature Extraction (Micro-XRT Workflow *Stage 6* [Fig. 4.2])

The aim of the image analysis stage is the extraction of quantitative information related to the object's structural attributes. This step of the micro-XRT characterisation workflow (Fig. 4.2, *Stage 6*) drastically reduces the complexity of the micro-XRT image data to scalar measurement values, which allows further comparison and interpretation. The implemented image analysis routine consists of multiple methods specifically designed to capture complex object information relevant for a better understanding of the sample transformation in the manufacturing process or its performance. An overview of the implemented methodologies is provided in the following sections. All features are assigned to property-related categories of size, shape, porosity, surface or location/orientation.

Basic features are derived from image moments (M_{pqr}). For 3D digital image data with intensity ($I(x, y, z)$) distributions in the x, y and z dimension, these can be calculated using Equation 4.1. The zeroth order image moment (M_{000}) for a binary digital image gives the total object voxel volume. The first order moments (M_{100}, M_{010}, M_{001}) contain information on the object centroid. The central moments shown in Equation 4.2 include the components of the image centroid, $x_c = \frac{M_{100}}{M_{000}}$, $y_c = \frac{M_{010}}{M_{000}}$ and $z_c = \frac{M_{001}}{M_{000}}$. The central moments are translation-invariant. The image moments are used to extract features of object size, location and orientation. Details on the use of image moments for feature extraction are described in the corresponding sections below.

$$M_{pqr} = \sum_x \sum_y \sum_z x^p y^q z^r I(x, y, z) \tag{4.1}$$

$$\mu_{pqr} = \sum_x \sum_y \sum_z (x - x_c)^p (y - y_c)^q (z - z_c)^r I(x, y, z) \tag{4.2}$$

4.3.5.1 Size

The size of an object is one of the most commonly used property to describe solid products, especially multi-particulate systems e.g. powders. Various methodologies can be employed to capture size-related information from micro-XRT image data. An overview of the implemented methods for size quantification is given in Table 4.3. Selected examples are further visualised in Fig. 4.7.

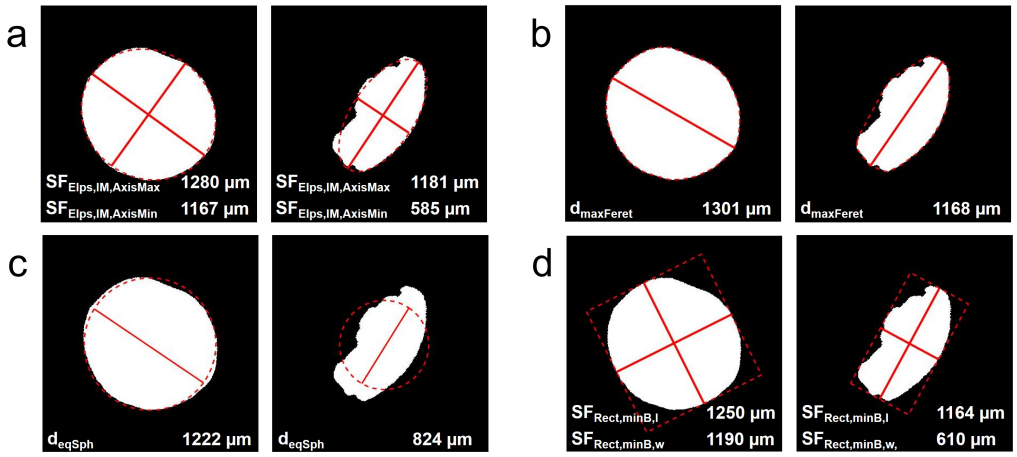

Figure 4.7: Micro-XRT image analysis subroutine for the extraction of structure-based object size descriptors: (a, $SF_{Elps,IM,AxisMax/AxisMin}$) ellipse fitting, (b, $d_{maxFeret}$) maximum Feret diameter, (c, d_{eqSph}) equivalent sphere diameter and (d, $SF_{Rect,minB,l/w}$) characteristic lengths of a minimum bounding rectangle fit.

The absolute object volume (V) is the sum of voxels, the zeroth order image moment (M_{000}, Equation 4.1), multiplied with the image pixel/voxel size. The equivalent sphere diameter (d_{eqSph}) is calculated from a sphere with the same volume as the absolute object volume ($V_{eqSph} = V$) and is often used for size comparison across multiple characterisation platforms. The maximum Feret diameter ($d_{maxFeret}$) corresponds to the longest vector length between two voxels on the object surface and is useful as an expression of the length of the object. Additionally implemented size measurements are derived from characteristic lengths of basic geometric shapes that were fitted to the object e.g. $SF_{Elps,IM,AxisMax}$ (Fig. 4.7 a) and $SF_{Rect,minB,l}$ (Fig. 4.7 d). The ability of individual descriptors to accurately capture the size of the analysed object strongly depends on the morphology of the object. For the examples shown in Fig. 4.7, d_{eqSph} (Fig. 4.7 c) fails as a size measurement of particles with non-spherical shape, however, other descriptors compensate for the non-spherical particle morphology (e.g. $SF_{Elps,IM,AxisMax}$, $d_{maxFeret}$ and

Table 4.3: Overview of structural features used to describe the object size. [a] CMAC, [b] MATLAB Image Processing Toolbox, [c] literature/Mathworks File Exchange

Feature	Description
Object Volume (V)[b]	Absolute size of all pixels/voxels of the object volume (translation- and rotation-invariant, 2D/3D, $\in \mathbb{R}^+$).
Eqv. Sphere Diameter (d_{eqSph})[b]	Equivalent spherical diameter of the object volume (translation- and rotation-invariant, 2D/3D, $\in \mathbb{R}^+$).
Bounding Box (V_{BB}, $\mathrm{SF}_{\mathrm{BB}}$)[b]	Size and characteristic lengths of the minimum bounding box incorporating the object volume (translation-invariant, 2D/3D, $\in \mathbb{R}^+$).
Max Feret Diameter (d_{maxFeret})[a]	Maximum distance between two points on the object surface (translation- and rotation-invariant, 2D/3D, $\in \mathbb{R}^+$).
Mean Breadth Diameter (d_{Bdth})[c]	Mean breadth of the object orthogonal to the object length (translation- and rotation-invariant, 2D/3D, $\in \mathbb{R}^+$)
Ellipsoid Fitting ($\mathrm{SF}_{\mathrm{Elps,IM}}$)[b]	Characteristic lengths of a fitted ellipsoid/ellipse with equivalent second central image moments (translation- and rotation-invariant, 2D/3D, $\in \mathbb{R}^+$).
Ellipsoid Fitting ($\mathrm{SF}_{\mathrm{Elps,SA}}$)[c]	Characteristic lengths of a surface-fitted ellipsoid/ellipse (translation- and rotation-invariant, 2D/3D, $\in \mathbb{R}^+$) [228].
Ellipsoid Fitting ($\mathrm{SF}_{\mathrm{Elps,minB}}$)[c]	Characteristic lengths of the minimum bounding ellipsoid/ellipse incorporating the object volume (translation- and rotation-invariant, 2D/3D, $\in \mathbb{R}^+$) [229].
Sphere Fitting ($\mathrm{SF}_{\mathrm{Sph,minB}}$)[a,c]	Radius of the minimum bounding circle/sphere incorporating the object volume (translation- and rotation-invariant, 2D/3D, $\in \mathbb{R}^+$) [229].
Half Sphere Fitting ($\mathrm{SF}_{\mathrm{HalfSph,minB}}$)[c]	Characteristic lengths of the minimum bounding half circle/sphere incorporating the object volume (translation- and rotation-invariant, 2D, $\in \mathbb{R}^+$) [229].
Rectangle Fitting ($\mathrm{SF}_{\mathrm{Rect,minB,l}}$)[c]	Characteristic lengths of the minimum bounding rectangle incorporating the object volume (translation- and rotation-invariant, 2D, $\in \mathbb{R}^+$) [229].
Triangle Fitting ($\mathrm{SF}_{\mathrm{Tri,minB}}$)[c]	Characteristic lengths of the minimum bounding triangle incorporating the object volume (translation- and rotation-invariant, 2D, $\in \mathbb{R}^+$) [229].

$\mathrm{SF}_{\mathrm{Rect,minB,l}}$) to achieve a more accurate measurement of the maximum particle size.

4.3.5.2 Shape

Shape features are used to describe the overall object morphology and can range from a simple comparison to ideal geometric shapes (e.g. cube, sphere, ellipsoid) to more complex approaches used for pattern recognition involving Zernike polynomials [230, 231] and Fourier coefficients [232]. An overview of the implemented methods for shape quantification is given in Table 4.4. Selected examples are further visualised in Fig. 4.8.

The shape and morphology of multi-particle systems are often described using a sphericity index. The particle sphericity potentially has further implications on the particle size measurement as discussed in Section 4.3.5.1. Multiple approaches can be used to quantify particle sphericity. Ψ_{gl} is a simple ratio of the detected object volume to its surface area [233], $\mathrm{SF}_{\mathrm{Sph,minB,F}}$ evaluates the goodness-of-fit for a circle fully enclosing the object (Fig. 4.8 a) and $\Psi_{\mathrm{lR,R}}$ employs a more sophisticated approach for local sphericity calculations (Fig. 4.8 b) [182].

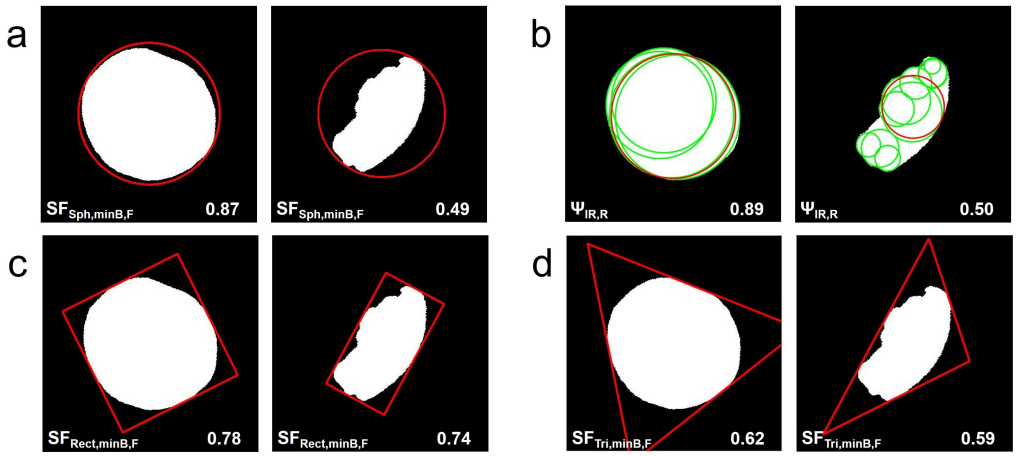

Figure 4.8: Micro-XRT image analysis subroutine for the extraction of structure-based object shape descriptors: (a, $SF_{Sph,minB,F}$) minimum bounding circle fit, (b, Ψ_{IR}) local roundness analysis, (c, $SF_{Rect,minB,F}$) minimum bounding rectangle fit and (d, $SF_{Tri,minB,F}$) minimum bounding triangle fit.

For crystalline solids with changing habit, the aspect ratio (AR) might be of particular interest e.g. to distinguish between block-shaped and elongated, rod-shaped crystal habits. The AR calculations employ a rotation-invariant ellipse ($AR_{Elps,IM}$, Fig. 4.7 a) or rectangle (AR_{Rect}, Fig. 4.8 c) shape fitting algorithm. Additional basic geometric shapes used for feature extraction are triangles (Fig. 4.8 d), parallelograms or half spheres.

4.3.5.3 Porosity

Porosity features are means to describe and quantify the internal object (micro-) voids. Object porosity is identified after a subtraction of the object's solid phase (V) from the object ROI (V_ROI). The porosity can be further sub-categorized in open and closed porosity, which refers to internal voids with and without a connection to the V_ROI surface, respectively. Open and closed porosity is calculated based on the full information of the 3D image stack.

An example for the detected open (blue) and closed (green) porosity is shown in Fig. 4.9 using 3DVB-*Skrinkwrap_oP* for generating the object V_ROI. The example emphasises the use of the full 3D image stack to distinguish between open and closed porosities. The particle object has a central opening (Fig. 4.9 b, top-left) connecting the vast majority of the internal voids as open porosity to its surface. For this object, a significant part of the open porosity can therefore not be detected in a micro-XRT image analysis approach limited to the characterisation of individual 2D cross-sections (Fig. 4.9 a). However, the connection of all internal voids to the particle

Table 4.4: Overview of structural features describing to object shape. [a] CMAC, [b] MATLAB Image Processing Toolbox, [c] literature/Mathworks File Exchange

Feature	**Description**
Eccentricity (ECC)[b]	Ratio of the distance between the foci of the ellipse and its major axis length (translation- and rotation-invariant, 2D, $\in [1, \infty] \subset \mathbb{R}^+$).
Aspect Ratio ($AR_{Elps,IM}$, $AR_{Rect,minB}$)[a]	Ratio between longest and shortest characteristic length of a fitted ellipsoid with equivalent second central image moments or a minimum bounding rectangle (translation- and rotation-invariant, 2D/3D, $\in [1, \infty] \subset \mathbb{R}^+$).
Sphericity, global (Ψ_{gl})[a]	Sphericity index calculated as the ratio of the detected object volume to its surface ($= \pi^{1/3} \cdot (6 \cdot V_{V\_ROI})^{2/3} / A_{Sf,V\_ROI}$,translation- and rotation-invariant, 2D/3D, $\in [0, 1] \subset \mathbb{R}^+$) [233].
Local Roundness (Ψ_{lR})[c]	Detection of local roundness including local roundness ratios and smallest local surface curvature ratio (translation- and rotation-invariant, 2D, $\in [0, 1] \subset \mathbb{R}^+$) [182]
Sphere Fitting ($SF_{maxFeretSph,F}$)[a]	Goodness-of-fit for circle/sphere with equivalent maximum Feret diameter (translation- and rotation-invariant, 2D, $\in [0, 1] \subset \mathbb{R}^+$).
Ellipsoid Fitting ($SF_{Elps,SA,F}$)[c]	Goodness-of-fit for surface-fitted ellipsoid/ellipse. Linear least squares optimisation (translation- and rotation-invariant, 2D/3D, $\in \mathbb{R}^+$) [228].
Ellipsoid Fitting ($SF_{Elps,minB,F}$)[c]	Goodness-of-fit for minimum bounding ellipsoid/ellipse incorporating the object volume (translation- and rotation-invariant, 2D/3D, $\in [0, 1] \subset \mathbb{R}^+$) [229].
Sphere Fitting ($SF_{Sph,minB,F}$)[c]	Goodness-of-fit for minimum bounding circle/sphere incorporating the object volume (translation- and rotation-invariant, 2D, $\in [0, 1] \subset \mathbb{R}^+$) [229].
Half Sphere Fitting ($SF_{HalfSph,minB,F}$)[c]	Goodness-of-fit for minimum bounding half circle/sphere incorporating the object volume (translation- and rotation-invariant, 2D, $\in [0, 1] \subset \mathbb{R}^+$) [229].
Rectangle Fitting ($SF_{Rect,minB,F}$)[c]	Goodness-of-fit for minimum bounding rectangle incorporating the object volume (translation- and rotation-invariant, 2D, $\in [0, 1] \subset \mathbb{R}^+$) [229].
Parallelogram Fitting ($SF_{Pg,minB,F}$)[c]	Goodness-of-fit for minimum bounding parallelogram incorporating the object volume (translation- and rotation-invariant, 2D, $\in [0, 1] \subset \mathbb{R}^+$) [229].
Triangle Fitting ($SF_{Tri,minB,F}$)[c]	Goodness-of-fit for minimum bounding triangle incorporating the object volume (translation- and rotation-invariant, 2D, $\in [0, 1] \subset \mathbb{R}^+$) [229].
Zernike (Z_A)[c]	Amplitude of complex zernike moment (translation- and rotation-invariant, 2D, $\in [0, 1] \subset \mathbb{R}^+$) [231].

surface becomes apparent after integrating additional information from the full object image stack as shown in Fig. 4.9 b.

The quantified open and closed porosity volume further strongly depends on the applied ROI method described in Section 4.3.3.4. Here, the open porosity only increases slightly from 32.03% to 33.91% comparing 3DVB-*Skrinkwrap_oP* to a simple 3DVB-*Convexhull3D*. For objects with a high extent of concave surfaces, the detected open porosity volume can drastically increase using a Convex-Hull ROI approach (see application in Chapter 6). The results also demonstrate the importance of an accurate description of the applied porosity analysis process and its implications on the extracted porosity values during quantification.

The validation of quantitative porosity information from micro-XRT image data can be accomplished using complementary experimental methods. A detailed overview of complementary techniques for the characterisation of pore structures of pharmaceutical tablets, but with the po-

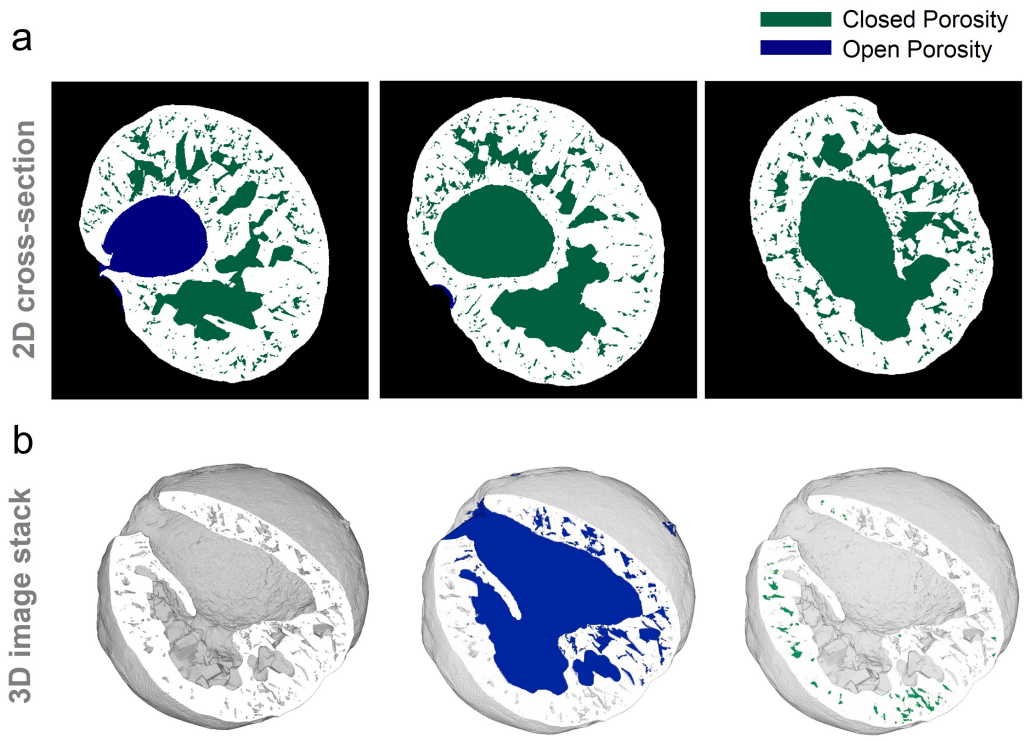

Figure 4.9: Micro-XRT image analysis subroutine for the extraction of object porosity descriptors. (a) A simple 2D cross-section analysis is unable to detect 3D connected object porosities, overestimating the object's closed porosity volume. (b) The 3D particle model shows a large opening on its surface. Working with the full image stack allows the accurate detection of (blue) open and (green) closed porosity.

Table 4.5: Overview of structural features used to describe the object porosity. [a] CMAC, [b] MATLAB Image Processing Toolbox, [c] literature/Mathworks File Exchange

Feature	**Description**
Porosity (P)[a]	Absolute area/volume of the object's open, closed or total porosity (translation- and rotation-invariant, 2D/3D, $\in \mathbb{R}^+$).
Convex-hull Solidity ($SV_{CH,V}$)[a,b]	Ratio between object volume and its convex-hull volume (translation- and rotation-invariant, 2D/3D, $\in [0,1] \subset \mathbb{R}^+$).
Solidity (SV)[a]	Ratio between object volume and its ROI volume (translation- and rotation-invariant, 2D/3D, $\in [0,1] \subset \mathbb{R}^+$).
Extent (Ex)[b]	Ratio between object volume and minimum bounding box volume (translation-invariant, 2D/3D, $\in [0,1] \subset \mathbb{R}^+$).

tential for wider applicability to other pharmaceutical solid products is provided by Markl et al. [66]. The micro-XRT characterisation might be unable to detect and quantify small micro-porosities (< 1 - 25 μm) within or below the spatial resolution of the micro-XRT system. The impact of changing micro-XRT image quality as well as of the employed image processing/-analysis algorithms on the quantification of these micro-porosities can be assessed within a sensitivity analysis as demonstrated in Chapter 5.

4.3.5.4 Surface

Surface features of an object in the micro-XRT images relate to local attributes of the sample-air (foreground-background) interface. A_{Sf} is a simple quantification of the surface area, but can significantly differ between the object volume ($A_{Sf,V}$) and the object ROI (A_{Sf,V_ROI}) since $A_{Sf,V}$ also includes contributions of internal surface areas. As a result, $A_{Sf,V}$ highly correlates with the overall particle porosity and A_{Sf,V_ROI} is commonly used to express the primary, outer object surface area. SV_{CH,V_ROI} uses a Convex-Hull algorithm in order to detect concave surface volumes of V_ROI. Quantitative information of SV_{CH,V_ROI} can be used to interpret the extent of surface buckling (see Chapter 6) or surface roughness (see Chapter 5).

Table 4.6: Overview of structural features used to describe the object surface. [a] CMAC, [b] MATLAB Image Processing Toolbox, [c] literature/Mathworks File Exchange

Feature	Description
Surface Area (A_{Sf})[b]	Absolute area of the object boundary region (translation- and rotation-invariant, 2D/3D, $\in \mathbb{R}^+$).
Surface Roughness (SV_{CH,V_ROI})[a,b]	Ratio between object ROI volume and the convexhull volume (translation- and rotation-invariant, 2D/3D, $\in [0,1] \subset \mathbb{R}^+$).

4.3.5.5 Location and Orientation

Information and on the object location can be expressed as the centroid-coordinates of the object and the translation vector can be calculated from the first order image moment ($[x_c, y_c, z_c] = [M_{100}, M_{010}, M_{001}]$, Equation 4.1). Additional information on the object orientation are determined using the second order central moments (Equation 4.2). The Euler angles (α_E, β_E, γ_E) are three angles describing the object orientation within the pre-defined coordinate system of the image stack [234].

Table 4.7: Overview of structural features used to describe the object surface. [a] CMAC, [b] MATLAB Image Processing Toolbox, [c] literature/Mathworks File Exchange

Feature	Description
Centroid (x_c, y_c, z_c)[b]	Coordinates of the regional centre of mass from first image moment (rotation-invariant, 2D/3D, $\in \mathbb{R}^+$).
Euler angles (α_E, β_E, γ_E)[b]	Euler angle between the characteristic object eigenvectors determined from the second centralised image moments (translation-invariant, 3D, $\in [-180, 180] \subset \mathbb{R}$).
Orientation (α)[b]	Angle between the x-axis and the major axis of a fitted ellipse with equivalent second central image moments (translation-invariant, 2D, $\in [-180, 180] \subset \mathbb{R}$).
Zernike (Z_P)[c]	Phase angle of Zernike moment (translation-invariant, 2D, $\in [-180, 180] \subset \mathbb{R}$) [231].

Information on the object's centroid-coordinates and the Euler angles can be used to compensate changes in location and orientation. This was applied to reliably extract translation- and rotation-invariant object cross-sections of 3D objects, which can be characterised with 2D image analysis algorithms (see application in Chapter 5, Section 5.2.3). Information on the object orientation or location in pharmaceutical products is of particular interest to assess effects of preferential orientation or powder segregation/packing [235].

4.3.6 Application of micro-XRT for the Analysis of Solid Pharmaceutical Products

Potential applications of micro-XRT cover a broad range of products and drug product intermediates within the pharmaceutical downstream manufacturing pipeline from single particles/crystals to fully formulated tablets or capsules. An overview of analysed samples using micro-XRT is shown in Fig. 4.10. This section aims to illustrate the application of micro-XRT for selected case studies of single particles, powder blends and 3D-printed tablets exemplifying the use of the developed micro-XRT image analysis framework for samples with changing research objectives.

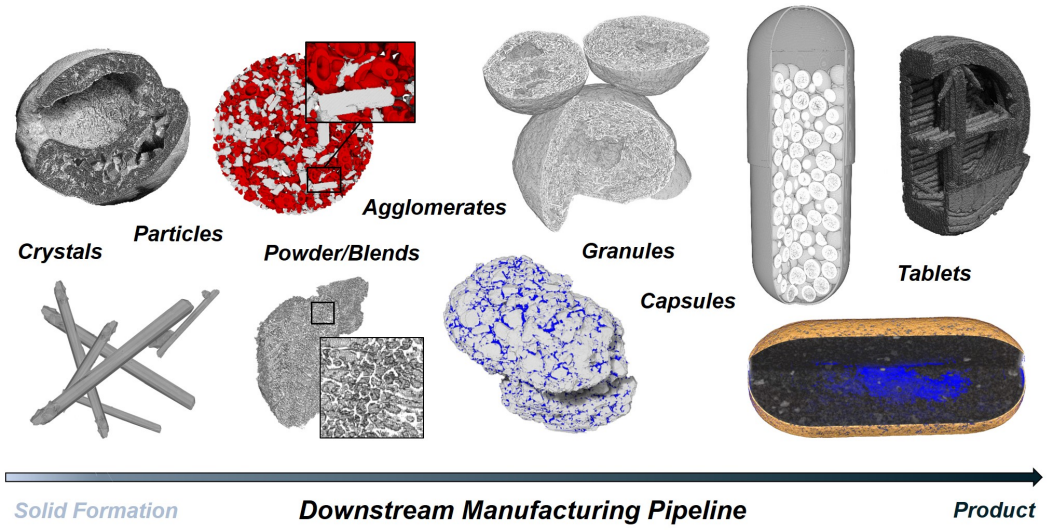

Figure 4.10: Overview of micro-XRT samples with applications covering a wide range of the pharmaceutical downstream manufacturing pipeline from single crystals/particles to multi-particle systems including powders and fully formulated final dosage forms e.g. capsules and tablets.

4.3.6.1 Single particles

Introduction: An important aspect of particle engineering application is the quantitative characterisation of particle properties that guide rational decision making towards optimised particle attributes e.g. with an effect on dissolution for tailored bioavailablity [236], flowability for powder handling [237] or direct compaction for tableting [238, 239]. Single droplet drying (SDD) experiments are used in combination with micro-XRT to investigate the solidification of particles from solution droplets assessing the influence of formulation parameters on the particle formation process and the final particle structure [7]. This case study further demonstrates the use of micro-XRT to characterise single particles and visualises the diversity of potential particle structures for a range of small molecules and large, macro-molecular polymers.

Methods: Particles from SDD experiments were obtained after reaching a fully dry state and analysed using micro-XRT. An overview of the examined particle samples is provided in Table 4.8. Local thickness calculations using a proprietary sphere-fitting approach were performed in CTAn (v1.16.4.1, Bruker). The sphere-fitting approach aims to determine the local thickness equivalent to the maximum sphere diameter which can be expanded within the structure volume at any given point.

Table 4.8: Overview of prepared solution for SDD experiments.

ID	Compound	Solvent	c_0 [mg/mL]	Size ($d_{maxFeret}$) [μm]
GLY_P1	Glycine	DI-water	150.00	2390
GLY_P2	Glycine	DI-water	150.00	2195
CBZ_P	Carbamazepine	methanol	10.40	1167
TRE_P	Trehalose	DI-water	150.00	725
LAC_P	Lactose	DI-water	150.00	1919
MAN_P	D-mannitol	DI-water	150.00	1561
PVP_P	PVP	DI-water	150.00	1929
PVP-INA_P	PVP / Isonicotinamide	DI-water:ethanol 50:50 v/v	75.00 / 25.00	1191
PVP-GLY_P	PVP / Glycine	DI-water	100.00 / 50.00	1844

Results: An overview of particle morphologies for changing compounds is shown in Fig. 4.11. Fig. 4.11 a-c show three highly crystalline particles of GLY (Fig. 4.11 a-b) and CBZ (Fig. 4.11 c). The particle structure is dominated by the size and the habit of the primary crystalline solids. GLY_P1 and GLY_P2 exhibit significant differences in the primary crystal size distribution. GLY_P1 crystals are large and highly aggregated. In contrast, GLY_P2 crystals nucleate

late with a small primary particle size (< 25 μm). CBZ_P consist of thin, needle-shaped primary crystals, which form a highly agglomerated round particle. Quantitative information on individual crystals within the particle requires a segmentation approach to isolate the primary objects as described in Section 4.3.4). However, small crystal sizes and strong aggregation limit the successful application of a structure-based segmentation. In this case, a structural thickness calculation allows a quantification of the crystal size. After pre-processing the micro-XRT image data using 3DVB (Section 4.3.3) for noise reduction and binarisation, the local thickness of the primary crystals of GLY_P1, GLY_P2 and CBZ_P was evaluated using a sphere-fitting approach. As expected, GLY_P1 has the largest structural thickness of 69 $\pm$ 54 μm. The large deviation in the local structural thickness might indicate ongoing crystal nucleation over the course of the particle formation process with significant changes in the available growth times for individual crystals or might indicate differences in the crystal habit for changing GLY polymorphs. Two crystal habits, blocks and rods, can be visually identified in the GLY_P1 aggregate. GLY_P2 has the smallest structural thickness of 5 $\pm$ 2 μm, which comes close to the expected resolution limitations of the employed micro-XRT system. The needle-shaped primary crystals of CBZ_P have a structural thickness of 7 $\pm$ 3 μm. The complex relationship between substance- and process-related effects on the habit and size of the primary crystals can lead to drastic changes in the overall particle structure. The performed SDD experiments in conjunction with micro-XRT allowed an investigation of local structure for three highly crystalline particles solidifying from solution.

Carbohydrates are common excipients in pharmaceutical products and popular for spray drying applications. The particle morphologies of TRE, LAC and MAN particles are shown in Fig. 4.11 d-f. Droplet drying and particle formation has a dominant effect on the final particle morphology. TRE solidifies as dense spheres without apparent crystal formation. During drying, LAC forms a rigid crust on the droplet surface from which crystals nucleate and slowly grow towards the droplet center as observed from image data collected on the SAL and micro-XRT system. LAC_P is dominated by an amorphous/micro-crystalline crust and large inner void. Compared to other carbohydrates, MAN has a high crystallisation tendency [240, 241]. The obtained MAN_P shows a highly crystalline internal structure. Individual MAN crystals grow from nucleation zones on the droplet surface and stabilize the spherical particle shape. In spray drying, excipients with high crystallisation tendency have lower residual moisture levels [242]

and are used as carrier particles [243, 241]. In direct comparison, excipients with low crystallisation tendency find applications as glass formers for the stabilisation of amorphous drug products [113, 140], but can introduce risks of solid state transformations [244, 245, 246]. The detected particle porosity (= 1-V/V_ROI) increases with increasing crystallinity for these three particles from 0.8% for TRE_P to 33.6% for LAC_P and 69.9% for MAN_P. Information on the crystallisation tendency of pharmaceutical excipients and its implications on the final particle internal micro-structure are crucial for process and product design.

Particles from SDD experiments containing PVP are shown in Fig. 4.11 g-i. The pure PVP solution solidifies as particles with large internal, central voids (Fig. 4.11 g). In contrast, particles of INA-PVP (Fig. 4.11 i) are dense and do not exhibit these large voids. The particle morphology suggests that the crust formation process of PVP is prohibited with the addition of INA. Nicotinamide and Nicotinamide-derivatives are well known hydrotropes, which solubilise hydrophobic compounds in aqueous solutions. These compounds have been used particularly for formulations of poorly water-soluble drug candidates to increase solubility [247]. Here, the change in the particle structure suggests molecular interactions between INA and PVP solubilising the polymer. The change in the particle morphology can be quantified using the 3DVB-*Convexhull3D* method to create a particle ROI (V_ROI). The internal void space (= 1-V/V_ROI) decreases significantly comparing PVP_P (41.30%) or GLY-PVP_P (50.44%) to INA-PVP (5.18%). For formulations of PVP, insights from the micro-XRT characterisation were essential to better understand the particle formation process observed in the SDD experiments and its implications on the final particle morphology.

Conclusion: Micro-XRT enabled the non-destructive characterisation of single particles obtained from SDD experiments. The results demonstrate the high complexity and diversity of particle structures affected by individual compounds, solidification kinetics and molecular interactions. In combination with SDD data, micro-XRT provides valuable insights into the particle morphology aiming to establish a link between particle formation and final structure. This approach has further been used for a quantitative investigation of the particle design space for a multi-component formulation of MET, MAN and HPMC K100LV (see Chapter 6).

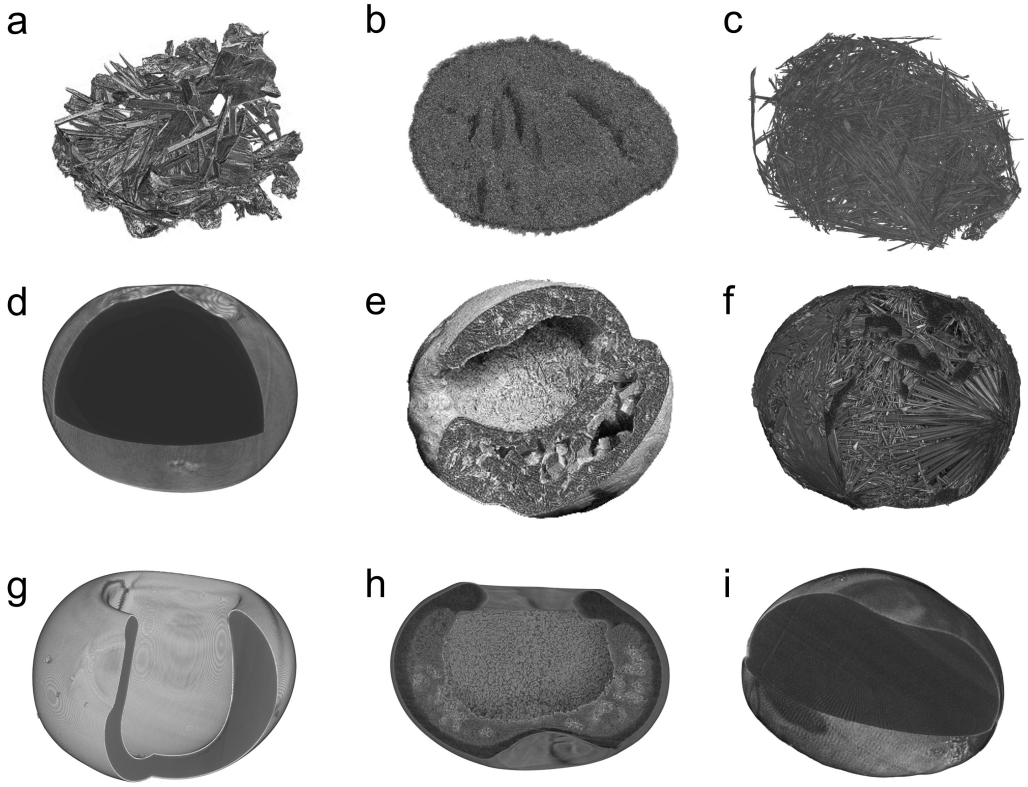

Figure 4.11: Particles from SDD experiments characterised with micro-XRT to investigate their final structure: (a) GLY_P1 (early nucleation, large crystals), (b) GLY_P2 (late nucleation, micro-crystals), (c) CBZ_P (needle-shaped crystals), (d) TRE_P (dense, amorphous), (e) LAC_P (partial crystalline), (f) MAN_P (highly crystalline), (g) PVP (skin formation, large central void), (h) PVP-GLY_P (skin formation, internal crystal growth) and (i) PVP-INA_P (dense solid).

4.3.6.2 Powders

Introduction: Powders are complex multi-particulate systems which can consist of a single compound or multi-component mixtures. Blending is the process of powder mixing to create a homogeneous powder composition and is widely used within pharmaceutical manufacturing processes e.g. to prepare solids for tableting [248] or prior to hot-melt extrusion [249]. Micro-XRT was used to assess the homogeneity of a 50:50 w% physical mixture of crystalline metformin hydrochloride (MET) and polymeric PVP. Focus of this study was the pixel-wise classification of the micro-XRT image data collected for powders containing MET and PVP particles using an unsupervised machine learning (ML) algorithm.

Methods: Powder blends of a 50:50 w% physical mixture of MET and PVP were characterised using micro-XRT. Iodine vapour staining allowed to selectively increase the effective X-ray attenuation of the polymer phase. For this purpose, 100 mg of the powder blend were spread across a petri dish to obtain a homogeneous single particle layer. Four pieces of iodine with diameters of approximately 1 mm each were attached to the lid using Parafilm. The petri dish was then sealed with additional Parafilm for 32 days prior to the micro-XRT analysis. An unsupervised k-means algorithm was used for a pixel-wise classification of the micro-XRT image data for an automated identification and segmentation of MET and PVP particles. Micro-XRT image pixels were classified in one of the following three clusters: (kC1) MET, (kC2) MET-PVP mixture and (kC3) PVP. A custom script using a step-wise 3D region growing algorithm was applied subsequently to re-assign pixels of kC2 to either kC1 (MET) or kC3 (PVP). The classification performance was assessed against a manually segmented cross-section (user-defined ground-truth) with 1406676 pixels (MET 639824 pixels, PVP 766852 pixels).

Results: The micro-XRT image data is shown in Fig. 4.12. Visually, individual particles of MET and PVP can be distinguished in the reconstructed cross-section images (Fig. 4.12 a) by the local X-ray attenuation, the particle shape and internal porosities. In direct comparison, MET exhibits a lower X-ray attenuation coefficient on average and its crystalline shape has planar surfaces with clearly defined edges. Iodine stained PVP particles show high X-ray attenuating and the polymeric particles have a round particle morphology with large inner voids. Examples of a MET and PVP particle are shown in Fig. 4.12 g. Differences in the particles related to its

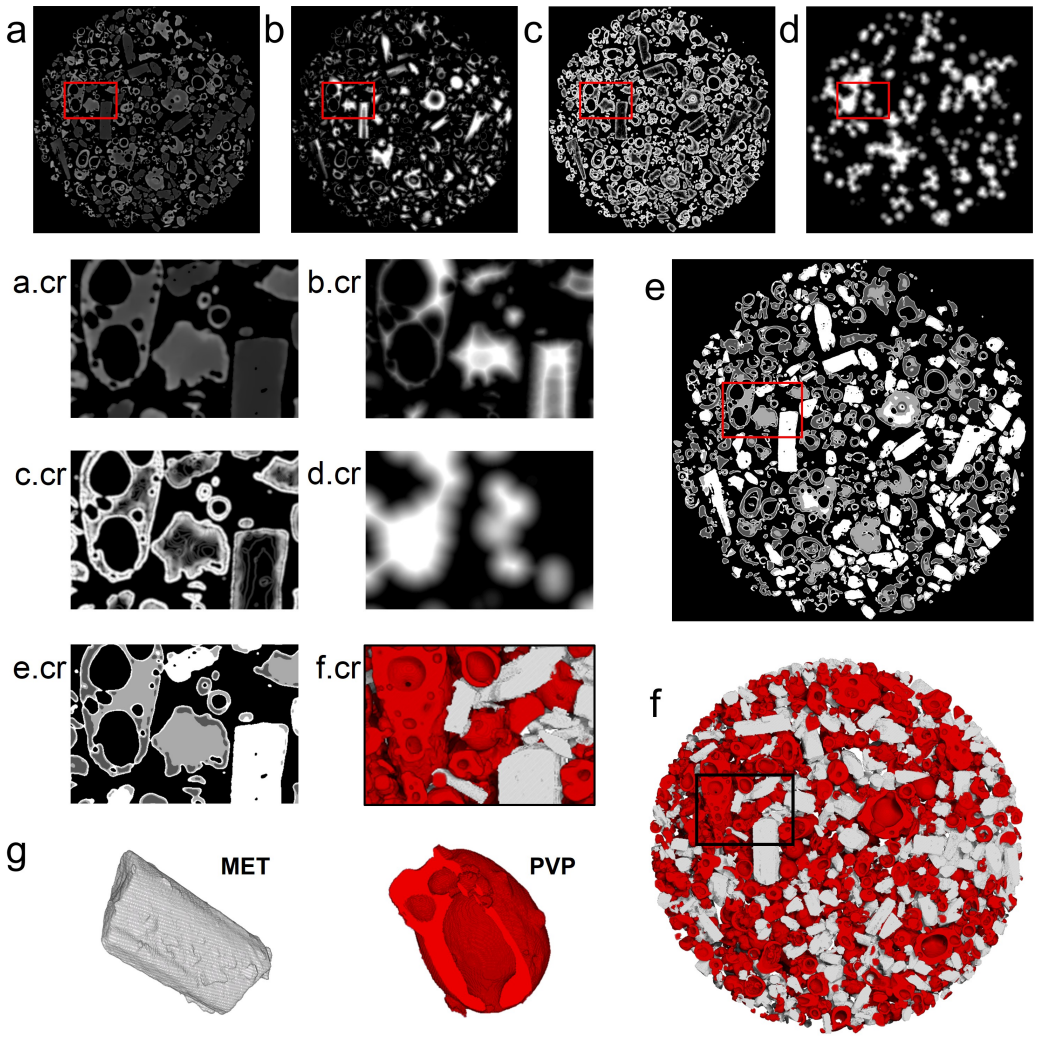

Figure 4.12: Micro-XRT characterisation of a physical mixture of MET crystals and PVP polymer particles. Image transformations aimed to capture information on (a) local X-ray attenuation, (b) structural thickness, (c) local X-ray attenuation homogeneity and (d) proximity to round particle voids. (e) The transformed micro-XRT image data enabled a pixel-wise classification assigning each pixel to kC1 (white), kC2 (light grey) and kC3 (dark grey). (f) Region-growing was used to re-assign kC2 pixels to (white) MET and (red) PVP volume elements. (a.cr - f.cr) Magnification of selected regions from images a - f. (g) Isolated MET and PVP particle.

local X-ray attenuation coefficient (Fig. 4.12 a), particle structural thickness (Fig. 4.12 b), image entropy (Fig. 4.12 c) and porosity proximity (Fig. 4.12 d) were exploited for an unsupervised k-means pixel-wise classification. The results of the k-means clustering approach are shown in Fig. 4.12 e (kC1 - white, kC2 - light grey and kC3 - dark grey). The classification accuracy was 85.00% and 99.95% for kC1 and kC3, respectively. kC1 and kC3 were used as local region markers of MET and PVP to re-assign pixels of kC2, which contains a mixture of pixels related

to MET (13.09%) and PVP (86.91%). After the processing of the micro-XRT image data with a local region-growing algorithm (Fig. 4.12 f), the final segmentation had an accuracy of 99.03% for kC1 and 97.94% for kC3 assessed against a user-defined ground-truth. The successfully segmented micro-XRT image data allows a direct assessment of local blending homogeneity. For the MET- PVP powder mixture, the analysis gave a volume ratio for MET:PVP of 46.69% : 53.31%, v/v. The mass ratio can be estimated using published true density data for MET of 1.36 g/cm^3 [250] and PVP of 1.18 g/cm^3 [251] resulting in a mass ratio for MET:PVP of 53.81% : 46.26%, w/w.

Conclusion: Micro-XRT allowed the successful characterisation of a multi-particle powder using a pixel-wise classification model for image segmentation. This approach has great potential for the investigation of blending processes to assess bulk and single particle properties. The demonstrated capabilities for a pixel-wise classification can be further translated to other sample systems using targeted image transformation routines to capture the nature of the micro-XRT image data on a pixel level.

4.3.6.3 3D-printed tablets

Introduction: 3D printing is often seen as a disruptive technology with applications in engineering sciences bringing major improvements to rapid prototyping with decentralised, accelerated and low-cost, low-volume production. In the pharmaceutical industry, 3D printing has been adapted to serve as a manufacturing platform for unique pharmaceutical dosage forms. Fused filament fabrication (FFF) 3D printing is a technique utilising drug loaded polymer filaments enabling the production of dose forms with complex 3D structures and the potential to customise release characteristics for personalised medicines [252, 253]. In this study, we explore the use of micro-XRT to support process development for the 3D-printing of pharmaceutical tablets.

Methods: Hot-melt extrusion was used for the production of filaments from 80 wt% polyvinyl alcohol (Parteck MXP, PVA), 10 wt% D-sorbitol (SOR) and a paracetamol (PCM) drug loading of 10 wt%. The filaments were subsequently tested for the production of 3D-printed tablets using a commercial, table top 3D printer (CEL Robox, UK). The tablets were printed with increasing selected levels of internal density (*filling*) levels of 20%, 50%, 80%, and 100%. Micro-XRT

was used to characterise the 3D-printed tablets and quantify the internal tablet porosity. Tablets were designed with a height of 3 mm, a diameter of 9 mm and rounded edges. The tablets have a target volume of 179 mm^3.

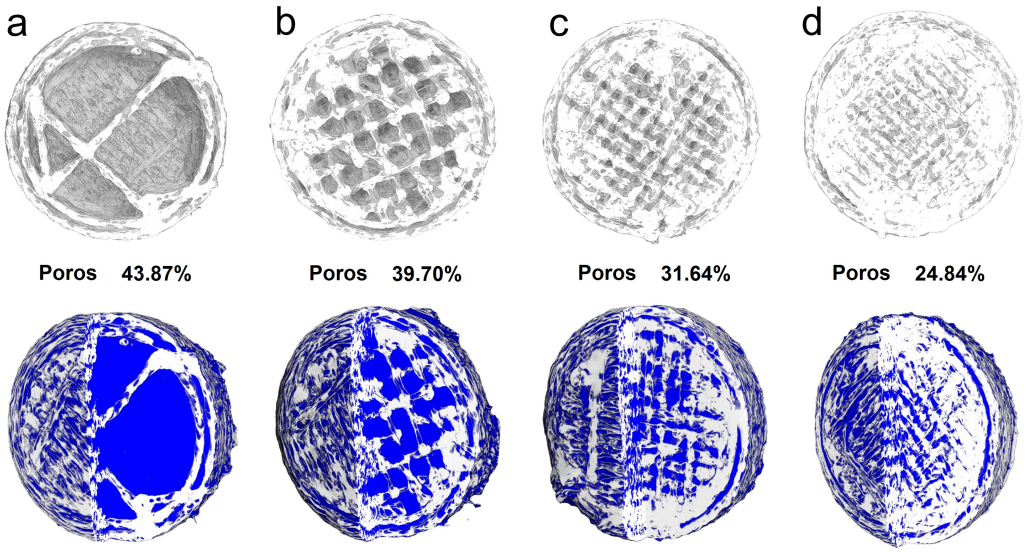

Figure 4.13: Surface-rendered micro-XRT visualisation of 3D printed HPMC-PCM tablets with increasing internal density (*filling*) of (a) 20%, (b) 50%, (c) 80%, and (d) 100% selected during manufacturing. The tablet porosity was determined using micro-XRT ($V_{P,XRT}$, blue) and shows a reduction from 43.87% (20% *filling*) to 24.84% (100% *filling*). The quantified tablet solid phase volume (V_{XRT}, white) was used to estimate its true density.

Results: Fig. 4.13 shows the four assessed 3D printed tablets and their determined tablet porosity volumes (blue). As expected, the tablet porosity (Fig. 4.13 blue) decreases with increasing selected *filling* level. A linear regression of the measured porosity levels yields a maximum porosity of 49.90% (intercept) suggesting that the tablet surface layers, which remain constant over all selected internal density levels, take up around half of the total tablet volume. The tablet porosity then decreases linearly by 0.24% per%-*filling* (R^2 0.97). The tablet volume ROI (V_ROI = tablet solid phase (V_{XRT}, Fig. 4.13 white) + porosity ($V_{P,XRT}$, Fig. 4.13 blue)) remains constant for all printed tablets at 179.5 $\pm$ 1.6 mm^3 indicating that the internal structure has no significant impact on the overall stability of the tablet body for selected *filling* levels between 20 - 100%. The determined tablet volumes calculated from the micro-XRT image data (V_{XRT}) are listed in Table 4.9. The tablet further includes the estimated tablet volumes ($V_{c,Mass}$) using the tablet weight and the reported true density of PVA between 1.19 - 1.31 g/cm^3 [254].

The values show a good correlation between V_{XRT} and $V_{c,Mass}$ and were used to validate the micro-XRT analysis results. The true density of the 3D printed tablets calculated from the micro-XRT data for all four tablets is very consistent and has a value of 1.227 ± 0.002 g/cm^3.

Table 4.9: Comparison of estimated tablet solid phase volume from weighed tablet mass ($V_{c,Mass}$) and micro-XRT (V_{XRT}).

Tablet (*Infill*)	**Mass [mg]**	**$V_{c,Mass}$ [mm^3]**	**V_{XRT} [mm^3]**	**$Mass_{XRT}$ [mg]**
Tblt100 (100%)	166.83	127.35 - 140.19	136.20	162.08 - 178.43
Tblt80 (80%)	149.16	113.86 - 125.34	121.76	144.89 - 159.50
Tblt50 (50%)	131.44	100.34 - 110.45	107.05	127.39 - 140.24
Tblt20 (20%)	122.48	93.50 - 102.92	99.65	118.58 - 130.54

Conclusion: Micro-XRT allowed the non-destructive visual inspection of 3D-printed tablets with a specific focus on the link between their internal porosity volumes and selected process *filling* levels for the 3D printer. The quantitative results are used directly to inform the tablet printing process. In conjunction with a performance analysis during dissolution, the results could allow an optimisation of the tablet design and its absolute dose.

4.3.7 Coupled micro-XRT and ToF-SIMS analysis for chemical mapping

Introduction: Micro-XRT has great applicability for the investigation of structural properties of a wide range of solid pharmaceutical products. Furthermore, changes in the local solid phase composition can be captured where there are differences in the effective X-ray attenuation. The micro-XRT image data, however, do not allow a direct identification of chemical entities. The use of complementary chemical imaging (CI) techniques are therefore crucial to further interpret the micro-XRT image data and correlate X-ray attenuation to solid phase composition. Time of Flight-Secondary Ion Mass Spectrometry (ToF-SIMS) is a surface mass spectrometry (MS) technique with a high spatial resolution, which enables the local identification of chemical entities. The technique can be used to map the molecular composition of pharmaceutical formulations [255, 256]. For this study, ToF-SIMS was applied in combination with micro-XRT to resolve the local chemical composition of particles obtained from SDD experiments containing metformin hydrochloride (MET) and D-mannitol (MAN).

Methods: Particles of MET and MAN (50:50, w/w) were obtained from SDD experiments in an acoustic levitator (SAL) and characterised using micro-XRT. Details of the SAL-XRT approach

for the characterisation of SDD experiments are described elsewhere [7]. After micro-XRT data acquisition, the particles were manually opened using a spatula to access internal surface areas. An IONTOF TOF.SIMS 5 instrument (IONTOF GmbH, Münster, Germany), equipped with a bismuth liquid metal ion gun (LMIG) and a gridless reflectron time-of-flight mass analyser, was employed for CI in selected regions of the internal surface to analyse the local chemical composition. High spatial resolution secondary ion images (400 - 600 nm, 20/80 edge-resolution analysis, see details Fig. A1 (ESI, page A2)) were collected over areas of 500 µm × 500 µm using a 30 keV Bi_3^+ primary ion beam. A total primary ion dose density (PIDD) of approximately $3 \cdot 10^{11}$ (primary ions/cm^2) was delivered for each image. The mass spectral information was recorded in the positive and negative secondary ion polarities, and an analyser pulsed delayed extraction was applied for improved mass-resolving power. To overcome charge build-up on the isolative samples, a low-energy electron beam (21 eV) flood gun was employed and the sample surface potential was optimised for each analysis. ToF-SIMS data were processed using SurfaceLab 6.7 software (IONTOF, Münster, Germany) to generate colour-overlay images displaying the local chemical composition of MET and MAN.

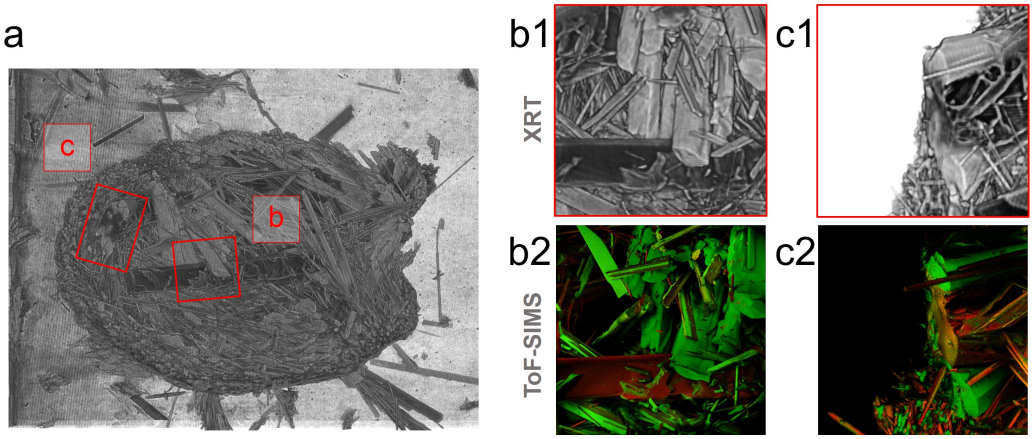

Figure 4.14: Micro-XRT coupled with ToF-SIMS for the analysis of particles with a two-compound crystalline structure (MET and MAN). (a) Intensity differences in the micro-XRT image data can be related to (b1,c1) the local chemical composition validated with (b2,c2) a chemical analysis of exposed crystal surfaces using ToF-SIMS. Regions with high X-ray attenuation correspond to MET (ToF-SIMS: green) whilst MAN (ToF-SIMS: red) crystals exhibit low X-ray attenuation.

Results: The results of a combined micro-XRT-ToF-SIMS characterisation approach are shown in Fig. 4.14. The MET-MAN particle is highly crystalline and individual crystals can easily be identified in the micro-XRT image data (Fig. 4.14 b1). The X-ray attenuation differs signif-

icantly between individual crystals. Within the dynamic range of the micro-XRT image data, lighter and darker areas correspond to regions with higher and lower X-ray attenuation, respectively. The micro-XRT image data also exhibit areas with a mix of lighter and darker pixel intensities (Fig. 4.14 c1), which suggests strong partial aggregation of MET and MAN. The clear differences in the effective X-ray attenuation indicate a local separation of both chemical entities. The local chemical composition was further characterised with ToF-SIMS (Fig. 4.14 b2-c2). MET and MAN were identified by their protonated molecular ions $C_4H_{12}N_5^+$ (m/z 130.11) and $C_6H_{15}O_6^+$ (m/z 183.09), respectively. A comparison of the image data allowed the assignment of individual chemical entities, MET and MAN, to the dynamic range of the micro-XRT image data with MET corresponding to lighter and MAN to darker pixel intensities.

The specific contribution of each component to the micro-XRT image histogram was further investigated using a manually segmented micro-XRT image. The intensity distribution in the micro-XRT image cross-sections exhibits a strong overlap in the grayscale distributions of MET and MAN as shown in Fig. 4.15 b. Intensity means are at 100.71 ± 27.36 and 39.69 ± 15.27 for MET and MAN, respectively. The considerable overlap in the intensity distribution introduces uncertainty in assigning local pixel intensity values to MET and MAN, respectively. For a qualitative assessment of the local distribution of MET and MAN, a color map was applied to the dynamic range of the micro-XRT image data to represent the local propensity for high MET (green) or MAN (red) concentrations. A visualisation is shown in Fig. 4.15 a. The particle consist of large MAN rod-shaped crystals and wide-spread MET coverage. Despite the high crystallinity of the particle's internal solid phase, there are regions, particularly towards the particle surface, where solids of both compounds form strong aggregates without extensive crystal growth.

Conclusion: ToF-SIMS has great potential as a complementary characterisation technique for micro-XRT applications to link local differences in X-ray attenuation to high-resolution chemical information. Here, the combination of ToF-SIMS and micro-XRT allowed the investigation of the local chemical composition within a particle containing MET and MAN. Data fusion methodologies could further improve the exploitation of CI to interpret 3D micro-XRT image data.

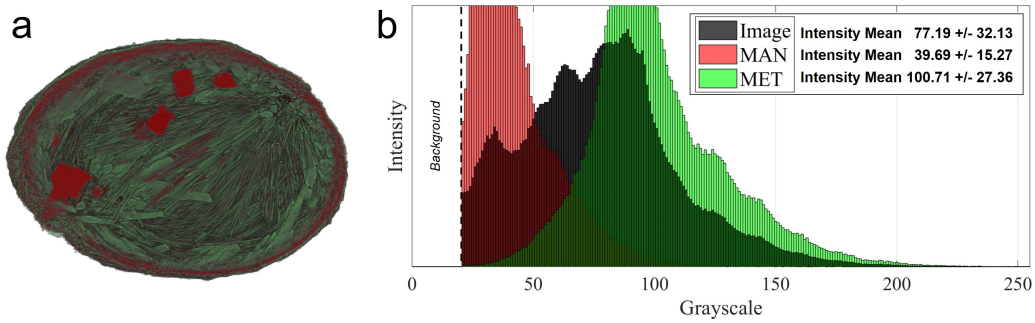

Figure 4.15: Pixel intensity-assignment for a qualitative assessment of the chemical distribution across the particle volume. (a) Visualisation of the internal particle composition with customised color-coded dynamic range for MET (green) and MAN (red). (b) An analysis of the dynamic range of the micro-XRT images to evaluate the contributions of MET and MAN, respectively.

4.4 Conclusions

Micro-XRT has demonstrated great applicability for the characterisation of pharmaceutical solid products and drug product intermediates along the downstream manufacturing pipeline from single crystals/particles to final formulated systems (tablets, capsules). Micro-XRT permits an in-depth investigation of structural product attributes as well as solid phase homogeneity. Image processing and analysis enabled the extraction of quantitative information from collected micro-XRT image data. The implemented image analysis framework aims to integrate available methodologies of image processing and advanced data analysis to become part of a systematic and robust micro-XRT characterisation workflow for pharmaceutical products. This project aimed to address image processing challenges of noise reduction, image binarisation and further (automated) image segmentation. Partially, image processing parameters have to be optimised and user-validated to achieve a reliable quantification. Automated, self-optimisation strategies have great potential to further improve the analysis framework, improving accessibility for non-experts and reducing potential user-specific bias towards the quantification.

Complementary characterisation techniques are essential for additional data validation during method development and provide additional possibilities for micro-XRT data mining approaches via data fusion. In case of ToF-SIMS for CI, high-resolution chemical information supported the identification of local solid phase composition, which was extrapolated to the full 3D micro-XRT image stack for a visualisation of the local solid phase composition. This approach could be extended to other imaging techniques including Raman spectroscopy, X-ray

photoelectron spectroscopy or light microscopy.

Extracted information from micro-XRT can be used to inform manufacturing processes during development or optimisation. Future work will be focused on the further development of the micro-XRT image analysis framework and the demonstration of its applicability to a broader range of pharmaceutical products. This aims to support the adoption of micro-XRT as a routine offline characterisation technique in the area of pharmaceutical sciences. The work described in this contribution hopes to provide a basis for these future applications and introduce concepts which allow a transition towards a quantitative analysis of the micro-XRT image data.

Contributions

FJSD and AJF conceived the study. FJSD developed the micro-XRT analysis workflow and implemented the image analysis framework. FJSD performed single droplet drying experiments and powder blending. EPr, MTI and JR supplied 3D printed tablet samples. EPa performed ToF-SIMS analysis. FJSD wrote the original draft of the manuscript, which was reviewed by FJSD and AJF with input from all other co-authors.

Acknowledgement

The authors would like to acknowledge additional samples provided by Elanor Brammer (3D printed tablet), Carlota Mendez (granules) and Francesca Perciballi (spherical agglomerates) displayed in Fig. 4.10. The authors would like to thank EPSRC and the Doctoral Training Centre in Continuous Manufacturing and Crystallisation (Grant Ref: EP/K503289/1) and the EPSRC Future Continuous Manufacturing and Advanced Crystallisation Research Hub (Grant Ref EP/P006965/1). The authors would like to acknowledge that this work was carried out in the CMAC National Facility supported by UKRPIF (UK Research Partnership Fund) award from the Higher Education Funding Council for England (HEFCE) (Grant Ref: HH13054).

5 A micro-XRT Image Analysis and Machine Learning Methodology for the Characterisation of Multi-Particulate Capsule Formulations

Declaration: *This chapter was accepted as an original research article in the journal International Journal of Pharmaceutics and is the result of a collaboration between Frederik J.S. Doerr[a,b] and Alastair J. Florence[a,b]. Parts of this work were presented at the Bruker microCT User meeting (2018) and PARTEC (2019).*

Abstract: The application of X-ray microtomography for quantitative structural analysis of pharmaceutical multi-particulate systems was demonstrated for commercial capsules, each containing approximately 300 formulated ibuprofen pellets. The implementation of a marker-supported watershed transformation enabled the reliable segmentation of the pellet population for the 3D analysis of individual pellets. Isolated translation- and rotation-invariant object cross-sections expanded the applicability to additional 2D image analysis techniques. The full structural characterisation gave access to over 200 features quantifying aspects of the pellets' size, shape, porosity, surface and orientation. The extracted features were assessed using a ReliefF feature selection method and a supervised Support Vector Machine learning algorithm to build a model for the detection of *broken* pellets within each capsule. Data of three features from distinct structure-related categories were used to build classification models with an accuracy of more than 99.55% and a minimum precision of 86.20% validated with a test dataset of 886 pellets. This approach to extract quantitative information on particle quality attributes combined with advanced data analysis strategies has clear potential to directly inform manufacturing processes, accelerating development and optimisation.

[a] *EPSRC CMAC Future Manufacturing Research Hub, Technology and Innovation Centre, Glasgow, UK*

[b] *Strathclyde Institute of Pharmacy & Biomedical Sciences (SIPBS), University of Strathclyde, Glasgow, UK*

Keywords: Pharmaceutical Formulation, Micro-XRT Particle Analysis, Watershed Image Segmentation, Sensitivity Analysis, Feature Selection, Machine Learning, Classification Model

Highlights

- Full three-dimensional image segmentation of a pharmaceutical capsule using a marker-supported watershed transformation.
- Information on particle 3D-orientation were utilised to extract translation- and rotation-invariant object cross-sections.
- Successful extraction of over 200 quantitative pellet descriptors linked to size, shape, porosity, surface and orientation.
- Sensitivity analysis and ReliefF feature selection approach to identify predictive features for pellet classification.
- Feature-based binary SVM classification model for the detection of broken pellets within the formulated system.
- Coupling micro-XRT analysis with feature selection and machine learning for advanced pharmaceutical product characterisation.

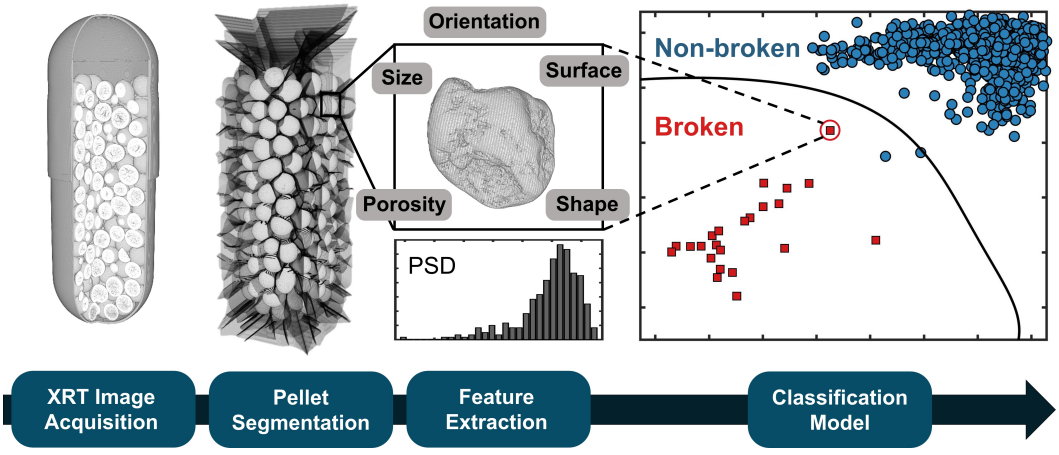

Figure 5.1: Graphical abstract Chapter 5.

5.1 Introduction

The measurement of morphological descriptors and structural properties is widely applied in the pharmaceutical industry to evaluate quality attributes of solid products that affect their performance in the manufacturing process or upon final administration to the patient. Methods to aid understanding the effect of process and material parameters on the final product characteristics enable a Quality by Design (QbD) approach to achieve consistent, safe and effective quality products [257]. The diversity of structure-related critical quality attributes has led to a broad range of analytical techniques being used to investigate size, shape and porosity of pharmaceutical products and drug product intermediates [258, 66]. Employed analysis techniques are often limited to bulk information or to the characterisation of individual particles when working with multi-particulate systems. Commonly, multiple complementary techniques are required to achieve a full characterisation of all the relevant structural properties [259, 136]. Often the techniques are destructive or require larger quantities of sample material for a successful characterisation.

X-ray microtomography (micro-XRT) can be applied to investigate non-destructively a wide range of particle properties for (multi-) particle systems. The reconstructed cross-sections of the micro-XRT image data allow three dimensional visual inspections of the scanned object. The smallest structural attribute that can be resolved typically requires multiple pixels/voxels (volume pixel) due to the partial volume effect, which describes the blurring of intensity edges in digital micro-XRT images [260]. Nowadays, commercial micro-XRT systems commonly achieve spatial resolutions of around 1 μm - 10 μm, which corresponds to the projected sample size on a minimum of 3-5 pixels [153, 261]. Image processing capabilities can be further used to extract quantitative information simultaneously on bulk and single particle properties. Specific applications of micro-XRT with subsequent image processing have been reported for (multi-) particle systems targeting structural features related to particle size [7, 156], surface [7, 156], morphology [7, 156, 182, 183, 184, 185], porosity [186, 7, 156, 139] and attributes of the local micro-structure [157, 158]. The image processing strategies are often tailored to meet specific analysis requirements to further relate individual sample properties to the manufacturing process or product performance [157, 185]. The quality of the collected micro-XRT image data and the applied image processing algorithms can both have an impact on extracted quantitative

information [262]. A sensitivity analysis allows the user to evaluate the risk for data variability with changing parameters during collection and image processing, which has been described in details elsewhere [263].

Extracted quantitative information from collected micro-XRT image data can be exploited to inform machine learning (ML) models which are designed to provide answers to complex questions involving automated decision making processes without the need to provide explicit instructions. ML approaches can be used effectively to identify patterns and inference within large feature-based datasets [264]. Support Vector Machines (SVMs) are a class of supervised ML algorithms originally designed to solve binary classification problems to define decision boundaries in multidimensional feature datasets [265, 264]. SVM models have since been utilised for a wide range of applications including solubility prediction [266] or crystal shape classification [51], analysis of biomedical data [267, 268] and network anomaly detection in computer science [269]. SVMs are particularly effective for outlier detection in highly imbalanced datasets avoiding over-fitting (One-Class SVM, [269]) and can address not fully separable classification problems using non-linear decision boundaries with soft margins for higher regularization. Details on alternative statistical learning methods for ML applications is provided by Hastie et al. [264].

For the first time, this study employs a micro-XRT system to access over 200 structural features for a pharmaceutical multi-particulate product and presents strategies for the extraction and evaluation of 3D quantitative morphological descriptors by means of image processing and analysis. The introduction of translation- and rotation-invariant object cross-sections additionally enables the reliable application of 2D image analysis methodologies. The extracted features are used to solve a classification problem for the detection of *broken* pellets within the pellet population of each sample. The selection of reliable structural features for this classification problem included a micro-XRT sensitivity analysis to assess the impact of image quality and image processing parameters as well as a feature selection approach using the popular ReliefF method described in detail elsewhere [270, 271, 272, 273]. The ReliefF feature selection approach evaluates the correlation between nearest neighbour instances and their class membership labels as defined in the training dataset. This allows the assessment of feature-feature correlation which is common for micro-XRT features from similar property-related categories. computationally efficient The micro-XRT investigation of particle systems is demonstrated on

commercially available capsules containing formulated ibuprofen pellets for oral administration.

5.2 Materials and methods

5.2.1 Commercial ibuprofen capsule

Capsules with ibuprofen pellets for sustained drug-release (Galpharm Healthcare Ltd, Lot# 020288) were used as a model pharmaceutical multi-particulate system. The pellets of each capsule consist of 200 mg ibuprofen formulated with micro-crystalline cellulose, Eudragit NE30D, hypromellose, talc and colloidal silicon dioxide. The capsule shell is made from gelatin, titanium dioxide (E171), patent blue V (E131) and erythrosine (E127). In total, six capsules were investigated during this study. Three capsules were used for model training (references DTR: C0, C1 and C2) with three additional capsules used to generate the test dataset (references DTT: C3, C4 and C5). The membership labels, *broken* vs *non-broken*, were assigned manually by the user during a visual inspection of the segmented micro-XRT image dataset of the capsule pellets described in Section 5.2.3.

5.2.2 X-ray tomography

A Skyscanner 2211 X-ray tomograph (NanoCT, Bruker, Kontich, Belgium) with cone-beam arrangement was employed for micro-XRT data collection. The samples were scanned with an image pixel size of 2.5 μm - 6 μm, frame averaging of 3 and a rotation step size of 0.2 ° (details listed in Table A2, ESI, page A3). The acquisition settings were varied in order to assess the impact of data acquisition parameters on the pellet classification model described in Section 5.2.4. The capsules C0 and C3 were scanned with high image quality. For all other capsules the data collection was optimised to reduce overall data acquisition times whilst accepting a decreased sample resolution (C1, C2, C4, C5). The X-ray acceleration voltage was 40 keV. A reference scan was collected at the end of each run to enable post-alignment correction and therefore compensate for potential shifts during the scan. Image reconstruction included beam hardening corrections and ring artefact reduction which were performed using NRecon with InstaRecon (version 1.7.1.6, Bruker, Kontich, Belgium). Visualisations of the image stacks were rendered using CTVox (version 3.2.0, Bruker, Kontich, Belgium).

5.2.3 3D Image Processing and Single Particle Analysis

Micro-XRT image processing and analysis strategies were implemented in MATLAB R2018a (version 9.4.0.813654, MathWorks, United States). Structural features were extracted globally for the full sample from each capsule and for each individual pellet within the capsules.

Global features were defined as the capsules dimensions (i.e. max. length, mean diameter) and internal porosity distribution. The measured porosities were further separated in order to distinguish inter- and intra-pellet porosity. This required a custom-made script to establish a region-of-interest (ROI) for the pellet distribution (V_CP_ROI) using a 3D-morphological closing operation and a secondary enclosed background filter integrated in a feedback-loop for detected internal background volumes previously described to define single particle ROIs [7]. Voxel-based arithmetic operations were used to calculate the internal capsule volume (V_CS_InV), the total intra-pellet porosity (V_CP_Poros) and inter-pellet void space (V_CS_Poros) of the capsule sample. Details on the calculations are included in Section A2.2 (ESI, page A3).

A marker-controlled watershed transformation algorithm [274] was applied to separate all connected "touching" primary objects within V_CP_ROI and to allow a subsequent structural analysis of each individual pellet. The image processing workflow for a successful volume segmentation using a marker-controlled watershed transformation of two connected objects is shown in Fig. 5.2. Reconstructed image cross-sections (Fig. 5.2a) are initially pre-processed using an edge-preserving local contrast image filter to reduce random image noise on grayscale. Image binarization (Fig. 5.2b) is performed with a histogram-based thresholding algorithm to convert the images to a monochromatic logic-mask [221]. Remaining noise in the created binary image stack is removed with a series of noise reduction algorithms including a 3D sweep operation for non-connected binary object volumes. The image ROI (V_CP_ROI, Fig. 5.2c) is transformed into an Euclidean distance map with primary object markers superimposed in the local 3D minima (Fig. 5.2d). The distance-based grayscale image stack allows the successful application of the marker-supported watershed transformation to achieve a separation of the primary objects (Fig. 5.2e).

The segmented pellets from each capsule were further processed and analysed individually to extract a total of 206 features related to size, shape, porosity, surface and orientation. A detailed overview of the extracted features is provided in Chapter 4, Section 4.3.5. Basic features are

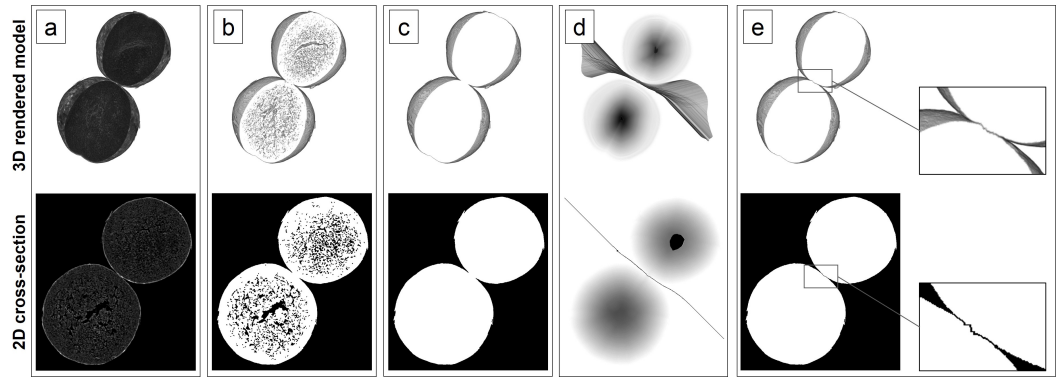

Figure 5.2: Image processing sequence to separate connected particle volumes. (a) Raw image data, (b) image binarization, (c) particle ROI, (d) marker-controlled watershed segmentation using a distance transformation with superimposed region markers and (e) separated particles.

derived from the evaluation of image moments [275]. The zeroth order image moment for a binary digital image gives the total object voxel volume (3D). The first order moments contain information on the object centroid. The central moments include the components of the image centroid to provide translation invariance. The second order central moments allow the extraction of information about the object orientation within the 3D image space. Information on the object orientation and location were further used to isolate translation- and rotation-invariant 2D cross-sections (IEV) normal to the eigenvectors of an ellipsoid with matching second order central moment. For this 3D-to-2D transformation, the eigenvectors were utilised to consistently re-slice the 3D image stack as visualised in Fig. 5.3 independent of the pellet position and its 3D orientation. These 2D cross-sections (IEV1 - IEV3) enabled additional applications for feature extraction with established 2D image algorithms. 162 features of the total 206 pellet features are extracted from the analysis of the images IEV1 - IEV3.

5.2.4 Feature-based Particle Classification: ReliefF and SVM

A feature-based particle classification model was implemented to detect *broken* objects within the population of pellets. The ReliefF algorithm is a filter-method approach which can be used in conjunction with a labelled training dataset for the selection of features in categorical multi-dimensional classification problems [270, 271, 272, 273]. ReliefF ranks features according to their correlation with a labelled training dataset using a k nearest neighbors method. Extracted features were evaluated to identify those with the highest predictive power for this binary object

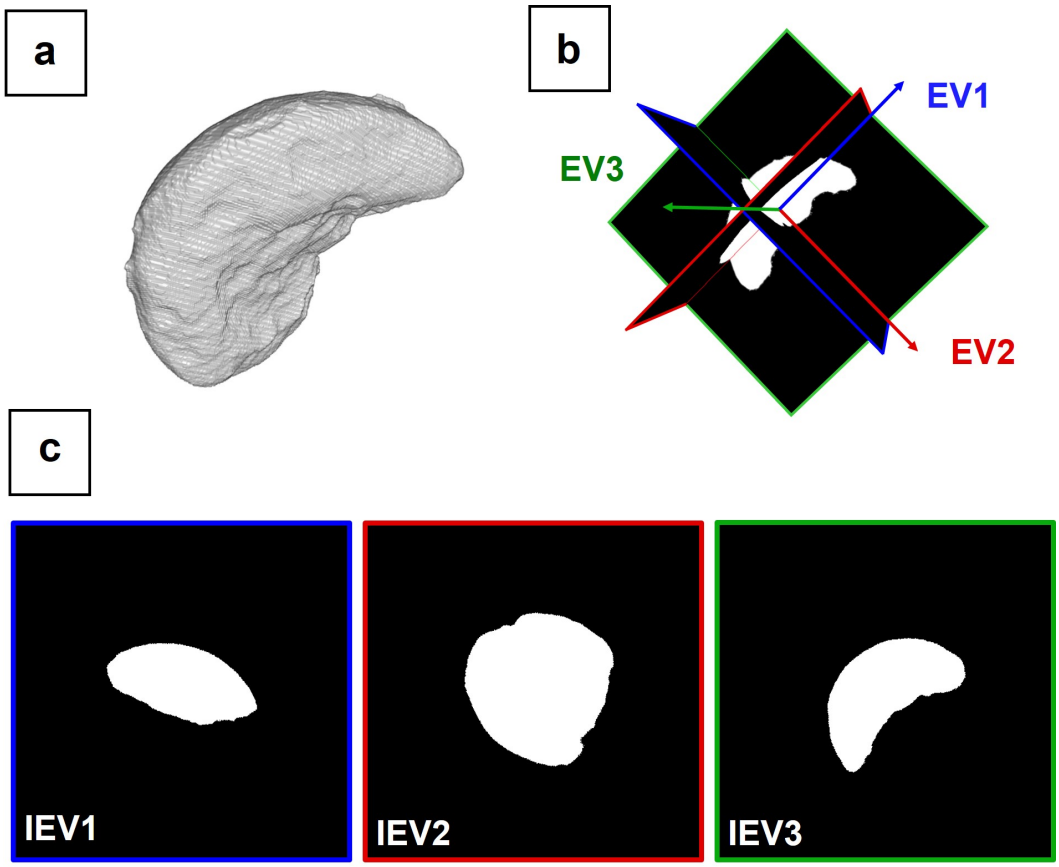

Figure 5.3: 3D-to-2D image transformation: (a) The image eigenvectors are calculated from the 3D particle model (V_ROI) based on its second central image moment. (b) The 3D stack is re-sliced along the planes normal to the eigenvectors. (c) Three characteristic translation- and rotation-invariant 2D cross-sections (IEV1 - IEV3) are isolated.

classification problem: *broken* versus *non-broken* pellets. The ReliefF feature selection method was available in MATLAB and was performed using the training dataset (DTR). The number of nearest neighbors was selected to include the maximum number of labelled training objects providing class balance (k = min([# *non-broken*, # *broken*]) = 23). Including all observations of the minority class ensures maximum robustness against noise, but limits the detection of feature dependencies in the context of nearest neighbor locality to the majority class [271]. Additional details are provided in Section A2.5.1 (Appendix, page A16).

SVMs were employed to build a feature-based object classification model in order to identify *broken* pellets within the population [264]. The n-dimensional training dataset (DTR, each observation $x_i \in R^n$) was used to build One-Class and Two-Class SVM models in MATLAB. The feature data were standardized to avoid scale effects on the classification outcome. The

employed SVM kernel function was a radial basis function (RBF) to better adapt the optimal separating hyperplane (OSH) to non-linear data distributions. The One-Class SVM (OC-SVM) model was generated only considering observations of the *non-broken* pellets in the training dataset to create a close decision boundary around the majority class. The Two-Class SVM (TC-SVM) model was built using soft margins and prior probabilities proportional to the class membership distribution in DTR (*broken*:*non-broken*,1:38). The kernel scale and the box constraints for the TC-SVM model were selected automatically employing a Bayesian strategy for global optimisation using 4-fold cross-validation [264]. Additional details are provided in Section A2.5.3 (Appendix, page A17).

5.3 Results and Discussion

The micro-XRT characterisation of each sample consists of basic steps of micro-XRT data acquisition, micro-XRT image reconstruction and an initial optimisation of image processing parameters for noise reduction (Fig. 5.4, *Stage 1 - 4*). This chapter focuses on the subsequent analysis of the micro-XRT image data. Specific to this sample, the ibuprofen capsules were initially investigated to describe the multi-particulate system with specific measurements of size and overall porosity distribution (see Section 5.3.1). The segmentation of the pellet population permits an in-depth assessment of the structural attributes for each isolated pellet related to properties describing object size, shape, porosity, surface and orientation (Fig. 5.4, *Stage 5 - 6*, see Section 5.3.2 - Section 5.3.3). All extracted features were assessed as part of a sensitivity analysis to evaluate the feature robustness against changes in micro-XRT image quality and image processing parameters (Fig. 5.4, *Stage 6*, see Section 5.3.3). Three features were further identified with a ReliefF feature selection approach and used within a SVM classification model to detect *broken* pellets (Fig. 5.4, *Stage 7 - 8*, see Section 5.3.4). The features were selected to target distinct attributes of the pellet related to its size, shape and surface.

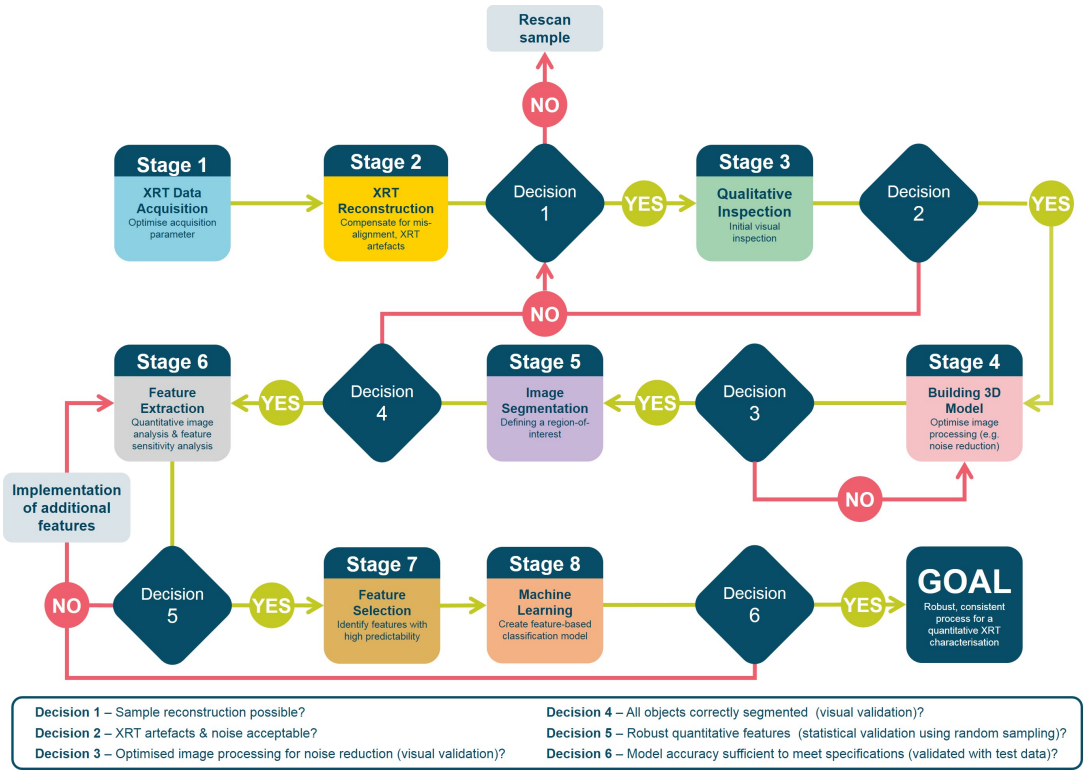

Figure 5.4: Full workflow combining micro-XRT analysis and machine learning methodologies for the characterisation of multi-particulate capsule formulations.

5.3.1 Capsule - Full Sample Analysis

The dataset C0 was initially investigated using two manually defined regions-of-interest of the capsule shell (V_CS_ROI) and the pellet population (V_CP_ROI). This initial analysis exemplifies potential applications of micro-XRT extracting information on a global sample level to obtain an overview of key characteristics for this multi-particulate system. The results are listed in Table 5.1. They include a quantification of the sample's volume distribution as well as measurements of selected sample attributes which are linked to the capsule production process. Whilst beyond the scope of this study, this information could ultimately be used for process optimisation and/or to support a predictive framework, for instance to assess the product's final performance [276].

The total internal capsule volume (V_CS_InV) is sub-divided into the pellet volume occupied by its solid phase (V_CP), large inter-pellet void space (V_CS_Poros) and intra-pellet porosity (V_CP_Poros). The pellets account for 48.39% of the internal capsule volume, less than half of V_CS_InV, corresponding to a fill height of 16.09 mm. The capsule dimensions are expressed

Table 5.1: Quantification of capsule volume distribution and individual measurements including capsule ROI surface area (A_{S,V_CS_ROI}), pellets ROI surface area (A_{S,V_CP_ROI}), outer diameter of the capsule body (d_c) and capsule wall thickness (s_c).

Absolute Volume Distribution		**Individual Measurements**	
Capsule Volume (V_CS_ROI)	603 mm^3	Max. Length (Feret)	19.45 mm
Capsule Shell Volume (V_CS)	56 mm^3	Filled Height	16.09 mm
Capsule Internal Volume (V_CS_InV)	548 mm^3	Filled Volume	48.39%
Capsule Void Space (V_CS_Poros)	279 mm^3	A_{S,V_CS_ROI}	562.6 mm^2
Pellet Volume (V_CP_ROI)	269 mm^3	A_{S,V_CP_ROI}	1253.9 mm^2
Pellet Solid Phase Volume (V_CP)	201 mm^3	d_c	6.55 ± 0.01 mm
Pellet Porosity Volume (V_CP_Poros)	68 mm^3	s_c	112 ± 3 μm

using its maximum length (Feret) and the outer diameter of the capsule body (d_c) which are 19.45 mm and 6.54 mm, respectively. Additionally, the capsule wall thickness (s_c) and its surface area (A_{S,V_CS_ROI}) were quantified with the associated variation in thickness across the sampled regions which are 112 ± 3 μm and 562.6 mm^2, respectively.

Fig. 5.5 shows the distribution of the pellet solid phase volume (V_CP), the pellet porosity volume (V_CP_Poros) and inter-pellet capsule void volume (V_CS_Poros) as a function of the capsule length. This data representation allows a quick assessment of the overall solid phase homogeneity within the capsule. In the distribution of V_CP and V_CS_Poros, the capsule head-space can be easily identified at a capsule height of 16.09 mm defined by a sharp decrease of V_CP and V_CP_Poros. The measured length of the capsule body is 16.78 mm and therefore, the pellets reach 95.89% of its maximum filling height.

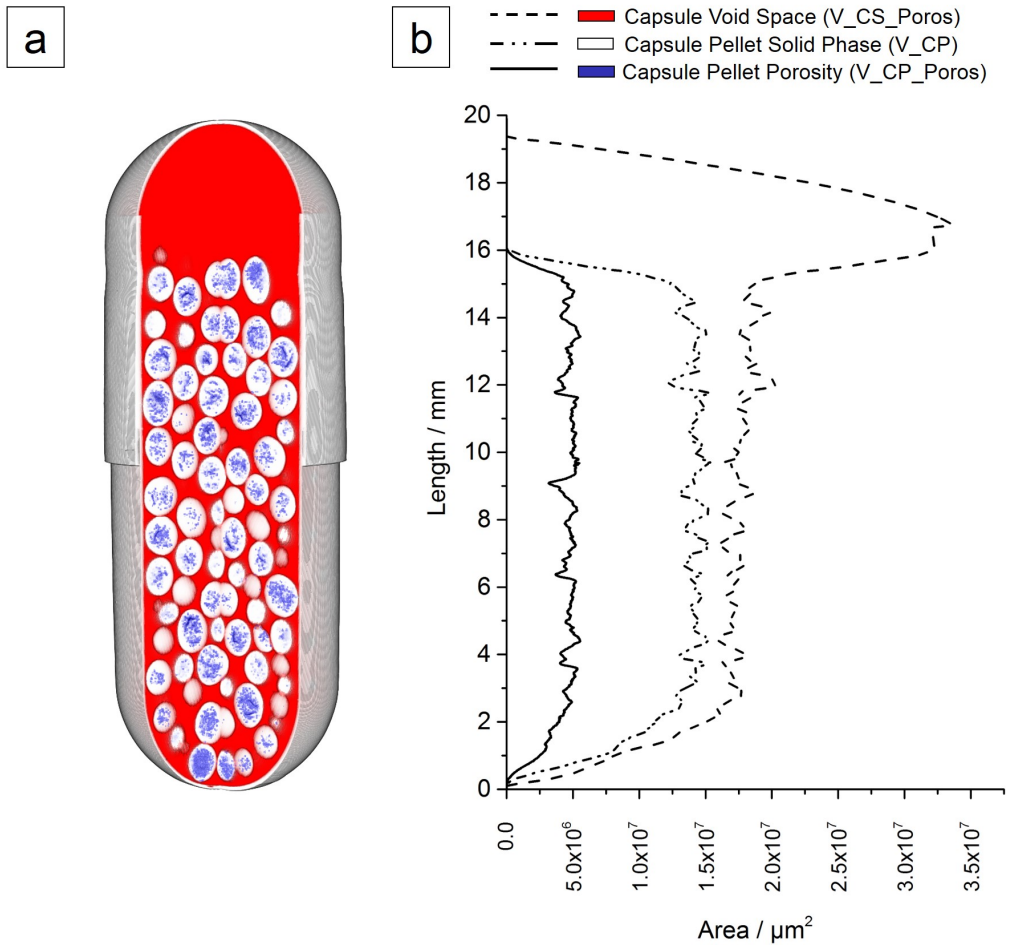

Figure 5.5: *Global* sample analysis (a) detecting internal capsule void space (V_CS_Poros, red, – – –), pellet solid phase volume (V_CP, white, – · · –) and intra-pellet porosity (V_CP_Poros, blue, ——). (b) The volume distribution along the capsule height is quantified through the detected local cross-section area in the micro-XRT image stack.

5.3.2 Capsule - Pellet Segmentation

The extraction of structural features from individual pellets of the capsules' population requires the successful separation and isolation of all connected "touching" objects in the total pellet volume (V_CP_ROI, Fig. 5.6a). A marker-controlled watershed transformation was applied to enable a robust volume segmentation of V_CP_ROI. The calculated watershed lines indicate the optimised separation planes determined within the 3D image and are shown in Fig. 5.6b. Region markers greatly improve overall robustness against risks of over-segmentation, a common problem associated with applications of the watershed algorithm [223]. The watershed algorithm is most robust for structures with large, uniform object bodies and light touching zones

since the optimisation of the separation planes is based on the 3D distance map of the object ROI. The spherical pellets maximise these attributes, hence, its application is particularly effective for this sample. The separation of the pellet population in C0 resulted in 300 individual pellets. Across all capsules (DTR and DTT) the population consisted of 294 ± 9 pellets. The watershed-transformation was validated through a visual inspection of the segmented image data and the isolated single pellets.

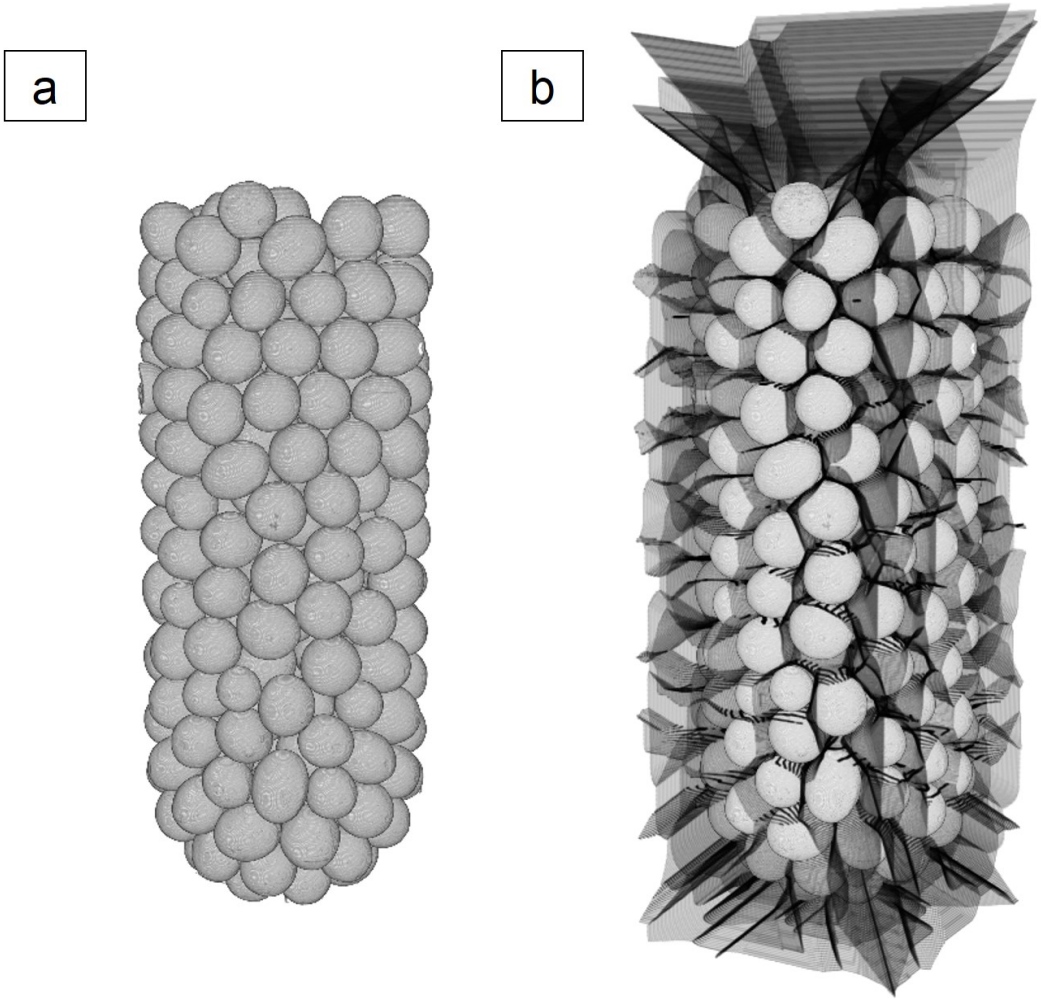

Figure 5.6: The segmentation of all "touching" pellets was achieved after applying a marker-supported watershed transformation to (a) the pellet ROI (V_CP_ROI). (b) The volume separating watershed lines are superimposed on the original image data to identify individual pellet volumes.

5.3.3 Capsule - Pellet Characterisation

Following the successful pellet segmentation (Section 5.3.2), the individual pellets were subject to individual analysis aimed at extracting quantitative information using 206 structural features. The features (n = 206) were categorised in terms of their relation to key particle attributes of size (n = 61), shape (n = 104), surface (n = 12), porosity (n = 14) and orientation (n = 15). An overview of all the features is provided in Chapter 4, Section 4.3.5. Each feature is calculated either directly from the 3D image stack of each pellet or from three characteristic translation- and rotation-invariant IEV cross-sections as described in Section 5.2.3.

Fig. 5.7 shows four selected features commonly used to describe the quality attributes of pellets from extrusion–spheronization processes that can be related to process parameters and input material attributes [277, 278]: equivalent sphere diameter ($d_{\mathrm{eqSph,V\_ROI}} \in [90\mu m, 1408\mu m]$, Fig. 5.7a), absolute surface area ($\mathrm{A_{Sf,V\_ROI}} \in [0.02 \cdot 10^6 \mu m^2, 4.35 \cdot 10^6 \mu m^2]$, Fig. 5.7b), solidity as a measure of internal porosity ($\mathrm{SV} = V_{\mathrm{V}}/V_{\mathrm{V\_ROI}} \in [0.55, 0.99]$, Fig. 5.7c,) and particle sphericity ($\Psi_{\mathrm{gl,V\_ROI}} \in [0.74, 0.99]$, Fig. 5.7d). The distribution of each of the four features is visualised to provide an indication of the range of values across all pellets in the capsule. Comparing the results of the analysis, the distributions are highly consistent for $d_{\mathrm{eqSph,V\_ROI}}$, $\mathrm{A_{Sf,V\_ROI}}$, and $\Psi_{\mathrm{gl,V\_ROI}}$ across all capsules. However, the distributions of SV in Fig. 5.7c show statistically significant differences (Two-sample t-test rejects H_0 of equal means at 5% significance level). This is however a consequence of the sensitivity of the measurement to the specific micro-XRT acquisition and image analysis parameters used. The changes in SV correlate with changing data acquisition parameters between capsules with high micro-XRT image quality (slow acquisition, C0 and C3) and low micro-XRT image quality (fast acquisition, C1, C2, C4 and C5). Accelerated micro-XRT image acquisition leads to an average increase of the measured solidity (SV) from 68.71 ± 4.72% to 95.88 ± 1.48%.

The quantification of features from image data is often subject to variability in the image data quality and the selection/optimisation of image processing parameters [263, 262]. Therefore, a sensitivity analysis was performed to assess the robustness of extracted features within the micro-XRT analysis workflow using a customised sampling method targeting implemented algorithms for noise reduction and binarization as described in Table A3 (ESI, page A4). Changes in micro-XRT image quality were simulated using a Gaussian filter to systematically introduce

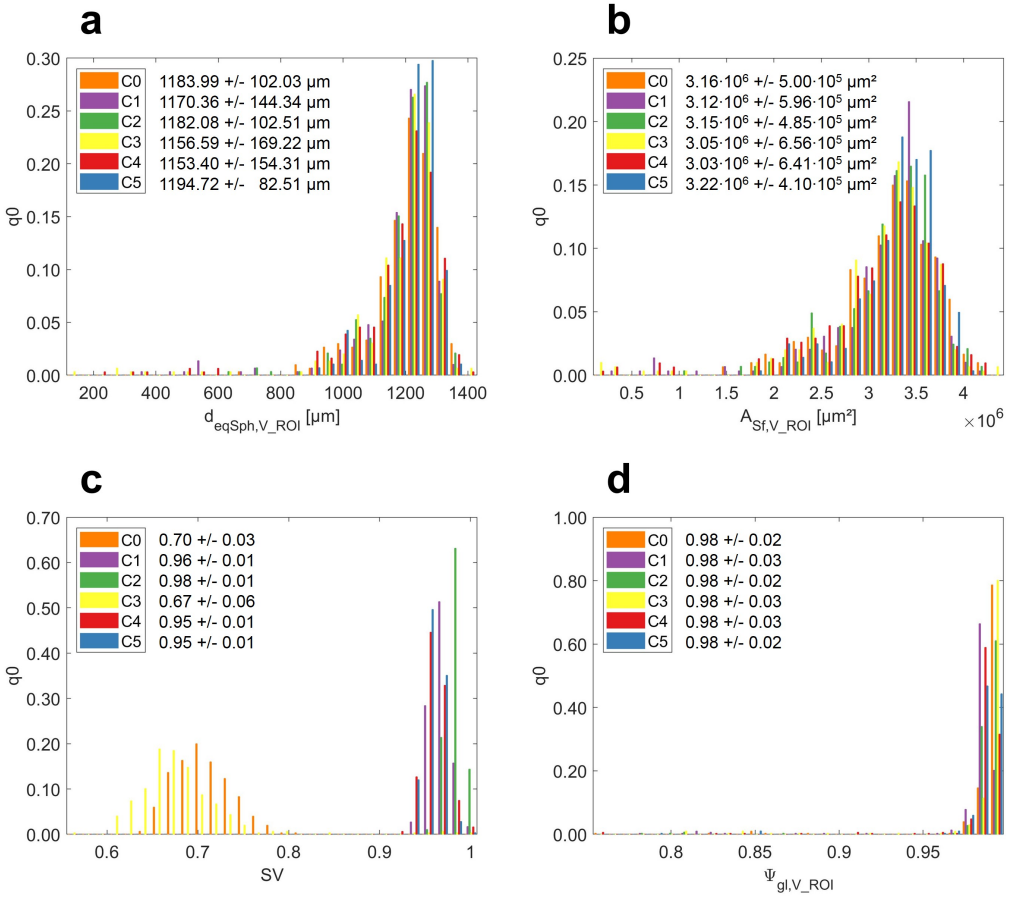

Figure 5.7: Normalised number density distributions (q0) of four selected features describing the pellet populations regarding (a) pellet size (d_{eqSph,V_ROI}), (b) pellet surface area (A_{Sf,V_ROI}), (c) pellet porosity (SV) and (d) pellet shape (Ψ_{gl,V_ROI}).

image blurring. Sensitivity analysis was carried out with a dataset of five randomly selected pellets of each class (*non-broken* and *broken*) from C0. Features related to the particle porosity (V_P_Poros), the absolute particle volume (V_P) and its orientation exhibit the highest variability for different micro-XRT image data qualities and image processing parameters. This variability is linked predominantly to difficulties in the detection of micro-porosities with a local thickness below 25 μm (details are provided in Table A4, ESI, page A5). These micro-porosities contribute to 98.82 $\pm$ 1.56% of the total pellet porosity. Their critical length scale of 25 μm corresponds to a minimum of 4 - 5 pixels in the low resolution (C1, C2, C4 and C5) and 10 pixel in the high resolution (C0 and C3) micro-XRT images, respectively. Failing to detect internal micro-porosities decreases the measured V_P_Poros and simultaneously gives an apparent rise in V_P. Small variations in V_P can further have a significant impact on the determined orientation, especially for highly isotropic objects. In total, 132 features exhibit

values above a 10% variability threshold comparing the feature residuals at individual sampling points relative to the user defined ground truth (visual validation). The remaining 74 features are assumed to be robust within the employed image analysis framework. Details of the sensitivity analysis are presented qualitatively and quantitatively in Section A2.3 (ESI, page A4, Fig. A2 and Fig. A3). Depending on the objective for the micro-XRT analysis, features with a high-sensitivity to micro-XRT image quality and parameters of the image processing/analysis workflow require careful validation with complementary sample characterisation techniques. The variability of individual features depends significantly on the nature of the sample, which may have to be monitored and re-evaluated for changing specimens. Here, features with a variability of more than 10% were excluded from the feature-based object classification models. Details on features removed on this basis are listed in Table A5 (ESI, page A12).

5.3.4 Capsule - Pellets Classification

Extracted features were utilised as part of a classification model for the automatic detection and quantification of *broken* pellets within the population. The successful implementation included a feature selection approach (Section 5.3.4.1). Selected features were used to build and validate SVM classification models (Section 5.3.4.2). The training dataset (DTR) combined pellet information from three capsules, C0 (high resolution mode), C1 and C2 (fast acquisition mode). The remaining data (C3 , C4 and C5) were included in a test dataset (DTT) to validate and evaluate the model performance.

5.3.4.1 Feature Selection

74 structural pellet features were assessed using a feature selection approach to identify a subset best suited for a feature-based pellet classification model for the reliable detection of *broken* pellets within the population. The feature selection approach aims to reduce the dimensionality of the captured feature space removing redundant or noisy features. Features with a limited positive impact on the classification performance can be excluded from future micro-XRT image analysis, accelerating routine characterisation as well as improving model accuracy and robustness against overfitting. The identification and selection of predictive features is particularly important for datasets with imbalanced class membership distributions to include features that provide inter-class discrepancy and to exclude features with high intra-class noise [279].

A ReliefF feature selection approach was utilised to evaluate and rank the correlation of all features with the class membership of DTR. A high correlation of individual features with the assigned *broken/unbroken* class membership suggests a high predictive power for the subsequent feature-based classification model. The top 5 features of the ReliefF ranking relate to shape properties. As expected for this sample with highly spherical pellets, the highest ranking feature describes the overall pellet sphericity comparing the pellet volume to a sphere with equal maximum Feret diameter ($SF_{maxFeretSph,F,V\_ROI}$, rank 1, Fig. 5.8a). Additional high-ranked features from other structure-related categories are quantitative information on the pellets' size ($SF_{Elps,SA,r3,V\_ROI}$, rank 6, Fig. 5.8b) and surface attributes ($SV_{CH,V\_ROI,IEV1}$, rank 7, Fig. 5.8c). Interestingly, $SV_{CH,V\_ROI,IEV1}$ is closely related to $SV_{CH,V,IEV1}$ which captures particle porosity information using a 2D Convex-Hull. Applied to V_ROI, the same algorithm quantifies concave areas on the object surface [7]. Therefore, $SV_{CH,V\_ROI,IEV1}$ can be regarded as a measure of surface roughness. $SF_{Elps,SA,r3,V\_ROI}$ is linked to the pellet size and is an absolute measure of the shortest characteristic length of a surface-fitted ellipsoid to V_ROI. In contrast, the other remaining characteristic lengths of this ellipsoid, $SF_{Elps,SA,r1,V\_ROI}$ and $SF_{Elps,SA,r2,V\_ROI}$, are at position 39 and 36 of the ReliefF ranking, respectively. The high performance of $SF_{Elps,SA,r3,V\_ROI}$ not only relates to the expected smaller absolute sizes of the *broken* pellets, but also to its ability to capture specific shape-related aspects with an increasing deviation between $SF_{Elps,SA,r1,V\_ROI}$ and $SF_{Elps,SA,r3,V\_ROI}$ for non-spherical objects. The combination of both, aspects of size and shape, is beneficial to distinguish between *broken* and *non-broken* pellets. The results of the ReliefF ranking align well with calculated p-Values for DTR, where 72 of the 74 features show a statistically significant deviation between the feature distribution of *non-broken* and *broken* pellets (Two-sample t-test rejects H_0 of equal means at 5% significance level). F-scores are an alternative approach to select features for SVM classifiers [280] and were compared to validate the feature selection approach. They show a similar feature ranking, however, fail to address important feature-feature dependencies. The full ReliefF ranking of the 74 investigated pellet features and their calculated ReliefF weights, p-Values and F-scores are listed in Table A6 (ESI, page A15).

Three features, $SF_{maxFeretSph,F,V\_ROI}$, $SF_{Elps,SA,r3,V\_ROI}$ and $SV_{CH,V\_ROI,IEV1}$, from distinct structure-related categories describing shape, size and surface properties were included in the selected feature subset for a pellet classification model. Each feature is presented in Fig. 5.8 a-c

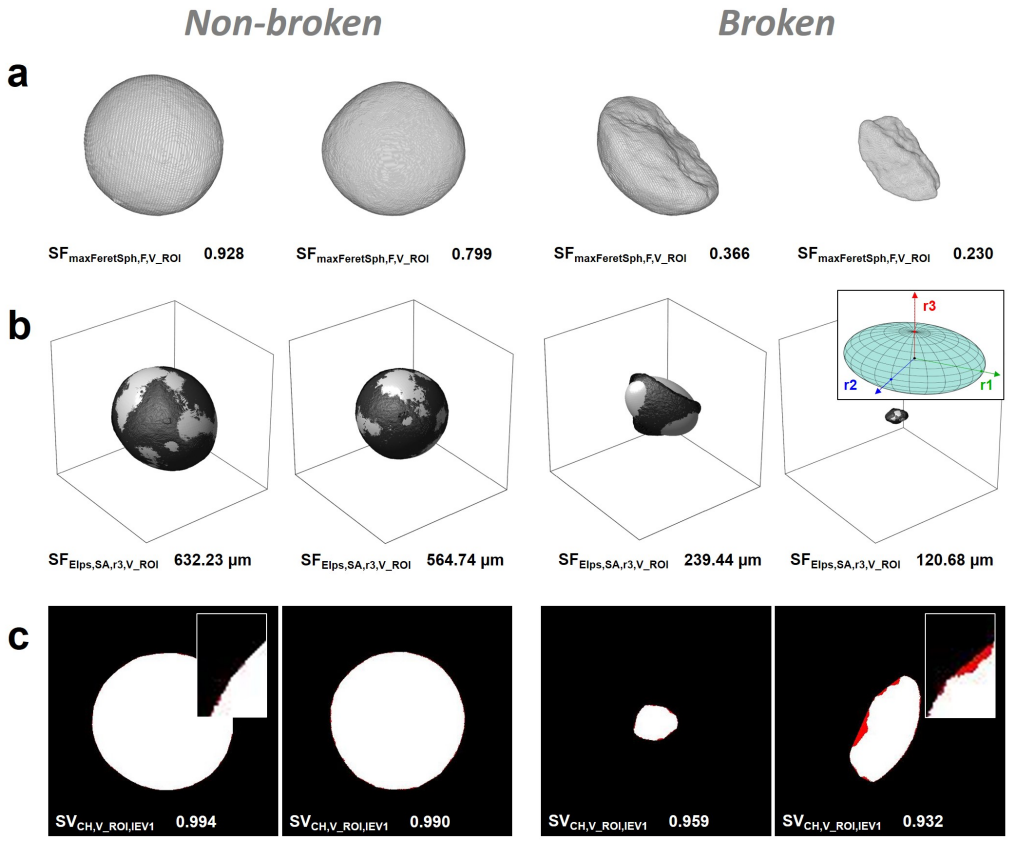

Figure 5.8: Selected features for a classification of (left) *non-broken* and (right) *broken* pellets: (a) sphericity ($SF_{maxFeretSph,F,V\_ROI}$), (b) shortest characteristic length of a fitted ellipsoid ($SF_{Elps,SA,r3,V\_ROI}$), and (c) surface roughness ($SV_{CH,V\_ROI,IEV1}$).

with representative examples of its extreme values (first and fourth pellet from the left) as well as an example at the population mean of each, *non-broken* and *broken* pellets (second and third pellet from the left). Scatter-plots of all feature combinations are provided in Fig. A4 (ESI, page A16). $SF_{maxFeretSph,F,V\_ROI}$ and $SF_{Elps,SA,r3,V\_ROI}$ have both a broad distribution in comparison to $SV_{CH,V\_ROI,IEV1}$. The narrow distribution of $SV_{CH,V\_ROI,IEV1}$ correlates to the high convexity of the spherical shape and aligns with visual inspections of individual pellets which exhibit highly smoothed surfaces, even for *broken* pellets. This could indicate that pellet breakage occurs predominantly during the spheronization process itself, where freshly created *broken* pellet pieces experience high attrition and smoothing of their edges. The selected feature subset from distinct structure-related categories aims to increase the robustness of the classification model against potential variability in individual structure-related categories with risks of high feature correlation.

5.3.4.2 Support Vector Machine for binary Classification of Formulated Pellets

The number of broken pellets is expected to be highly under-represented in the overall pellet population with an expected probability of less than 5%. In case of DTR the *broken* pellets account for 2.33% (C0, n = 7), 3.77% (C1, n = 11) and 1.75% (C2, n = 5) of the total pellet population, respectively. The combined training dataset (DTR) has a class imbalance of 1:38 for *broken*:*non-broken* pellets. A One-Class SVM (OC-SVM) model and a Two-Class SVM (TC-SVM) model are compared in the following to assess their performance addressing risks of a high class imbalance. The results are shown in Fig. 5.9a and b, respectively.

OC-SVMs generate models with highly sensitive decision surfaces, which are often used for outlier-detection, where only very limited or no training data for outliers, the minority class, are available [269]. The trained OC-SVM model is shown in Fig. 5.9a. The OC-SVM creates a tight decision boundary around the feature data of the *non-broken* pellet population of the pre-classified DTR data (n = 854, dark blue circles). Population outliers in this model are related to observations of *broken* pellets (n = 23, red squares). Using a RBF kernel, the decision boundary can be improved to capture non-linear feature distributions. Expanding the feature space to include information on the pellet surface roughness ($SV_{CH,V\_ROI,IEV1}$) leads to a re-classification of 5 *non-broken* pellets (Fig. 5.9a, × *Re-Labelled n-Dim*), slightly improving the OC-SVM model with a total classification accuracy of 99.55% (precision *broken* pellets: 86.20%) assessed using test data of a population of 886 pellets in DTT. The high sensitivity of the OC-SVM model decision surface leads to a misclassification of 4 *non-broken* pellets as *broken*, which corresponds to 0.46% of the 861 *non-broken* pellets in the DTT. In contrast, all *broken* pellets were correctly identified. Increasing the training dataset over time after reviewing and including observations of pellets in the OSH margin region can further improve the classification accuracy for *non-broken* pellets, but might shift the decision boundary towards the *broken* pellet population.

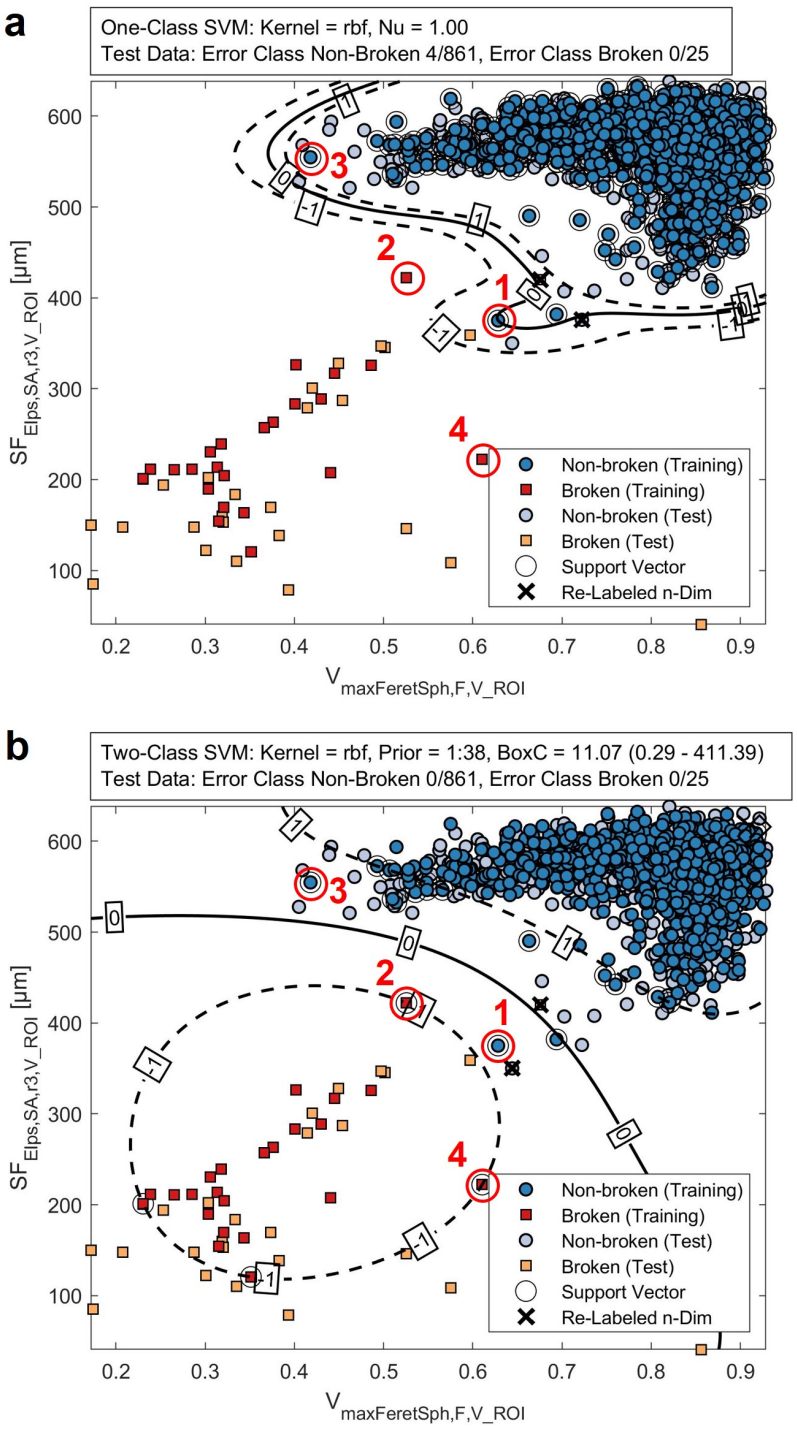

Figure 5.9: SVM models with RBF kernels for the feature-based classification of 886 pellets in DTT (—— OSH: SVM score 0, − − − OSH margin: SVM score $\in [-1, 1]$). (a) OC-SVM generates a tight OSH around the feature point-cloud of all *non-broken* pellets with a high sensitivity towards data outliers. The OC-SVM has an accuracy of 99.55% (precision *broken* pellets: 86.20%). (b) TC-SVM successfully classified all pellets in DTT. (×) Individual objects were re-classified after expanding the feature space including $SV_{CH,V\_ROI,IEV1}$. (∘ 1 - 4) Selected TC-SVM support vectors are compared in details in Fig. 5.10.

Alternatively, the training data (DTR) can be used as part of a TC-SVM to create a OSH considering feature information from both classes of *broken* and *non-broken* pellets. The trained TC-SVM model with RBF kernel is shown in Fig. 5.9b. Prior probabilities were selected proportional to the known class membership distribution of DTR (1:38, *broken*:*non-broken*) specifically penalizing the misclassification of *broken* pellets and shifting the OSH towards the majority class. The TC-SVM models' hyperparameter optimisation yielded changing values for the applied box constraints (BoxC) of both classes with high regularization for the majority *non-broken* pellet class (BoxC = 0.29) and low regularization with hard margins for the minority *broken* pellet class (BoxC = 411.39), indicating significant differences in the model capability to generalize observations of both classes. The TC-SVM model correctly classified all 886 pellets in the test set (DTT) using feature data of $SF_{maxFeretSph,F,V\_ROI}$, $SF_{Elps,SA,r3,V\_ROI}$ and $SV_{CH,V\_ROI,IEV1}$. In comparison to the OC-SVM model, the classification accuracy is further improved, however, the TC-SVM model increases risks for the misclassification of *broken* pellets, significantly extending the OSH margins for *non-broken* pellets. Especially for areas of the feature space represented by only few or no observations in the DTR, the TC-SVM model could fail to detect population anomalies with highly unusual feature combinations. These could result from significant changes in the manufacturing process and are expected to be located in the OSH margin. Similar to the OC-SVM model, individual cases in proximity to the OSH margin can be reviewed in order to identify potential cases of pellet misclassification and further improve the model robustness over time. For the TC-SVM model the number of observations in the OSH margin increases to 40 pellets (*non-broken* 30, *broken* 10) compared to 4 pellets (*non-broken* 4, *broken* 0) for the OC-SVM model.

Selected pellets acting as support vectors of the TC-SVM model are shown with their corresponding feature combinations in Fig. 5.10. These pellets contain feature combinations located in proximity of the OSH. The direct comparison supports the selection of features from distinct structure-related categories to capture the full spread of the *broken* pellet population. Pellet 2 has a $SF_{Elps,SA,r3,V\_ROI}$ of 421.95 μm, which is larger than the smallest *non-broken* pellet in DTR (Pellet 1, 375.11 μm). However, Pellet 2 can be easily distinguished using information on surface roughness ($SV_{CH,V\_ROI,IEV1}$), where the population of *non-broken* pellets exhibits a narrow distribution of 0.989 ± 0.002. In contrast, Pellet 3 has a low sphericity quantified using $SF_{maxFeretSph,F,V\_ROI}$, but a large absolute size expressed in $SF_{Elps,SA,r3,V\_ROI}$. In general, smaller

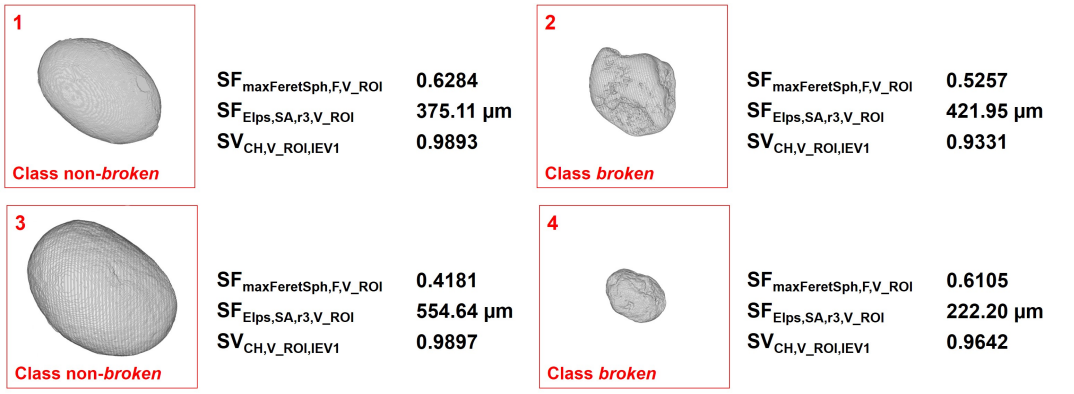

Figure 5.10: Individual (1,3) *non-broken* and (2,4) *broken* pellets with feature combinations associated to support vectors of the TC-SVM classification model defining the OSH margin. The examples visualise the importance of a multi-dimensional feature space targeting distinct pellet properties related to shape, size and surface characteristics. Large *broken* pellets (pellet 2, high $SF_{Elps,SA,r3,V\_ROI}$) can be distinguished by their surface characteristics ($SV_{CH,V\_ROI,IEV1}$). Small, rounded pellet pieces (pellet 4) can be identified using $SF_{Elps,SA,r3,V\_ROI}$.

broken pellets tend to exhibit a wider distribution of shape- and surface-related features (e.g. Pellet 4). Here, $SF_{Elps,SA,r3,V\_ROI}$ as an absolute measurement of the pellet size ensures a robust classification.

The high accuracy and precision of the SVM models suggest a strong performance of the selected feature space to solve this classification problem aiming to identify *broken* pellets in each capsule. The successful quantitative characterisation of the population of pellets across all measured capsules can be used to evaluate the sample against product specifications for quality control or to assess the impact of changing formulation and/or process parameters. Additionally, the non-destructive nature of the micro-XRT analysis allows a correlation of extracted information to the sample's performance data, which may explain and ultimately predict final product performance such as dissolution where particle breakage may have an effect. The presented micro-XRT analysis approach has the potential to be translated to other pharmaceutical systems such as crystallisation, spherical agglomeration, granulation and tableting. Feature selection and classification models can be adapted to target changing research objectives. The extraction of quantitative information from these systems with complex multi-dimensional structural properties can help to improve the understanding of product transformations within individual unit operations to optimise pharmaceutical manufacturing processes and accelerate process development. In combination with quality controls for managing extensive experimental data,

ML strategies can be utilised to identify patterns and inference in the product characteristics.

5.4 Conclusions

Micro-XRT was successfully employed to characterise a solid pharmaceutical multi-particulate product quantifying structural attributes of the entire sample and of its primary particles. The implemented algorithms to reliably extract features of the primary particles were essential to allow an in-depth statistical evaluation of the population and were utilised in the first instance to assess pellet uniformity. Feature robustness was further tested against variations in image quality and image processing parameters showing significant feature-dependent deviations, hence promoting the importance of a sensitivity analysis for applications of a quantitative micro-XRT characterisation. The combination of image analysis with feature selection and ML methodologies was essential for the recognition of underlying patterns in these high dimensional datasets with complex structure-related feature combinations. Here, it allowed the automatic detection of all 25 *broken* pellets within a test dataset of 886 pellets at a minimum accuracy of 99.55% and a minimum precision for the classification of *broken* pellets of 86.20%. The application of this systematic characterisation workflow combining quantitative micro-XRT analysis with ML models shows promising performance as a novel approach for an automated analysis of micro-XRT image data. These analysis frameworks are invaluable across a wide range of pharmaceutical multi-particle systems, and only restricted by limitations of the micro-XRT image acquisition system. Quantitative information on structural particle properties have direct applicability in quality control and can be utilised to inform product and process development. The non-destructive nature of this characterisation method permits the additional assessment of the product performance to gain valuable insights into structure-performance relationships for pharmaceutical systems. Future work will focus on the translation of the demonstrated capabilities to a wider range of pharmaceutical solid products.

Contributions

FJSD and AJF conceived the study. FJSD developed and performed methodologies for micro-XRT image analysis and SVM machine learning applications of capsule formulations. FJSD wrote the original draft of the manuscript, which was reviewed by FJSD and AJF.

Acknowledgement

The authors would like to thank EPSRC and the Doctoral Training Centre in Continuous Manufacturing and Crystallisation (Grant Ref: EP/K503289/1) and the EPSRC Future Continuous Manufacturing and Advanced Crystallisation Research Hub (CMAC, Grant Ref: EP/P006965/1) for funding this work. The authors would like to acknowledge that this work was carried out in the CMAC National Facility supported by UKRPIF (UK Research Partnership Fund) award from the Higher Education Funding Council for England (HEFCE, Grant Ref: HH13054). Data underpinning this publication are available from the University of Strathclyde KnowledgeBase at https://doi.org/10.15129/e5d22969-77d4-46a8-83b8-818b50d8ff45 from 2022 onwards, following the cessation of an embargo period. Further details relating to the data and the embargo can be accessed from the portal.

6 Quantitative Investigation of the Particle Design Space of Novel Pharmaceutical Formulations using Single Droplet Evaporation Experiments and X-Ray Tomography

Declaration: *This chapter was published as an original research article in the journal Advanced Powder Technology as part of a special issue for the 8th World Congress on Particle Technology and is the result of a collaboration between Frederik J.S. Doerr[a,b], Iain D.H. Oswald[a,b] and Alastair J. Florence[a,b] [7]. Parts of this work were presented at the 8th World Congress on Particle Technology (2018).*

Abstract: The implementation of a particle design platform that can be applied to novel pharmaceutical systems using acoustic levitation (SAL) and X-ray tomography (XRT) is discussed. Acoustic levitation was employed to provide a container-less particle design environment for single droplet evaporation experiments. Dried particles were subject to further visual and quantitative structural analysis using X-ray tomography to assess the three-dimensional volume space. The workflow of the combined SAL-XRT platform has been applied to investigate the impact of increasing HPMC K100LV concentrations on the evaporation, drying and final particle morphology of particles from a model pharmaceutical formulation containing metformin hydrochloride and D-mannitol. The morphology and internal structure of the formulated particles after drying are dominated by a crystalline core of D-mannitol partially suppressed with increasing HPMC K100LV additions. The final structure can be correlated to the observed evaporation kinetics. The characterisation of formulated MET hydrochloride particles with increasing polymer content demonstrated the importance of an early-stage quantitative assessment of formulation-related particle properties. The ability to study the

[a] *EPSRC CMAC Future Manufacturing Research Hub, Technology and Innovation Centre, Glasgow, UK*

[b] *Strathclyde Institute of Pharmacy & Biomedical Sciences (SIPBS), University of Strathclyde, Glasgow, UK*

evolution of solid phase formation and its influence on the final particle morphology can enable the selection of formulation and process parameter that deliver the desired particle structure and consequent performance by design.

Keywords: Pharmaceutical Formulation Development, Single Droplet Evaporation, XRT Particle Structure Analysis, Crystallisation, Acoustic Levitation

Highlights:

- Using acoustic levitation and X-ray tomography for particle formulation development.
- Péclet numbers to interpret experimental observations of particle formation.
- Reduced liquid evaporation rates due to the polymer prior to solid skin formation
- Quantitative descriptors for particle morphology from X-ray tomography
- Changes in the internal microstructure have an impact on the final particle shape

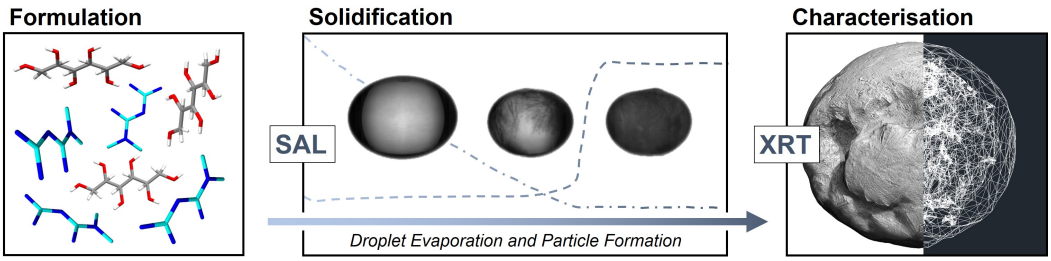

Figure 6.1: Graphical abstract Chapter 6.

6.1 Introduction

Spray Drying is a one-step continuous drying and isolation process broadly applied in the pharmaceutical and food industry to transform a liquid solution or primary particle suspension into a dry, solid powder [3]. Entering the drying chamber, the continuous flow is dispersed into a spray of droplets which are brought into contact with a dry hot gaseous flow. The complex evaporation and solidification processes are dominated by simultaneous transfer of heat, mass and momentum. The process conditions influence a number of particle properties including particle size, shape, morphology, porosity, density and mechanical stability [42, 1, 281, 282]. Spray Drying also has the potential to produce crystalline or amorphous materials as well as

formulated systems which can be used to achieve drug formulations with distinct performance qualities [283, 284, 116, 285, 18, 114, 67].

The need for small-scale experimental platforms especially for continuous drying applications has previously been highlighted by academia and industry [286]. Systems for small scale droplet drying experiments allow the characterisation of the evaporation process for individual droplets and have been used to study the influence of the compound system and the process conditions on the attributes of the obtained final particles. Monitoring the evaporation and particle evolution enables the extraction of quantitative kinetic information that can support semi-empirical modelling of the drying process to inform development before moving to lab-scale. Groups have been using droplet drying experiments to investigate droplet shrinkage [69], skin formation [70, 83, 102] and buckling phenomena of droplets undergoing drying [287, 41]. Acoustic levitation provides a container-less environment for single droplet evaporation experiments with a minimised risk for heterogeneous nucleation events and conductive heat transfer compared to similar experiments with individual droplets suspended on a filament. Quasi-stationary levitated droplets can be monitored to study liquid evaporation and particle formation processes. Applications utilising acoustic levitation to study single droplet evaporation or to perform single particle experiments of various compound systems have been reported in detail in the literature [102, 12, 288, 107, 289, 290, 101, 103]. The particles from such experiments can be assessed in terms of their critical solid state properties and performance. Optimisation of these particle properties through a deep understanding of the solid formation process is a key objective of particle engineering. Control or improvement of material-handling in the manufacturing process and the enhancement of product performance linked to attributes such as mechanical stability [103], compressibility [60, 238], solubility [284, 49] and solid state stability [290] are just two potential areas of interest. X-ray tomography (XRT) has been applied to a number of pharmaceutical systems for sample visualisation and / or to extract quantitative data on particle size, surface, shape and porosity [157, 291, 158]. XRT can be applied non-destructively to characterise a broad range of solid samples and is not limited to individual bulk or single particle properties. Importantly, the results of XRT analysis can be further related to the dynamics of the solidification process observed in the single droplet evaporation experiments, which is an aspect of increasing interest and reseach efforts [83, 41].

In this paper we demonstrate the investigation of particle formation processes using an acous-

tic levitator (SAL) and the subsequent structural characterisation with XRT. The combined SAL-XRT platform can capture and quantify time-related effects such as evaporation kinetics, solid phase nucleation and drying rates as well as gives access to information on the final solid structure. The SAL uses optical and thermal imaging to monitor the evaporation process [287, 107, 292]. High-resolution XRT measurements enable to link the particle formation process to its final morphology and internal structure. This bespoke approach is applied to develop a single particle formulation for metformin hydrochloride (MET). As one of the World Health Organization's List of Essential Medicines, MET is widely used to treat non-insulin-dependent diabetes mellitus [293]. In solid form, metformin is commonly available as a highly water-soluble HCl salt and typically compressed into tablets for oral administration with high dose per tablet of 500 mg to 1500 mg. The high drug load can cause problems during tableting and the short biological half-life commonly requires repeated administrations [294, 295]. A number of groups worked on formulated systems to produce MET-tablets with optimised compaction properties and/or dissolution properties to control the drug release profile [238, 294, 295, 296, 297]. Commercial derivatives of hydroxypropyl methylcellulose (HPMC) are frequently included in these oral controlled-release formulations and exist in various modifications and molecular sizes [298]. D-mannitol (MAN) is a common excipient for spray drying applications and can be used in formulations for diabetes mellitus treatment. MAN was added as a diluent to reduce the drug-load below 50 wt%.

6.2 Materials and methods

6.2.1 Chemicals / Samples

MET and MAN were sourced from Sigma-Aldrich (St. Louis, USA). HPMC was kindly donated from Ashland (Benecel K100LV PH PRM, Covington, USA). Stock solutions were prepared at a concentration of 300 mg/mL for MET, 150 mg/mL for MAN, and 10 mg/mL for HPMC K100LV. The stock solutions were used to prepare the solutions for each formulation listed in Table 6.1. Solution concentrations used for the drying experiments of pure and formulated systems were selected to achieve a comparable absolute solute mass enabling reliable imaging and levitation. All samples were prepared with filtered and deionised water (WAT, Milli-Q, Merck KGaA, Germany) and thoroughly mixed with a table vortex before usage.

Table 6.1: Preparation schemata for solutions of metformin hydrochloride, D-mannitol and Benecel K100LV PH PRM with sample ID and starting concentrations (c_0).

Sample	$c_{0,MET}$ [mg/mL]	$c_{0,MAN}$ [mg/mL]	$c_{0,HPMC}$ [mg/mL]
MET_75	75	-	-
MAN_75	-	75	-
HPMC_10	-	-	10
MS_0	18.75	18.75	-
MS_1	18.75	18.75	0.375
MS_2	18.75	18.75	0.750
MS_3	18.75	18.75	2.250
MS_4	18.75	18.75	4.500

6.2.2 Single Axis - Acoustic Levitator

A single-axis acoustic levitator (SAL, Materials Development, Inc., Arlington Heights, USA) was used to perform container-less single droplet evaporation experiments (Fig. 6.2). The acoustic levitator has been described in detail elsewhere [288]. An additional custom-build electric incubation system (Okolab, Naples, Italy) was employed as an enclosure of the SAL to provide control over the surrounding temperature and humidity levels. The enclosure consists of heated walls and windows for both imaging systems. Nitrogen was used as a drying gas. The nitrogen was filtered and pre-heated before entering the chamber at 0.4 L/min. The temperature was kept constant and was constantly measured with a temperature and humidity sensor (AM2302, Adafruit Industries, USA) integrated in the enclosure. The measured relative humidity in all experiments was less than 2.5%RH. The average ambient temperature in the enclosure was 42.76 ± 0.15 °C. Prior to any experiments, the system was given a warm-up period of at least one hour to reach stable conditions monitored in terms of humidity, temperature and the generated acoustic signal.

In order to characterise the droplet evaporation process, each experiment was monitored utilising a Fastcam SA1.1 high speed camera (Photron, Tokyo, Japan) and an A6702sc thermal camera (FLIR Systems Inc., Wilsonville, USA). Images from the live stream of the high speed camera were collected at 1 fps. The images were used to monitor the evaporation process and to detect the onset of solid phase formation. During acoustic levitation, the droplet is deformed into an oblate spheroid. The volume and surface area were calculated from the major and minor axis using an ellipse fitting method for each image of the 2D droplet projection. The evaporation mass flux ($\dot{m}$) was calculated iteratively from the changing droplet volume over time and

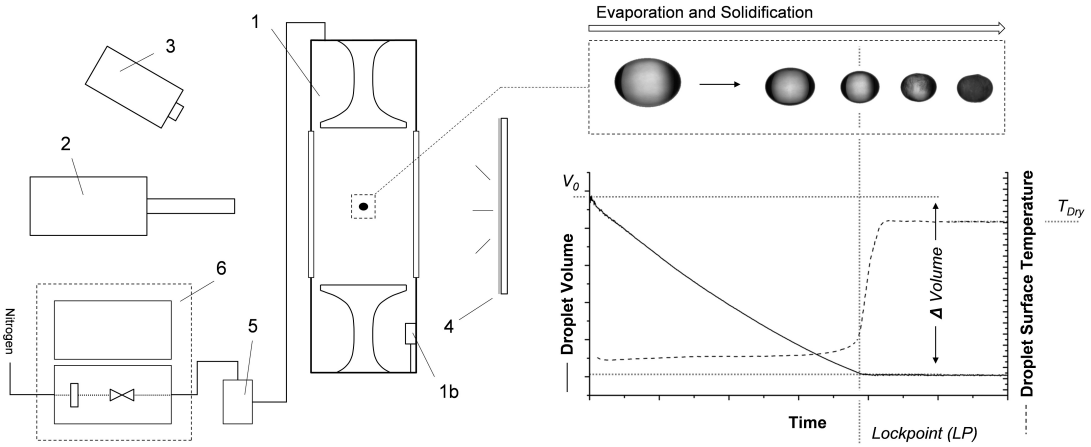

Figure 6.2: (Left) Experimental Setup with (1) acoustic levitator with two opposed transducers and an enclosure with (1b) a sensor for measuring temperature and relative humidity. The evaporation process is monitored using (2) a high speed - and (3) thermal imaging systems. The droplets are back-illuminated with (4) an LED light source plus diffuser. Nitrogen is filtered, heated and the flow is regulated with a system from Okalab (5 - 6). (Right) Image analysis allows the extraction of information on the droplet volume and surface temperature for the course of the evaporation process to detect initial solid skin formation (*Lockpoint*, LP) and reaching a state with constant end temperature (T_{Dry}).

is expressed in relation to the available droplet surface area. Here, the initial point of skin formation at the droplet lockpoint (LP) is defined by a discontinuous change of the mass flux at the final inflection point of the droplet volume curve before reaching a constant end-volume. An example is presented in Fig. A6 (ESI, page A20). Thermal images were used to extract surface temperature information from the droplets and particles after reaching LP. The recorded surface temperature information can be used to identify the state of liquid evaporation at wet-bulb temperature and characterise the particle surface heating kinetics after skin formation until reaching a stable end-temperature for the dried particle [107, 292]. The droplet surface temperature information from thermal imaging were corrected with an emissivity factor of 0.96 for water [292] . Following LP, the thermal emission can change depending on the characteristic thermal radiation emitted from the solid phase composition. Therefore, the thermal emissivity factor for each solid phase composition was estimated from the recorded temperature of the particle surface after reaching a constant end-temperature level (T_{Dry}) and the corresponding recorded ambient temperature (T_∞). The applied thermal emissivity correction factors (ε) for each tested composition are listed in Table A7 (ESI, page A19).

Measured heat- and mass-transfer kinetics of the liquid phase during droplet drying in the acous-

tic levitator can be impacted through effects related to acoustic streaming as described in Section 1.2.2. The impact of acoustic streaming was not further investigated in this study and calculations are focused on a description of the solute diffusion inside the droplet droplet assuming steady-state evaporation in accordance with the d2-law (Equation 6.3).

6.2.3 X-ray Tomography and XRT Image Analysis

A SKYSCAN 2211 X-ray tomograph (*NanoCT*, Bruker, Kontich, Belgium) with cone-beam arrangement was employed for this project. The samples were scanned with an image pixel size of 1.2 μm - 1.8 μm, frame averaging of 4 and a rotation step size of 0.2° (total rotation of 180°). The X-ray acceleration voltage was set to 40 keV. A reference scan was collected at the end of each run to enhance post-alignment and compensate for potential shifts during the scan. Image reconstruction was performed using SkyScan NRecon with InstaRecon (version 1.7.1.6, Bruker, Kontich, Belgium).

XRT image processing was carried out with custom scripts developed in MATLAB (MathWorks, USA). Images of each processing stage are displayed in Fig. 6.3. Individual reconstructed images were pre-processed using an edge-preserving image filter (anisotropic diffusion [218, 299]) or local low-contrast smoothing in case of HPMC K100LV to reduce random noise and prepare the images for subsequent binarisation (Fig. 6.3 a). The binarisation was performed with a histogram-based algorithm [221] or optimised manually. Ultimately, remaining noise was removed using a size threshold of 10 voxel for black and white speckles and a 3D volume connectivity detection algorithm to remove non-connected binary volumes. The pre-processed and binarized images yielded the detected solid phase volume (V, Fig. 6.3 b). An additional 3D-morphological closing operation with a subsequent enclosed background filter and an integrated feedback-loop on detected internal background volumes was applied to define a region of interest for the particle solid phase volume (V_ROI, Fig. 6.3 c). Extracted information of each particle are descriptors of the particle shape and its volume distribution. The absolute particle solid phase can be quantified directly from V (Fig. 6.3 b). The particle porosity (ΔV_ROI, Fig. 6.3 d) can be calculated from a simple subtraction of V from V_ROI. In order to quantify concave surface volumes (ΔV_ROI_CH, Fig. 6.3 e) as a descriptor for particle surface buckling, V_ROI was subtracted from the volume space of a 3D convex hull around V_ROI [300]. The detected volumes were related to the maximum particle space represented by

a sphere with equivalent maximum Feret diameter ($V_{eqSph,Feret}$) to counter the impact of deviations in the initial droplet volume on the detected particle volume fractions. For visualisation, image stacks were imported in CTVox (version 3.2.0, Bruker, Kontich, Belgium).

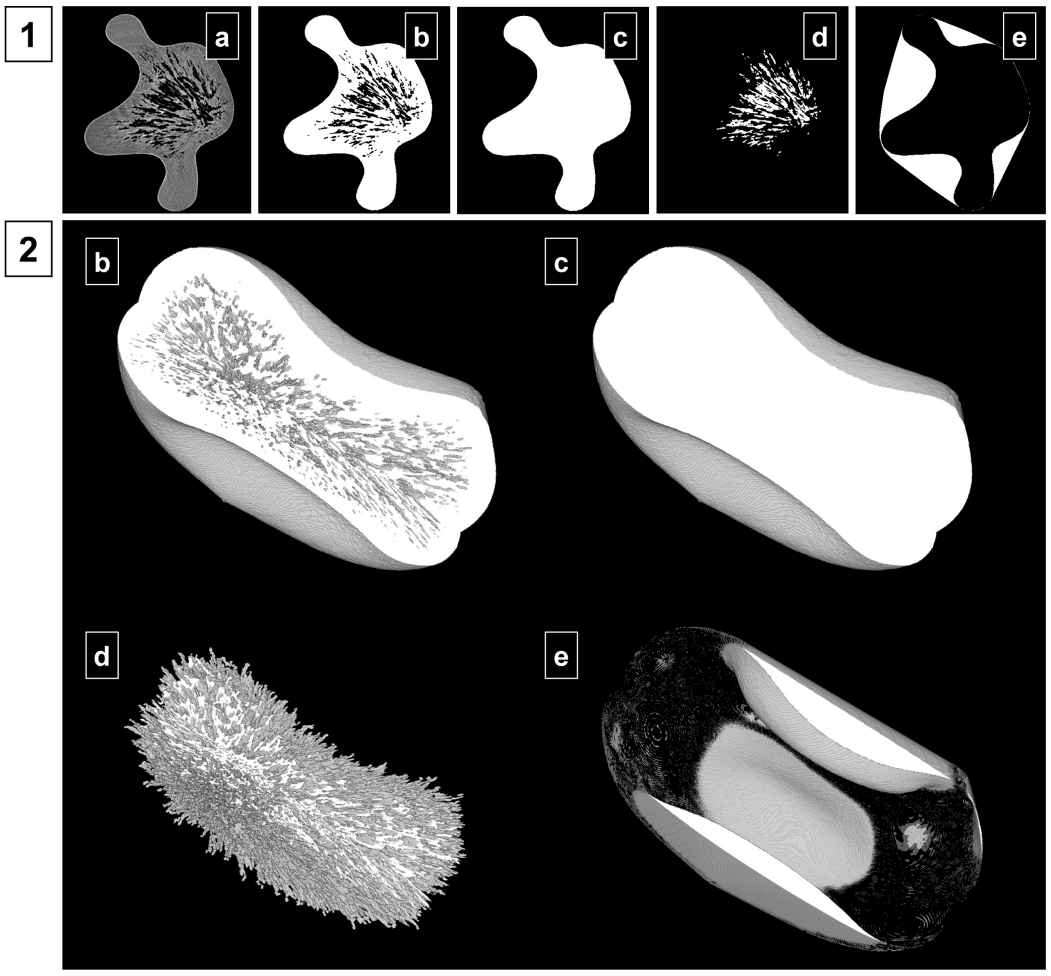

Figure 6.3: XRT image processing to extract quantitative descriptors for particle size, shape, porosity and surface buckling. (1) Selected single 2D cross-section images and (2) volume-rendered 3D image stacks with insections to show internal microstructure. (a) Grayscale images after reconstruction, (b) binarized images after thresholding and noise reduction (V), (c) region of interest for primary particle volume (V_ROI), (d) particle porosity (ΔV_ROI) and (e) particle concave surface volume (ΔV_ROI_CH).

6.3 Results and Discussion

6.3.1 Solidification and Skin Formation of HPMC K100LV and formulated Systems of MET

Single droplet experiments of a HPMC K100LV solution with a starting concentration of 10 mg/mL (HPMC_10, Table 6.1) were performed in comparison to pure water. Fig. 6.4 shows the recorded normalised droplet diameter and droplet surface temperature of the evaporating HPMC K100LV solution in direct comparison to pure water. Over the course of the SAL experiment, the liquid evaporation of HPMC K100LV droplets increasingly deviates from the evaporation of pure water. Despite these clear differences in the evaporation rate, the measured surface temperatures remain similar, which might be the result of changing liquid emissivity for the HPMC K100LV solution droplets whilst assuming an emissivity of water during this phase of pure liquid evaporation (see details in Section 6.2.2). The lockpoint (LP) due to polymer skin formation is detected after 179.79 ± 12.93 s/mm^2. After the initial skin formation the rate of water evaporation of HPMC_10 droplets is further reduced. The permeation and evaporation of additional water through the polymeric surface layer leads to a radial pressure gradient that causes a collapse of the particle surface inside the droplet core (SC) and the formation of a vacuole. The generated surface enhances the evaporation of the remaining moisture, which causes a two-step transition to the end-temperature level as shown in the recorded surface temperature curve after LP. Pure water droplets do not display a discontinuous reduction in the evaporation kinetics as observed for droplets of HPMC K100LV. The final mean diameter of six water droplet measured during the evaporation experiments was 345.43 μm. Below that size a levitation of the droplets with the SAL set-up was not stable due to secondary acoustic reflections from the enclosure.

Subsequent to the single droplet evaporation experiments, each HPMC K100LV particle was collected and analysed using XRT to quantify the solid phase volume and extract other structural descriptors on size, shape and particle porosity (Section 6.3.2). The solid phase volume of the particles and the solid phase mass can be used to determine the solid phase true density (Equation 6.1) assuming insignificant contributions of micro-pores with sizes < 5-10 μm, which are below the reliable detection limit of the micro-XRT analysis (see for additional details Chapter

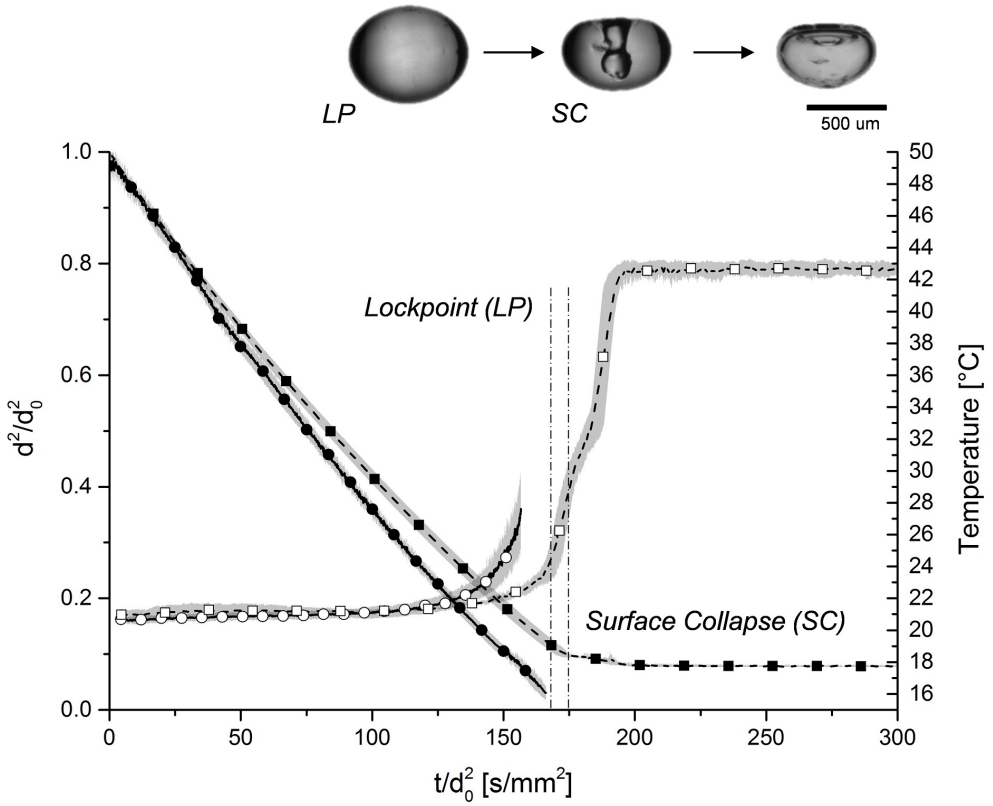

Figure 6.4: Drying curves for (– – ◐ – –) WAT and (—◧—) aqueous HPMC K100LV solution (HPMC_10, c_0 10 mg/mL). The data show an increasing deviation of the evaporation kinetics for HPMC_10 compared to pure water over time and prior to the detection of skin formation (LP). After LP, the particle surface collapses (SC) before reaching an ambient end-temperature level resulting in a two-step transition mechanism. Black symbols - normalised squared diameter, white symbols - surface temperature. Data from replicates with n ≥ 3. Markers are sub-sampled from original data.

4 and Chapter 5). The solid phase mass is derived from the starting solute concentration (c_0) and the initial droplet volume ($V_{Droplet,0}$). The solid phase volume (V_{CT}) can be directly quantified from the XRT image data.

$$\rho = \frac{m}{V} = \frac{c_0 \cdot V_{Droplet,0}}{V_{CT}} \tag{6.1}$$

To approximate the HPMC K100LV diffusion coefficient in water, it is assumed that there is no internal mixing and that the surface concentration of HPMC K100LV (c_s) reaches solid true density at LP ($\rho = \rho_{crit} = c_s$) by solving Equation 6.2 for a diffusion controlled surface enrichment (E) during steady-state evaporation in accordance with the d2-law (Equation 6.3) for Péclet numbers (Pe) below 20 [19, 20].

$$E = \frac{c_s}{c_m} = 1 + \frac{Pe}{5} + \frac{Pe^2}{100} + \frac{Pe^3}{4000} \quad \text{with} \quad Pe = \frac{\kappa}{8 \cdot D_s} \tag{6.2}$$

$$d^2(t) = d_0^2 - \kappa \cdot t \tag{6.3}$$

Table 6.2: Calculated density of HPMC K100LV and its molecular diffusion coefficient in water based on experimental results from three individual SAL experiments and XRT analysis. XRT analysis was performed on the individually obtained particles after reaching a dry state in the SAL experiments.

HPMC_10	m_0 [μg]	ρ_{crit} [g/cm^3]	D_s [10^{-11} m^2/s]
Exp1	92.17	1.34	4.622
Exp2	92.60	1.38	4.872
Exp3	96.97	1.38	4.343
Mean		1.36 ± 0.02	4.612 ± 0.264

The mean solute concentration of the droplet (c_m) can be determined from the starting concentration of the solution and the observed absolute change in the droplet volume at LP. The calculated solid true density (ρ_{crit}) and diffusion coefficient (D_s) from three individual single droplet experiments are listed in Table 6.2. ρ_{crit} of HPMC K100LV was calculated to be 1.36 ± 0.02 g/cm^3, which is in agreement with data available from literature for other HPMC derivatives of 1.33 g/cm^3 [251]. Solving Equation 6.2 for each experiment yields an approximated diffusion coefficient for HPMC K100LV in water of 4.61 E-11 ± 0.26 E-11 m^2/s at a LP surface temperature of 29.18 ± 1.01 °C with an evaporation rate (κ) of 5487.10 ± 137.76 μm^2/s and Pe of 14.92 ± 1.23. For comparison, calculated diffusion coefficients for HPMC K100LV in water

over the course of the SDD experiment using the Stokes-Einstein equation ($D_{s,SE}$, Equation A17 in Section A3.1) is provided in Fig. A7 (ESI, page A21) and shows the impact of solution viscosity on changes of $D_{s,SE}$ during liquid evaporation. For low polymer concentrations, D_s are in reasonable agreement with $D_{s,SE}$ = 1.66 E-11 ± 0.26 E-11 m^2/s at $c_{0,\text{HPMC K100LV}}$ of 10 mg/mL, but $D_{s,SE}$ quickly deviates with increasing polymer concentration assuming a uniform HPMC K100LV concentration (c_m). It has to be noted that the Stokes-Einstein equation assumes single chain properties throughout the drying process represented by a rigid sphere with radius (R_h) determined from the intrinsic viscosity ([η]) [301] and is commonly restricted to dilute solutions. Further details are provided in Section A3.1 (ESI, page A20). In both cases, the approximated diffusion coefficient of HPMC K100LV in water is significantly lower than the diffusion coefficients of MET and MAN reported in literature of 7.56 E-10 m^2/s (29.18 °C, calculated see Fig. A5 (ESI, page A19)) and 1.17 E-09 m^2/s (37 °C), respectively [302, 303, 304]. According to Equation 6.2, smaller diffusion coefficients will lead to an increase in surface enrichment. This indicates that HPMC K100LV is expected to predominately solidify as part of the particle surface layer during skin formation at LP. The comparatively high diffusion coefficients of MET and MAN allow both small organic compounds to compensate part of their radial concentration profile caused by liquid evaporation on the droplet surface. Therefore, MET and MAN would be expected to predominantly solidify as part of the particle core.

The evaporation and drying of formulations of MET with MAN and HPMC K100LV (MS_0 - MS_4, Table 6.1) were investigated in a series of single droplet drying experiments with starting volumes of 9.93 ± 1.15 μL using the SAL. Fig. 6.5 shows the results for three selected formulations (MS_0, no HPMC K100LV; MS_1, low HPMC K100LV; MS_4, high HPMC K100LV). The results indicate that the addition of HPMC K100LV significantly influences the kinetics of liquid evaporation and particle drying after solid skin formation (LP) even at relative mass concentrations of HPMC K100LV less than 1 wt% as in the case of MS_1. This suggests a reduction in the water activity at the droplet surface due to the polymer addition in comparison to the solution of MS_0 without HPMC K100LV. The impact of HPMC K100LV can be observed most dominantly during the phase of liquid evaporation with a reduced evaporation rate and, subsequently, in a delay in the initial solid phase nucleation. The reduced evaporation of water from the droplet surface in MS_1 and MS_4 leads to an increased droplet surface temperature during liquid evaporation compared to MS_0. The delay of LP can be observed for solutions

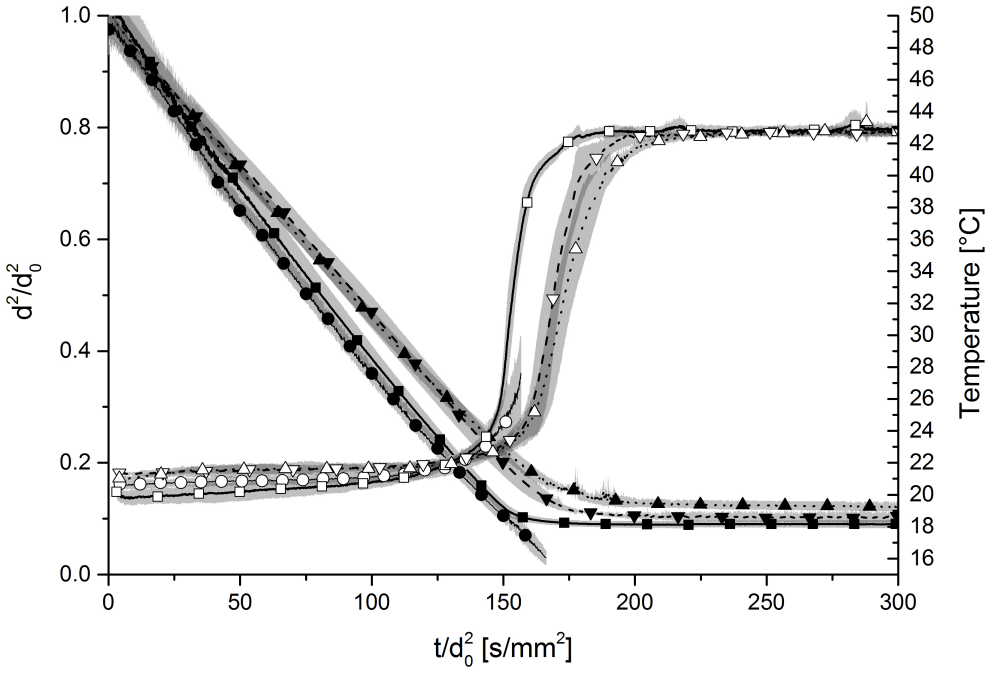

Figure 6.5: Drying curves for formulations of MET and MAN with equal starting concentrations of 18.75 mg/mL and increasing additions of HPMC K100LV: (– – ◐ – –) WAT, (—◧—) MS_0, c_0 0 mg/mL, (– – ▽ – –) MS_1, c_0 0.375 mg/mL and (··· ◭ ···) MS_4, c_0 4.5 mg/mL. MS_0 without HPMC K100LV exhibits significantly higher evaporation kinetics compared to MS_1 and MS_4. Black symbols - normalised squared diameter, white symbols - surface temperature. Data from replicates with n ≥ 5. Markers are sub-sampled from original data.

with additions of HPMC K100LV of up to 4.5 mg/mL (MS_4) compared to MS_0 despite a higher total solute starting concentration. At LP, the droplets have a remaining water content of 47.38 ± 4.15 wt%, 49.86 ± 4.38 wt% and 57.20 ± 2.45 wt% for MS_0, MS_1 and MS_2, respectively.

Fig. 6.6 shows the derived liquid evaporation mass flux and the heating rate of the particle surface during drying for the single droplet evaporation experiments presented in Fig. 6.5. The droplet evaporation mass flux is calculated iteratively from the change in droplet volume over time and normalised using the available surface area. After LP, the evaporation mass flux cannot be further tracked using a shape-based analysis of the image data and, therefore, is set transparent in Fig. 6.6. The experienced maximum mass flux ($\dot{m}_{max}$) and maximum heating rate ($\dot{T}_{max}$) for single droplet experiments of HPMC K100LV and MET formulations are listed in Table 6.3. The maximum heating rate is the first time-derivative of the surface temperature profile at the point of inflection undergoing a transition from the wet-bulb temperature to the final constant temperature corresponding to the ambient temperature ($T_{Dry} = T_{\infty}$). The results indicate that the evaporative flux across the droplet surface is significantly reduced for droplets with additions of HPMC K100LV and is further reduced for increasing HPMC K100LV starting concentrations. The reduction of water mass transfer prior to reaching LP supports the previous considerations of HPMC K100LV surface enrichment with an impact on the overall water surface permeability and evaporation. In all cases, the evaporation flux increases over time before reaching a maximum and a subsequent discontinuous reduction due to solid skin formation at LP. The drying rates of the particles after LP are equally reduced with increasing HPMC K100LV concentrations, which indicates decelerated mass transfer of remaining moisture to the particle surface leading to lower drying kinetics. This could be caused by a reduction in the water permeability through the particle surface layers due to an increasing thickness of the polymer skin around the particle. The maximum drying rates are limited by the accessible drying temperatures that can be applied in combination with the current SAL setup. Work to extend this method to encompass temperature regimes that more closely mimic those experienced across the full range of drying platforms of industrial relevance is ongoing.

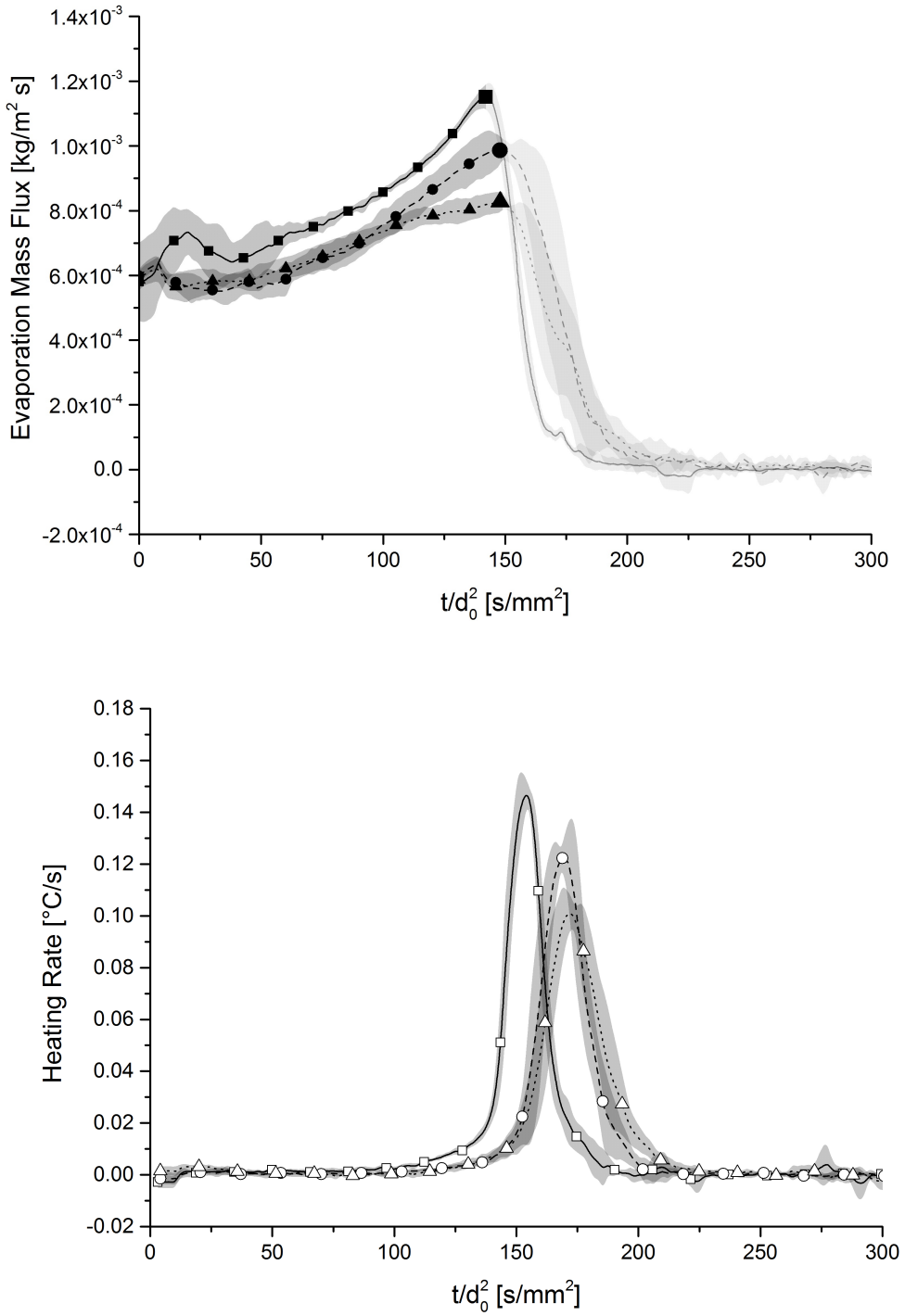

Figure 6.6: Solidification kinetics of formulation of MET and MAN with equal starting concentrations of 18.75 mg/mL and varying additions of HPMC K100LV: (—■—) MS_0, c_0 0 mg/mL, (– – ◐ – –) MS_1, c_0 0.375 mg/mL and (··· ◭ ···) MS_4, c_0 4.5 mg/mL. The evaporation flux increases over time and is significantly lower for droplets with added HPMC K100LV. The drying kinetics are reduced with increasing HPMC K100LV concentrations. Black symbols - evaporation mass flux, white symbols - surface heating rate. Data from replicates with n ≥ 5. Markers are sub-sampled from original data.

Table 6.3: Maximum mass flux ($\dot{m}_{max}$) and heating rate ($\dot{T}_{max}$) during droplet drying experiments for HPMC K100LV (HPMC_10) and five tested MET formulations (MS_0 - MS_4).

Sample	n	$\dot{m}_{max}$ [10^{-4} kg/(m^2·s)]	$\dot{T}_{max}$ [°C/s]
HPMC_10	3	9.89 ± 0.12	0.113 ± 0.006
MS_0	6	11.62 ± 0.39	0.148 ± 0.004
MS_1	8	10.12 ± 0.10	0.135 ± 0.006
MS_2	5	9.96 ± 0.23	0.131 ± 0.007
MS_3	3	9.18 ± 0.48	0.123 ± 0.006
MS_4	6	8.36 ± 0.29	0.106 ± 0.003

6.3.2 Particle Morphology Characterisation using XRT

Particles from single droplet experiments were subject to a further in-depth structural characterisation using XRT. Fig. 6.7 shows the resulting particle morphologies within the investigated particle design space during the evaporation process (SAL Image Data) and after characterisation with XRT (XRT Image Data), respectively.

The SAL Image Data depict the moment of LP detection (top) and of the final dried particle (bottom) for each pure compound (Fig. 6.7.1-3) as well as for five formulations of MET with changing additions of HPMC K100LV (Fig. 6.7.4 a-e, MS_0 - MS_4). The SAL images allow a first visual, qualitative assessment of the final particle characteristics as they evolve over time. Pure solutions of MET (Fig. 6.7.1, MET_75) and MAN (Fig. 6.7.2, MAN_75) solidify as highly crystalline particles with emerging crystalline solid phase obscuring the light transmissive droplet centre at LP. In contrast, MS_0 (Fig. 6.7.4 a) with a combination of equal concentrations of MET and MAN reaches LP without the visual appearance of large structured solid primary particles. Here, the obscuration of the droplet centre occurs post-LP at elevated temperatures before reaching a fully dried state indicating a temporary suppression of crystal nucleation for this system. This effect is further enhanced with increasing polymer additions and several polymers including HPMC have been shown to inhibit crystal nucleation and/or growth, although the mechanisms are not well understood [305]. Whilst beyond the scope of this study, the SAL-XRT platform does provide a convenient means to systematically investigate both the onset of nucleation and the resultant difference in internal particle microstructure for different polymer and solute formulations.

The XRT Image Data are volume rendered visualisations of the 3D image space after binarisation and are also included in Fig. 6.7 to show the particle morphology (top) as well as the

internal particle structure (bottom). Details of the internal structure for three selected particles are displayed in Fig. 6.8 (a - MAN_75, b - MS_0 and c - MS_4). MET shows large block-like solids that are agglomerated to form dense, flattened particles (Fig. 6.7.1). MAN particles are highly spherical and highly porous (Fig. 6.7.2, details see Fig. 6.8 a). The particles consist of large rod-shaped crystalline primary solids. The obtained MAN particles have a similar internal structure as reported for MAN particles from co-current spray drying at reduced evaporation kinetics using an inlet temperature of 65 °C and from counter-current spray drying with extended drying times [306, 307]. HPMC K100LV particles have smooth surfaces and large inner voids (Fig. 6.7.3). This morphology has been reported previously in the literature for other large molecules such as glycoproteins at large Péclet numbers of 5.6 and 16.8 [1].

The XRT Image Data for formulated particles of MET with MAN and HPMC K100LV (MS_0 - MS_4) are displayed in Fig. 6.7.4 a-e and demonstrate the impact of both excipients on the final particle morphology. The direct comparison indicates a qualitative change in the overall particle morphology from near sphericity to highly buckled particles with increasing HPMC K100LV concentrations. The observed inner particle structure suggests that the extent and size of the internal crystal core is reduced for increasing HPMC K100LV solid mass concentrations most significantly for HPMC K100LV solid mass ratios ($= m_{\text{HPMC K100LV}}/m_{\text{particle}}$) of 5.66 wt% (MS_3) and 10.71 wt% (MS_4). At decreasing solid mass ratios of HPMC K100LV below 1.96 wt% (MS_2), the rod-like crystal habit of MAN, as identified in particles from pure MAN solution (MAN_75, Fig. 6.8 a), creates an inner particle structure that supports the overall spherical morphology of the particle. This reduction in size of the rod-shaped primary solids as part of the crystalline particle core further correlates with a decline in the particle porosity for increasing HPMC K100LV concentrations. The drastic size reduction of the primary, rod-shaped solids within the crystalline particle core and its impact on the final particle porosity are best visualised in a direct comparison for two selected particles without the addition of HPMC K100LV (MS_0) and with a HPMC K100LV solid mass ratio of 10.71 wt% (MS_4) shown in detail in Fig. 6.8 b and c, respectively.

The impact of the polymer on the particle morphology and internal microstructure can be quantified using descriptors for particle size, shape and porosity. Fig. 6.9 (bottom) shows the detected volumes for the primary solid phase (V, white), the particle porosity (ΔV_ROI, blue) and the detected concave surface volumes (ΔV_ROI_CH, red) for a single cross-section of

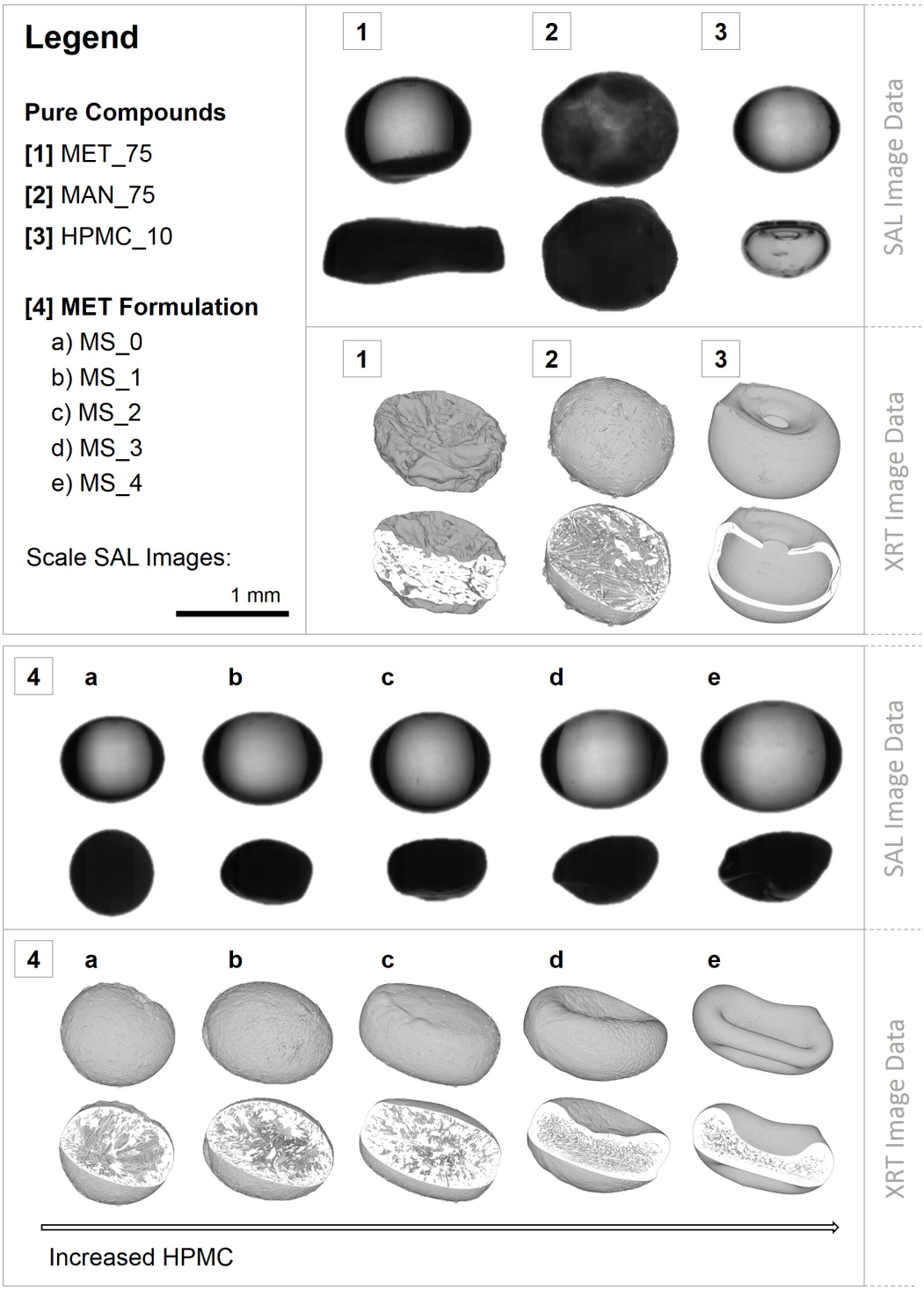

Figure 6.7: Visualisation of the investigated particle design space for solids obtained from single droplet evaporation experiments (SAL Image Data) and after XRT characterisation (XRT Image Data). The individual pure compounds (1-3) show distinct particle characteristics with an impact on the particle morphology for tested formulations of MET (MS_0 - MS_4, 4 a-e).

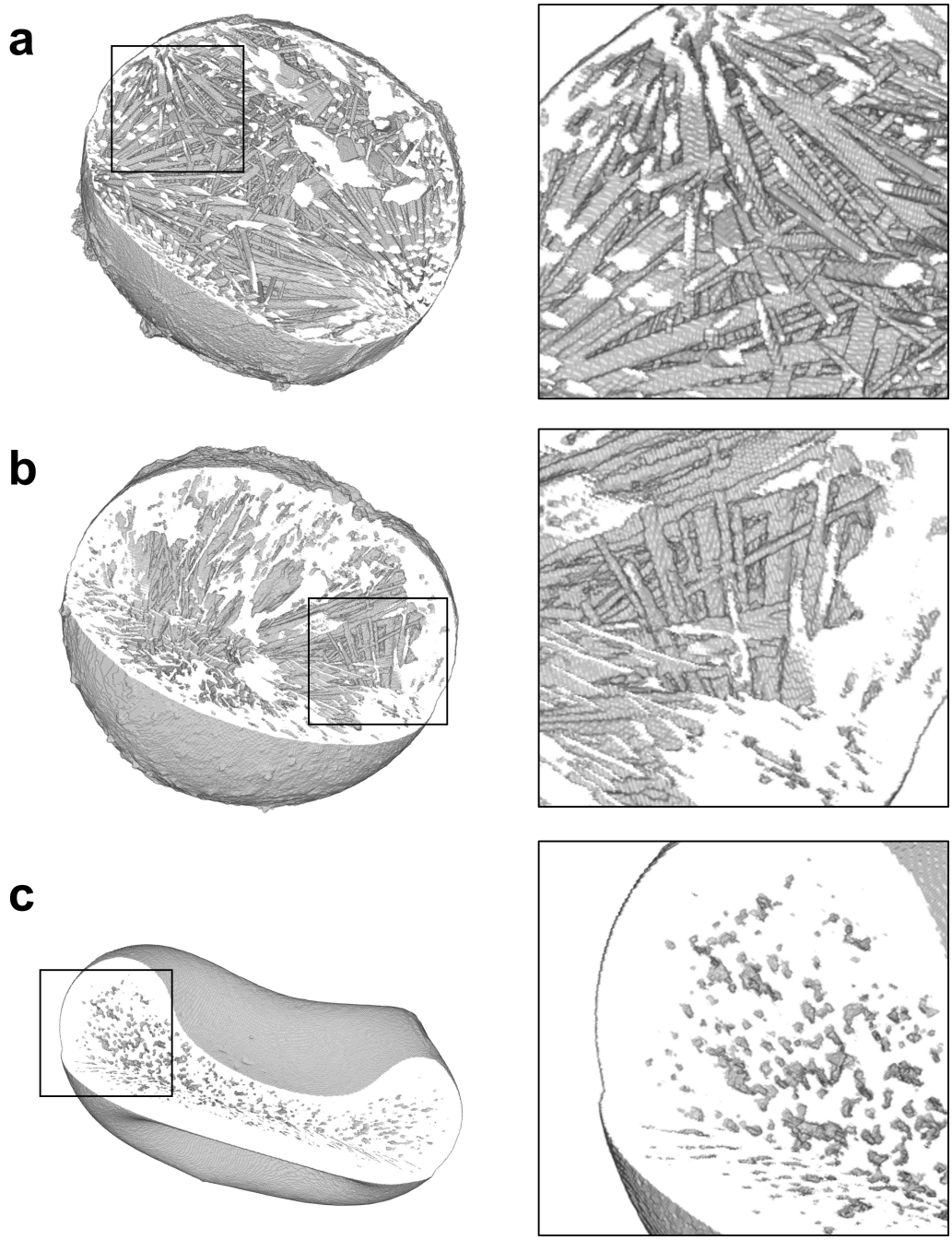

Figure 6.8: XRT reveals the internal structure and morphology of particles collected from single droplet evaporation experiments of (a) pure MAN solution (MAN_75), (b) MET formulation without HPMC K100LV (MS_0) and (c) MET formulation with 10.71 wt% HPMC K100LV (MS_4). The cores of particles from MAN_75 solution are dominated by rod-shaped primary crystalline solids. For formulated particles, the extent and the size of these primary crystalline solids are significantly suppressed with increasing polymer solid mass ratios.

the XRT image stack from each tested formulated system (MS_0 - MS_4). In Fig. 6.10, the extracted quantified volumes for V, ΔV_ROI and ΔV_ROI_CH are normalised against the vol-

ume of a sphere with equivalent maximum Feret diameter ($V_{eqSph,Feret}$) and correlated with the HPMC K100LV starting concentration. The data support the initial visual observations for formulated MET particles with a reduction in the particle porosity fraction of 83.59% between MS_0 and MS_4. Detected concave surface volume fractions (ΔV_ROI_CH) are proportionally higher for pure MET-MAN (MS_0) particles compared to systems with additions of HPMC K100LV below 1.96 wt% as in case of MS_1 and MS_2. This initial over-proportional decrease of ΔV_ROI_CH at low HPMC K100LV concentrations can be related to substantial changes in the particle surface roughness. Here the polymer leads to a reduction in local crystal growth most dominantly expressed in the particle surface layers. For higher HPMC K100LV concentrations and despite further chnages in the particle shape, ΔV_ROI_CH rises from its minimum of 1.11 ± 0.41% for MS_1 to 6.16 ± 1.50% for MS_4 as a result of increasingly strong particle surface buckling with large concave surface volumes.

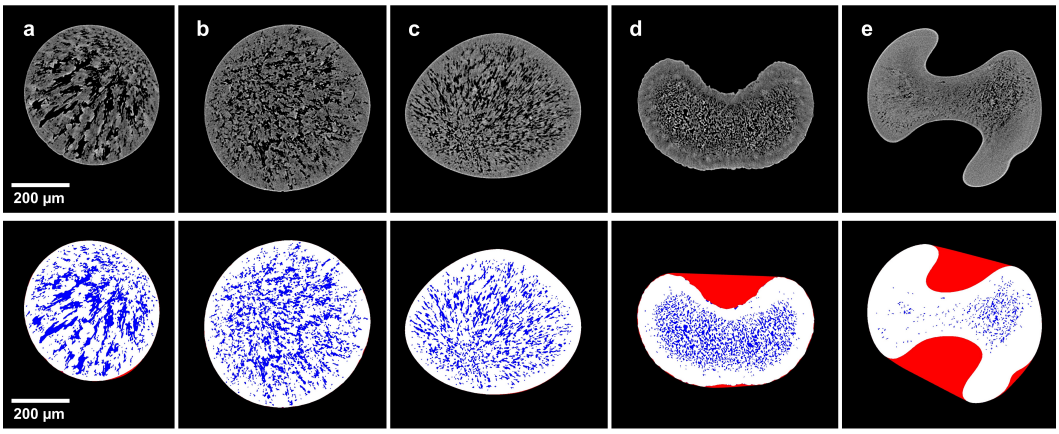

Figure 6.9: Selected 2D cross-sections (top - grayscale, bottom - binarized) of formulated MET particles with MAN and increasing additions of HPMC K100LV: (a) MS_0, (b) MS_1, (c) MS_2, (d) MS_3, (e) MS_4). The images show the detected particle volume (white), porosity (blue) and concave surface volume (red) for the presented cross-sections after binarisation.

In order to quantify the influence of the drug formulation on the overall particle morphology, descriptors for the particle shape were extracted from the XRT data (Table 6.4). The particle sphericity was calculated as a function of V_ROI and its surface area using a definition by Wadell [233] (described in Table 4.4, Ψ_{gl}). Additionally, an aspect ratio of each particle was determined from the major and minor characteristic axes of an ellipsoidal fit with the same normalized second central moment as V_ROI. The extracted quantitative shape descriptors reflect the visual impression of increased particle deformation and surface buckling with rising

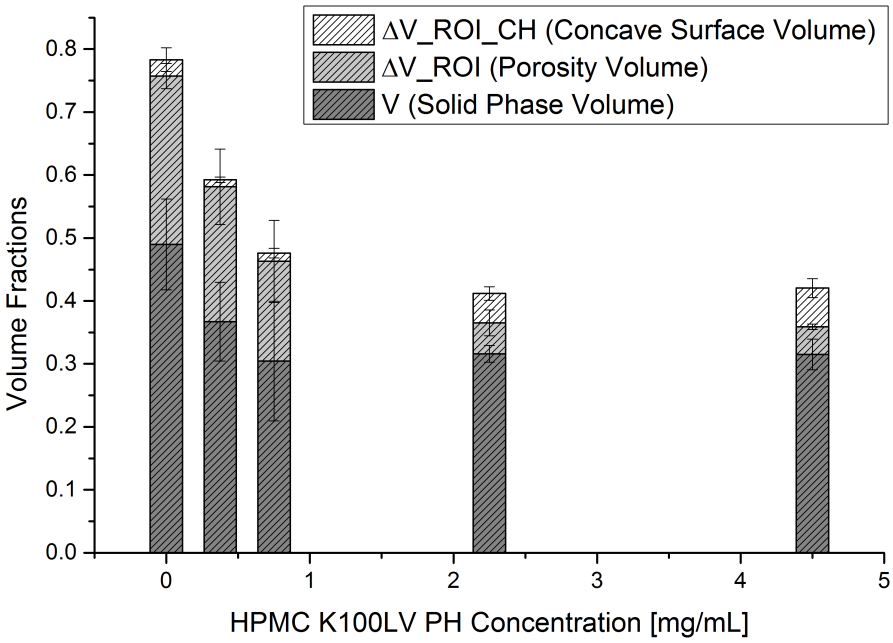

Figure 6.10: Ratios of particle solid phase volume (V), particle porosity volume (ΔV_ROI), and particle concave surface volume (ΔV_ROI_CH) for MS_0 - MS_4. All volumes are normalised to the volume of a sphere with equivalent maximum Feret diameter ($V_{eqSph,Feret}$).

concentrations of HPMC K100LV. Particles from a solution of MET and MAN without the addition of HPMC K100LV (MS_0) exhibit the smallest aspect ratio with 1.20 ± 0.05 and highest sphericity of 0.95 ± 0.04. For formulations with HPMC K100LV (MS_1 - MS_4), the aspect ratio and sphericity are in strong correlation with the amount of added HPMC K100LV. Changes in the shape are most pronounced in particles with HPMC K100LV starting concentrations of 0.75 mg/mL (MS_3) and 2.25 mg/mL (MS_4). This supports the detected increase in surface buckling for formulations with higher HPMC K100LV solid mass ratios since the generated additional particle surface and the reduced V_ROI are both directly used to calculate the particle sphericity as defined by Wadell. The high deformations and surface buckling effects of particles with HPMC K100LV solid mass ratios of 5.66 wt% and 10.71 wt% could potentially decrease particle flowability and, therefore, manufacturability in the downstream process. The implemented XRT image analysis capabilities are a valuable extension of an initial qualitative visual interpretation and offer the opportunity to quantify key particle properties including particle size, shape and internal microstructure. The evaluation of these particle descriptors showed a

strong correlation of the particle structure to its formation process monitored on the SAL. The non-destructive nature of the presented XRT methodologies enable a further assessment of the particle performance characteristics i.e. undergoing dissolution or during compaction. Whilst not explored here, these extensions of capability to 3D structure, provides a basis for future work to develop structure-property relationships.

Table 6.4: Overview of extracted shape descriptors from formulated MET particle systems MS_0 - MS_4 (n = number of particles).

Sample	n	Aspect Ratio	Sphericity
MS_0	7	1.20 ± 0.05	0.95 ± 0.04
MS_1	8	1.96 ± 0.52	0.90 ± 0.05
MS_2	3	1.93 ± 0.28	0.89 ± 0.05
MS_3	5	2.49 ± 0.35	0.80 ± 0.05
MS_4	5	2.52 ± 0.20	0.73 ± 0.03

6.4 Conclusions

The reported SAL-XRT platform allows the direct measurement of single droplet drying kinetics and the resultant particle structure as a function of solution composition. The combined characterisation links the solid formation process to a 3D quantitative investigation of the particle. The capabilities of this platform and the developed methodologies for an *in situ* characterisation have been applied to a model pharmaceutical formulation in order to investigate the effect of HPMC K100LV on the formation kinetics and final structure of formulated MET particles during droplet evaporation. The reduced molecular diffusion of HPMC K100LV compared with MET and MAN leads to a radial composition profile with increasing polymer-solute ratios towards the droplet surface that in turn lower solvent evaporation. This has implications for drying kinetic models that assume pure liquid evaporation prior to reaching LP. Specifically, particle formation kinetics are delayed with HPMC K100LV additions despite higher absolute solute starting concentrations.

For the MET system, XRT analysis shows a negative correlation between HPMC K100LV concentration and particle porosity, with the total normalised void space decreasing by 83.59% between 0 and 10.71 wt% HPMC K100LV. Near spherical and highly buckled particles are produced. The quantification of detected concave surface volumes revealed competing effects of HPMC K100LV with an impact on the particle surface. Low concentrations of HPMC K100LV lead to smoother surfaces compared to particles without the addition of polymer. For higher

HPMC K100LV levels, significant particle surface buckling is observed and quantified. The surface buckling itself may not only be related to the kinetics of the solid phase formation at LP but, furthermore, to molecular interactions that cause a partial suppression of the crystalline core. This change in the particle microstructure, its porosity, surface area and surface topology can potentially effect powder flow, compaction behaviour, dissolution and aerodynamic performance of the material.

Advanced models capable to fully describe the complex particle formation mechanisms from solution and their dynamics need to be able to connect molecular interactions and changing spatial compositions to the emerging solid phase structures during processing. Quantitative information from an experimental assessment of the particle design space can feed into a rational particle design approach for novel pharmaceutical systems targeted towards the control or optimisation of particle properties. The ultimate goal of such endeavours is to achieve desirable values for shape, porosity and/or solid phase microstructure that can deliver the optimal performance whether during subsequent downstream processes or upon ultimate delivery to the patient. This work serves as the basis of a workflow for the rapid exploration of particle formation processes. It would be desirable to extend its application towards investigating additional formulations and their impact on the final particle structure. Coupled with effective means of performance evaluation, this approach could provide an accelerated design tool for formulated particle systems and processes.

Contributions

FJSD and AJF conceived the study. FJSD developed and performed single droplet drying experiments and micro-XRT analysis. FJSD wrote the original draft of the manuscript, which was reviewed by FJSD, IDHO and AJF.

Acknowledgement

The authors would like to thank EPSRC and the Doctoral Training Centre in Continuous Manufacturing and Crystallisation (Grant Ref: EP/K503289/1) and the EPSRC Future Continuous Manufacturing and Advanced Crystallisation Research Hub (Grant Ref: EP/P006965/1) for funding this work. Iain D. H. Oswald would like to thank EPSRC for their funding (Grant Ref:

EP/N015401/1). The authors would like to acknowledge that this work was carried out in the CMAC National Facility supported by UKRPIF (UK Research Partnership Fund) award from the Higher Education Funding Council for England (HEFCE) (Grant Ref: HH13054). Data underpinning this publication are openly available from the University of Strathclyde KnowledgeBase at http://dx.doi.org/10.15129/5e63d56e-3a02-43d1-b89d-8eebaf3aae13.

7 Peptide Isolation via Spray Drying: Investigating Particle Formation and Means of Process Implementation for the Production of Spray Dried s-Glucagon Powders

Declaration: *This chapter is the result of a pre-competitive industrial collaboration between Frederik J.S. Doerr[a,b], Lee J. Burns [c], Becky Lee [d], Jeremy Hinds [c], Rebecca L. Davis-Harrison [c], Scott A. Frank [c] and Alastair J. Florence [a,b].*

Abstract: Spray drying is widely used in the pharmaceutical industry for product development of sensitive bio-pharmaceutical formulations. Process design, implementation and optimisation require in-depth knowledge of process-product interactions. Here, an integrated approach for rapid spray drying process development is presented. Single droplet drying experiments were used to investigate the particle formation process and quantify the impact of formulation parameters on the final particle morphology. Process implementation was supported by an initial characterisation of the lab-scale spray dryer assessing a range of relevant independent process variables including drying temperature and feed rate. The platform response was captured using Process Analytical Technology within a data acquisition framework recording local temperatures, exhaust gas humidity, pressure and feed rate. During process implementation, off-line product characterisation provided additional information to establish a link between selected process conditions and key product properties related to residual moisture, solid state structure, particle size/morphology and peptide fibrillation/degradation. A simplistic process model based on heat- and mass-balance considerations allowed the identification of feasible

[a] *EPSRC CMAC Future Manufacturing Research Hub, Technology and Innovation Centre, Glasgow, UK*

[b] *Strathclyde Institute of Pharmacy & Biomedical Sciences (SIPBS), University of Strathclyde, Glasgow, UK*

[c] *Eli Lilly and Company, Small Molecule Design and Development, Indianapolis, USA*

[d] *Eurofins Lancaster Laboratories PSS, Indianapolis, USA*

operating conditions successfully demonstrated for the spray drying of trehalose achieving high yields of up to 84.67 % and significantly reduced levels of residual moisture and particle agglomeration. The process was further translated to produce powders of s-glucagon and s-glucagon-trehalose formulations with yields of >83.24 %. Extensive peptide aggregation or degradation was not observed. The presented data collection strategies are part of a data-driven process development concept which can be applied to address future isolation problems on lab-scale and facilitate a systematic implementation of spray drying for the manufacturing of sensitive bio-pharmaceutical formulations.

Keywords: Spray Drying, Process Development, Process Analytical Technology, Peptide Formulation

Highlights

- Single droplet experiments in a novel multi-transducer single-axis acoustic levitator (MSAL) used to investigate particle formation of trehalose and s-glucagon.
- Spray drying: data integration and platform characterisation to guide process implementation using custom-designed Process Analytical Technology.
- Off-line product characterisation for a broad range of particle properties with a direct impact for downstream processing and product efficacy.
- Successful identification of optimised process conditions for spray drying trehalose and s-glucagon-trehalose formulations.

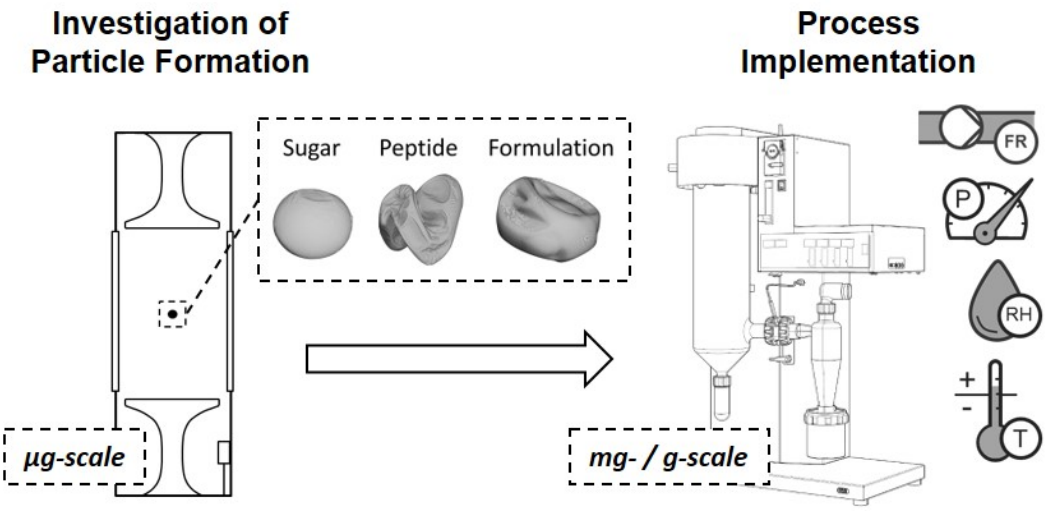

Figure 7.1: Graphical abstract Chapter 7.

7.1 Introduction

Techniques for the isolation of peptide-based systems are of increasing interest for the pharmaceutical industry to accelerate the development of novel pharmaceutical peptide products [308, 309]. Freeze drying and spray drying are often first methods of choice for the solidification of unstable or sensitive bio-pharmaceutical formulations. Freeze-drying usually falls behind in terms of productivity and costs in direct comparison to spray drying, which is a rapid drying process with capabilities for high product throughput and which can be employed as a continuous drying process [3]. In developing a spray drying process, conditions must be controlled to avoid risks for the material that can include thermal damage due to exposure to excessive drying temperatures or mechanical damage caused by shear stress during the pumping of the liquid feed and atomisation at the spray nozzle. Despite these process risks, the rapid drying kinetics and the evaporative cooling effect allow the processing of heat sensitive materials. Spray drying has been successfully utilised for the production of novel bio-pharmaceutical formulations containing peptides, proteins and related heat-sensitive bio-pharmaceutical products [126, 310, 311, 312, 313, 147]. For particle engineering applications, spray drying further enables the direct control of product properties including residual moisture as well as particle size and shape, important for stability and performance [314]. Spray drying of peptide-based systems typically includes the use of stabilizers to protect against peptide denaturation during production and to improve storage stability. Carbohydrates are often employed as excipients for

peptide-based systems as they can preserve the protein's active conformation via preferential exclusion, water replacement and glass immobilization mechanism [315, 316, 317, 318, 319]. On a lab-scale, available drying times are often limited due to short residence times, which require high liquid atomisation rates and/or high drying temperatures. The selected drying conditions have to balance the risk of peptide damage and achieving a stable dry particle state. A design-of-experiment (DoE) approach is often used in order to assess and identify suitable process conditions [131, 111, 313, 320, 132]. However, a full-factorial design of relevant accessible process parameter is material and time intensive. The process implementation can be assisted using modelling approaches in order to identify most promising or adverse process regimes. Spray drying models can be based on empirical correlations between selected, independent process variables and measured product properties or derived from first-principles [321, 120, 322]. In both cases, experimental data are imperative to quantify process-product dependencies or for model validation. The employment of purely data-driven, machine learning models for spray drying process optimisation further intensifies the need for a systematic and standardized approach of experimental data collection [323, 324].

Process Analytical Technologies (PAT) are means to analyse, monitor and control pharmaceutical manufacturing processes. Their use is highlighted by regulatory agencies encouraging manufacturers to integrate PAT during process implementation [129]. The use of PAT has been demonstrated in spray drying to measure conditions of the drying gas in regards to temperature and humidity levels e.g. using thermo-hygrometers or capture information on particle properties such as their size distribution with in-line laser diffraction [325, 137, 326]. Despite its utility, PAT is often not considered for lab-scale applications, relying solely on a offline characterisation of the product.

Single droplet drying experiments (SDD) have been used to investigate the drying and solidification of novel compound systems whilst working on a single droplet scale. A popular containerless platform to perform SDD experiments is acoustic levitation [7, 102, 12, 101, 103]. Despite comparatively large droplet sizes and reduced drying kinetics, information on droplet evaporation and particle formation can be utilised to inform spray drying models and support process development [327, 107]. Applications of acoustic levitation in combination with micro-X-ray tomography (micro-XRT) aim for a better understanding of the particle formation process linking formulation parameters and the observed drying kinetics to the final particle morphology

and internal micro-structure. In this context, the use of micro-XRT allows the non-destructive extraction of relevant quantitative descriptors on particle size, shape and porosity [7].

Here we report the successful implementation of a spray drying process for the isolation of a peptide-based model system containing s-glucagon (GLUC). GLUC was selected as a model peptide with well-documented aggregation pathways [328, 329, 330, 331]. The experimental strategy consists of single droplet drying (SDD) experiments, a spray drying platform characterisation and the final process implementation. SDD experiments and micro-XRT were used to investigate particle formation linking formulation parameters to the final particle structure and morphology. Moving towards the spray drying platform, an inexpensive, commercially available, integrated gas sensor with an in-house designed and 3D printed sensor-mount was employed as a novel PAT in order to enable in-line analysis of the exhaust gas, measuring local temperature, relative humidity and absolute pressure. The collected information was used to characterise the spray dryer and validate accessible drying conditions identified within a process model based on considerations around heat- and mass-balance for the system. Trehalose (TRE) is a common stabilizing excipient in peptide-based systems [147, 332] and was used to produce formulated GLUC-powders. Primary objective for a successful process implementation was a high product recovery of active peptide material.

7.2 Materials and methods

7.2.1 Chemicals

7.2.1.1 Trehalose

TRE is a disaccharide comprising two glucose molecules with an alpha-alpha (1,1) glycosidic bond. It is a non-reducing sugar inhibiting reactions with amino acids in a Maillard reaction [333]. For spray drying, TRE is generally preferred over sucrose as it has a higher glass transition temperature (T_g) of 115°C compared to T_g of 74 °C for sucrose [334]. TRE is commercially available as a crystalline dihydrate. Its structure is shown in Fig. 7.2.

D-(+)-Trehalose dihydrate (TRE-h) was purchased from Sigma-Aldrich (Lot #SLBR1467V, St. Louis, United States). For spray drying, TRE-h was dissolved in mixtures of deionised (DI)-water and ethanol with varying solvent ratio of 100:0 v/v, 99:1 v/v and 50:50 v/v with a final TRE concentration of 30 mg/mL. A total volume of 100 mL was freshly prepared before each

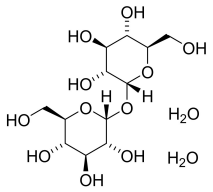

Figure 7.2: Molecular Structure of D-(+)-Trehalose dihydrate.

experiment. Details on the TRE solutions are listed in Table A11 (Appendix, page A25).

7.2.1.2 s-Glucagon

GLUC is a single-chain polypeptide that contains 29 amino acids [335]. It is a commercial pharmaceutical hormone used against insulin-induced hypoglycemia [336]. The amino acid sequence is presented below and has an isoelectric point (IEP) of 7.21 [337]. Various groups have investigated the aggregation of GLUC in acidic and alkaline conditions identifying a complex aggregation mechanism and kinetics related to various factors including pH, concentration, temperature and hydrodynamics [328, 329, 330, 331]. The hydration of peptides or larger proteins affect their folding, stability, dynamics and function [338]. Organic solvents such as ethanol can act as chaotropic agents disrupting the hydrogen bonding network of the peptide hydration shell and furthermore, weakening hydrophobic intra-molecular interactions [339, 340, 341]. This can lead to a chaotropic solvational behaviour inhibiting ordered fibril formation of proteins, as observed for insulin at ethanol-concentrations of more than 10 wt.% [342, 343].

Amino Acid Sequence: His-Ser-Gln-Gly-Thr-Phe-Thr-Ser-Asp-Tyr-Ser-Lys-Tyr-Leu-Asp-Ser-Arg-Arg-Ala-Gln-Asp-Phe-Val-Gln-Trp-Leu-Met-Asn-Thr

Synthesized and freeze-dried GLUC was sourced from Bachem (Lot #1056459, Switzerland). Solutions of GLUC were freshly prepared for each experiment. For the solution ethanol was added to 0.05 N hydrochloric acid with a final ethanol ratio of 0 v/v%, 1 v/v% and 50 v/v%, respectively. A 1 v/v% ethanol solvent ratio aimed to identify potential inter-molecular effects for the peptide stabilisation during particle formation. In comparison, 50 v/v% ethanol solvent ratios are expected to have an additional impact on process conditions including droplet atomisation characteristics and evaporation kinetics. Details on the prepared feed compositions are

listed in Table A11 (Appendix, page A25).

7.2.2 Single droplet drying experiments

SDD experiments were performed with a Multi-emitter Single-axis Acoustic Levitator (MSAL). The levitator geometry was developed by Marzo *et al.* [193] and re-designed to function as an integrated characterisation platform for SDD experiments. This includes image acquisition/analysis capabilities and the implementation of a gas sensor to measure local temperature, humidity and pressure levels. The MSAL gas inlet was connected to a system from Okalab (Naples, Italy) providing a controlled dry nitrogen flow of 0.8 L/min, which was diffused over the back of the upper transducer plate. A schematic of the experimental setup is shown in Fig. 7.3. The droplet evaporation and solidification was recorded with a Fastcam SA1.1 high speed camera (Photron, Tokyo, Japan). The relative humidity, ambient temperature and absolute pressure were constantly monitored and recorded using a pre-calibrated BME280 environmental sensor (Bosch Sensortec GmbH, Germany). The recorded relative humidity in all experiments was less than 3.5 %RH with an average recorded gas temperature in the enclosure of 34.66 ± 0.51 °C. Solutions of TRE ($c_{0,\mathrm{TRE}} = 30$ mg/mL), GLUC ($c_{0,\mathrm{GLUC}} = 5$ mg/mL) and a GLUC-TRE formulation ($c_{0,\mathrm{TRE}} = 30$ mg/mL, $c_{0,\mathrm{GLUC}} = 5$ mg/mL) were prepared for SDD experiments, which are included in Table A11 (Appendix, page A25). Droplets with a volume of 5.05 ± 1.63 μl were manually suspended within the central pressure node using a Research plus 20 μl micropipette (Eppendorf,Hamburg, Germany). Image data of the SDD experiments were processed and analysed to track the droplet drying stages and determine the lock point (LP). The image analysis routine is described in details in Chapter 6.2.2.

The structure of the dried particles was further investigated using micro-X-ray tomography. The particles were scanned with a Skyscanner 2211 X-ray tomograph (NanoCT, Bruker, Kontich, Belgium) in a cone-beam arrangement. The samples were scanned with an image pixel size of 0.8 μm, frame averaging of 8 and a rotation step size of 0.2°. The X-ray acceleration voltage was 40 keV. A reference scan was collected at the end of each run to enable post-alignment and therefore, compensate for potential shifts during the scan. Image reconstruction included beam hardening corrections and ring artefact reduction, which was performed using NRecon with InstaRecon (version 1.7.1.6, Bruker, Kontich, Belgium). The image stacks were visualised with CTVox (version 3.2.0, Bruker, Kontich, Belgium). Image processing and analysis allowed

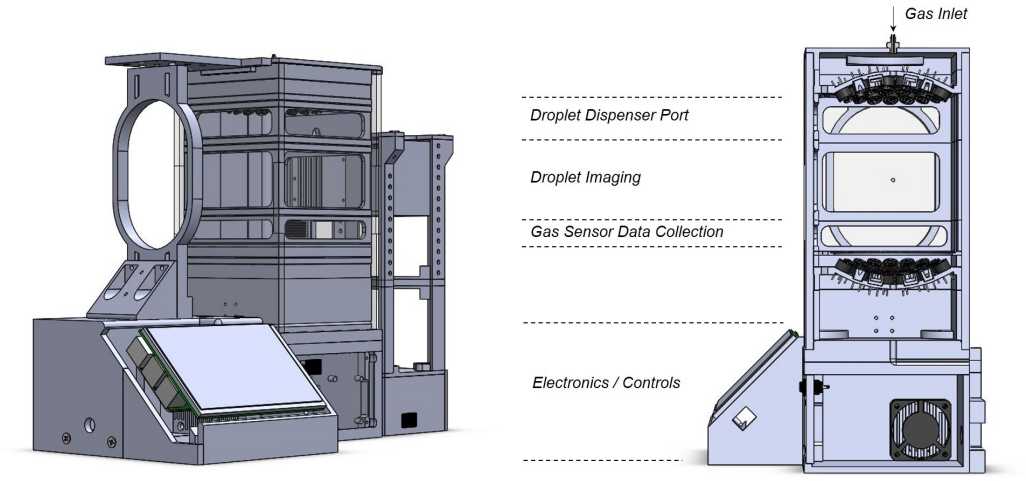

Figure 7.3: Acoutic Levitation Setup (MSAL) used to investigate particle formation of peptide-based systems from single droplet drying experiments. The system includes capabilities for image acquistion to monitor the drying process and for an analysis of the drying gas to record local temperature, humidity and pressure.

a qualitative assessment of the particle size, morphology and internal micro-structure.

7.2.3 Spray drying

7.2.3.1 Spray-drying procedure

Spray drying experiments were performed using a lab-scale B-290 Mini-Spray Dryer (Büchi Labortechnik, Switzerland) in open mode configuration. The equipment set-up is shown in Fig. 7.4. The feed was atomised using a two-fluid nozzle with cap orifice diameter of 0.7 mm (Fig. 7.4-P3). The nozzle was constantly cooled with a circulating flow from a F-25 (JULABO GmbH, Germany) set to 10 °C (Fig. 7.4-P12). A *high performance* cyclone (Büchi Labortechnik, Switzerland, Fig. 7.4-P6) was employed for product recovery. The cyclone was wired with copper and grounded to reduce potential electrostatic charges building up during the solid/gas separation process, aiming to further improve product recovery, hence maximising the overall process yield. The outlet fine particle filter (Fig. 7.4-P8) was equipped with a PTFE membrane to allow the potential recovery of particle fines smaller than ~ 2 μm.

Each spray drying experiment can be divided in a *Dry Air* phase (DAP) to characterise the air pushed through the open loop system, a *Pure Solvent* phase (PSP) to allow system equilibration in the presence of evaporating solvent, a *Production* phase (PrP) for the spray drying of the sample solution and an instrument *Shut-down* phase (S) prior to the disassembly and cleaning of all relevant glassware. An example of all experimental stages and their impact on the collected process variables is shown in Fig. 7.5. The PSP for each experiment was >30 minutes until steady state conditions were reached. Detailed information on the performed experiments are listed in Table A11.

The process yields were calculated using Equation 7.1 and are compensated against the residual moisture as determined with TG-MS (see Section 7.2.4.1).

$$\text{Yield [\%]} = \frac{\text{Product [mg]} \cdot \ (1 - \text{TG-MS RM}_{180}\ \text{[wt\%]})}{\text{Solute Concentration Feed [mg/mL]} \cdot \ \text{Spray Dried Feed [mL]}} \tag{7.1}$$

7.2.3.2 Process Data Integration

A gas sensor (BME680, Bosch Sensortec GmbH, Germany) was used to monitor and record temperature ($T_{P9,R}$), relative humidity ($RH_{P9,R}$), absolute pressure ($p_{P9,R}$) and volatile organic solvents ($VOC_{P9,R}$, non-calibrated) levels in the exhaust air. The sensor mount was custom-

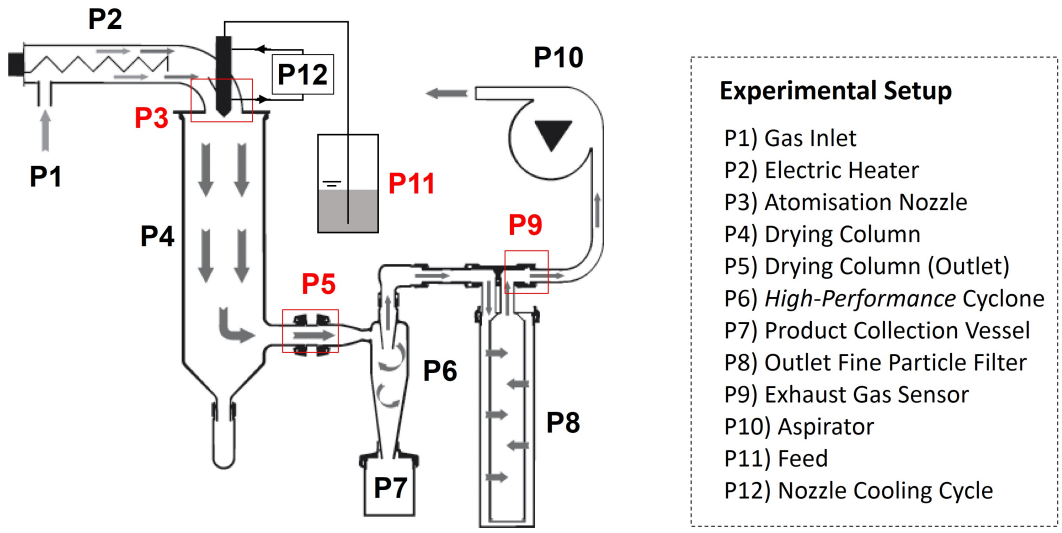

Figure 7.4: Experimental setup of the lab-scale spray dryer (Type: B290, Büchi Labortechnik) in open loop configuration. Red markers indicate locations of process data collection. Figure adapted from Operation Manual - Mini Spray Dryer B-290 [127].

designed for the B290 mini-spray dryer and 3D printed using a polyjet printer (Stratasys, United States, material: Vero Black Plus RGD875). The integrated piece for in-line exhaust gas analysis was installed in the gas stream after the B290 fine particle filter (Fig. 7.4-P9). Additional process information from the B290 spray-dryer were readily available via its RS232 serial interface and included selected set points (e.g. drying temperature $T_{P3,S}$, pump speed, aspirator speed) as well as measured local temperature information at the gas inlet ($T_{P3,R}$, Fig. 7.4-P3) and exiting the drying chamber ($T_{P5,R}$, Fig. 7.4-P5). Information on the feed rate were recorded gravimetrically from the RS232 serial interface of a XS60002S balance (Mettler Toledo, Switzerland, Fig. 7.4-P11). An overview of the implemented capabilities and a representative example of the collected dataset for each spray drying experiment is presented in Fig. 7.5.

7.2.3.3 Post-Drying of spray dried powders

Vacuum drying was assessed as a secondary drying step for the produced spray dried powders to further reduce residual moisture levels. Powder samples of 30 - 50 mg were transferred in HPLC vials and placed in a vacuum drying oven at 50 °C and 20 mbar. The samples were weighed periodically until the weight reached a stable end-value, which was observed after a maximum of approximately 320 hours. Information of this gravimetric analysis also allowed a direct comparison of the results with the residual moisture values measured using TG-MS (see Section 7.2.4.1).

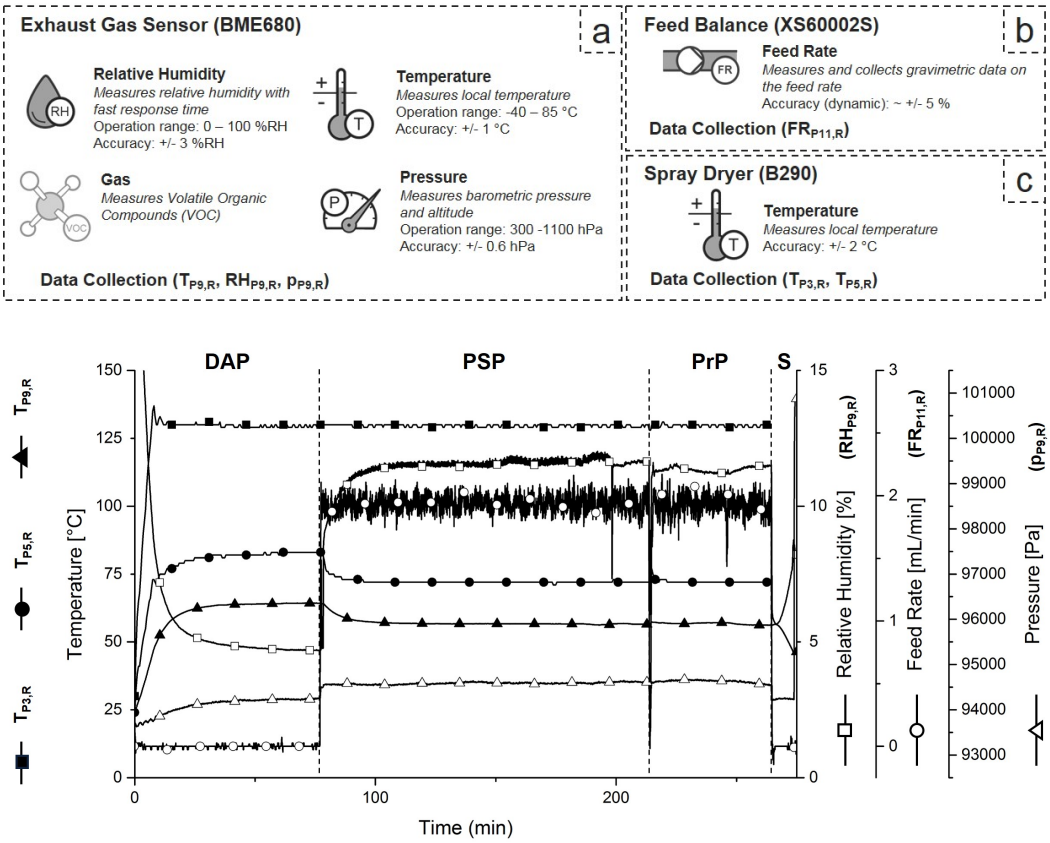

Figure 7.5: Visualisation of the data integration approach with details on the process parameters monitored and recorded during each spray drying experiment from (a) an implemented exhaust gas sensor, (b) a feed balance and (c) the B290 spray dryer. The plot contains information on local temperatures (—■— $T_{P3,R}$, —●— $T_{P5,S}$, —▲— $T_{P9,R}$), relative humidity (—□— $RH_{P9,R}$), local pressure (—△— $p_{P9,R}$) and feed rate (—○— $FR_{P11,R}$). All phases during the lab-scale spray drying process are described in more detail in Section 7.2.3.1. Additional information on the local concentration of volatile organic compounds (VOC) in the exhaust gas were recorded, but are omitted here.

7.2.4 Spray dried powder characterisation

7.2.4.1 Residual moisture and solid state structure

Thermogravimetric Analysis - Mass Spectrometry (TG-MS): TG-MS was used to quantify the residual moisture of the spray dried products and identify residual solvents. For the TG-MS analysis a TGA Q5000 (TA Instruments, United States) was connected to an ThermoStar GSD 301 T3 (Pfeiffer Vacuum, Germany). Powder samples were heated to 200 °C at a heating rate of 10 K/min. Mass spectra of the exhaust gas were recorded and evaluated for changes in the ion currents that are linked to evaporating solvents including m/z 18 (water, H_2O^+) and m/z 31

or m/z 45 (ethanol, CH_3O^+, $CH_3CH_2O^+$) [344].

Differential Scanning Calorimetry (DSC): A *Discovery DSC* (TA Instruments, United States) was employed to evaluate product melting, dehydration/desolvation or glass transition temperatures for the produced TRE powders. For each sample, 2 - 8 mg of material were transferred to two aluminium pans, *T-Zero* and crimped *Hermetic* pan (TA Instruments, United States). The pans were heated to 200 °C at a heating rate of 10 K/min. The glass transition temperature (T_G) was determined with Trios V4.0 (TA Instruments, United States).

Powder X-ray Diffraction (XRPD): XRPD was used to test all samples for potential crystallinity. The XRPD data were collected with a D4 Endeavor (Bruker Corporation, United States) at room temperature. X-rays were generated from a copper source (Cu Kα 35 KV x 50 mA). A VÅNTEC detector collected scattered light in a range between 4 – 30 ° (step size 0.016 °, integration time 1 sec). Approximately 15 - 25 mg of the powder samples were transferred to quartz specimen holders and levelled using a glass slide. Crystallinity in the powders was assessed qualitatively from the collected powder diffraction patterns.

7.2.4.2 Particle size and morphology

Scanning Electron Microscopy (SEM): Electron micrographs were collected using a Teneo SEM (ThermoFisher Scientific) under low vacuum conditions of 0.4 mbar, using a large field detector, 10 kV accelerating voltage, 0.1 nA and a working distance of 10 mm. For preparation, spray dried powder samples were fixed on aluminum stubs with adhesive carbon discs. The samples were sputter coated for 90 seconds with 60:40 gold:palladium in a EMS575X sputter coater (Electron Microscopy Sciences) with a final coating thickness of approximately 18 nm.

Laser Diffraction (LD): The particle size distribution (PSD) was evaluated with laser diffraction using a Mastersizer 2000 (Malvern Panalytical Ltd, United Kingdom) equipped with a wet dispersion unit *Hydro 2000S* (Malvern Instruments Ltd, United Kingdom). The PSD was calculated using Fraunhofer-theory (dispersant refractive index 1.38). Samples were suspended in Hexane with 0.1 v/v Span80 and vortexed for 30 seconds prior to the initial measurement. Subsequent measurements were performed in triplicates in order to assess potential particle deagglomeration / attrition during stirring (speed 2100 rpm). In order to further assess and com-

pare the potential presence and strength of particle aggregates in all samples, the suspensions were exposed to ultrasound (100%), which was applied for 30 seconds between measurements-triplicates. The LD de-agglomeration procedure with ultrasound was repeated twice (R_0: no ultrasound, R_2: 2 x 30sec ultrasound).

7.2.4.3 Peptide fibrillation and degradation

Thioflavin T Assay: The Thioflavin T (ThT) assay enables the measurement of relative changes in the fluorescence intensity of ThT upon binding to amyloid fibrils [345, 346, 347]. It can be used as part of a high-throughput method to monitor amyloid fibril formation kinetics, which allows a semi-quantitative characterisation of the aggregation kinetics for GLUC. The chemical structure of ThT is shown in Fig. 7.6. Upon binding to amyloid fibrils, the two rotational planes of both, the benzylamine and a benzathiole ring, become immobilized, which maintains the excited state of the molecule. The ThT staining efficiency depends on fibril type. The fluorescence signal is most intense for protofilament fibrils and twisted mature fibrils [346].

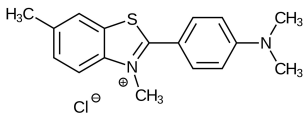

Figure 7.6: Molecular Structure of Thioflavin T with its two rotational planes, a benzylamine and a benzathiole ring.

For the ThT Assay, powder samples were dissolved in 0.05 N hydrochloric acid and immediately transferred to a 96 multi-well plate format (MTP). The assay aimed to gather information on the potential fibrillation kinetics in the feed with increasing ethanol solvent fractions of 0.00 v/v (S1), 0.01 v/v (S2), 0.10 v/v (S3), 0.25 v/v (S4) and 0.50 v/v (S5), respectively. The ethanol was added to the aqueous GLUC solution to reach a solute concentrations of 1 mg/mL (C1), 5 mg/mL (C2) and 15 mg/mL (C3), respectively and allowed an assessment of the impact of increasing GLUC concentrations. In total, the solution in each MTP-well had a volume of 100 μl with a ThT concentration of 4 μM. The MTP was covered with a MTP-sealing tape to avoid sample evaporation. The MTP was scanned every 10 minutes for 24 hours in a fluorescence plate reader SpectraMax i3x (Molecular Devices, Unites States) with an excitation wavelength of 450 nm and a collected emission wavelength of 480 nm. Prior to each reading cycle, the plate was shook for 3 seconds. The signal is directly compared to a solvent blank to detect onset and

growth kinetics.

High Performance Liquid Chromatography (HPLC): HPLC analysis was performed in order to acquire semi-quantitative information on the level of GLUC aggregation and peptide degradation within the spray dried GLUC samples. The analysis was performed using two methods for purity and potency determination, which aimed to quantify impurities or degradation products and the absolute concentration of GLUC in the samples, respectively. *Impurity Method*: ACE3 C18 column (4.6 x 150 mm, 3.0 micron particle size) with a mobile phase of a 150 mM KH_2PO_4 buffer and Acetonitrile (mobile phase A: 80/20 buffer/ACN, mobile phase B: 60/40 H_2O/ACN). The 150 mM KH_2PO_4 buffer was adjusted with H_3PO_4 to pH 2.7. *Potency Method*: Phenomenex Aeris PEPTIDE XB-C18 (3.0 x 150 mm, 2.6 micron particle size) with a mobile phase A: 80/20 buffer/ACN, mobile phase B: 60/40 H_2O/ACN. A pre-filtration step with a 0.22 μm PTFE filter aimed to hold back larger GLUC aggregates before diluting the solution in a 80/20 buffer/ACN stock solution to a concentration of 0.6 mg/mL. HPLC samples were collected to evaluate semi-quantitatively the potential impact of process time (pF = feed sample experiment start, pP = feed sample experiment end), the aggregation and the potential degradation of GLUC after spray drying (P) and after secondary drying (VacDry). Details on the HPLC analysis including the mobile phase gradient is provided in Fig. A14 (Appendix, page A31) and Fig. A13 (Appendix, page A31) for the impurity and the potency assay, respectively.

7.3 Results and discussion

7.3.1 Single droplet drying experiments

SDD experiments were conducted with subsequent X-ray tomography to investigate the particle formation process, drying behaviour and final particle morphologies of solution-droplets containing TRE and/or GLUC. Details of the SDD experiments including the drying curves are presented in Fig. A15 (ESI, page A32). Fig. 7.7 shows the morphologies of particles collected from the MSAL system with quantified morphological descriptors of particle sphericity (ψ_{gl,V_ROI}) and solidity (SV). TRE and GLUC particles exhibit distinct morphological characteristics. TRE particles are dense and spherical (Fig. 7.7a). GLUC particles are highly buckled (Fig. 7.7b). The formulation of both compounds (Fig. 7.7c) demonstrates that part of the surface buckling presented for GLUC-particles can be compensated with the addition of TRE. Formulated GLUC particles further exhibit internal porosities not present in pure TRE or GLUC particles.

The particle morphologies align qualitatively with expected morphologies following a diffusion-dominated particle formation mechanism. The *Lock Point* (LP) during the droplet evaporation process is defined as the moment when the local concentration on the droplet surface (c_s) reaches a critical value and a solid phase emerges from solution and was determined using image analysis as described in Section 6.2.2. The Péclet number (*Pe*, Equation 7.2) describes the relation between the diffusion of the solute (D_s) and the receding droplet surface expressed through the liquid evaporation rate (κ). *Pe* directly impacts the surface enrichment of the solute (E), which is the ratio between c_s and the mean solute concentration in the droplet (c_m) and can be estimated using Equation 7.3, assuming steady-state evaporation in accordance with d2-law (see Section 1.1.3.1) and for *Pe* below 20 [19, 20]. For similar liquid evaporation rates (κ), the difference in the diffusion coefficients (D_s) of TRE and GLUC leads to changing levels of surface enrichment, which correlates with the ability of the solutes to compensate their radial concentration profiles between the droplet center and its receding surface. In general, a $Pe \leq 1$ leads to a flat radial concentration profile and dense, round particles as observed for TRE ($D_{\mathrm{TRE}} > \kappa_{\mathrm{SDD}}$). $Pe \gg 1$ results in a non-linear increase of the radial concentration profile towards the droplet surface. For $Pe \geq 10$, this can cause early skin formation with subsequent

particle buckling as observed for GLUC ($D_{\mathrm{GLUC}} < \kappa_{\mathrm{SDD}}$).

Understanding the particle formation mechanism helps to interpret the impact of formulation and process parameters on the final particles [7]. Molecular interactions between different solutes leading to solubilization (e.g. hydrotropes), a low solubility of individual compounds or a high surface activity can lead to significant deviations from the diffusion-dominated particle formation mechanism emphasising the importance of small-scale droplet drying experiments [57, 287].

$$Pe = \frac{\kappa}{8 \cdot D_s} \tag{7.2}$$

$$E = \frac{c_s}{c_m} \approx 1 + \frac{Pe}{5} + \frac{Pe^2}{100} + \frac{Pe^3}{4000} \tag{7.3}$$

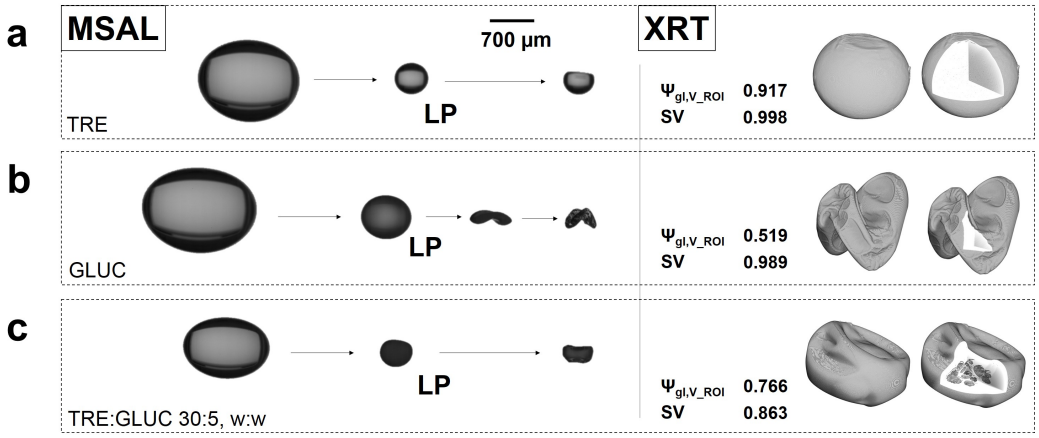

Figure 7.7: Particle morphologies of (a) TRE, (b) GLUC and (c) a formulation of GLUC:TRE (5:30, w/w) as collected from the MSAL system and analysed using XRT. The particle models from the XRT analysis reveal their internal micro-structure and allow a quantification of particle sphericity (ψ_{gl,V_ROI}) and solidity (SV). TRE particles are dense and spherical. Dried GLUC particles are highly buckled. The GLUC-TRE formulation shows a morphology intermediate between the two extremes and exhibits internal porosities.

7.3.2 Spray drying - process implementation

Following the SDD experiments, the process implementation on a lab-scale spray dryer is described in the following section and can be divided into three distinct steps: (1) the characterisation of the spray drying platform aiming to identify process regions with feasible drying conditions (Section 7.3.2.1), (2) the use of TRE as a potential excipient for peptide formulations

and to validate the process model (Section 7.3.2.2). (3) The translation of identified process conditions for the isolation of GLUC via spray drying (Section 7.3.2.3).

7.3.2.1 Spray drying - system characterisation

The B-290 Mini-Spray Dryer was initially characterised to identify suitable conditions for stable process operation and support subsequent process implementation. *Dry air* (DAP) and *pure solvent* runs (PSP) were conducted with water-ethanol mixtures of up to 50 v/v% organic solvent ratio. Data integration as described in Section 7.2.3.2 allowed the monitoring and recording of independent process variables such as feed rate ($FR_{P11,S}$) and selected drying temperature ($T_{P3,S}$), as well as various dependent process variables including local temperatures ($T_{P3,R}$, $T_{P5,R}$, $T_{P9,R}$), relative humidity level ($RH_{P9,R}$) and absolute pressure ($p_{P9,R}$). An example dataset for assessing the response of the spray dryer at various drying temperature set-points ($T_{P3,S}$) is provided in Fig. A9 (Appendix, page A28). An overview of the sensor positions within the spray dryer is shown in Fig. 7.4. The presented data is subject to errors related to the accuracy of these inline measurements. Details on the sensor accuracies as supplied by the manufacturers are included in Fig. 7.5.

Relative humidity response surface: The steady-state conditions for combinations of process variables were utilised to construct a quadratic response surface of $RH_{P9,R}$ as function of $FR_{P11,R}$ and $T_{P3,R}$. The response surface is shown in Fig. 7.8a. PSP with insufficient drying conditions at increasing $FR_{P11,R}$ and/or decreasing $T_{P3,R}$ are marked in red and were excluded from the quadratic fitting approach. Insufficient drying conditions resulted in visible depositions of droplet on the wall within the top section of the drying column in direct proximity to the atomisation nozzle and/or through condensation in the cyclone. The critical operation zone (Fig. 7.8a, - - - -) was defined between the iso-levels of recorded minimum and maximum $RH_{P9,R}$ with insufficient and sufficient drying conditions, respectively. Back-projected on the response surface for $RH_{P9,R}$, the critical zone for process operation lies between 57.64%RH (max-passed) and 63.72%RH (min-failed). Relative humidity is defined as the ratio of the partial vapour pressure of water in relation to its temperature-dependent saturation vapour pressure. Its local gradient is the main driver for liquid evaporation and drying. Therefore, $RH_{P9,R}$ is not only a measure for the capacity of the drying gas to absorb additional moisture, but is also a direct indicator to

evaluate the kinetics of the vaporization. Droplet accumulation in the drying chamber at $RH_{P9,R}$ > 64.78%RH suggests that the droplet drying on the lab-scale spray dryer is mainly kinetically limited due to reduced evaporation rates at high levels of relative humidity. Information on $RH_{P9,R}$ can be utilised to optimise the spray drying process in terms of residual moisture levels, critical particle attributes and overall process economics [325]. Higher liquid atomization could be used to increase the specific surface area of the droplets and further enhance liquid evaporation kinetics, which might further extend the identified zone for feasible process operation towards higher $RH_{P9,R}$ levels. However, for this application, higher liquid atomisation was excluded to avoid risks of excessive fine production at low solute concentrations below 5 wt% (see Section 7.3.2.2).

Energy balance: Fig. 7.8b further visualises measured temperature levels in the B-290 Mini-Spray Dryer for $T_{P3,S}$ between 40 °C and 130 °C and $FR_{P11,R}$ of pure DI-water between 1.86 mL/min and 5.50 mL/min. The temperature reduction due to evaporative cooling was directly calculated from the difference between $T_{P5,R,0}$ during DAP ($FR_{P11,R} = 0$ mL/min) and during PSP ($T_{P5,R}$) deconvoluting heat consumption for liquid vaporization and heat loss over the length of the drying column. For a $FR_{P11,R}$ of 1.86 mL/min, the temperature decreases by 11.66 ± 0.46 °C due to evaporative cooling (Fig. 7.8b, marked in red), which remains almost constant over the investigated range of $T_{P3,S}$ indicating rapid droplet evaporation in proximity of the atomisation nozzle. In contrast, heat loss occurs over a longer time-scale along the length of the drying chamber. Temperature differences between $T_{P3,R}$ and $T_{P5,R,0}$ can be observed for increasing $T_{P3,S}$ caused by significant heat-loss through the drying column due to thermal conduction and emission of the non-jacketed glassware. Insulation of the drying column would reduce overall thermal losses and significantly improve the thermal control for this system. At a $T_{P3,S}$ of 40 °C and a $FR_{P11,R}$ of 1.86 mL/min, the data shows a reversed heat-flow from the outside environment to the drying gas due to extensive evaporative cooling with a measured $T_{P5,R}$ of 20.00 °C below the recorded levels of $T_{P9,R}$ (24.39 °C).

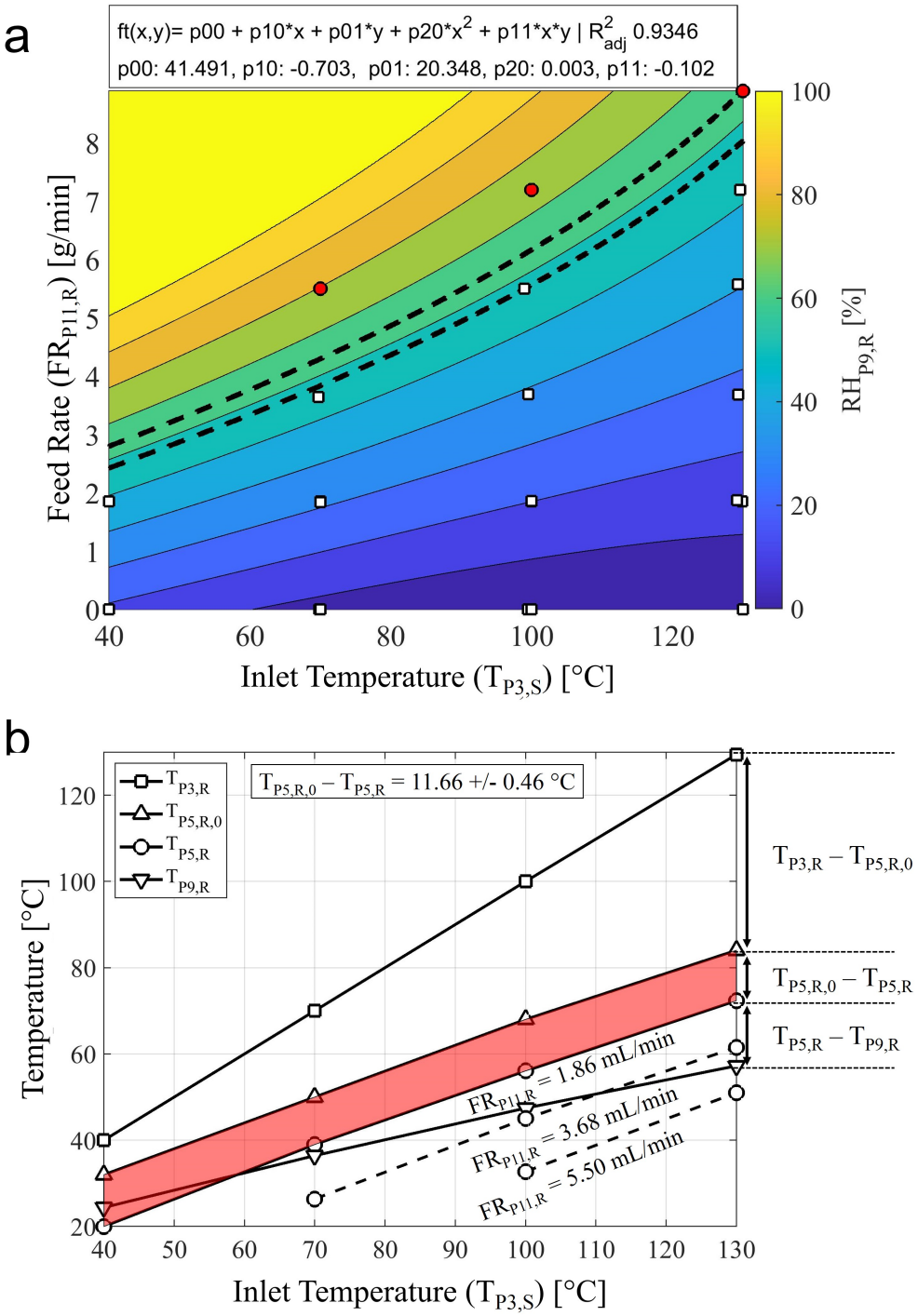

Figure 7.8: B290 spray dryer system characterisation: (a) response surface of the measured relative humidity of the exhaust air ($RH_{P9,R}$) as a function of selected drying temperatures ($T_{P3,S}$) and recorded feed rates ($FR_{P11,R}$). Process parameters with insufficient drying conditions fore pure water are marked in red. The results identified a critical operation zone (- - - -) between iso-level of $RH_{P9,R}$ 57.64%RH - 63.72%RH. (b) Basic thermal assessment for selected temperatures between 40 °C and 130 °C. Heat-loss due to evaporative cooling ($T_{P5,R,0}$ - $T_{P5,R}$) was 11.66 ± 0.46 °C independent of the selected $T_{P3,S}$. Additional heat-loss through heat emissions via the drying column ($T_{P3,R}$ - $T_{P5,R,0}$) increases linearly with increasing $T_{P3,S}$.

Identification of feasible process conditions: Measured dependent process variables of the PSP dataset were exploited to pre-inform potential conditions for operation. A simplistic approach for the identification and selection of suitable operating conditions focuses on considerations around product manufacturability related to the material's cohesion and adhesion referred to as stickiness, often apparent for sugar-rich materials [3, 125]. Material stickiness can lead to losses due to wall-depositions of particles within the spray dryer. The stickiness of particles containing amorphous sugars is related to the difference in the local temperature (T_{db}, dry bulb temperature) from the glass transition temperature (T_g) of the material. In general, the sticky point temperature is defined at $T_{db} - T_g$ = 10 - 20 °C [348, 349] and is a function of both, T_{db} and the relative humidity, which can have a significant impact on T_g [350]. Moisture acts as a plasticizer lowering the glass transition temperature of the material. Thus, a correlation between the relative humidity levels and the material's moisture uptake is needed to predict product stickiness within the spray dryer. Collected literature data for water sorption isotherms of amorphous TRE are shown in Fig. A10 (Appendix, page A29). The glass transition temperatures of amorphous TRE (mass fraction w_{TRE}) with changing residual moisture levels (mass fraction w_w) can be estimated using the Gordon-Taylor equation (GT, Equation 7.4) [351].

$$T_g = \frac{w_{TRE} \cdot T_{g,TRE} + K \cdot w_w \cdot T_{g,w}}{w_{TRE} + K \cdot w_w} \tag{7.4}$$

The GT-fit for the binary TRE-water system using Equation 7.4 with reported T_g values of water ($T_{g,w}$ = 136 K [352]) and TRE ($T_{g,TRE}$ = 389 K [334]) yields a GT-constant (K) of 6.04 (GT-fit details provided in Fig. A11 (Appendix, page A30)). K lies between other published values for the TRE-water system ranging from 5.20 - 7.90 depending on differences in the selected $T_{g,w}$ and $T_{g,TRE}$ [352, 353, 124].

Fig. 7.9 shows the calculated stickiness curve using predicted T_g values of the TRE-water system within a psychrometric chart providing a simplistic spray dryer model to identify suitable process conditions. The graph further includes estimated steady-state conditions within the spray dryer (P1-P9, see Fig. 7.4) for two selected drying temperatures, $T_{P3,S}$ of 70 °C (Fig. 7.9, —□—) and 130 °C (Fig. 7.9, —■—), respectively. The temperature in P4 was estimated considering only the evaporative cooling effect whilst additional heat loss over the drying chamber wall occurs between P4 and P5 (slower heat conduction as discussed in

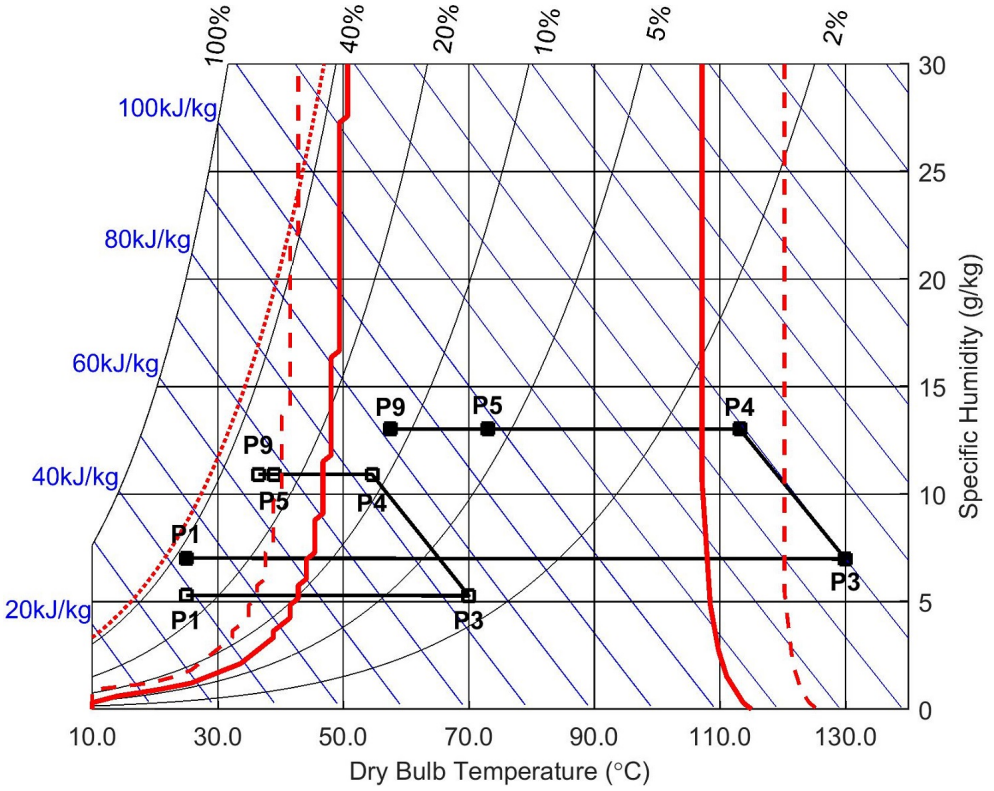

Figure 7.9: Psychrometric chart with the theoretically derived stickiness curve for the TRE-water system (——— $T_{db} = T_g$, − − − $T_{db} = T_g + 10K$). Risk for TRE-h nucleation above RH = 44% (·····). $T_{P3,S}$ 70 °C (—□—) and 130 °C (—■—) operate at distinct positions in relation to the stickiness curve.

Energy balance). The specific humidity in P3 - P5 was derived from measurements of the ambient air (P1) and the exhaust gas (P9). Details are provided in Section A4.1 (Appendix, page A22). The process model suggests distinct performances for both drying temperatures. $T_{P3,S}$ of 70 °C passes over the critical $T_{db} = T_g$ line and is in close proximity to the material's sticky point (− − − $T_{db} = T_g + 10K$). This could lead to material losses between P5 - P9 during the particle separation process in the cyclone with a high propensity of particle-wall interactions. $T_{P3,S}$ of 130 °C might allow safer operation with process conditions at P5 well situated between the critical $T_{db} = T_g + 10K$ boundaries. A lower $T_{P3,S}$ of 40 °C operates at conditions with relative humidity levels of up to 51.91%RH (P9), which are reported to carry risks for di-hydrate TRE crystal formation [354, 355]. Ethanol has a T_g at 97 K [356] and therefore, its effect as a plasticizer at equal moisture levels is expected to be even more significant in direct comparison to water.

Concluding the B-290 Mini-Spray Dryer characterisation, process conditions for a subsequent experimental evaluation were selected using a rational design approach based on a heat-/mass-balance process model with data obtained from PSP experimental data. Experiments at two distinct drying temperatures, $T_{P3,S}$ 70 °C and $T_{P3,S}$ 130 °C, allowed an assessment of the impact on final product attributes as well as the manufacturability validating the process model. $T_{P5,R}$ is reduced with decreasing $T_{P3,S}$ and is the expected maximum temperature experienced by the product [3]. Reduced drying temperatures can be of interest particularly for processing heat-sensitive materials. The selected feed rate of $FR_{P11,R}$ of 1.86 mL/min is well within the operational safe zone considering potential fluctuations due to changes in the process conditions linked to the open-loop system (e.g. increased relative humidity of the environment) and uncertainties related to the overall measurement accuracy. Furthermore, it avoids risks of a reversed heat-flow due to extensive evaporative cooling effects as well as critical humidity levels that might induce TRE-h formation. The spray gas was selected after a qualitative evaluation aiming to (1) provide droplet atomisation conditions that permit drying within the lab-scale spray dryer and (2) achieve maximum particle sizes to improve solid-gas separation in the cyclone. The aspirator rate was kept at its maximum to provide optimised enthalpy throughput for the drying process [126].

7.3.2.2 Spray drying - trehalose

TRE was selected as a potential excipient for formulated GLUC-based systems. The spray drying conditions were selected using the process model presented in Section 7.3.2.1. The experiments focused on an assessment of the manufacturability of TRE powders at two inlet temperature levels ($T_{P3,S}$ low - 70 °C, high - 130 °C) and three ethanol solvent ratios (0 v/v%, 1 v/v% and 50 v/v%). An overview of the results for all TRE spray drying experiments is provided in Table 7.1. The TRE experiments were performed prior to testing GLUC or GLUC-TRE formulations to validate the process development approach and allow an investigation on the potential impact of selected process conditions on the final product characteristics of pure TRE powders. The data enable a comparison to the spray dried GLUC-TRE formulations and help to interpret the effect of TRE for the manufacturability of peptide formulation with this excipient.

The achieved process yields exhibit large variations between experiments with feed solutions

Table 7.1: Results for the performed TRE spray drying experiments. Key factors for a process evaluation were the measured process conditions and achieved product yields.

Experiment	**Ethanol**	**Feed Rate**	**B290**			**Yield**
	[v/v]	$FR_{P11,R}$ [mL/min]	$T_{P3,S}$ [°C]	$T_{P5,R}$ [°C]	$RH_{P5,C}$ [%]	[%]
SPT1 (low T, no EtOH)	0.00	1.61	70.00	36.00 ± 0.00	36.57 ± 0.37	75.35
SPT2 (high T, no EtOH)	0.00	1.94	130.00	66.00 ± 0.00	9.75 ± 0.09	83.13
SPT3 (low T, low EtOH)	0.01	1.75	70.00	34.43 ± 0.53	39.17 ± 1.16	72.46
SPT4 (high T, low EtOH)	0.01	1.97	130.00	66.00 ± 0.00	9.07 ± 0.01	84.65
SPT5 (low T, high EtOH)	0.50	1.75	70.00	39.00 ± 0.00	20.40 ± 0.03	24.41
SPT6 (high T, high EtOH)	0.50	1.81	130.00	67.43 ± 0.53	6.52 ± 0.13	34.88

prepared with and without ethanol as well as a function of drying temperature ($T_{P3,S}$). Decreased yields in spray drying are commonly caused by (I) insufficient drying conditions leading to droplet depositions on the walls of the drying column, (II) operating above the material's T_g with high wall depositions in the drying column and cyclone [325, 126, 125] or (III) the discharge of fines with the exhaust gas due to the specific cyclone performance characteristics during the solid/gas separation [126].

I Insufficient droplet drying on the B-290 Mini-Spray Dryer is commonly constituted by droplet/particle deposition within the drying chamber (Fig. 7.2.3-P4). Feed rate and droplet atomisation were optimised during the platform characterisation. Droplet deposition in the drying column was not observed despite potential changes in the evaporation kinetics for the TRE solution compared to pure water during PSP [5].

II Despite reaching a dry state, local process temperatures above the solids' T_g can additionally cause significant wall-depositions most pronounced in areas with increased propensity of particle-wall interactions. A qualitative inspection of the glassware at the end of each experiment suggests significant differences in the local fouling for changing process conditions. Thin homogeneous films inside the drying column (Fig. 7.4-P4) were observed for elevated drying temperatures of $T_{P3,S} = 130$ °C, which might indicate the deposition of highly viscous, sticky particles impacting the wall during droplet drying. More severely, increased wall depositions can be observed in the cyclone (Fig. 7.4-P6) at reduced $T_{P3,S}$ and even more dominantly with high ethanol feed-solvent ratios of 50 v/v%. An example is presented in Fig. A23 (Appendix, page A39) and shows a direct comparison of the local fouling in the cyclone at the end of the experiments SPT2 and SPT6 operating at the same drying temperature ($T_{P3,S} = 130$ °C), but with an ethanol solvent ratio of 0 v/v% and 50

v/v%, respectively. The observations and measured yields correlate well with considerations of an estimated stickiness curve for pure TRE-water system presented in Fig. 7.9.

III The risk for the production of fines below the cyclone's cut-off size is a result of high droplet atomisation and/or low solute concentration. The particle cut-off size ($\bar{d}_{50}$) of 0.94 μm for the B-290 Mini-Spray Dryer with its specific system configuration used in this project was estimated using Barth's classic model [357] with Equation A22 (Appendix, page A22) and a drying gas volume flow (Q) of approximately 15.51 m^3/h obtained solving Equation A23 (Appendix, page A23). Particles down to this size are expected to move outwards in the cyclone's vortex and are separated. Potential fines produced during the spray drying process which are not separated from the gaseous stream in the cyclone, are retained in the fine particle filter (Fig. 7.2.3-P8). Extensive deposition of fines in the filter increases the cross-filter resistance and therefore, the trans-membrane pressure drop $p_{P9,R}$. Recorded data of $p_{P9,R}$ do not exhibit a significant change in the local pressure ($\mid \Delta p_{P9,max} \mid < \pm 5\%$ relative to the starting conditions t_{LinReg}, details in Table A13 (Appendix, page A27)). This suggests that the amount of fines produced during the process were insignificant to cause measurable changes in the cross-filter resistance and most of the solids were successfully separated from the gaseous stream using the *high performance* cyclone (Fig. 7.2.3, P6).

The collected process information for spray dried TRE solutions show distinct outcomes linked to the operating conditions in respect to the material's T_g. Increased ethanol solvent ratios of 50 v/v% have a higher impact on reducing the measured process yield than selected $T_{P3,S}$. Problems related to the drying of TRE can be addressed by actively dehumidifying the drying gas in the open mode configuration or further reducing the feed rate.

7.3.2.3 Spray drying - s-glucagon

The data presented in Section 7.3.2.1 and Section 7.3.2.2 were the basis for the implementation of a spray drying process for GLUC, aiming at pure compound isolation as well as the drying of GLUC formulations with TRE. The results for the most promising process conditions are shown in Table 7.2. Similar to the observations for TRE, the results demonstrate a dominant impact of increasing ethanol ratios in the feed composition on the overall process yields, which are

significantly decreased for SPG2 (1 v/v% ethanol) and SPG3 (50 v/v% ethanol). The highest process yields were achieved for aqueous GLUC solutions with only a slight decrease of the product yield at reduced $T_{P3,S}$. Therefore, a $T_{P3,S}$ of 70 °C can be used for pure GLUC isolation as an alternative to a $T_{P3,S}$ of 130 °C to minimise any potential risk for thermal stress on the peptide material. A reduced $T_{P3,S}$ also has an impact on the relative humidity levels ($RH_{P5,C}$), which rise from 6.02%-rH to 27.46%-rH.

Table 7.2: Results for the performed GLUC spray drying experiments. Key factors for a process evaluation were the measured process conditions and achieved product yields.

Experiment	**Ethanol**	**Feed Rate**	**B290**			**Yield**
	[v/v]	$FR_{P11,R}$ [mL/min]	$T_{P3,S}$ [°C]	$T_{P5,R}$ [°C]	$RH_{P5,C}$ [%]	[%]
SPG1 (high T, no EtOH)	0.00	1.87	130.00	72.00 ± 0.00	6.02 ± 0.00	> 95
SPG2 (high T, low EtOH)	0.01	1.87	130.00	72.00 ± 0.00	6.07 ± 0.00	78.16
SPG3 (high T, high EtOH)	0.50	1.79	130.00	75.00 ± 0.00	4.18 ± 0.01	64.36
SPG4 (low T, no EtOH)	0.00	1.84	70.00	38.00 ± 0.00	27.46 ± 0.03	93.50
SPG5 (Formulation)	0.00	1.87	130.00	72.00 ± 0.00	6.18 ± 0.00	83.24

In SPG5, TRE was added as an excipient to the feed solution in order to protect the peptide against denaturation and aggregation during drying [358, 359] and improve the overall particle morphology as indicated in the SDD experiments. SPG5 exhibited a yield of 83.24%, which correlates with yields for spray dried pure TRE of 83.13% (SPT2). The inspection of the glassware showed no significant wall-depositions in the cyclone suggesting instead an increased material loss through particle adhesion in the drying column as observed for SPT2. This indicates the dominant character of TRE for process implementation and further illustrates manufacturability risks for formulations with carbohydrates leading to material loss due to wall-depositions of sticky particles in the drying column discussed in detail in Section 7.3.2.2.

7.3.2.4 Post-drying

Vacuum drying was assessed as a secondary, post-process drying step for spray dried samples of TRE and GLUC. The measured weight changes for selected samples over a period of up to 250 hours are shown in Fig. 7.10. Additional information on the total weight loss for all samples is provided in Table 7.3. A stable end-weight was reached for all samples after approximately 100 hours. For samples of pure GLUC, the data match well with the residual moisture levels as determined with TG-MS. Samples with TRE show larger deviations indicating difficulties removing residual moisture bound to the product dried at changing $T_{P3,S}$. Challenges of drying carbohydrates are commonly attributed due to their high hygroscopicity [125]. Compared to

unbound residual moisture levels estimated with TG-MS (ΔRM_{80} = RM_{80} - RM_{25}), vacuum drying can reduce ΔRM_{80} of spray dried TRE powders by more than 63.00 wt% (SPT4). For spray dried powders of GLUC, vacuum drying even reduces ΔRM_{80} by more than 90.47 wt% (SPG3) and up to > 95 wt% (SPG1, SPG4). The weight change for the formulation of GLUC with TRE (SPG5) during vacuum drying even exceeds ΔRM_{80} determined with TG-MS, which could be a result of kinetic constraints during moisture evaporation for the TG-MS measurements or the desolvation of additional free moisture under vacuum. This is further discussed in Section 7.3.3. The results demonstrate that vacuum drying could be utilised on lab-scale as a secondary drying step for spray dried powders, but is most effective for pure GLUC peptide solids.

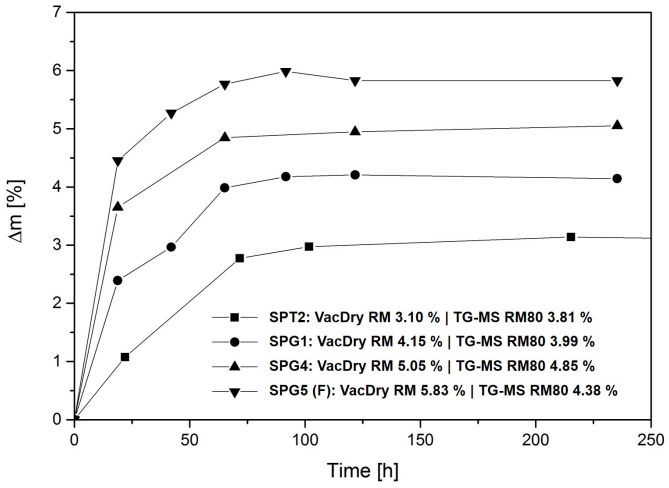

Figure 7.10: Mass change of spray dried TRE and GLUC samples utilising vacuum drying as a secondary drying step. For the selected samples shown here, more than 75 wt% of the residual moisture as determined with TG-MS (RM_{80}) can be removed using vacuum drying at 50 °C. This secondary drying step requires around 100 h before reaching a stable end-weight.

7.3.3 Spray drying - product characterisation

Beside the successful identification of feasible lab-scale spray drying conditions for the production of TRE and GLUC powders with high process yields presented in Section 7.3.2, the produced powders were further characterised offline to understand the impact of the manufacturing conditions on key particle properties related to storage stability and performance. The product characterisation was focused on an assessment of particle size and morphology, residual

moisture content, solid state properties and aspects of particle aggregation. The peptide-based GLUC powders were further assessed in terms of potential changes in the GLUC potency caused by peptide fibrillation or degradation during feed preparation and/or the drying process.

Particle size and morphology: Fig. 7.11 shows SEM micrographs of selected spray dried powder samples. Spray dried TRE (SPT2 and SPT6, Fig. 7.11a-b) exhibits a highly spherical particle morphology. The SEM images suggest a reduction of the particle size distribution (PSD) with increasing ethanol solvent ratios in the feed of up to 50 v/v% linked to higher liquid atomisation due to a reduced surface tension, a reduced viscosity and/or an increased density for aqueous-organic mixtures [360]. SPG1 (Fig. 7.11c) and SPG5 (Fig. 7.11d) are a direct comparison of the particle morphologies between a spray dried feed of pure GLUC and the spray dried GLUC - TRE formulation (GLUC:TRE, 5:30, w/w). The images suggest that the added TRE reduces overall particle buckling. This aligns with the observed particle morphology during the drying of the peptide formulation with TRE using SDD experiments (see Section 7.3.1). Here, the particle morphology was interpreted using a diffusion-dominated particle formation mechanism based on different Pe values for TRE and GLUC. The low diffusivity of GLUC ($D_{\mathrm{GLUC}} \ll \kappa \rightarrow Pe \gg 1$) leads to early skin formation and subsequent surface buckling. This effect is further enhanced due to the rapid evaporation kinetics in the spray dryer compared to the SDD experiments ($\kappa_{\mathrm{SP}} \gg \kappa_{\mathrm{SDD}}$). Qualitatively, the observed particle morphologies align well with reported particle morphologies for spray dried TRE [147] and larger macro-molecular peptides/proteins shown elsewhere [131, 111].

Quantitative information on the particle size distribution (PSD) were collected using laser diffraction (LD). The results for selected spray drying samples are displayed in Fig. 7.12. Further details of Dx_10, Dx_50 and Dx_90 are included in Table 7.3. For TRE, reduced drying temperatures lead to a shift in the PSD towards larger particles with a highly multi-modal distribution e.g. between SPT2 ($T_{P3,S}$ 130°C) and SPT1 ($T_{P3,S}$ 70 °C). In direct comparison, pure and formulated GLUC particles, SPG1 and SPG5, do not exhibit extensive changes in the PSD. The highest volume densities for all measured PSDs lie between 1 μm and 10 μm, which aligns with the particle sizes as visualised using SEM (Fig. 7.11).

Spray dried TRE samples with high residual moisture exhibit highly multi-modal PSDs suggesting strong particle agglomeration and aggregation. As shown in Fig. 7.12, particle agglomer-

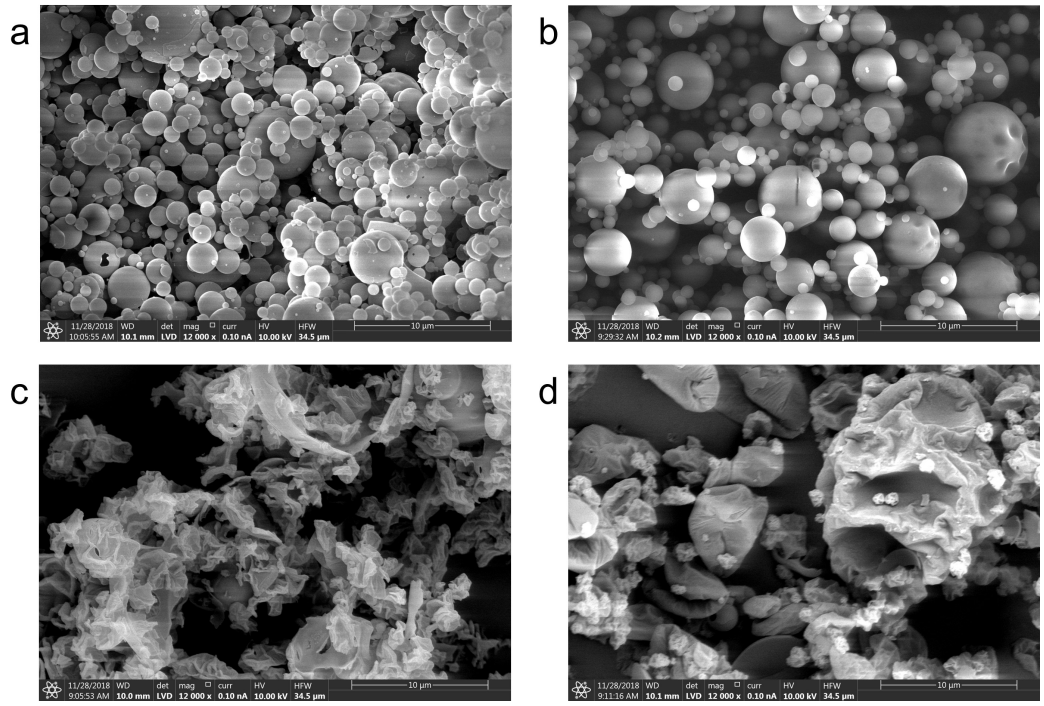

Figure 7.11: SEM micrographs of spray dried powder samples. (a) SPT2 (TRE, $T_{P3,S}$ 130°C, ethanol 0.0 v/v) and (b) SPT6 (TRE, $T_{P3,S}$ 130°C, ethanol 0.5 v/v), (c) SPG1 (GLUC, $T_{P3,S}$ 130°C, ethanol 0.0 v/v) and (d) SPG5 (GLUC-TRE, 5:30 w/w, 130°C, ethanol 0.0 v/v). The images suggest an impact of ethanol on the final particle size distribution. Particles in SPT2 appear larger with high variations in size from nano-range to approaximatly 7 μm. SPT6 exhibits a more homogenous particle size distribution.

ation can be partially reversed using ultrasound, which is demonstrated by a shift of the PSDs from larger particle sizes (> 20 μm) towards smaller particle sizes (< 10 μm) after applying the LD de-agglomeration protocol (R_0: no ultrasound, R_2: 2 x 30sec ultrasound). In case of SPT1, the data suggest that extensive particle aggregates remain present even after repeated ultrasound exposures. In general, the presence and strength of particle agglomerates and/or aggregates correlate with low $T_{P3,S}$ and subsequently, high residual moisture levels. Aggregates in the TRE powders are a result of high molecular mobility leading to cohesion and unbound surface liquids enabling particle bridging and caking. Samples of spray dried GLUC did not show any evidence to suggest the presence of large amounts of particle agglomerates. Interestingly, the formulation of GLUC with TRE (SPG5) showed distinct changes in the collected PSD to pure TRE powders. The data suggest a significant reduction in agglomeration despite higher residual moisture levels (RM_{110} of 7.16%), which could be explained by an enrichment of the particle surface with GLUC, inhibiting particle bridging and therefore, agglomeration

and further aggregation. These considerations follow earlier interpretations of a potential surface enrichment of GLUC compared to TRE due to differences in their diffusion coefficients ($D_{\mathrm{GLUC}} \ll D_{\mathrm{TRE}}$) as discussed in Section 7.3.1. Similar effects have been observed for other formulations containing macro-molecules such as whey proteins altering the particle surface of sugar-rich materials increasing process yields and reducing particle-to-particle and particle-to-wall stickiness [361, 362].

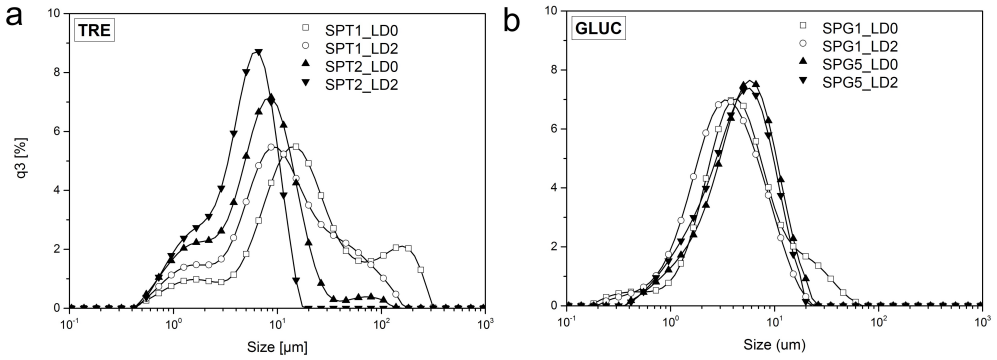

Figure 7.12: Selected LD-PSDs for spray dried samples of TRE and GLUC samples. (a) For spray dried TRE samples, a decreased drying temperature (SPT1 - $T_{P3,S}$ 70 °C, SPT2 - $T_{P3,S}$ 130 °C) correlates with strong particle agglomeration expressed by a multi-modal PSD. (b) Tested GLUC powders show low agglomeration characteristics in the collected PSDs even for formulations including TRE as shown for SPT5.

Residual moisture and solid state structure: As previously discussed in Section 7.3.2.1, residual moisture acts as a plasticiser reducing T_g and enhancing molecular mobility [363]. Therefore, residual moisture in the spray dried powders can significantly reduce the solid state stability against thermodynamically more favourable crystalline forms. TRE acts as a moisture sink binding water in its dihydrate crystal lattice. Additional surface (unbound) moisture can induce particle agglomeration and aggregation [125]. The residual moisture in the spray dried samples was quantified by TG-MS. The results are listed in Table 7.3. RM_{80}, RM_{110} and RM_{180} refer to the measured relative mass changes during the TG-MS analysis at 80 °C, 110 °C and 180 °C, respectively. As expected, the residual moisture levels have an inverse correlation with the drying temperature. For $T_{P3,S}$ of 70 °C, residual moisture levels of spray dried TRE samples reached up to 8.24 wt% (SPT1, RM_{180}). In direct comparison, increasing $T_{P3,S}$ to 130 °C reduced the residual moisture by 49.90% to 4.13 wt% (SPT2, RM_{180}). Furthermore, differences

between RM_{80} and RM_{110} (= ΔRM_{110}) might indicate local TRE-h formation which is not removed as unbound moisture and mostly evaporates above 97 °C where dehydration of TRE-h occurs [364]. Based on ΔRM_{110}, the theoretical maximum crystalline content varies between 1.28 wt% (SPT5) and 19.70 wt% (SPT1). Powders produced at higher $T_{P3,S}$ of 130 °C show a stronger correlation between RM_{80} and RM_{110}, which suggests no/low crystallisation of TRE-h. The solid state structure was further analysed using XRPD and DSC. The collected XRPD and DSC data for all samples are provided in Fig. A16 (Appendix, page A33) and Fig. A17 (Appendix, page A34), respectively. A qualitative inspection of XRPD data for all TRE samples except SPT3 showed no significant level of crystallinity i.e. the amount of TRE-h is below the detectable limits. This aligns with collected DSC data, where no characteristic endotherm of the TRE-h dehydration (T_d) was observed for any of the TRE samples except for SPT3. In case of SPT3, the high levels of unbound residual moisture ($RM_{80} = 4.78\%$) induced a partial TRE-h formation (XRPD: crystal peaks visible, DSC: T_d = 97 °C). Measured T_g values of the TRE samples are included in Table 7.3 and correlate with recorded TG-MS data with significantly reduced T_g values for increasing RM levels. Additional weight changes between RM_{110} and RM_{180} (= ΔRM_{180}) are above the T_g of amorphous TRE ($T_{g,TRE}$ = 115 °C). Residual moisture at these temperatures may be entrapped inside the particle structure or larger particle aggregates. The values correlate with selected $T_{P3,S}$ reaching a maximum of 3.91 wt% for SPT1 ($T_{P3,S}$ 70 °C). Overall, the data has shown that a $T_{P3,S}$ of 130 °C would be preferable to minimise residual moisture levels and reduce risks of local TRE-h formation.

Residual moisture levels in spray dried GLUC powders were less impacted by operating at $T_{P3,S}$ of 70 °C or 130 °C. At $T_{P3,S}$ of 130 °C RM_{180} is reduced by 10.41% compared to $T_{P3,S}$ of 70 °C i.e. RM_{180} is reduced from 8.72 wt% (SPG4) to 7.81 wt% (SPG1). The measured weight loss occurs in two main steps at ΔRM_{80} (20 - 80 °C) and ΔRM_{180} (110 - 180 °C) giving a measure that can distinguish between unbound and bound moisture, respectively. ΔRM_{80} correlates with selected $T_{P3,S}$ where higher drying temperatures lead to a reduction of 17.73% comparing SPG1 and SPG4 (Table 7.3). However, ΔRM_{180} is relative consistent for all non-formulated GLUC powders with an average value of 3.69 ± 0.14 wt%. For spray dried GLUC powders from pure aqueous solutions, ΔRM_{180} is 3.57 ± 0.02 wt% independent of the assessed $T_{P3,S}$ of 70 °C (SPG4) and 130 °C (SPG1), respectively. For the freeze dried GLUC powders, ΔRM_{180} was 1.83 wt%. This striking consistency in ΔRM_{180} for the spray dried GLUC powders regardless

of the drying temperature ($T_{P3,S}$) may suggest that GLUC water interactions are unaffected by the spray drying process, leading to a near constant bound residual moisture content in the absence of TRE. Furthermore, peptides can undergo pyrolysis, which includes dehydration, decarboxylation and deammination leading to changes in the sample mass, but are commonly observed at temperatures above 180-200 °C [365, 366]. GLUC-water interactions are essential in the folding, stability, dynamics, and function of proteins [338] where spray drying could show beneficial stability effects over freeze drying. For the GLUC-TRE formulation (SPG5), temperatures over 170 °C lead to a significant mass loss and browning of the powder, which indicates a Millard reaction at these temperature levels. Details on the TG-MS data are provided in Fig. A18 (Appendix, page A34) for TRE and Fig. A19 (Appendix, page A35) for GLUC.

Table 7.3: Product characterisation of spray dried TRE and GLUC samples. Each powder sample was assessed for residual moisture, particle size distribution and peptide and glass transition temperature.

Experiment	**TG-MS** [wt%]			**VacDry** [wt%]	**LD_{R_2}** [μm]			**DSC** [°C]
	RM_{80}	RM_{110}	RM_{180}	RM	Dx_10	Dx_50	Dx_90	T_G
SPT1	2.45	4.33	8.24	6.34	1.75	9.57	47.94	42.35
SPT2	3.81	4.10	4.13	3.10	1.26	4.62	9.27	60.26
SPT3	4.78	5.82	6.48	4.70	1.37	5.98	24.07	40.32
SPT4	3.57	3.87	3.90	2.25	1.20	4.40	10.16	65.12
SPT5	4.77	4.90	5.58	4.28	1.27	3.67	9.63	38.98
SPT6	3.80	3.99	4.49	2.61	1.31	3.96	9.48	57.16
SPG1	3.99	4.27	7.81	4.15	1.11	3.18	8.38	-
SPG2	3.77	4.07	7.82	3.55	1.25	3.75	9.87	-
SPG3	3.78	4.19	8.08	3.42	1.13	2.79	6.00	-
SPG4	4.85	5.14	8.72	5.05	1.22	3.30	7.26	-
SPG5 (F)	4.38	7.16	-	5.83	1.30	4.20	9.82	-

Peptide fibrillation and degradation: A ThT assay was employed to assess potential changes in the fibrillation kinetics of spray dried GLUC in direct comparison to a freeze-dried reference powder. The results of the ThT assay for the spray dried samples and the freeze dried reference material are shown in Fig. A21 (Appendix, page A37) and Fig. A20 (Appendix, page A36), respectively. Fibrillation is detected when the signal intensity of the fluorescence deviates from the signal baseline measured with pure solvent (blank). As reported elsewhere [330], the data show that the lag time before detecting GLUC fibrillation is reduced with increasing GLUC concentrations. Moreover, the data suggest that the fibrillation kinetics, but not the fibrillation onset can be further altered with increasing ethanol solvents ratios. For ethanol solvent ratios of 50 v/v%, no significant ThT fluorescence signal was detected suggesting a suppression of

large GLUC fibrils with extensive β-sheet folding. These observations align with a qualitative assessment of the stability of GLUC solutions where gelling was significantly delayed with increasing ethanol solvent ratios of up to 50 v/v% indicating a reduction in fibril formation and growth (details in Fig. A22 (Appendix, page A38)). This may suggest a potential competitive mechanism between ethanol solvation and peptide fibrillation. A chaotropic solvational behaviour of increased ethanol solvent ratios has been described for other peptides e.g. insulin [342, 343]. In comparison to the freeze-dried material, spray dried samples show significantly reduced levels of ThT fluorescence. This could be linked to changes in the peptide hydration as observed during the TG-MS analysis, which may an impact on the fibrillation kinetics and pathway. Whilst out of scope for this study, additional information on potential molecular modifications or changes in the peptide conformation during spray drying leading to alterations in the *in-vivo* performance would be required for a final validation of the spray drying manufacturing process. Circular dichroism (CD) or Fourier transform infrared (FTIR) spectroscopy could be used as part of the offline product analysis to validate the preservation of the peptide conformation after redissolving of the spray dried powders [367, 329].

Spray dried GLUC was further characterised in terms of its post-process potency using HPLC. The results of the HPLC quantification of spray dried GLUC samples are shown in Fig. 7.13 and included a pre-filtration step to remove large peptide aggregates. This analysis was able to semi-quantitatively differentiate between samples with strong GLUC fibrillation (AGS_N) and freshly prepared GLUC solutions (Ctrl). The quantified concentration in the permeate (= potency) of the spray dried powders indicate no major aggregation during the manufacturing process. Small deviations of P to pF and pP are related to residual moisture in the weighed samples which was not accounted for during the HPLC sample preparation. Post-drying in a vacuum oven increases the measured potency levels due to a reduction in moisture except for SPG5 (formulation GLUC - TRE, 5:30, w/w). This indicates that vacuum drying can be used as a secondary drying method of pure GLUC powders, but might promote GLUC aggregation in the formulation with TRE. Further experiments would be required to investigate the impact of TRE on the GLUC formulation addressing potential risks related to molecular mobility with an impact on peptide aggregation and therefore, overall product stability during distribution and storage.

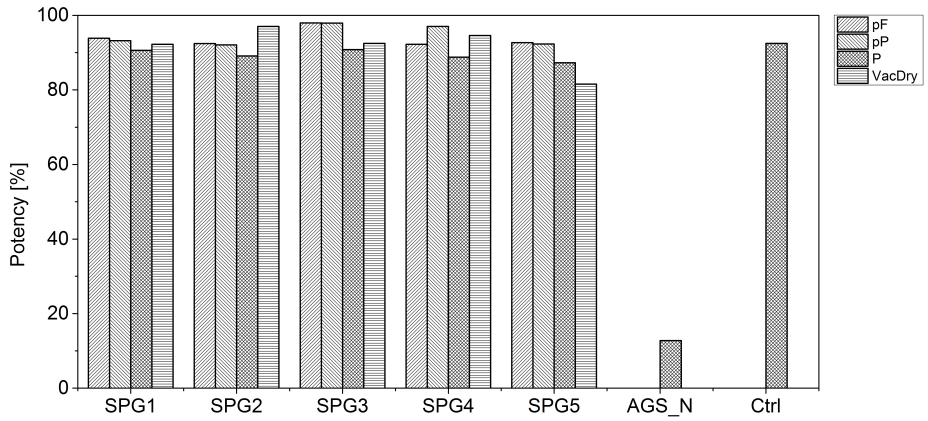

Figure 7.13: Results of the employed HPLC potency assay assessing feed stability (pF, pP), the spray dried powder (P) and vacuum drying as a secondary drying step (VacDry). The values show a high remaining potency as determined with HPLC. Results are compared qualitatively to a strongly aggregated *worst-case* GLUC sample (AGS_N) and a freshly prepared GLUC solution (Ctrl) validating the HPLC quantification approach. All values are normalised against a GLUC standard.

7.4 Conclusions

Spray drying conditions were successfully identified for the efficient drying and isolation of a peptide-based GLUC formulation. Single droplet drying (SDD) experiments combined with micro-XRT analysis gave valuable insights into the particle formation process and demonstrated the impact of TRE on the final particle morphology in GLUC formulations. The final particle structure can be interpreted on the basis of a diffusion-controlled particle formation mechanism, which implies an enrichment of the particle surface with GLUC.

Novel PAT capabilities for lab-scale spray dryer were used for an initial characterisation of the spray drying platform assessing independent process variables to identify feasible drying conditions for process operation. A heat and mass balance was used to create a process model supporting a rational selection of experiments for a DoE approach. The production of spray dried TRE showed a strong negative correlation between achievable process yields and increasing ethanol solvent fractions in the feed. This can be linked to changes in the material's T_g with residual solvent moisture acting as a plasticiser leading to significant particle adhesion in the cyclone. Particle agglomeration was more pronounced at reduced drying temperatures and most pronounced for pure aqueous TRE - solutions as assessed semi-quantitatively using a LD de-agglomeration protocol. TG-MS and DSC data suggest a partial crystallisation of TRE-h, at

or below the detection limit of XRPD, which is linked to high humidity levels in the drying gas. Spray drying of TRE at $T_{P3,S}$ 130 °C allowed the production of amorphous powders with yields of up to 84.65%. Similarly, high yields (>95%) and low residual unbound moisture (ΔRM_{80} of 3.99 wt%) was achieved for spray dried aqueous solutions of GLUC using a $T_{P3,S}$ of 130 °C and a $FR_{P11,R}$ of 1.87 mL/min. A reduced $T_{P3,S}$ of 70 °C can be considered for heat-sensitive bio-molecules, but here, it significantly increased the unbound residual moisture (ΔRM_{80} to 4.85 wt%), which could lead to unwanted TRE-h nucleation or long term chemical stability issues. Vacuum drying can be used as a secondary drying step to remove > 90% of unbound moisture of pure GLUC powders (ΔRM_{80}). The formulation of GLUC with TRE exhibited increased residual moisture levels, however, also a partially inflated particle morphology and low levels of particle agglomeration and aggregation indicating a surface modification compared to pure TRE powders. The results further support the hypothesis of a particle surface enriched with GLUC encapsulating a particle core of TRE, which correlates well with considerations on the particle formation mechanism observed during SDD experiments. Compared to the freeze dried starting material, spray drying of GLUC had an impact on the peptide fibrillation pathway and kinetics assessed using a ThT assay. Extensive GLUC fibrillation was not observed and spray dried powders retained potencies between 81.57% and 97.04% as determined with HPLC.

The experiments showed promising results using spray drying as a peptide isolation process for the rapid production of GLUC powders. The demonstrated strategies for data capturing and analysis enable a systematic approach within a data-driven spray drying process development and implementation workflow which can be applied for the isolation of novel biopharmaceutical formulations on lab-scale. Collected offline information and live PAT data on lab-scale can be used to accelerate scale-up and to implement a model predictive process control system.

Contributions

FJSD, SAF and AJF conceived the study. FJSD developed the exhaust air sensor and software implementation for the data integration framework. FJSD performed spray drying experiments. LJB significantly supported lab activities and method development for product characterisation.

FJSD and RLD designed and performed ThT assays. BL performed HPLC analysis. JH performed SEM analysis. FJSD wrote the original draft of the manuscript, which was reviewed by FJSD, SAF and AJF with input from all other co-authors.

Acknowledgement

The authors would also like to thank EPSRC and the Doctoral Training Centre in Continuous Manufacturing and Crystallisation (Grant Ref: EP/K503289/1) and the EPSRC Future Continuous Manufacturing and Advanced Crystallisation Research Hub (Grant Ref: EP/P006965/1) for funding this work. The authors would like to acknowledge that parts of this work was carried out in the CMAC National Facility supported by UKRPIF (UK Research Partnership Fund) award from the Higher Education Funding Council for England (HEFCE) (Grant Ref: HH13054).
This project was part of a pre-competitive research collaboration between the CMAC Future Manufacturing Research Hub and Eli Lilly. The authors would like to thank Ian Houson (CMAC), Rebekah Russell (CMAC) and Christopher Burcham (Eli Lilly) for their support organising this industrial collaboration. Further, the authors would like to acknowledge support in this project from Brian Pack (expertise, Eli Lilly), Mark Strege (expertise, Eli Lilly), Tim Woods (lab support, Eli Lilly), David Coates (lab support, Eli Lilly), Ryan Linder (lab support, Eli Lilly), David Remick (lab support, Eli Lilly), the SMDD Peptide Synthesis Group & Delta V Team (equipment, Eli Lilly), Robert Price (NMR, Eli Lilly), Chris Dobbins (3D printing service, Eli Lilly) and Monish Chaddha (HPLC analysis, Eurofins). Acknowledgement for the support and helpful discussions with Ali Anwar (CMAC) and John Robertson (CMAC), specifically for giving access to their 3D printers during early prototyping.

8 Conclusion and Future Work

The presented research explored aspects for the measurement, optimisation and control of particle properties in pharmaceutical manufacturing processes with a focus on droplet drying platforms such as spray drying. Advances in the use of micro-XRT for a systematic, quantitative characterisation of solid pharmaceutical products combined the development of an image analysis framework with machine learning (ML) methodologies. The outlined micro-XRT characterisation workflow in Chapter 4 was demonstrated on a variety of case studies from single crystals to fully formulated final products with potential applicability throughout the pharmaceutical downstream manufacturing pipeline. System-related restrictions to reliably resolve attributes with sizes below $\sim$10 μm could be improved with future advances in the micro-XRT hardware. Methodologies integrated in the image analysis framework aim to provide a basis for other researchers to perform quantitative micro-XRT measurements. The use of complementary characterisation techniques, e.g. ToF-SIMS for chemical imaging, showed promising results to further enhance the interpretability of the micro-XRT image data.

Micro-XRT was also employed to characterise pharmaceutical capsules as a multi-particulate product each containing approximately 300 ibuprofen-pellets. More than 200 structural features were extracted to quantify attributes of the pellets' size, shape, porosity, surface, and location/orientation. This allowed an in-depth statistical evaluation of the pellet population and its uniformity. A Support Vector Machine was used to build a classification model for the automatic identification of *broken* ibuprofen-pellets. The model was assessed using a test dataset of 886 pellets and had a minimum accuracy of 99.55% (minimum precision *broken* pellets of 86.20%).

Acoustic levitation was employed as a single droplet drying (SDD) platform for small-scale particle engineering applications. The technique allows the investigation of liquid evaporation kinetics and particle formation under controlled drying conditions. Combined with a micro-XRT

characterisation of the final particle, the SAL-XRT platform was used to assess the impact of formulation parameters on the final particle morphology in order to better understand key factors underpinning solidification from solution. For droplets from a multi-component solution of metformin hydrochloride, D-mannitol and HPMC K100LV, increasing polymer concentrations significantly reduced liquid evaporation, inhibited local crystal growth and led to substantial changes in the particle morphology, including its internal micro-structure and extensive surface buckling. Here, particle formation was interpreted based on differences in the Péclet number between small organic molecules (metformin hydrochloride and D-mannitol) and the larger macro-molecular polymer (HPMC K100LV) resulting in a HPMC K100LV-enriched particle surface. Observed changes in the particle morphology are expected to decrease particle flowability and, therefore, manufacturability in the downstream process with increasing HPMC K100LV additions.

Ultimately, such endeavours aim to facilitate a rational approach for pharmaceutical process development exploiting small scale experiments and advanced metrology. In a pre-competitive industrial collaboration, this research was translated to a lab-scale isolation process of peptides via spray drying. Process optimisation and control required the implementation of customised Process Analytical Technology (PAT) to provide means of data acquisition for key process variables including feed rate, local temperature, relative humidity and local pressure. The project successfully demonstrated the utilisation of SDD experiments, of a comprehensive PAT data collection strategy and of applied offline characterisation techniques for a systematic experimental investigation on the impact of process parameters and solvent composition on product attributes relevant to manufacturability and drug performance. The successful identification of optimised process conditions within a spray drying model allowed the reliable production of spray dried s-glucagon-powders, which demonstrated the potential of using spray drying as an alternative to lyophilization isolation techniques for this model peptide system.

8.1 Future Work

The developed micro-XRT characterisation workflow creates the basis for the quantitative analysis of a wide range of pharmaceutical products and drug product intermediates. The work aimed to establish micro-XRT as an offline analysis technique to be applied more routinely for

the characterisation of pharmaceutical samples. Most promising applications might be spherical agglomeration, (dry/wet) granulation or tableting, which are within a size range that allow high-resolution micro-XRT image acquisition of the full sample and of individual local structural attributes. In this context, micro-XRT could provide valuable information about primary particle properties as well as about the overall object regarding its porosity, size, shape surface and orientation/location. Quantification of these micromeritic properties can be linked to parameters for formulation and process operation influencing their functional attributes [208, 161]. Future developments of the micro-XRT characterisation workflow may create further opportunities to improve the existing image analysis framework, incorporating additional micro-XRT image data analysis methods. Specifically, data-driven ML solutions might benefit from a systematic data acquisition and analysis approach. Similar developments led to distinct breakthroughs in image segmentation, annotation or analysis in other scientific fields [368, 192, 369].

SDD experiments are efficient to explore the particle design space of complex pharmaceutical formulations monitoring liquid evaporation and solidification. The combination of acoustic levitation for SDD experiments and micro-XRT aimed to explore the links between droplet drying and the final particle structure and morphology. The obtained particles could be further assessed regarding their performance during dissolution [370] or undergoing compaction [103] to further explore the implications of the particle micro-structure on its final performance. This would allow the implementation of a Quality-by-Design approach for pharmaceutical products of multi-particulate systems with a back-propagation of design instructions to inform the selection of initial formulation and process parameters.

The implementation of an advanced spray drying process model might allow the additional exploitation of the SDD data for process parameter estimation [105, 322, 371]. Challenges remain for experiments conducted in the acoustic levitator, such as a comparatively large droplet size, effects of acoustic streaming with an impact on liquid evaporation and current limitations around the accessible drying conditions. The developed multi-emitter single-axis acoustic levitator (MSAL) enabled the stable levitation of smaller and irregular shaped droplets/particles as small as 150 μm and could be a step towards an improved SDD platform for spray drying process development. Smaller droplet sizes however, also are disadvantageous for monitoring the evaporation process with the currently employed imaging techniques and might limit the applicability of micro-XRT as a characterisation of the final particles.

Spray drying models require experimental data for empirical parameter estimation or model validation [120, 321, 322], but the use of Process Analytical Technology (PAT) is often not considered for lab-scale. Developed capabilities for data acquisition on a lab-scale spray dryer included the implementation of an affordable PAT sensor for exhaust gas analysis, which can be used to monitor future lab-scale experiments and support the process implementation of novel (bio-) pharmaceutical systems. Spray drying process models benefit from these experimental data and were employed to support a systemic experimental approach for accelerated process development. Combing process models with PAT would also allow the implementation of a model-predictive control strategy on lab-scale. This could further improve the reliability of lab-scale spray drying as a small-scale, rapid isolation platform for low-volume manufacturing campaigns e.g. decentralised (continuous) micro-factories [372] or during drug product development for (non-) clinical studies [373].

Bibliography

[1] Reinhard Vehring. Pharmaceutical particle engineering via spray drying. *Pharmaceutical Research*, 25(5):999–1022, 2008. ISSN 07248741. doi: 10.1007/s11095-007-9475-1.

[2] Stephen Byrn, Maricio Futran, Hayden Thomas, Eric Jayjock, Nicola Maron, Robert F. Meyer, Allan S. Myerson, Michael P. Thien, and Bernhardt L. Trout. Achieving Continuous Manufacturing for Final Dosage Formation: Challenges and How to Meet Them. *Journal of pharmaceutical sciences*, 104(3):792–802, 2015. doi: 10.1002/jps.24247.

[3] K Masters. Spray Drying Handbook George Godwin. *London, England*, page 67, 1985.

[4] C. S. Handscomb, M. Kraft, and A. E. Bayly. A new model for the drying of droplets containing suspended solids. *Chemical Engineering Science*, 64(4):628–637, 2009. ISSN 00092509. doi: 10.1016/j.ces.2008.04.051.

[5] W. E. Ranz and W. R. Marshall. Evaporation from drops - Part 1, 1952. ISSN 0360-7275.

[6] S. Nešić and J. Vodnik. Kinetics of droplet evaporation. *Chemical Engineering Science*, 46(2):527–537, 1991. ISSN 00092509. doi: 10.1016/0009-2509(91)80013-O.

[7] F.J.S. Doerr, I.D.H. Oswald, and A.J. Florence. Quantitative investigation of particle formation of a model pharmaceutical formulation using single droplet evaporation experiments and X-ray tomography. *Advanced Powder Technology*, 29(12):2996–3006, 2018. ISSN 15685527. doi: 10.1016/j.apt.2018.09.027.

[8] S. X.Q. Lin and X. D. Chen. Changes in milk droplet diameter during drying under constant drying conditions investigated using the glass-filament method. *Food and Bioproducts Processing*, 82(3 C):213–218, 2004. ISSN 09603085. doi: 10.1205/fbio.82.3.213.44178.

[9] Heiko Schiffter and Geoffrey Lee. Single-droplet evaporation kinetics and particle formation in an acoustic levitator. Part 2: drying kinetics and particle formation from microdroplets of aqueous mannitol, trehalose, or catalase. *Journal of pharmaceutical sciences*, 96(9):2284–2295, 2007. ISSN 1520-6017. doi: 10.1002/jps.20858.

[10] Robert Sedelmayer, Matthias Griesing, Annelie Heide Halfar, Werner Pauer, and Hans Ulrich Moritz. Experimental investigation of the morphology formation of polymer particles in an acoustic levitator. *Macromolecular Symposia*, 333(1):142–150, 2013. ISSN 10221360. doi: 10.1002/masy.201300088.

[11] Mani Ordoubadi, Florence K.A. Gregson, Omar Melhem, David Barona, Rachael E.H. Miles, Dexter D'Sa, Sandra Gracin, David Lechuga-Ballesteros, Jonathan P. Reid, Warren H. Finlay, and Reinhard Vehring. Multi-Solvent Microdroplet Evaporation: Modeling and Measurement of Spray-Drying Kinetics with Inhalable Pharmaceutics. *Pharmaceutical Research*, 36(7), 2019. ISSN 1573904X. doi: 10.1007/s11095-019-2630-7.

[12] Jakob Sloth, Søren Kiil, Anker D Jensen, Sune K Andersen, Krare Jørgensen, Heiko Schiffter, and Geoffrey Lee. Model based analysis of the drying of a single solution droplet in an ultrasonic levitator. *Chemical Engineering Science*, 61(8):2701–2709, 2006. ISSN 00092509. doi: 10.1016/j.ces.2005.11.051.

[13] Nikolai Albertovich Fuchs. *Evaporation and droplet growth in gaseous media*. Elsevier, 2013.

[14] Pablo G Debenedetti and Frank H Stillinger. Review article Supercooled liquids and the glass transition. *Nature*, 410(March):259, 2001.

[15] Minoru Yoshioka, Bruno C. Hancock, and George Zografi. Crystallization of indomethacin from the amorphous state below and above its glass transition temperature. *Journal of Pharmaceutical Sciences*, 83(12):1700–1705, 1994. ISSN 15206017. doi: 10.1002/jps.2600831211.

[16] Bruno C Hancock, Sheri L Shamblin, and George Zografi. Molecular mobility of amorphous pharmaceutical solids below their glass transition temperatures. *Pharmaceutical research*, 12(6):799–806, 1995.

[17] Bruno C. Hancock and George Zografi. Characteristics and Significance of the Amorphous State in Pharmaceutical Systems. *Journal of Pharmaceutical Sciences*, 86(1):1, 1997. ISSN 00223549. doi: 10.1021/js9601896.

[18] Abhishek Singh and Guy van den Mooter. Spray drying formulation of amorphous solid dispersions. *Advanced drug delivery reviews*, 100:27–50, 2016. ISSN 0169-409X. doi: 10.1016/j.addr.2015.12.010.

[19] A. Muginstein, M. Fichman, and C. Gutfinger. Gas absorption in a moving drop containing suspended solids. *International Journal of Multiphase Flow*, 27(6):1079–1094, 2001. ISSN 03019322. doi: 10.1016/S0301-9322(00)00063-X.

[20] Reinhard Vehring. Pharmaceutical particle engineering via spray drying. *Pharmaceutical research*, 25(5):999–1022, 2008.

[21] John William Mullin. *Crystallization*. Elsevier, 2001.

[22] Alan G Jones. *Crystallization process systems*. Elsevier, 2002. ISBN 978-0-7506-5520-0.

[23] Allan Myerson. *Handbook of industrial crystallization*. Butterworth-Heinemann, 2002.

[24] Jaroslav Nyvlt, Rudolf Rychly, Jaroslav Gottfried, and Jivrina Wurzelová. Metastable zone-width of some aqueous solutions. *Journal of crystal growth*, 6(2):151–162, 1970.

[25] Li Yu Wang, Liang Zhu, Li Bin Yang, Yan Fei Wang, Zuo Liang Sha, and Xiao Yu Zhao. Thermodynamic equilibrium, metastable zone widths, and nucleation behavior in the cooling crystallization of gestodene-ethanol systems. *Journal of Crystal Growth*, 437:32–41, 2016. ISSN 00220248. doi: 10.1016/j.jcrysgro.2015.12.020.

[26] Somnath S. Kadam, Samir A. Kulkarni, Roger Coloma Ribera, Andrzej I. Stankiewicz, Joop H. ter Horst, and Herman J.M. Kramer. A new view on the metastable zone width during cooling crystallization. *Chemical Engineering Science*, 72:10–19, 2012. ISSN 00092509. doi: 10.1016/j.ces.2012.01.002.

[27] S. G. Agrawal and A. H.J. Paterson. Secondary Nucleation: Mechanisms and Models. *Chemical Engineering Communications*, 202(5):698–706, 2015. ISSN 15635201. doi: 10.1080/00986445.2014.969369.

[28] D. Chiou and T. a G Langrish. A comparison of crystallisation approaches in spray drying. *Journal of Food Engineering*, 88(2):177–185, 2008. ISSN 02608774. doi: 10.1016/j.jfoodeng.2008.02.004.

[29] Harry G Brittain. *Polymorphism in pharmaceutical solids*. CRC Press, 2016.

[30] Yumiko Kobayashi, Shusei Ito, Shigeru Itai, and Keiji Yamamoto. Physicochemical properties and bioavailability of carbamazepine polymorphs and dihydrate. *International Journal of Pharmaceutics*, 193:137–146, 2000.

[31] Fabiana Sussich, Ranieri Urbani, Francesco Princivalle, and Attilio Cesàro. Polymorphic amorphous and crystalline forms of trehalose. *Journal of the American Chemical Society*, 120(31):7893–7899, 1998. ISSN 00027863. doi: 10.1021/ja9800479.

[32] W. C. Schinzer, M. S. Bergren, D. S. Aldrich, R. S. Chao, M. J. Dunn, A. Jeganathan, and L. M. Madden. Characterization and interconversion of polymorphs of premafloxacin, a new quinolone antibiotic. *Journal of Pharmaceutical Sciences*, 86(12):1426–1431, 1997. ISSN 00223549. doi: 10.1021/js970063o.

[33] Kailas S. Khomane, Parth K. More, Guru Raghavendra, and Arvind K. Bansal. Molecular understanding of the compaction behavior of indomethacin polymorphs. *Molecular Pharmaceutics*, 10(2):631–639, 2013. ISSN 15438384. doi: 10.1021/mp300390m.

[34] Chenguang Wang and Changquan Calvin Sun. Identifying Slip Planes in Organic Polymorphs by Combined Energy Framework Calculations and Topology Analysis. *Crystal Growth and Design*, 18(3):1909–1916, 2018. ISSN 15287505. doi: 10.1021/acs.cgd.8b00202.

[35] Yoshihisa Matsuda, Sachiyo Kawaguchi, Hitomi Kobayashi, and Jujiro Nishijo. Physicochemical characterization of spray-dried phenylbutazone polymorphs. *Journal of pharmaceutical sciences*, 73(2):173–179, 1984. ISSN 1520-6017. doi: 10.1002/jps.2600730209.

[36] Yuxin Mo, Leping Dang, and Hongyuan Wei. Solubility of α-form and β-form of l-glutamic acid in different aqueous solvent mixtures. *Fluid Phase Equilibria*, 300(1-2):105–109, 2011. ISSN 03783812. doi: 10.1016/j.fluid.2010.10.020.

[37] D. H. Charlesworth and W. R. Marshall. Evaporation from drops containing dissolved solids. *AIChE Journal*, 6(1):9–23, 1960. ISSN 15475905. doi: 10.1002/aic.690060104.

[38] Christopher Samuel Handscomb. *Simulating Droplet Drying And Particle Formation in Spray Towers*. PhD thesis, University of Cambridge, 2008.

[39] D E Walton and C J Mumford. The Morphology of Spray-Dried Particles: The Effect of Process Variables upon the Morphology of Spray-Dried Particles. *Chemical Engineering Research and Design*, 77(5):442–460, 1999. ISSN 02638762. doi: 10.1205/026387699526296.

[40] Tarric M El-Sayed, David A Wallack, and C Judson King. Changes in particle morphology during drying of drops of carbohydrate solutions and food liquids. 1. Effect of composition and drying conditions. *Industrial {&} Engineering Chemistry Research*, 29 (12):2346–2354, 1990. ISSN 0888-5885. doi: 10.1021/ie00108a007.

[41] E. M. Both, A. M. Karlina, R. M. Boom, and M. A.I. Schutyser. Morphology development during sessile single droplet drying of mixed maltodextrin and whey protein solutions. *Food Hydrocolloids*, 75:202–210, 2017. ISSN 0268005X. doi: 10.1016/j.foodhyd.2017.08.022.

[42] D E Walton and C J Mumford. Spray Dried Products—Characterization of Particle Morphology. *Chemical Engineering Research and Design*, 77(1):21–38, 1999. ISSN 02638762. doi: 10.1205/026387699525846.

[43] L. Alamilla-Beltrán, J. J. Chanona-Pérez, A. R. Jiménez-Aparicio, and G. F. Gutiérrez-Lopez. Description of morphological changes of particles along spray drying. *Journal of Food Engineering*, 67(1-2):179–184, 2005. ISSN 02608774. doi: 10.1016/j.jfoodeng.2004.05.063.

[44] J.T. Carstensen and Ping-Ching Chan. Relation between particle size and repose angles of powders. *Powder Technology*, 15(1):129–131, 1976. ISSN 00325910. doi: 10.1016/0032-5910(76)80037-x.

[45] Weili Yu, Koji Muteki, Lin Zhang, and Gloria Kim. Prediction of bulk powder flow performance using comprehensive particle size and particle shape distributions. *Journal*

of Pharmaceutical Sciences, 100(1):284–293, 2011. ISSN 15206017. doi: 10.1002/jps.22254.

[46] Abarasi Hart. Effect of Particle Size on Detergent Powders Flowability and Tabletability. *Journal of Chemical Engineering & Process Technology*, 06(01):1–4, 2015. ISSN 21577048. doi: 10.4172/2157-7048.1000215.

[47] J. S. Chang, S. Vigneswaran, J. K. Kandasamy, and L. J. Tsai. Effect of pore size and particle size distribution on granular bed filtration and microfiltration. *Separation Science and Technology*, 43(7):1771–1784, 2008. ISSN 01496395. doi: 10.1080/01496390801974605.

[48] Changquan Calvin Sun. Decoding powder tabletability: Roles of particle adhesion and plasticity. *Journal of Adhesion Science and Technology*, 25(4-5):483–499, 2011. ISSN 01694243. doi: 10.1163/016942410X525678.

[49] Norbert Rasenack, Helge Hartenhauer, and Bernd W Müller. Microcrystals for dissolution rate enhancement of poorly water-soluble drugs. *International Journal of Pharmaceutics*, 254(2):137–145, 2003. ISSN 0378-5173. doi: 10.1016/S0378-5173(03)00005-X.

[50] Susan Hoe, James W Ivey, Mohammed A Boraey, Abouzar Shamsaddini-Shahrbabak, Emadeddin Javaheri, Sadaf Matinkhoo, Warren H Finlay, and Reinhard Vehring. Use of a Fundamental Approach to Spray-Drying Formulation Design to Facilitate the Development of Multi-Component Dry Powder Aerosols for Respiratory Drug Delivery. *Pharmaceutical Research*, 31(2):449–465, 2014. ISSN 0724-8741. doi: 10.1007/s11095-013-1174-5.

[51] David R Ochsenbein, Thomas Vetter, Stefan Schorsch, Manfred Morari, and Marco Mazzotti. Agglomeration of Needle-like Crystals in Suspension : I . Measurements. *Crystal Growth & Design*, 15(4):1923–1933, 2015. doi: 10.1021/acs.cgd.5b00094.

[52] Javier Cardona, Carla Ferreira, John McGinty, Andrew Hamilton, Okpeafoh S. Agimelen, Alison Cleary, Robert Atkinson, Craig Michie, Stephen Marshall, Yi Chieh Chen, Jan Sefcik, Ivan Andonovic, and Christos Tachtatzis. Image analysis frame-

work with focus evaluation for in situ characterisation of particle size and shape attributes. *Chemical Engineering Science*, 191:208–231, 2018. ISSN 00092509. doi: 10.1016/j.ces.2018.06.067.

[53] Hao Hou and Changquan Calvin Sun. Quantifying effects of particulate properties on powder flow properties using a ring shear tester. *Journal of Pharmaceutical Sciences*, 97(9):4030–4039, 2008. ISSN 15206017. doi: 10.1002/jps.21288.

[54] Wolfgang Beckmann. *Crystallization: Basic concepts and industrial applications*. John Wiley & Sons, 2013.

[55] Wei Ming Lu and Kuo Jen Hwang. Mechanism of cake formation in constant pressure filtrations. *Separations Technology*, 3(3):122–132, 1993. ISSN 09569618. doi: 10.1016/0956-9618(93)80012-G.

[56] N. Y K Chew and H. K. Chan. Use of solid corrugated particles to enhance powder aerosol performance. *Pharmaceutical Research*, 18(11):1570–1577, 2001. ISSN 07248741. doi: 10.1023/A:1013082531394.

[57] Reinhard Vehring, Willard R Foss, and David Lechuga-Ballesteros. Particle formation in spray drying. *Journal of Aerosol Science*, 38(7):728–746, 2007. ISSN 00218502. doi: 10.1016/j.jaerosci.2007.04.005.

[58] Budi Zhao and Jianfeng Wang. 3D quantitative shape analysis on form, roundness, and compactness with μ CT. *Powder Technology*, 291:262–275, 2016. ISSN 0032-5910. doi: 10.1016/j.powtec.2015.12.029.

[59] Tanja Stirnimann, Susanna Atria, Joachim Schoelkopf, Patrick A C Gane, Rainer Alles, Jörg Huwyler, and Maxim Puchkov. Compaction of functionalized calcium carbonate, a porous and crystalline microparticulate material with a lamellar surface. *International Journal of Pharmaceutics*, 466(1-2):266–275, 2014. ISSN 18733476. doi: 10.1016/j.ijpharm.2014.03.027.

[60] Sherif I Farag Badawy, David B. Gray, and Munir A. Hussain. A study on the effect of wet granulation on microcrystalline cellulose particle structure and performance.

Pharmaceutical Research, 23(3):634–640, 2006. ISSN 07248741. doi: 10.1007/s11095-005-9555-z.

[61] Rita Vanbever, Jeffrey D. Mintzes, Jue Wang, Jacquelyn Nice, Donghao Chen, Richard Batycky, Robert Langer, and David A. Edwards. Formulation and Physical Characterization of Large Porous Particles for Inhalation. *Pharmaceutical Research*, 16(11):1735–1742, 1999. doi: 10.1023/A:1018910200420.

[62] Daniel Markl and J. Axel Zeitler. A Review of Disintegration Mechanisms and Measurement Techniques. *Pharmaceutical Research*, 34(5):890–917, 2017. ISSN 1573904X. doi: 10.1007/s11095-017-2129-z.

[63] Luis A. Dellamary, Thomas E. Tarara, Dan J. Smith, Christopher H. Woelk, Anastasios Adractas, Michael L. Costello, Howard Gill, and Jeffry G. Weers. Hollow porous particles in metered dose inhalers. *Pharmaceutical Research*, 17(2):168–174, 2000. ISSN 07248741. doi: 10.1023/A:1007513213292.

[64] S. P. Duddu, S. A. Sisk, Y. H. Walter, T. E. Tarara, K. R. Trimble, A. R. Clark, M. A. Eldon, R. C. Elton, M. Pickford, P. H. Hirst, S. P. Newman, and J. G. Weers. Improved lung delivery from a passive dry powder inhaler using an engineered PulmoSphere® powder. *Pharmaceutical Research*, 19(5):689–695, 2002. ISSN 07248741. doi: 10.1023/A:1015322616613.

[65] Morishima Kenji, Kawashima Yoshiaki, Takeuchi Hirofumi, Niwa Toshiyuki, Hino Tomoaki, and Kawashima Yoichi. Tabletting properties of bucillamine agglomerates prepared by the spherical crystallization technique. *International Journal of Pharmaceutics*, 105(1):11–18, 1994. ISSN 03785173. doi: 10.1016/0378-5173(94)90230-5.

[66] Daniel Markl, Alexa Strobel, Rüdiger Schlossnikl, Johan Bøtker, Prince Bawuah, Cathy Ridgway, Jukka Rantanen, Thomas Rades, Patrick Gane, Kai Erik Peiponen, and J. Axel Zeitler. Characterisation of pore structures of pharmaceutical tablets: A review. *International Journal of Pharmaceutics*, 538(1-2):188–214, 2018. ISSN 18733476. doi: 10.1016/j.ijpharm.2018.01.017.

[67] Rebecca A. Halliwell, Rajni M. Bhardwaj, Cameron J. Brown, Naomi E.B. Briggs, Jaclyn

Dunn, John Robertson, Alison Nordon, and Alastair J. Florence. Spray Drying as a Reliable Route to Produce Metastable Carbamazepine Form IV. *Journal of Pharmaceutical Sciences*, 106(7):1874–1880, 2017. ISSN 15206017. doi: 10.1016/j.xphs.2017.03.045.

[68] Sherry L. Morissette, Stephen Soukasene, Douglas Levinson, Michael J. Cima, and Örn Almarsson. Elucidation of crystal form diversity of the HIV protease inhibitor ritonavir by high-throughput crystallization. *Proceedings of the National Academy of Sciences of the United States of America*, 100(5):2180–2184, 2003. ISSN 00278424. doi: 10.1073/pnas.0437744100.

[69] Nan Fu, Meng Wai Woo, Cordelia Selomulya, and Xiao Dong Chen. Shrinkage behaviour of skim milk droplets during air drying. *Journal of Food Engineering*, 116(1):37–44, 2013. ISSN 0260-8774. doi: 10.1016/j.jfoodeng.2012.11.005.

[70] F Parisse and C Allain. Drying of Colloidal Suspension Droplets: Experimental Study and Profile Renormalization. *Langmuir*, 13(14):3598–3602, 1997. ISSN 0743-7463. doi: 10.1021/la951521g.

[71] N Tsapis, E R Dufresne, S S Sinha, C S Riera, J W Hutchinson, L Mahadevan, and D A Weitz. Onset of Buckling in Drying Droplets of Colloidal Suspensions. *Physical Review Letters*, 94(1):18302, 2005. ISSN 0031-9007. doi: 10.1103/PhysRevLett.94.018302.

[72] Samuel Rogers, Winston Duo Wu, Lin, Sean Xu Qi, and Xiao Dong Chen. Particle shrinkage and morphology of milk powder made with a monodisperse spray dryer. *Biochemical Engineering Journal*, 62:92–100, 2012. ISSN 1369703X. doi: 10.1016/j.bej.2011.11.002.

[73] Alberto Baldelli, Mohammed A Boraey, David S Nobes, and Reinhard Vehring. Analysis of the Particle Formation Process of Structured Microparticles. *Molecular pharmaceutics*, 12(8):2562–2573, 2015. doi: 10.1021/mp500758s.

[74] Alberto Baldelli, Rory M. Power, Rachael E. H. Miles, Jonathan P. Reid, and Reinhard Vehring. Effect of crystallization kinetics on the properties of spray dried microparticles. *Aerosol Science and Technology*, 50(7):693–704, 2016. ISSN 0278-6826. doi: 10.1080/02786826.2016.1177163.

[75] James W. Ivey, Pallavi Bhambri, Tanya K. Church, David A. Lewis, and Reinhard Vehring. Experimental investigations of particle formation from propellant and solvent droplets using a monodisperse spray dryer. *Aerosol Science and Technology*, 6826:1–15, 2018. ISSN 0278-6826. doi: 10.1080/02786826.2018.1451818.

[76] Selin Manukyan, Hans M. Sauer, Ilia V. Roisman, Kyle A. Baldwin, David J. Fairhurst, Haida Liang, Joachim Venzmer, and Cameron Tropea. Imaging internal flows in a drying sessile polymer dispersion drop using Spectral Radar Optical Coherence Tomography (SR-OCT). *Journal of Colloid and Interface Science*, 395(1):287–293, 2013. ISSN 00219797. doi: 10.1016/j.jcis.2012.11.037.

[77] Jacob Bouman, Paul Venema, Renko J. de Vries, Erik van der Linden, and Maarten A I Schutyser. Hole and vacuole formation during drying of sessile whey protein droplets. *Food Research International*, 84:128–135, 2016. ISSN 09639969. doi: 10.1016/j.foodres.2016.03.027.

[78] F. Sondej, M. Peglow, A. Bück, and E. Tsotsas. Experimental investigation of the morphology of salt deposits from drying sessile droplets by white-light interferometry. *AIChE Journal*, 00(00):1–15, 2018. ISSN 15475905. doi: 10.1002/aic.16085.

[79] Jui-chen Lin, James W Gentry, Jui-chen Lin, and James W Gentry. Spray Drying Drop Morphology: Experimental Study. *Aerosol Science & Technology*, 37(1):15–32, 2003. doi: 10.1080/02786820300888.

[80] Christian Chauveau, Madjid Birouk, and Iskender Gökalp. An analysis of the d2-law departure during droplet evaporation in microgravity. *International Journal of Multiphase Flow*, 37(3):252–259, 2011. ISSN 03019322. doi: 10.1016/j.ijmultiphaseflow.2010.10.009.

[81] L. Malafronte, L. Ahrné, E. Kaunisto, F. Innings, and A. Rasmuson. Estimation of the effective diffusion coefficient of water in skim milk during single-drop drying. *Journal of Food Engineering*, 147(C):111–119, 2015. ISSN 02608774. doi: 10.1016/jjfoodeng.2014.09.032.

[82] L. Malafronte, L. Ahrné, E. Schuster, F. Innings, and A. Rasmuson. Exploring drying

kinetics and morphology of commercial dairy powders. *Journal of Food Engineering*, 158:58–65, 2015. ISSN 02608774. doi: 10.1016/j.jfoodeng.2015.02.029.

[83] T T H Tran, J G Avila-Acevedo, and E Tsotsas. Enhanced methods for experimental investigation of single droplet drying kinetics and application to lactose/water. *Drying Technology*, 34(10):1185–1195, 2016. doi: 10.1080/07373937.2015.1100202.

[84] Elke Lorenzen and Geoffrey Lee. Trehalose and sorbitol alter the kinetic pattern of inactivation of glutamate dehydrogenase during drying in levitated microdroplets. *Journal of Pharmaceutical Sciences*, 102(12):4268–4273, 2013. ISSN 00223549. doi: 10.1002/jps.23743.

[85] Natalie Keil and Geoffrey Lee. Use of acoustic levitation to examine the drying behavior of microdroplets of polymer latex dispersions. *Colloid and Polymer Science*, 294(12): 1921–1928, 2016. ISSN 0303-402X. doi: 10.1007/s00396-016-3954-z.

[86] Holger Grosshans, Matthias Griesing, Mathias Mönckedieck, Thomas Hellwig, Benjamin Walther, Srikanth R. Gopireddy, Robert Sedelmayer, Werner Pauer, Hans Ulrich Moritz, Nora A. Urbanetz, and Eva Gutheil. Numerical and experimental study of the drying of bi-component droplets under various drying conditions. *International Journal of Heat and Mass Transfer*, 96:97–109, 2016. ISSN 00179310. doi: 10.1016/j.ijheatmasstransfer.2015.12.062.

[87] Marine Nuzzo, Jakob Sloth Overgaard, Björn Bergenståhl, and Anna Millqvist-Fureby. The morphology and internal composition of dried particles from whole milk—From single droplet to full scale drying. *Food Structure*, 13:35–44, 2017. ISSN 22133291. doi: 10.1016/j.foostr.2017.02.001.

[88] E. M. Both, M. Nuzzo, A. Millqvist-Fureby, R. M. Boom, and M. A.I. Schutyser. Morphology development during single droplet drying of mixed component formulations and milk. *Food Research International*, 109(March):448–454, 2018. ISSN 18737145. doi: 10.1016/j.foodres.2018.04.043.

[89] Yuki Niimura and Koji Hasegawa. Evaporation of droplet in mid-air: Pure and binary droplets in single-axis acoustic levitator. *PLoS ONE*, 14(2):1–15, 2019. ISSN 19326203. doi: 10.1371/journal.pone.0212074.

[90] Louis Vessot King. On the acoustic radiation pressure on spheres. *Proceedings of the Royal Society of London. Series A-Mathematical and Physical Sciences*, 147(861):212–240, 1934.

[91] Oliver Kastner, Günter Brenn, Dirk Rensink, and Cameron Tropea. The acoustic tube levitator - A novel device for determining the drying kinetics of single droplets. *Chemical Engineering and Technology*, 24(4):335–339, 2001. ISSN 09307516. doi: 10.1002/1521-4125(200104)24:4<335::AID-CEAT335>3.0.CO;2-8.

[92] W J Xie, C D Cao, Y J Lü, and B Wei. Levitation of iridium and liquid mercury by ultrasound. *Physical review letters*, 89(10):104304, 2002. ISSN 0031-9007. doi: 10.1103/PhysRevLett.89.104304.

[93] Rudolf Tuckermann. *Gase, Aerosole, Tropfen und Partikel in stehenden Ultraschallfeldern: Eine Untersuchung zur Anreicherung schwerer Gase , Verdampfung levitierter Tropfen , Kristall- und Partikelbildung*. Ph.d., Technical University Carolo-Wilhelmina, 2002.

[94] Rudolf Tuckermann, Sigurd Bauerecker, and Bernd Neidhart. Schwebende Tröpfchen: Levitation in Ultraschallfeldern. *Physik in unserer Zeit*, 32(2):69–75, 2001. ISSN 00319252. doi: 10.1002/1521-3943(200103)32:2<69::aid-piuz69>3.3.co;2-r.

[95] A L Yarin, G Brenn, O Kastner, D RENSINK, and C Tropea. Evaporation of acoustically levitated droplets. *Journal of Fluid Mechanics*, 399:151–204, 1999. ISSN 0022-1120. doi: 10.1017/S0022112099006266.

[96] Chun P. Lee and Taylor G. Wang. Near-boundary streaming around a small sphere due to two orthogonal standing waves. *The Journal of the Acoustical Society of America*, 85 (3):1081–1088, 1989. ISSN 0001-4966. doi: 10.1121/1.397491.

[97] N Kawahara, A L Yarin, G Brenn, O Kastner, and F Durst. Effect of acoustic streaming on the mass transfer from a sublimating sphere. *Physics of Fluids*, 12(4):912, 2000. ISSN 10706631. doi: 10.1063/1.870347.

[98] Jui-Chen Lin and James W Gentry. Spray Drying Drop Morphology: Experimental

Study. *Aerosol Science and Technology*, 37(1):15–32, 2003. ISSN 0278-6826. doi: 10.1080/02786820300888.

[99] Eva Wulsten and Geoffrey Lee. Surface temperature of acoustically levitated water microdroplets measured using infra-red thermography. *Chemical Engineering Science*, 63 (22):5420–5424, 2008. ISSN 00092509. doi: 10.1016/j.ces.2008.07.020.

[100] Eva Wulsten, Filip Kiekens, Frederic van Dycke, Jody Voorspoels, and Geoffrey Lee. Levitated single-droplet drying: case study with itraconazole dried in binary organic solvent mixtures. *International Journal of Pharmaceutics*, 378(1-2):116–121, 2009. ISSN 0378-5173. doi: 10.1016/j.ijpharm.2009.05.060.

[101] M. Griesing, H. Grosshans, T Hellwig, R Sedelmayer, S.R. Gopireddy, W. Pauer, E. Gutheil, and H.-U. Moritz. Influence of the Drying Air Humidity on the Particle Formation of Single Mannitol-Water Droplets. *Chemie-Ingenieur-Technik*, submitted(7): 1–9, 2015. ISSN 15222640. doi: 10.1002/cite.201500087.

[102] Abdulkadir Osman, Lucas Goehring, Alessandro Patti, Hugh Stitt, and Nima Shokri. Fundamental Investigation of the Drying of Solid Suspensions. *Industrial and Engineering Chemistry Research*, 56(37):10506–10513, 2017. ISSN 15205045. doi: 10.1021/acs.iecr.7b02334.

[103] M. Kreimer, I. Aigner, S. Sacher, M. Krumme, T. Mannschott, P. van der Wel, A. Kaptein, H. Schroettner, G. Brenn, and J. G. Khinast. Mechanical strength of microspheres produced by drying of acoustically levitated suspension droplets. *Powder Technology*, 325: 247–260, 2018. ISSN 1873328X. doi: 10.1016/j.powtec.2017.11.013.

[104] N. Keil, S. Will, and G. Lee. Correlation of the kinetics of aggregation and inactivation of L-glutamate dehyrogenase during drying and particle formation of a levitated microdroplet. *Drying Technology*, 0(0):1–9, 2018. ISSN 15322300. doi: 10.1080/07373937.2018.1445097.

[105] Maarten A I Schutyser, Jimmy Perdana, and Remko M. Boom. Single droplet drying for optimal spray drying of enzymes and probiotics. *Trends in Food Science and Technology*, 27(2):73–82, 2012. ISSN 09242244. doi: 10.1016/j.tifs.2012.05.006.

[106] GEA Process Engineering. GEA Niro DRYNETICS ™. URL https://www.gea.com/en/binaries/drying-spray-drynetic-gea{_}tcm11-34873.pdf.

[107] T. Ullum, J. Sloth, A. Brask, and M. Wahlberg. Predicting Spray Dryer Deposits by CFD and an Empirical Drying Model. *Drying Technology*, 28(5):723–729, 2010. ISSN 0737-3937. doi: 10.1080/07373931003799319.

[108] Jakob Sloth. Method for improving spray drying equipment and product properties. *InterCeram: International Ceramic Review*, 59(3):193–197, 2010. ISSN 00205214.

[109] Marine Nuzzo, Jakob Sloth, Birgit Brandner, Björn Bergenstahl, and Anna Millqvist-Fureby. Confocal Raman microscopy for mapping phase segregation in individually dried particles composed of lactose and macromolecules. *Colloids and Surfaces A: Physicochemical and Engineering Aspects*, 481:229–236, 2015. ISSN 18734359. doi: 10.1016/j.colsurfa.2015.04.044.

[110] David A. Edwards and Craig Dunbar. Bioengineering of Therapeutic Aerosols. *Annual Review of Biomedical Engineering*, 4(1):93–107, 2002. ISSN 1523-9829. doi: 10.1146/annurev.bioeng.4.100101.132311.

[111] Morten Jonas Maltesen, Simon Bjerregaard, Lars Hovgaard, Svend Havelund, and Marco van de Weert. Quality by design - Spray drying of insulin intended for inhalation. *European Journal of Pharmaceutics and Biopharmaceutics*, 70(3):828–838, 2008. ISSN 09396411. doi: 10.1016/j.ejpb.2008.07.015.

[112] Orla Ní Ógáin, Lidia Tajber, Owen I. Corrigan, and Anne Marie Healy. Spray drying from organic solvents to prepare nanoporous/nanoparticulate microparticles of protein: Excipient composites designed for oral inhalation. *Journal of Pharmacy and Pharmacology*, 64(9):1275–1290, 2012. ISSN 00223573. doi: 10.1111/j.2042-7158.2012.01488.x.

[113] Michael Maury, Keith Murphy, Sandeep Kumar, Alexander Mauerer, and Geoffrey Lee. Spray-drying of proteins: Effects of sorbitol and trehalose on aggregation and FT-IR amide I spectrum of an immunoglobulin G. *European Journal of Pharmaceutics and Biopharmaceutics*, 59(2):251–261, 2005. ISSN 09396411. doi: 10.1016/j.ejpb.2004.07.010.

[114] V. Vanhoorne, P. J. Van Bockstal, B. Van Snick, E. Peeters, T. Monteyne, P. Gomes, T. De Beer, J. P. Remon, and C. Vervaet. Continuous manufacturing of delta mannitol by cospray drying with PVP. *International Journal of Pharmaceutics*, 501(1-2):139–147, 2016. ISSN 18733476. doi: 10.1016/j.ijpharm.2016.02.001.

[115] Robert O Williams III, Alan B Watts, and Dave A Miller. *Formulating poorly water soluble drugs*, volume 3. Springer Science {&} Business Media, 2011.

[116] Amrit Paudel, Zelalem Ayenew Worku, Joke Meeus, Sandra Guns, and Guy van den Mooter. Manufacturing of solid dispersions of poorly water soluble drugs by spray drying: formulation and process considerations. *International Journal of Pharmaceutics*, 453(1):253–284, 2013. ISSN 0378-5173. doi: 10.1016/j.ijpharm.2012.07.015.

[117] Ian C. Kemp and David E. Oakley. Modelling of Particulate Drying in Theory and Practice. *Drying Technology*, 20(9):1699–1750, 2002. ISSN 0737-3937. doi: 10.1081/DRT-120015410.

[118] Jianguo Zhang, Frédéric Leroy, and Florian Müller-Plathe. Evaporation of nanodroplets on heated substrates: A molecular dynamics simulation study. *Langmuir*, 29(31):9770–9782, 2013. ISSN 07437463. doi: 10.1021/la401655h.

[119] Weihong Zhang, Yan Li, Yunshu Qi, Han Yuan, and Ning Mei. Molecular dynamics simulation of characteristics of the nanodroplet evaporation. *Energy Procedia*, 153:125–130, 2018. ISSN 18766102. doi: 10.1016/j.egypro.2018.10.014.

[120] Mark Pinto, Ian Kemp, Sean Bermingham, Thoralf Hartwig, and Ariane Bisten. Development of an axisymmetric population balance model for spray drying and validation against experimental data and CFD simulations. *Chemical Engineering Research and Design*, 92(4):619–634, 2014. ISSN 02638762. doi: 10.1016/j.cherd.2013.12.019.

[121] Muzammil Ali, Tariq Mahmud, Peter John Heggs, Mojtaba Ghadiri, Andrew Bayly, Hossein Ahmadian, and Luis Martin de Juan. CFD modeling of a pilot-scale countercurrent spray drying tower for the manufacture of detergent powder. *Drying Technology*, 35(3):281–299, 2017. ISSN 15322300. doi: 10.1080/07373937.2016.1163576.

[122] Ivana M. Cotabarren, Diego Bertín, Mariela Razuc, M. Verónica Ramírez-Rigo, and Juliana Piña. Modelling of the spray drying process for particle design. *Chemical Engineering Research and Design*, 132:1091–1104, 2018. ISSN 02638762. doi: 10.1016/j.cherd.2018.01.012.

[123] Dr David E. Oakley. Spray Dryer Modeling in Theory and Practice. *Drying Technology*, 22(6):1371–1402, 2004. ISSN 0737-3937. doi: 10.1081/DRT-120038734.

[124] Niels Grasmeijer, Hans de Waard, Wouter L J Hinrichs, and Henderik W. Frijlink. A User-Friendly Model for Spray Drying to Aid Pharmaceutical Product Development. *PLoS ONE*, 8(9), 2013. ISSN 19326203. doi: 10.1371/journal.pone.0074403.

[125] Bhesh R. Bhandari, Nivedita Datta, and Tony Howes. Problems associated with spray drying of sugar-rich foods. *Drying Technology*, 15(2):671–684, 1997. ISSN 07373937. doi: 10.1080/07373939708917253.

[126] Michael Maury, Keith Murphy, Sandeep Kumar, Lei Shi, and Geoffrey Lee. Effects of process variables on the powder yield of spray-dried trehalose on a laboratory spray-dryer. *European Journal of Pharmaceutics and Biopharmaceutics*, 59(3):565–573, 2005. ISSN 0939-6411. doi: 10.1016/j.ejpb.2004.10.002.

[127] Buchi Switzerland. Operation Manual Mini Spray Dryer B-290. *BÜCHI Labortechnik AG*, pages 1–58, 2006. URL http://www.buchi.com/products/spray-drying-and-encapsulation/mini-spray-dryer-b-290.

[128] I. C. Kemp, T. Hartwig, R. Herdman, P. Hamilton, A. Bisten, and S. Bermingham. Spray drying with a two-fluid nozzle to produce fine particles: Atomization, scale-up, and modeling. *Drying Technology*, 34(10):1243–1252, 2016. ISSN 0737-3937. doi: 10.1080/07373937.2015.1103748. URL http://www.tandfonline.com/doi/full/10.1080/07373937.2015.1103748.

[129] P A T A Framework. Guidance for Industry Guidance for Industry PAT — A Framework for Innovative Pharmaceutical. (September), 2004.

[130] Lars Norbert Petersen, John Bagterp Jørgensen, and James B. Rawlings. Economic optimization of spray dryer operation using Nonlinear Model Predictive Control with

state estimation. *IFAC-PapersOnLine*, 28(8):507–513, 2015. ISSN 24058963. doi: 10.1016/j.ifacol.2015.09.018.

[131] Kristina Ståhl, Malin Claesson, Pontus Lilliehorn, Helena Lindén, and Kjell Bäckström. The effect of process variables on the degradation and physical properties of spray dried insulin intended for inhalation. *International Journal of Pharmaceutics*, 233:227–237, 2002.

[132] Gaurav Kanojia, Geert-Jan Willems, Henderik W. Frijlink, Gideon F.A. Kersten, Peter C. Soema, and Jean-Pierre Amorij. A Design of Experiment approach to predict product and process parameters for a spray dried influenza vaccine. *International Journal of Pharmaceutics*, 511(2):1098–1111, 2016. ISSN 03785173. doi: 10.1016/j.ijpharm.2016.08.022.

[133] A Aliseda, E J Hopfinger, J C Lasheras, D M Kremer, A Berchielli, and E K Connolly. Atomization of viscous and non-newtonian liquids by a coaxial, high-speed gas jet. Experiments and droplet size modeling. *International Journal of Multiphase Flow*, 34(2):161–175, 2008. ISSN 03019322. doi: 10.1016/j.ijmultiphaseflow.2007.09.003.

[134] João Vicente, João Pinto, José Menezes, and FILIPE Gaspar. Fundamental analysis of particle formation in spray drying. *Powder Technology*, 247:1–7, 2013. ISSN 00325910. doi: 10.1016/j.powtec.2013.06.038.

[135] Hung Leba, Ana Cameirao, Jean Michel Herri, Myriam Darbouret, Jean Louis Peytavy, and Philippe Glénat. Chord length distributions measurements during crystallization and agglomeration of gas hydrate in a water-in-oil emulsion: Simulation and experimentation. *Chemical Engineering Science*, 65(3):1185–1200, 2010. ISSN 00092509. doi: 10.1016/j.ces.2009.09.074.

[136] Cameron J. Brown, Thomas McGlone, Stephanie Yerdelen, Vijay Srirambhatla, Fraser Mabbott, Rajesh Gurung, Maria L. Briuglia, Bilal Ahmed, Hector Polyzois, John McGinty, Francesca Perciballi, Dimitris Fysikopoulos, Pól MacFhionnghaile, Humera Siddique, Vishal Raval, Tomás S. Harrington, Antony D. Vassileiou, Murray Robertson, Elke Prasad, Andrea Johnston, Blair Johnston, Alison Nordon, Jagjit S. Srai, Gavin

Halbert, Joop H. ter Horst, Chris J. Price, Chris D. Rielly, Jan Sefcik, and Alastair J. Florence. Enabling precision manufacturing of active pharmaceutical ingredients: workflow for seeded cooling continuous crystallisations. *Molecular Systems Design & Engineering*, 3(3):518–549, jun 2018. ISSN 2058-9689. doi: 10.1039/C7ME00096K.

[137] L W Chan, L H Tan, and Paul W S Heng. Process Analytical Technology : Application to Particle Sizing in Spray Drying. *AAPS PharmSciTech*, 9(1), 2008. doi: 10.1208/s12249-007-9011-y.

[138] D. E. Walton. The morphology of spray-dried particles a qualitative view. *Drying Technology*, 18(9):1943–1986, 2000. ISSN 07373937. doi: 10.1080/07373930008917822.

[139] Amin Farshchi, Ali Hassanpour, Rammile Ettelaie, and Andrew E. Bayly. Evolution of surface micro-structure and moisture sorption characteristics of spray-dried detergent powders. *Journal of Colloid and Interface Science*, 551:283–296, 2019. ISSN 10957103. doi: 10.1016/j.jcis.2019.04.069.

[140] Nicholas B. Carrigy, Mani Ordoubadi, Yushan Liu, Omar Melhem, David Barona, Hui Wang, Leanne Milburn, Conor A. Ruzycki, Warren H. Finlay, and Reinhard Vehring. Amorphous pullulan trehalose microparticle platform for respiratory delivery. *International Journal of Pharmaceutics*, 563(February):156–168, 2019. ISSN 18733476. doi: 10.1016/j.ijpharm.2019.04.004.

[141] L. Ozmen and T. A.G. Langrish. Comparison of glass transition temperature and sticky point temperature for skim milk powder. *Drying Technology*, 20(6):1177–1192, 2002. ISSN 07373937. doi: 10.1081/DRT-120004046.

[142] Liang Li, Siping Sun, Thaigarajan Parumasivam, John A. Denman, Thomas Gengenbach, Patricia Tang, Shirui Mao, and Hak Kim Chan. L-Leucine as an excipient against moisture on in vitro aerosolization performances of highly hygroscopic spray-dried powders. *European Journal of Pharmaceutics and Biopharmaceutics*, 102:132–141, 2016. ISSN 18733441. doi: 10.1016/j.ejpb.2016.02.010.

[143] Lian Yu and Kingman Ng. Glycine crystallization during spray drying: the pH effect on salt and polymorphic forms. *Journal of pharmaceutical sciences*, 91(11):2367–2375, 2002. ISSN 1520-6017. doi: 10.1002/jps.10225.

[144] Yan Ying Lee, Jian X. Wu, Mingshi Yang, Paul M. Young, Frans Van Den Berg, and Jukka Rantanen. Particle size dependence of polymorphism in spray-dried mannitol. *European Journal of Pharmaceutical Sciences*, 44(1-2):41–48, 2011. ISSN 09280987. doi: 10.1016/j.ejps.2011.06.002.

[145] Ahmad Ziaee, Ahmad B. Albadarin, Luis Padrela, Alexandra Faucher, Emmet O'Reilly, and Gavin Walker. Spray drying ternary amorphous solid dispersions of ibuprofen – An investigation into critical formulation and processing parameters. *European Journal of Pharmaceutics and Biopharmaceutics*, 120(August):43–51, 2017. ISSN 09396411. doi: 10.1016/j.ejpb.2017.08.005.

[146] M Adler and G Lee. Stability and surface activity of lactate dehydrogenase in spray dried trehalose. *Journal of Pharamceutical Sciences*, 88(2):199–208, 1999. ISSN 0022-3549. doi: 10.1021/js980321x.

[147] Anke Saß and Geoffrey Lee. Evaluation of some water-miscible organic solvents for spray-drying enzymes and carbohydrates. *Drug Development and Industrial Pharmacy*, 9045(6):749–757, 2014. doi: 10.3109/03639045.2013.782554.

[148] Michael Maury, Keith Murphy, Sandeep Kumar, Alexander Mauerer, and Geoffrey Lee. Spray-drying of proteins: Effects of sorbitol and trehalose on aggregation and FT-IR amide I spectrum of an immunoglobulin G. *European Journal of Pharmaceutics and Biopharmaceutics*, 59(2):251–261, 2005. ISSN 09396411. doi: 10.1016/j.ejpb.2004.07.010.

[149] James E Patterson, Michael B James, Angus H Forster, Robert W Lancaster, James M Butler, and Thomas Rades. Preparation of glass solutions of three poorly water soluble drugs by spray drying, melt extrusion and ball milling. *International Journal of Pharmaceutics*, 336(1):22–34, 2007. ISSN 0378-5173. doi: 10.1016/j.ijpharm.2006.11.030.

[150] M J Paulus, M J Paulus, S S Gleason, S S Gleason, S J Kennel, S J Kennel, P R Hunsicker, P R Hunsicker, D K Johnson, and D K Johnson. High resolution X-ray computed tomography: an emerging tool for small animal cancer research. *Neoplasia (New York, N.Y.)*, 2(1-2):62–70, 2000. ISSN 1522-8002.

[151] Islem Rekik, Stéphanie Allassonnière, Trevor K. Carpenter, and Joanna M. Wardlaw. Medical image analysis methods in MR/CT-imaged acute-subacute ischemic stroke lesion: Segmentation, prediction and insights into dynamic evolution simulation models. A critical appraisal. *NeuroImage: Clinical*, 1(1):164–178, 2012. ISSN 22131582. doi: 10.1016/j.nicl.2012.10.003.

[152] V Cnudde and M N Boone. High-resolution X-ray computed tomography in geosciences: A review of the current technology and applications. *Earth Science Reviews*, 123:1–17, 2013. ISSN 0012-8252. doi: 10.1016/j.earscirev.2013.04.003.

[153] Dorthe Wildenschild and Adrian P Sheppard. X-ray imaging and analysis techniques for quantifying pore-scale structure and processes in subsurface porous medium systems. *Advances in Water Resources*, 51:217–246, 2013. ISSN 03091708. doi: 10.1016/j.advwatres.2012.07.018.

[154] G Viggiani, E Ando, D Takano, and J C Santamarina. Laboratory X-ray Tomography: A Valuable Experimental Tool for Revealing Processes in Soils. *Geotechnical Testing Journal*, 38:61–71, 2014. doi: 10.1520/GTJ20140060.

[155] M Polacci, F Arzilli, G La Spina, N Le Gall, B Cai, M E Hartley, D Di Genova, N T Vo, S Nonni, R C Atwood, E W Llewellin, P D Lee, and M R Burton. Crystallisation in basaltic magmas revealed via in situ 4D synchrotron X-ray microtomography. *Scientific Reports*, 8(March):1–13, 2018. ISSN 2045-2322. doi: 10.1038/s41598-018-26644-6.

[156] Longwei Fang, Xianzhen Yin, Li Wu, Yaping He, Yuanzhi He, Wei Qin, Fanyue Meng, Peter York, Xu Xu, and Jiwen Zhang. Classification of microcrystalline celluloses via structures of individual particles measured by synchrotron radiation X-ray micro-computed tomography. *International Journal of Pharmaceutics*, 531(2):658–667, 2017. ISSN 18733476. doi: 10.1016/j.ijpharm.2017.05.019.

[157] Giacomo Perfetti, Elke Van De Casteele, Bernd Rieger, Willem J. Wildeboer, and Gabrie M H Meesters. X-ray micro tomography and image analysis as complementary methods for morphological characterization and coating thickness measurement of coated particles. *Advanced Powder Technology*, 21(6):663–675, 2010. ISSN 09218831. doi: 10.1016/j.apt.2010.08.002.

[158] Franziska Sondej, Andreas Bück, Katharina Koslowsky, Philipp Bachmann, Michael Jacob, and Evangelos Tsotsas. Investigation of coating layer morphology by micro-computed X-ray tomography. *Powder Technology*, 273:165–175, 2015. ISSN 1873328X. doi: 10.1016/j.powtec.2014.12.050.

[159] John F Gamble, Masako Terada, Christian Holzner, Leah Lavery, Sarah J Nicholson, Peter Timmins, and Mike Tobyn. Application of X-ray microtomography for the characterisation of hollow polymer-stabilised spray dried amorphous dispersion particles. *International Journal of Pharmaceutics*, 510(1):1–8, 2016. ISSN 0378-5173. doi: 10.1016/j.ijpharm.2016.05.051.

[160] Paul M Young, Kathy Nguyen, Allan S Jones, and Daniela Traini. Microstructural Analysis of Porous Composite Materials : Dynamic Imaging of Drug Dissolution and Diffusion Through Porous Matrices. *The AAPS journal*, 10(4):560–564, 2008. doi: 10.1208/s12248-008-9063-2.

[161] Daniel Markl, J. Axel Zeitler, Cecilie Rasch, Maria Høtoft Michaelsen, Anette Müllertz, Jukka Rantanen, Thomas Rades, and Johan Bøtker. Analysis of 3D Prints by X-ray Computed Microtomography and Terahertz Pulsed Imaging. *Pharmaceutical Research*, pages 1037–1052, 2016. ISSN 0724-8741. doi: 10.1007/s11095-016-2083-1.

[162] Glenn F Knoll. *Radiation detection and measurement*. John Wiley & Sons, 2010.

[163] Brian D Metscher. MicroCT for comparative morphology: simple staining methods allow high-contrast 3D imaging of diverse non-mineralized animal tissues. *BMC physiology*, 9:11, 2009. ISSN 1472-6793. doi: 10.1186/1472-6793-9-11.

[164] Brian D Metscher. MicroCT for developmental biology: a versatile tool for high-contrast 3D imaging at histological resolutions. *Developmental dynamics : an official publication of the American Association of Anatomists*, 238(3):632–640, 2009. ISSN 1058-8388. doi: 10.1002/dvdy.21857.

[165] Nathan S. Jeffery, Robert S. Stephenson, James A. Gallagher, Jonathan C. Jarvis, and Philip G. Cox. Micro-computed tomography with iodine staining resolves the arrangement of muscle fibres. *Journal of Biomechanics*, 44(1):189–192, 2011. ISSN 00219290. doi: 10.1016/j.jbiomech.2010.08.027.

[166] Oleg V. Aslanidi, Theodora Nikolaidou, Jichao Zhao, Bruce H. Smaill, Stephen H. Gilbert, Arun V. Holden, Tristan Lowe, Philip J. Withers, Robert S. Stephenson, Jonathan C. Jarvis, Jules C. Hancox, Mark R. Boyett, and Henggui Zhang. Application of micro-computed tomography with iodine staining to cardiac imaging, segmentation, and computational model development. *IEEE Transactions on Medical Imaging*, 32(1): 8–17, 2013. ISSN 02780062. doi: 10.1109/TMI.2012.2209183.

[167] Robert S Stephenson, Mark R Boyett, George Hart, Theodora Nikolaidou, Xue Cai, Antonio F Corno, Nelson Alphonso, Nathan Jeffery, and Jonathan C Jarvis. Contrast Enhanced Micro-Computed Tomography Resolves the 3-Dimensional Morphology of the Cardiac Conduction System in Mammalian Hearts. *PLoS ONE*, 7(4):1–11, 2012. doi: 10.1371/journal.pone.0035299.

[168] Hui Cao, Dimitris Karampalis, Yongliang Li, Joel Caragay, Alessio Alexiadis, Zhibing Zhang, and Peter J Fryer. Abrupt disintegration of highly porous particles in early stage dissolution. *Powder Technology*, 333:394–403, 2018. doi: 10.1016/j.powtec.2018.04.037.

[169] Xianzhen Yin, Haiyan Li, Zhen Guo, Li Wu, Fangwei Chen, Marcel de Matas, Qun Shao, Tiqiao Xiao, Peter York, You He, and Jiwen Zhang. Quantification of Swelling and Erosion in the Controlled Release of a Poorly Water-Soluble Drug Using Synchrotron X-ray Computed Microtomography. *The AAPS Journal*, 15(4):1025–1034, 2013. ISSN 1550-7416. doi: 10.1208/s12248-013-9498-y.

[170] Philip J. Withers. X-ray nanotomography. *Materials Today*, 10(12):26–34, 2007. ISSN 13697021. doi: 10.1016/S1369-7021(07)70305-X.

[171] Jennifer Wong, Dexter D'Sa, Matthew Foley, John Gar Yan Chan, and Hak-Kim Chan. NanoXCT: a novel technique to probe the internal architecture of pharmaceutical particles. *Pharmaceutical research*, 31(11):3085–3094, 2014. doi: 10.1007/s11095-014-1401-8.

[172] G.N. Hounsfield. Computerized transverse axial scanning (tomography): Part 1. Description of system. *British Journal of Radiology*, 46(552):1016–1022, 1973. ISSN 00071285. doi: 10.1259/0007-1285-46-552-1016.

[173] L A Feldkamp, L C Davis, and J W Kress. Practical cone-beam algorithm. *J. Opt. Soc. Am. A*, 1(6):612–619, jun 1984. doi: 10.1364/JOSAA.1.000612.

[174] E. Van de Casteele, D. Van Dyck, J. Sijbers, and E. Raman. An energy-based beam hardening model in tomography. *Physics in Medicine and Biology*, 47(23):4181–4190, 2002. ISSN 00319155. doi: 10.1088/0031-9155/47/23/305.

[175] Kenneth M Hanson. Technical Aspects of Computed Tomography. *Radiology of the Skull and Brain*, 5(1):3941–3955, 1981.

[176] Richard A Ketcham and William D Carlson. Acquisition, optimization and interpretation of X-ray.pdf. *Computers & Geosciences*, 27:381–400, 2001. ISSN 0098-3004. doi: Doi10.1016/S0098-3004(00)00116-3.

[177] Jan Sijbers and Andrei Postnov. Reduction of ring artefacts in high resolution micro-CT reconstructions. *Physics in Medicine and Biology*, 49(14), 2004. ISSN 00319155. doi: 10.1088/0031-9155/49/14/N06.

[178] G. R. Myers, S. C. Mayo, T. E. Gureyev, D. M. Paganin, and S. W. Wilkins. Polychromatic cone-beam phase-contrast tomography. *Physical Review A - Atomic, Molecular, and Optical Physics*, 76(4):2–5, 2007. ISSN 10502947. doi: 10.1103/PhysRevA.76.045804.

[179] S W Wilkins, T E Gureyev, D Gao, A Pogany, and A W Stevenson. Phase-contrast imaging using polychromatic hard X-rays. *Nature*, 384(6607):335–338, 1996. ISSN 1476-4687. doi: 10.1038/384335a0.

[180] P. Cloetens, W. Ludwig, J. Baruchel, D. Van Dyck, J. Van Landuyt, J. P. Guigay, and M. Schlenker. Holotomography: Quantitative phase tomography with micrometer resolution using hard synchrotron radiation x rays. *Applied Physics Letters*, 75(19):2912–2914, 1999. ISSN 00036951. doi: 10.1063/1.125225.

[181] T. Weitkamp, D. Haas, D. Wegrzynek, and A. Rack. ANKAphase: Software for single-distance phase retrieval from inline X-ray phase-contrast radiographs. *Journal of Synchrotron Radiation*, 18(4):617–629, 2011. ISSN 09090495. doi: 10.1107/S0909049511002895.

[182] J. Zheng and R.D. Hryciw. Traditional soil particle sphericity, roundness and surface roughness by computational geometry. *Géotechnique*, 65(6):494–506, 2015. ISSN 0016-8505. doi: 10.1680/geot.14.P.192.

[183] B Zhou, J Wang, and H Wang. Three-dimensional sphericity , roundness and fractal dimension of sand particles. *Géotechnique*, 2017. doi: 10.1680/jgeot.16.P.207.

[184] D Su and W M Yan. 3D characterization of general-shape sand particles using microfocus X-ray computed tomography and spherical harmonic functions , and particle regeneration using multivariate random vector. *Powder Technology*, 323:8–23, 2018. doi: 10.1016/j.powtec.2017.09.030.

[185] Maryam Asachi, Ali Hassanpour, Mojtaba Ghadiri, and Andrew Bayly. Experimental evaluation of the effect of particle properties on the segregation of ternary powder mixtures. *Powder Technology*, 336:240–254, 2018. ISSN 1873328X. doi: 10.1016/j.powtec.2018.05.017.

[186] M. Dadkhah and E. Tsotsas. Influence of process variables on internal particle structure in spray fluidized bed agglomeration. *Powder Technology*, 258:165–173, may 2014. ISSN 00325910. doi: 10.1016/j.powtec.2014.03.005.

[187] Laura Martinez-Marcos, Dimitrios A Lamprou, Roy T McBurney, and Gavin W Halbert. A novel hot-melt extrusion formulation of albendazole for increasing dissolution properties. *International Journal of Pharmaceutics*, 499(1-2):175–185, 2016. ISSN 0378-5173. doi: 10.1016/j.ijpharm.2016.01.006.

[188] Muqdad Alhijjaj, Samy Yassin, Mike Reading, J. Axel Zeitler, Peter Belton, and Sheng Qi. Characterization of Heterogeneity and Spatial Distribution of Phases in Complex Solid Dispersions by Thermal Analysis by Structural Characterization and X-ray Micro Computed Tomography. *Pharmaceutical Research*, 34(5):971–989, 2017. ISSN 1573904X. doi: 10.1007/s11095-016-1923-3.

[189] Xian-Zhen Yin, Ti-Qiao Xiao, Ashwini Nangia, Shuo Yang, Xiao-Long Lu, Hai-Yan Li, Qun Shao, You He, Peter York, and Ji-Wen Zhang. In situ 3D topographic and shape analysis by synchrotron radiation X-ray microtomography for crystal form identification

in polymorphic mixtures. *Scientific reports*, 6(February):24763, 2016. ISSN 2045-2322. doi: 10.1038/srep24763.

[190] Leon Farber, Gabriel Tardos, and James N. Michaels. Use of X-ray tomography to study the porosity and morphology of granules. *Powder Technology*, 132(1):57–63, 2003. ISSN 00325910. doi: 10.1016/S0032-5910(03)00043-3.

[191] Mohammad R. Arbabshirani, Brandon K. Fornwalt, Gino J. Mongelluzzo, Jonathan D. Suever, Brandon D. Geise, Aalpen A. Patel, and Gregory J. Moore. Advanced machine learning in action: identification of intracranial hemorrhage on computed tomography scans of the head with clinical workflow integration. *npj Digital Medicine*, 1(1), 2018. ISSN 2398-6352. doi: 10.1038/s41746-017-0015-z.

[192] F. Pasa, V. Golkov, F. Pfeiffer, D. Cremers, and D. Pfeiffer. Efficient Deep Network Architectures for Fast Chest X-Ray Tuberculosis Screening and Visualization. *Scientific Reports*, 9(1):2–10, 2019. ISSN 20452322. doi: 10.1038/s41598-019-42557-4.

[193] Asier Marzo, Adrian Barnes, and Bruce W. Drinkwater. TinyLev: A multi-emitter single-axis acoustic levitator. *Review of Scientific Instruments*, 88(8), 2017. ISSN 10897623. doi: 10.1063/1.4989995.

[194] Daniel Zwillinger. *CRC standard mathematical tables and formulae*. Chapman and Hall/CRC, 2002.

[195] Luc Salvo, Michel Suéry, Ariane Marmottant, Nathalie Limodin, and Dominique Bernard. 3D imaging in material science: Application of X-ray tomography. *Comptes Rendus Physique*, 11(9-10):641–649, 2010. ISSN 16310705. doi: 10.1016/j.crhy.2010.12.003.

[196] Hrishikesh Bale, Matthew Blacklock, Matthew R. Begley, David B. Marshall, Brian N. Cox, and Robert O. Ritchie. Characterizing three-dimensional textile ceramic composites using synchrotron x-ray micro-computed-tomography. *Journal of the American Ceramic Society*, 95(1):392–402, 2012. ISSN 00027820. doi: 10.1111/j.1551-2916.2011.04802.x.

[197] E. Maire and P. J. Withers. Quantitative X-ray tomography. *International Materials Reviews*, 59(1):1–43, 2014. ISSN 09506608. doi: 10.1179/1743280413Y.0000000023.

[198] Alessandro Re, Jacopo Corsi, Marco Demmelbauer, Margherita Martini, Giorgia Mila, and Chiara Ricci. X-ray tomography of a soil block: A useful tool for the restoration of archaeological finds. *Heritage Science*, 3(1):0–6, 2015. ISSN 20507445. doi: 10.1186/s40494-015-0033-6.

[199] Michael W. Czabaj, Mark L. Riccio, and William W. Whitacre. Numerical reconstruction of graphite/epoxy composite microstructure based on sub-micron resolution X-ray computed tomography. *Composites Science and Technology*, 105:174–182, 2014. ISSN 02663538. doi: 10.1016/j.compscitech.2014.10.017.

[200] Steven Claes, Jeroen Soete, Veerle Cnudde, and Rudy Swennen. A three-dimensional classification for mathematical pore shape description in complex carbonate reservoir rocks. *Mathematical Geosciences*, 48(6):619–639, 2016. ISSN 1874-8953. doi: 10.1007/s11004-016-9636-z.

[201] Arash Rabbani, Shahab Ayatollahi, Riyaz Kharrat, and Nader Dashti. Estimation of 3-D pore network coordination number of rocks from watershed segmentation of a single 2-D image. *Advances in Water Resources*, 94:264–277, 2016. ISSN 03091708. doi: 10.1016/j.advwatres.2016.05.020.

[202] L. Bocchi, G. Coppini, J. Nori, and G. Valli. Detection of single and clustered microcalcifications in mammograms using fractals models and neural networks. *Medical Engineering and Physics*, 26(4):303–312, 2004. ISSN 13504533. doi: 10.1016/j.medengphy.2003.11.009.

[203] Gaurav Bhatnagar, Q. M.Jonathan Wu, and Zheng Liu. A new contrast based multimodal medical image fusion framework. *Neurocomputing*, 157:143–152, 2015. ISSN 18728286. doi: 10.1016/j.neucom.2015.01.025.

[204] Wesley De Boever, Hannelore Derluyn, Denis Van Loo, Luc Van Hoorebeke, and Veerle Cnudde. Data-fusion of high resolution X-ray CT, SEM and EDS for 3D and pseudo-3D chemical and structural characterization of sandstone. *Micron*, 74:15–21, 2015. ISSN 09684328. doi: 10.1016/j.micron.2015.04.003.

[205] K. M. Kareh, P. D. Lee, R. C. Atwood, T. Connolley, and C. M. Gourlay. Revealing the micromechanisms behind semi-solid metal deformation with time-resolved X-ray tomography. *Nature Communications*, 5:1–7, 2014. ISSN 20411723. doi: 10.1038/ncomms5464.

[206] Tijana Kovacevic, Jonathan Schock, Franz Pfeiffer, and Heiko Briesen. Shape identification of primary particles in potash alum aggregates using three-dimensional tomography data. *Crystal Growth and Design*, 16(5):2685–2699, 2016. ISSN 15287505. doi: 10.1021/acs.cgd.5b01806.

[207] J Axel Zeitler and Lynn F Gladden. In-vitro tomography and non-destructive imaging at depth of pharmaceutical solid dosage forms. *European Journal of Pharmaceutics and Biopharmaceutics*, 71(1):2–22, 2008. ISSN 0939-6411. doi: 10.1016/j.ejpb.2008.08.012.

[208] A. K. Vynckier, H. Lin, J. A. Zeitler, J. F. Willart, E. Bongaers, J. Voorspoels, J. P. Remon, and C. Vervaet. Calendering as a direct shaping tool for the continuous production of fixed-dose combination products via co-extrusion. *European Journal of Pharmaceutics and Biopharmaceutics*, 96:125–131, 2015. ISSN 18733441. doi: 10.1016/j.ejpb.2015.07.023.

[209] Bilal Khorsheed, Ian Gabbott, Gavin K. Reynolds, Stefan C. Taylor, Ron J. Roberts, and Agba D. Salman. Twin-screw granulation: Understanding the mechanical properties from powder to tablets. *Powder Technology*, 341:104–115, 2019. ISSN 1873328X. doi: 10.1016/j.powtec.2018.05.013.

[210] Alexander Katsevich. Theoretically exact filtered backprojection-type inversion algorithm for spiral CT. *SIAM Journal on Applied Mathematics*, 62(6):2012–2026, 2002.

[211] Bruker MicroCT. SkyScan 2211 - User Manual, 2017. URL https://www.bruker.com/products/microtomography.html.

[212] M. R. Howells, T. Beetz, H. N. Chapman, C. Cui, J. M. Holton, C. J. Jacobsen, J. Kirz, E. Lima, S. Marchesini, H. Miao, D. Sayre, D. A. Shapiro, J. C.H. Spence, and D. Starodub. An assessment of the resolution limitation due to radiation-damage in X-ray diffrac-

tion microscopy. *Journal of Electron Spectroscopy and Related Phenomena*, 170(1-3): 4–12, 2009. ISSN 03682048. doi: 10.1016/j.elspec.2008.10.008.

[213] Thomas S Curry, James E Dowdey, and Robert C Murry. *Christensen's physics of diagnostic radiology*. Lippincott Williams & Wilkins, 1990.

[214] Jochen Hiller, Michael Maisl, and Leonard M. Reindl. Physical characterization and performance evaluation of an x-ray micro-computed tomography system for dimensional metrology applications. *Measurement Science and Technology*, 23(8), 2012. ISSN 13616501. doi: 10.1088/0957-0233/23/8/085404.

[215] Chye Hwang Yan, Robert T. Whalen, Gary S. Beaupré, Shin Y. Yen, and Sandy Napel. Reconstruction algorithm for polychromatic CT imaging: application to beam hardening correction. *IEEE Transactions on Medical Imaging*, 19(1):1–11, 2000. ISSN 02780062. doi: 10.1109/42.832955.

[216] Jae S Lim. Two-dimensional signal and image processing. *Englewood Cliffs, NJ, Prentice Hall, 1990, 710 p.*, 1990.

[217] M Kuwahara, K Hachimura, S Eiho, and M Kinoshita. *Processing of RI-Angiocardiographic Images*, pages 187–202. Springer US, Boston, MA, 1976. ISBN 978-1-4684-0769-3. doi: 10.1007/978-1-4684-0769-3_13.

[218] P Perona and J Malik. Scale-space and edge detection using anisotropic diffusion. *IEEE Transactions on Pattern Analysis and Machine Intelligence*, 12(7):629–639, 1990. ISSN 01628828. doi: 10.1109/34.56205.

[219] N Otsu. A Threshold Selection Method from Gray-Level Histograms. *IEEE Transactions on Systems, Man and Cybernetics*, 20(1):62–66, 1975.

[220] T Kurita, N Otsu, and N Abdelmalek. Maximum likelihood thresholding based on population mixture models. *Pattern Recognition*, 25(10):1231–1240, 1992. ISSN 00313203. doi: 10.1016/0031-3203(92)90024-D.

[221] S Ridler, T.W. Calvard. Picture Thresholding Using an Iterative Slection Method. *IEEE Transactions on Systems, Man and Cybernetics*, 8(8):630–632, 1978. ISSN 00189472. doi: 10.1109/TSMC.1978.4310039.

[222] Serge Beucher and Christian Lantuéjoul. Use of Watersheds in Contour Detection. In *International workshop on image processing, real-time edge and motion detection*, 1979.

[223] F Meyer and S Beucher. Morphological Segmentation. *Journal of Visual Communication and Image Representation*, 1(1):21–46, 1990. doi: 10.1016/1047-3203(90)90014-M.

[224] Duen Ren Liu and Ya Yueh Shih. Integrating AHP and data mining for product recommendation based on customer lifetime value. *Information and Management*, 42(3): 387–400, 2005. ISSN 03787206. doi: 10.1016/j.im.2004.01.008.

[225] Gerhard Münz, Sa Li, and Georg Carle. Traffic Anomaly Detection Using K-Means Clustering. In *GI/ITG Workshop MMBnet*, 2007.

[226] Sina Khanmohammadi, Naiier Adibeig, and Samaneh Shanehbandy. An improved overlapping k-means clustering method for medical applications. *Expert Systems with Applications*, 67:12–18, 2017. ISSN 09574174. doi: 10.1016/j.eswa.2016.09.025.

[227] Abdulsalam Yassine, Shailendra Singh, and Atif Alamri. Mining Human Activity Patterns From Smart Home Big Data for Health Care Applications. *Advances of Multisensory Services and Technologies for Healthcare in Smart Cities*, pages 13131 – 13141, 2017. ISSN 2169-3536. doi: 10.1109/ACCESS.2017.2719921.

[228] Yury Petrov. Ellipsoid fit (MATLAB FileExchange), 2015. URL https://uk.mathworks.com/matlabcentral/fileexchange/24693-ellipsoid-fit.

[229] John D'Errico. A suite of minimal bounding objects (MATLAB FileExchange), 2014. URL https://uk.mathworks.com/matlabcentral/fileexchange/34767-a-suite-of-minimal-bounding-objects.

[230] Sun Kyoo Hwang and Whoi Yul Kim. A novel approach to the fast computation of Zernike moments. *Pattern Recognition*, 39(11):2065–2076, 2006. ISSN 00313203. doi: 10.1016/j.patcog.2006.03.004.

[231] Amir Tahmasbi, Fatemeh Saki, and Shahriar B. Shokouhi. Classification of benign and malignant masses based on Zernike moments. *Computers in Biology and Medicine*, 41 (8):726–735, 2011. ISSN 00104825. doi: 10.1016/j.compbiomed.2011.06.009.

[232] Frank P. Kuhl and Charles R Giardina. Elliptic Fourier Features of a Closed Contour. *Computer Graphics and Image Processing*, 18:236–258, 1982.

[233] Hakon Wadell. Volume, Shape, and Roundness of Quartz Particles. *The Journal of Geology*, 43(3):250–280, 1935. doi: 10.1086/624298.

[234] Paul Heckbert. Graphic Gems 4, 1994.

[235] Xiaowei Fu, Meenakshi Dutt, A. Craig Bentham, Bruno C. Hancock, Ruth E. Cameron, and James A. Elliott. Investigation of particle packing in model pharmaceutical powders using X-ray microtomography and discrete element method. *Powder Technology*, 167 (3):134–140, 2006. ISSN 00325910. doi: 10.1016/j.powtec.2006.06.011.

[236] Jae Young Jung, Sun Dong Yoo, Sang Heon Lee, Kye Hyun Kim, Doo Sun Yoon, and Kyu Hyun Lee. Enhanced solubility and dissolution rate of itraconazole by a solid dispersion technique. *International Journal of Pharmaceutics*, 187(2):209–218, 1999. ISSN 03785173. doi: 10.1016/S0378-5173(99)00191-X.

[237] Meer Saiful Hassan and Raymond Wai Man Lau. Effect of particle shape on dry particle inhalation: Study of flowability, aerosolization, and deposition properties. *AAPS PharmSciTech*, 10(4):1252–1262, 2009. ISSN 15309932. doi: 10.1208/s12249-009-9313-3.

[238] Bhavesh Barot, Punit Parejiya, Tushar Patel, Rajesh Parikh, and Mukesh Gohel. Development of directly compressible metformin hydrochloride by the spray-drying technique. *Acta Pharmaceutica*, 60(2):165–175, 2010. ISSN 1846-9558. doi: 10.2478/v10007-010-0016-9.

[239] V. Vanhoorne, E. Peeters, B. Van Snick, J. P. Remon, and C. Vervaet. Crystal coating via spray drying to improve powder tabletability. *European Journal of Pharmaceutics and Biopharmaceutics*, 88(3):939–944, 2014. ISSN 18733441. doi: 10.1016/j.ejpb.2014.10.018.

[240] M. I.U. Islam, R. Sherrell, and T. A.G. Langrish. An investigation of the relationship between glass transition temperatures and the crystallinity of spray-dried powders. *Drying Technology*, 28(3):361–368, 2010. ISSN 07373937. doi: 10.1080/07373931003641586.

[241] Eva Maria Littringer, Axel Mescher, Susanna Eckhard, Hartmuth Schröttner, Christoph Langes, Manfred Fries, Ulrich Griesser, Peter Walzel, and Nora Anne Urbanetz. Spray drying of Mannitol as a drug carrier—the impact of process parameters on product properties. *Drying Technology*, 30(1):114–124, 2012. ISSN 15322300. doi: 10.1080/07373937.2011.620726.

[242] John Bronlund and Tony Paterson. Moisture sorption isotherms for crystalline, amorphous and predominantly crystalline lactose powders. *International Dairy Journal*, 14 (3):247–254, 2004. ISSN 09586946. doi: 10.1016/S0958-6946(03)00176-6.

[243] Mike Tobyn, John N Staniforth, David Morton, Quentin Harmer, and Mike E Newton. Active and intelligent inhaler device development. *International Journal of Pharmaceutics*, 277(September 2003):31–37, 2004. doi: 10.1016/j.ijpharm.2003.09.049.

[244] Graham Buckton, Etsuo Yonemochi, Jonathan Hammond, and Anthony Moffat. The use of near infra-red spectroscopy to detect changes in the form of amorphous and crystalline lactose. *International Journal of Pharmaceutics*, 168:231–241, 1998.

[245] Robert Price and Paul M Young. Visualization of the Crystallization of Lactose from the Amorphous State. *Journal of pharmaceutical sciences*, 93(1):155–164, 2004.

[246] Morteza Saffari and Timothy Langrish. Effect of lactic acid in-process crystallization of lactose/protein powders during spray drying. *Journal of Food Engineering*, 137:88–94, 2014. ISSN 0260-8774. doi: 10.1016/j.jfoodeng.2014.04.002.

[247] Jaehwi Lee, Sang Cheon Lee, Ghanashyam Acharya, Ching Jer Chang, and Kinam Park. Hydrotropic solubilization of paclitaxel: Analysis of chemical structures for hydrotropic property. *Pharmaceutical Research*, 20(7):1022–1030, 2003. ISSN 07248741. doi: 10.1023/A:1024458206032.

[248] Makoto Otsuka and Ikuro Yamane. Prediction of Tablet Properties Based on Near Infrared Spectra of Raw Mixed Powders by Chemometrics: Scale-Up Factor of Blending and Tableting Processes. *Journal of Pharmaceutical Sciences*, 98(11):4296–4305, 2009. ISSN 0022-3549. doi: 10.1002/jps.21748.

[249] Elke Prasad, Muhammad T. Islam, Daniel J. Goodwin, Andrew J. Megarry, Gavin W. Halbert, Alastair J. Florence, and John Robertson. Development of a Hot-Melt Extrusion (HME) process to produce drug loaded Affinisol™ 15LV filaments for Fused Filament Fabrication (FFF) 3D printing. *Additive Manufacturing*, 2019. ISSN 22148604. doi: 10.1016/j.addma.2019.06.027.

[250] Merck KGaA. Metformin (CAS-No. 1115-70-4) - Safety Data Sheet. Technical Report 1.3, 2006.

[251] R Rowe, P Sheskey, and M Quinn. Handbook of Pharmaceutical Excipients. *Handbook of pharmaceutical excipients, Sixth edition*, pages 549–553, 2009. ISSN 01683659. doi: 10.1016/S0168-3659(01)00243-7.

[252] C W Rowe, W E Katstra, R D Palazzolo, B Giritlioglu, P Teung, and M J Cima. Multimechanism oral dosage forms fabricated by three dimensional printing E. *Journal of Controlled Release*, 66:11–17, 2000.

[253] W E Katstra, R D Palazzolo, C W Rowe, B Giritlioglu, P Teung, and M J Cima. Oral dosage forms fabricated by Three Dimensional Printing E. *Journal of Controlled Release*, 66:1–9, 2000.

[254] ILO and WHO. Polyvinyl alcohol (ICSC), 2017. URL http://www.ilo.org/dyn/icsc/showcard.display?p{_}version=2{&}p{_}card{_}id=1489.

[255] Ivan J Hall Barrientos, Eleonora Paladino, Peter Szabó, Sarah Brozio, Peter J Hall, Charles I Oseghale, Melissa K Passarelli, Susan J Moug, Richard A Black, Clive G Wilson, Romana Zelkó, and Dimitrios A Lamprou. Electrospun collagen-based nano fi bres : A sustainable material for improved antibiotic utilisation in tissue engineering applications. *International Journal of Pharmaceutics*, 531(1):67–79, 2017. ISSN 0378-5173. doi: 10.1016/j.ijpharm.2017.08.071.

[256] Ivan J Hall Barrientos, Eleonora Paladino, Sarah Brozio, Melissa K Passarelli, Susan Moug, Richard A Black, Clive G Wilson, and Dimitrios A Lamprou. Fabrication and characterisation of drug-loaded electrospun polymeric nano fi bers for controlled release

in hernia repair. *International Journal of Pharmaceutics*, 517(1-2):329–337, 2017. ISSN 0378-5173. doi: 10.1016/j.ijpharm.2016.12.022.

[257] Lawrence X Yu. Pharmaceutical quality by design: product and process development, understanding, and control. *Pharmaceutical research*, 25(4):781–91, 2008. ISSN 0724-8741. doi: 10.1007/s11095-007-9511-1.

[258] Margot Fonteyne, Henrika Wickström, Elisabeth Peeters, Jurgen Vercruysse, Henrik Ehlers, Björn Hendrik Peters, Jean Paul Remon, Chris Vervaet, Jarkko Ketolainen, Niklas Sandler, Jukka Rantanen, Kaisa Naelapää, and Thomas De Beer. Influence of raw material properties upon critical quality attributes of continuously produced granules and tablets. *European Journal of Pharmaceutics and Biopharmaceutics*, 87(2):252–263, 2014. ISSN 18733441. doi: 10.1016/j.ejpb.2014.02.011.

[259] Helen Michie, Fridrun Podczeck, and John Michael Newton. The influence of plate design on the properties of pellets produced by extrusion and spheronization. *International Journal of Pharmaceutics*, 434(1-2):175–182, 2012. ISSN 03785173. doi: 10.1016/j.ijpharm.2012.05.050.

[260] Marine Soret, Stephen L. Bacharach, and Irène Buvat. Partial-volume effect in PET tumor imaging. *Journal of Nuclear Medicine*, 48(6):932–945, 2007. ISSN 01615505. doi: 10.2967/jnumed.106.035774.

[261] Letitia Schoeman, Paul Williams, Anton du Plessis, and Marena Manley. X-ray micro-computed tomography (μCT) for non-destructive characterisation of food microstructure. *Trends in Food Science and Technology*, 47:10–24, 2016. ISSN 09242244. doi: 10.1016/j.tifs.2015.10.016.

[262] Stephen S.F. Yip and Hugo J.W.L. Aerts. Applications and limitations of radiomics. *Physics in Medicine and Biology*, 61(13):R150–R166, 2016. ISSN 13616560. doi: 10.1088/0031-9155/61/13/R150.

[263] Ali Al-Sarraf, Tobi Vaudrey, Reinhard Klette, and Young Woon Woo. An approach for evaluating robustness of edge operators using real-world driving scenes. *23rd International Conference Image and Vision Computing New Zealand (IVCNZ)*, 2008. doi: 10.1109/IVCNZ.2008.4762096.

[264] Trevor Hastie, Robert Tibshirani, and Jerome Friedman. *The Elements of Statistical Learning*. Springer, second edi edition, 2009. ISBN 9780387848587.

[265] Bernhard E Boser, Vladimir N Vapnik, and Isabelle M Guyon. A Training Algorithm for Optimal Margin Classifiers. *Annual Workshop on Computational Learning Theory*, pages 144 – 152, 1992.

[266] Tiejun Cheng, Qingliang Li, Yanli Wang, and Stephen H. Bryant. Binary classification of aqueous solubility using support vector machines with reduction and recombination feature selection. *Journal of Chemical Information and Modeling*, 51(2):229–236, 2011. ISSN 15499596. doi: 10.1021/ci100364a.

[267] Stephan Dreiseitl, Melanie Osl, Christian Scheibb, and Michael Binder. Outlier Detection with One-Class SVMs: An Application to Melanoma Prognosis. *AMIA 2010 Symposium Proceedings*, pages 172–176, 2010.

[268] Janaina Mourão-miranda, David R Hardoon, Tim Hahn, Andre F Marquand, Steve C R Williams, John Shawe-taylor, and Michael Brammer. NeuroImage Patient classification as an outlier detection problem : An application of the One-Class Support Vector Machine. *NeuroImage*, 58(3):793–804, 2011. ISSN 1053-8119. doi: 10.1016/j.neuroimage.2011.06.042.

[269] Roberto Perdisci, Guofei Gu, and Wenke Lee. Using an Ensemble of One-Class SVM Classifiers to Harden Payload-based Anomaly Detection Systems. *Proceedings of the International Conference on Data Mining (ICDM)*, pages 488–498, 2006. doi: 10.1109/ICDM.2006.165.

[270] Kenji Kira and Larry A Rendell. The feature selection problem: Traditional methods and a new algorithm. In *AAAI-92 Proceedings*, pages 129–134, 1992.

[271] Igor Kononenko, Edvard Šimec, and Marko Robnik-Šikonja. Overcoming the myopic of inductive learning algorithms with RELIEFF. *Applied Intelligence*, 7(1):39–55, 1997.

[272] Marko Robnik-Šikonja and Igor Kononenko. An adaptation of Relief for attribute estimation in regression. *ICML '97 Proceedings of the Fourteenth International Conference on Machine Learning*, pages 296–304, 1997.

[273] Marko Robnik-Šikonja and Igor Kononenko. Theoretical and Empirical Analysis of ReliefF and RReliefF. *Machine Learning*, 53:23–69, 2003. doi: 10.1023/A:1025667309714.

[274] Fernand Meyer. Topographic distance and watershed lines. *Signal Processing*, 38(1): 113–125, 1994. ISSN 01651684. doi: 10.1016/0165-1684(94)90060-4.

[275] M.K. Hu. Visual pattern recognition by moment invariants. *IRE Transactions on Information Theory IT-8*, (179-187):66–70, 1962.

[276] Clive G. Wilson and Patrick J. Crowley. *Controlled Release in Oral Drug Delivery*. Springer, 2011. ISBN 9781461410034. doi: 10.1007/978-1-4614-1004-1.

[277] Lawrence X. Yu, Gregory Amidon, Mansoor A. Khan, Stephen W. Hoag, James Polli, G. K. Raju, and Janet Woodcock. Understanding Pharmaceutical Quality by Design. *The AAPS Journal*, 16(4):771–783, 2014. ISSN 1550-7416. doi: 10.1208/s12248-014-9598-3.

[278] M. P. Bryan, L. N. Atherton, S. Duffield, S. L. Rough, and D. I. Wilson. Stages in spheronisation: Evolution of pellet size and shape during spheronisation of microcrystalline cellulose-based paste extrudates. *Powder Technology*, 270(Part A):163–175, 2015. ISSN 1873328X. doi: 10.1016/j.powtec.2014.10.014.

[279] Nitesh V. Chawla, Nathalie Japkowicz, and Aleksander Kotcz. Editorial: special issue on learning from imbalanced data sets. *ACM SIGKDD Explorations Newsletter*, 6(1):1, 2004. ISSN 19310145. doi: 10.1145/1007730.1007733.

[280] Yi-Wei Chen and Chih-Jen Lin. Combining SVMs with Various Feature Selection Strategies. In *Feature Extraction*, number 1, pages 315–324. Springer, 2006. doi: 10.1007/978-3-540-35488-8_13.

[281] Asep Bayu Dani Nandiyanto and Kikuo Okuyama. Progress in developing spray-drying methods for the production of controlled morphology particles: from the nanometer to submicrometer size ranges. *Advanced Powder Technology*, 22(1):1–19, 2011. doi: 10.1016/J.APT.2010.09.011.

[282] Feng Lyu, Jing J Liu, Yang Zhang, and Xue Z Wang. Combined control of morphology

and polymorph in spray drying of mannitol for dry powder inhalation. *Journal of Crystal Growth*, 467:155–161, 2017. ISSN 0022-0248. doi: 10.1016/j.jcrysgro.2017.03.033.

[283] M I U Islam and T A G Langrish. An investigation into lactose crystallization under high temperature conditions during spray drying. *Food Research International*, 43(1):46–56, 2010. ISSN 09639969. doi: 10.1016/j.foodres.2009.08.010.

[284] In-Hwan Beak and Min-Soo Kim. Improved Supersaturation and Oral Absorption of Dutasteride by Amorphous Solid Dispersions. *Chemical and Pharmaceutical Bulletin*, 60(11):1468–1473, 2012. ISSN 0009-2363. doi: 10.1248/cpb.c12-00563.

[285] Shashank P. Patil, Sameer R. Modi, and Arvind K. Bansal. Generation of 1:1 Carbamazepine:Nicotinamide cocrystals by spray drying. *European Journal of Pharmaceutical Sciences*, 62:251–257, 2014. ISSN 18790720. doi: 10.1016/j.ejps.2014.06.001.

[286] Stephen Byrn, Maricio Futran, Hayden Thomas, Eric Jayjock, Nicola Maron, Robert F. Meyer, Allan S. Myerson, Michael P. Thien, and Bernhardt L. Trout. Achieving continuous manufacturing for final dosage formation: Challenges and how to meet them May 20-21, 2014 continuous manufacturing symposium. *Journal of Pharmaceutical Sciences*, 104(3):792–802, 2015. ISSN 15206017. doi: 10.1002/jps.24247.

[287] Marine Nuzzo, Anna Millqvist-Fureby, Jakob Sloth, and Björn Bergenstahl. Surface Composition and Morphology of Particles Dried Individually and by Spray Drying. *Drying Technology*, 33(6):757–767, 2015. ISSN 0737-3937. doi: 10.1080/07373937.2014.990566.

[288] J. K R Weber, C. A. Rey, J. Neuefeind, and C. J. Benmore. Acoustic levitator for structure measurements on low temperature liquid droplets. *Review of Scientific Instruments*, 80 (8):1–8, 2009. ISSN 00346748. doi: 10.1063/1.3196177.

[289] J. K R Weber, C. J. Benmore, A. N. Tailor, S. K. Tumber, J. Neuefeind, B. Cherry, J. L. Yarger, Q. Mou, W. Weber, and S. R. Byrn. A neutron-X-ray, NMR and calorimetric study of glassy Probucol synthesized using containerless techniques. *Chemical Physics*, 424:89–92, 2013. ISSN 03010104. doi: 10.1016/j.chemphys.2013.05.019.

[290] Chris J. Benmore, J.K.R. Weber, Amit N. Tailor, Brian R. Cherry, Jeffery L. Yarger, Qiushi Mou, Warner Weber, Joerg Neuefeind, and Stephen R. Byrn. Structural Characterization and Aging of Glassy Pharmaceuticals made Using Acoustic Levitation. *Journal of Pharmaceutical Sciences*, 102(4):1290–1300, apr 2013. ISSN 00223549. doi: 10.1002/jps.23464.

[291] Pavel Trtik, Miroslav Soos, Beat Munch, Alexandros Lamprou, Rajmund Mokso, and Marco Stampanoni. Quantification of a single aggregate inner porosity and pore accessibility using hard X-ray phase-contrast nanotomography. *Langmuir : the ACS journal of surfaces and colloids*, 27(21):12788–12791, 2011. ISSN 0743-7463. doi: 10.1021/la203432v.

[292] R Tuckermann, S Bauerecker, and H K Cammenga. IR-Thermography of Evaporating Acoustically Levitated Drops. *International Journal of Thermophysics*, 26(5):1583–1594, 2005. ISSN 1572-9567. doi: 10.1007/s10765-005-8105-6.

[293] World Health Organization. WHO Model List of Essential Medicines - 19th List (April 2015). *Essential Medicines*, (April):1–45, 2015. ISSN 14744457. doi: 10.1016/S1473-3099(14)70780-7.

[294] Giovanna Corti, Marzia Cirri, Francesca Maestrelli, Natascia Mennini, and Paola Mura. Sustained-release matrix tablets of metformin hydrochloride in combination with triacetyl-β-cyclodextrin. *European Journal of Pharmaceutics and Biopharmaceutics*, 68 (2):303–309, 2008. ISSN 09396411. doi: 10.1016/j.ejpb.2007.06.004.

[295] L. C. Block, L. O. Schemling, A. G. Couto, S. C. Mourão, and Tania Mari Bellé Bresolin. Pharmaceutical equivalence of metformin tablets with various binders. *Revista de Ciencias Farmaceuticas Basica e Aplicada*, 29(1):29–35, 2008. ISSN 18084532.

[296] Bhavesh S. Barot, Punit B. Parejiya, Tushar M. Patel, Rajesh K. Parikh, and Mukesh C. Gohel. Compactibility improvement of metformin hydrochloride by crystallization technique. *Advanced Powder Technology*, 23(6):814–823, 2012. ISSN 09218831. doi: 10.1016/j.apt.2011.11.002.

[297] Vinod Mokale, Rahul Rajput, Jayesh Patil, Sunil Yadava, and Jitendra Naik. Formulation of metformin hydrochloride nanoparticles by using spray drying technique and in vitro

evaluation of sustained release with 32-level factorial design approach. *Drying Technology*, 34(12):1455–1461, 2016. ISSN 15322300. doi: 10.1080/07373937.2015.1125916.

[298] Rania Hamed, Ali Al-Samydai, Tamadur Al Baraghthi, Ola Tarawneh, and Suhair Sunoqrot. Influence of HPMC K100LV and Compritol® HD5 ATO on Drug Release and Rheological Behavior of HPMC K4M Matrix Tablets. *Journal of Pharmaceutical Innovation*, 12(1):62–75, 2017. ISSN 19398042. doi: 10.1007/s12247-016-9269-2.

[299] G Gerig, O Kubler, R Kikinis, and F a Jolesz. Nonlinear anisotrophic filtering of MRI data. *IEEE Transactions on Medical Imaging*, 11(2):221–232, 1992. ISSN 0278-0062. doi: 10.1109/42.141646.

[300] C. Bradford Barber, David P. Dobkin, and Hannu Huhdanpaa. The quickhull algorithm for convex hulls. *ACM Transactions on Mathematical Software*, 22(4):469–483, 1996. ISSN 00983500. doi: 10.1145/235815.235821.

[301] J. K. Armstrong, R. B. Wenby, H. J. Meiselman, and T. C. Fisher. The hydrodynamic radii of macromolecules and their effect on red blood cell aggregation. *Biophysical Journal*, 87(6):4259–4270, 2004. ISSN 00063495. doi: 10.1529/biophysj.104.047746.

[302] Tominaga Toshihiro and Matsumoto Shigetoshi. Diffusion of polar and nonpolar molecules in water and ethanol. *Bulletin of the Chemical Society of Japan*, 63(2):533–537, 1990. doi: 10.1246/bcsj.63.533.

[303] Rachel Callendar and Derek G. Leaist. Diffusion coefficients for binary, ternary, and polydisperse solutions from peak-width analysis of Taylor dispersion profiles. *Journal of Solution Chemistry*, 35(3):353–379, 2006. ISSN 00959782. doi: 10.1007/s10953-005-9000-2.

[304] Divyakant Desai, Benjamin Wong, Yande Huang, Qingmei Ye, Dan Tang, Hang Guo, Ming Huang, and Peter Timmins. Surfactant-mediated dissolution of metformin hydrochloride tablets: Wetting effects versus ion pairs diffusivity. *Journal of Pharmaceutical Sciences*, 103(3):920–926, 2014. ISSN 15206017. doi: 10.1002/jps.23852.

[305] Niraj S Trasi, Kaoutar Abbou Oucherif, James D Litster, and Lynne S Taylor. Evalu-

ating the influence of polymers on nucleation and growth in supersaturated solutions of acetaminophen. *CrystEngComm*, pages 1242–1248, 2015. doi: 10.1039/c4ce02179g.

[306] E. M. Littringer, R. Paus, A. Mescher, H. Schroettner, P. Walzel, and N. A. Urbanetz. The morphology of spray dried mannitol particles - The vital importance of droplet size. *Powder Technology*, 239:162–174, 2013. ISSN 00325910. doi: 10.1016/j.powtec.2013.01.065.

[307] S. Shakiba, S. Mansouri, C. Selomulya, and M. W. Woo. In-situ crystallization of particles in a counter-current spray dryer. *Advanced Powder Technology*, 27(6):2299–2307, 2016. ISSN 15685527. doi: 10.1016/j.apt.2016.07.001.

[308] Rodney Lax, D Ph, Business Development, North America, and Polypeptide Group. The Future of Peptide Development in the Pharmaceutical Industry. *PharManufacturing The International Peptide Review*, pages 10–15, 2010.

[309] Allan A Kaspar and Janice M Reichert. Future directions for peptide therapeutics development. *Drug Discovery Today*, 18(17-18):807–817, 2013. ISSN 13596446. doi: 10.1016/j.drudis.2013.05.011.

[310] D. Chen, S. Kapre, A. Goel, K. Suresh, S. Beri, J. Hickling, J. Jensen, M. Lal, J. M. Preaud, M. LaForce, and D. Kristensen. Thermostable formulations of a hepatitis B vaccine and a meningitis A polysaccharide conjugate vaccine produced by a spray drying method. *Vaccine*, 28(31):5093–5099, 2010. ISSN 0264410X. doi: 10.1016/j.vaccine.2010.04.112.

[311] V. Saluja, J. P. Amorij, J. C. Kapteyn, A. H. de Boer, H. W. Frijlink, and W. L J Hinrichs. A comparison between spray drying and spray freeze drying to produce an influenza subunit vaccine powder for inhalation. *Journal of Controlled Release*, 144(2):127–133, 2010. ISSN 01683659. doi: 10.1016/j.jconrel.2010.02.025.

[312] Gemma Año, Amaia Esquisabel, Marta Pastor, Arturo Talavera, Bárbara Cedré, Sonsire Fernández, Sergio Sifontes, Yisabel Aranguren, Gustavo Falero, Luis García, Rosa Lydia Solís, and José Luis Pedraz. A new oral vaccine candidate based on the microencapsulation by spray-drying of inactivated Vibrio cholerae. *Vaccine*, 29(34):5758–5764, 2011. ISSN 0264410X. doi: 10.1016/j.vaccine.2011.05.098.

[313] Solmaz Behboudi-J, Christos Soukoulis, Lina Yonekura, Ian Fisk, Christos Soukoulis, Lina Yonekura, Ian Fisk, Solmaz Behboudi Jobbehdar, Lina Yonekura, Ian Fisk, Solmaz Behboudi-jobbehdar, Christos Soukoulis, Lina Yonekura, and Ian Fisk. Optimization of Spray-Drying Process Conditions for the Production of Maximally Viable Microencapsulated L . acidophilus NCIMB 701748 Optimization of Spray-Drying Process Conditions for the Production of Maximally Viable Microencapsulated. *Drying Technology*, 3937: 1274–1283, 2013. doi: 10.1080/07373937.2013.788509.

[314] Albert H L Chow, Henry H Y Tong, Pratibhash Chattopadhyay, and Boris Y Shekunov. Expert Review Particle Engineering for Pulmonary Drug Delivery. *Pharmaceutical Research*, 24(3), 2007. doi: 10.1007/s11095-006-9174-3.

[315] Tsutomu Arakawa and Serge N. Timasheff. Stabilization of Protein Structure by Sugars. *Biochemistry*, 21(25):6536–6544, 1982. ISSN 15204995. doi: 10.1021/bi00268a033.

[316] John F. Carpenter and John H. Crowe. An infrared spectroscopic study of the interactions of carbohydrates with dried proteins. *Biochemistry*, 28(9):3916–3922, 1989. ISSN 15204995. doi: 10.1021/bi00435a044.

[317] S. Dean Allison, Byeong Chang, Theodore W. Randolph, and John F. Carpenter. Hydrogen bonding between sugar and protein is responsible for inhibition of dehydration-induced protein unfolding. *Archives of Biochemistry and Biophysics*, 365(2):289–298, 1999. ISSN 00039861. doi: 10.1006/abbi.1999.1175.

[318] Jose G Sampedro and Salvador Uribe. Trehalose-enzyme interactions result in structure stabilization and activity inhibition. The role of viscosity. *Molecular and cellular biochemistry*, 256-257(1-2):319–27, 2004. ISSN 0300-8177.

[319] Liuquan Chang, Deanna Shepherd, Joanna Sun, David Ouellette, Kathleen L. Grant, Xiaolin Tang, and Michael J. Pikal. Mechanism of protein stabilization by sugars during freeze-drying and storage: Native structure preservation, specific interaction, and/or immobilization in a glassy matrix? *Journal of Pharmaceutical Sciences*, 94(7):1427–1444, 2005. ISSN 00223549. doi: 10.1002/jps.20364.

[320] Laila D Latip, Wahidu Zzaman, and Tajul A Yang. Optimization of Spray Drying Process in Commercial Hydrolyzed Fish Scale Collagen and Characterization by Scanning

Electron Microscope and Fourier Transform Infrared Spectroscopy. *Journal of Food Processing and Preservation*, 39:1754–1761, 2015. doi: 10.1111/jfpp.12407.

[321] Muzammil Ali, Tariq Mahmud, Peter John, Mojtaba Ghadiri, Dusan Djurdjevic, Hossein Ahmadian, Luis Martin, De Juan, Carlos Amador, Andrew Bayly, Whitley Road, Newcastle Upon, and Tyne Ne. A one-dimensional plug-flow model of a counter-current spray drying tower. *Chemical Engineering Research and Design*, 92(5):826–841, 2013. ISSN 0263-8762. doi: 10.1016/j.cherd.2013.08.010.

[322] T. T. H. Tran, M. Jaskulski, and E. Tsotsas. Reduction of a model for single droplet drying and application to CFD of skim milk spray drying. *Drying Technology*, 35(13): 1–13, 2017. ISSN 0737-3937. doi: 10.1080/07373937.2016.1263204.

[323] Tijana Mihajlovic, Svetlana Ibric, and Aleksandar Mladenovic. Application of Design of Experiments and Multilayer Perceptron Neural Network in Optimization of the Spray-Drying Process. *Drying Technology*, 29(14):1638–1647, 2011. ISSN 0737-3937. doi: 10.1080/07373937.2011.592960.

[324] Ashwinkumar D Patel, Anjali Agrawal, and Rutesh H Dave. Development of Polyvinylpyrrolidone-Based Spray-Dried Solid Dispersions Using Response Surface Model and Ensemble. *Journal of Pharmaceutical Sciences*, 102(6):1847–1858, 2013. ISSN 0022-3549. doi: 10.1002/jps.23526.

[325] P. Schuck, S. Méjean, A. Dolivet, and R. Jeantet. Thermohygrometric sensor: A tool for optimizing the spray drying process. *Innovative Food Science and Emerging Technologies*, 6(1):45–50, 2005. ISSN 14668564. doi: 10.1016/j.ifset.2004.10.001.

[326] Christian Fischer, Maciej Jaskulski, and Evangelos Tsotsas. Inline method of droplet and particle size distribution analysis in dilute disperse systems. *Advanced Powder Technology*, 28(11):2820–2829, 2017. ISSN 15685527. doi: 10.1016/j.apt.2017.08.009.

[327] Anders Brask, Thorvald Ullum, Pia Thybo, and S K Andersen. High-temperature ultrasonic levitator for investigating drying kinetics of single droplets. In *The Proceedings of the 6th Intl. Conf. on Multiphase Flow, Leipzig*, volume 913, 2007.

[328] Cristiano Luis Pinto Oliveira, Manja Annette Behrens, Jesper Søndergaard Pedersen, Kurt Erlacher, Daniel Otzen, and Jan Skov Pedersen. A SAXS Study of Glucagon Fibrillation. *Journal of Molecular Biology*, 387(1):147–161, 2009. ISSN 00222836. doi: 10.1016/j.jmb.2009.01.020.

[329] Shirin Ghodke, Søren B Nielsen, Gunna Christiansen, Hans A Hjuler, James Flink, and Daniel Otzen. Mapping out the multistage fibrillation of glucagon. *The FEBS Journal*, 279:752–765, 2012. doi: 10.1111/j.1742-4658.2011.08465.x.

[330] Shirin D Ghodke, Anne Søndergaard, Manja A Behrens, Jan Skov Pedersen, Niels Chr Nielsen, Roland Winter, and Daniel E Otzen. *Polymorphism , Metastable Species and Interconversion : The Many States of Glucagon Fibrils*. Elsevier, 2014. ISBN 9780123944313. doi: 10.1016/B978-0-12-394431-3.00034-1.

[331] Karolina L. Zapadka, Frederik J. Becher, Shahid Uddin, Paul G. Varley, Steve Bishop, A. L. Gomes Dos Santos, and Sophie E. Jackson. A pH-Induced Switch in Human Glucagon-like Peptide-1 Aggregation Kinetics. *Journal of the American Chemical Society*, 138(50):16259–16265, 2016. ISSN 15205126. doi: 10.1021/jacs.6b05025.

[332] Phillip M Lovalenti, Jeff Anderl, Luisa Yee, Van Nguyen, Behnaz Ghavami, Satoshi Ohtake, Atul Saxena, and Thomas Voss. Stabilization of Live Attenuated Influenza Vaccines by Freeze Drying , Spray Drying , and Foam Drying. *Pharmaceutical Research*, 33:1144–1160, 2016. doi: 10.1007/s11095-016-1860-1.

[333] Takanobu Higashiyama. Novel functions and applications of trehalose. *Pure and Applied Chemistry*, 74(7):1263–1269, 2002.

[334] Azita Saleki-Gerhardt and George Zografi. Non-Isothermal and Isothermal Crystallization of Sucrose from the Amorphous State. *Pharmaceutical Research*, 11(8):1166–1173, aug 1994. ISSN 1573-904X. doi: 10.1023/A:1018945117471.

[335] W. W. Bromer, L. G. Sinn, A. Staub, and Otto K. Behrens. The Amino Acid Sequence of Glucagon. *Journal of the American Chemical Society*, 78(15):3858–3860, 1956. ISSN 0002-7863. doi: 10.1021/ja01596a084.

[336] Guoqiang Jiang and Bei B. Zhang. Glucagon and regulation of glucose metabolism. *American Journal of Physiology - Endocrinology And Metabolism*, 284(4):E671–E678, 2003. ISSN 0193-1849. doi: 10.1152/ajpendo.00492.2002.

[337] Lukasz P. Kozlowski. IPC - Isoelectric Point Calculator. *Biology Direct*, 11(1):1–16, 2016. ISSN 17456150. doi: 10.1186/s13062-016-0159-9.

[338] Marie Claire Bellissent-Funel, Ali Hassanali, Martina Havenith, Richard Henchman, Peter Pohl, Fabio Sterpone, David Van Der Spoel, Yao Xu, and Angel E. Garcia. Water Determines the Structure and Dynamics of Proteins. *Chemical Reviews*, 116(13):7673–7697, 2016. ISSN 15206890. doi: 10.1021/acs.chemrev.5b00664.

[339] Richard Walgers, Tony C. Lee, and Arthur Cammers-Goodwin. An indirect chaotropic mechanism for the stabilization of helix conformation of peptides in aqueous trifluoroethanol and hexafluoro-2- propanol. *Journal of the American Chemical Society*, 120 (20):5073–5079, 1998. ISSN 00027863. doi: 10.1021/ja973552z.

[340] Nami Hirota, Kazuko Mizuno, and Yuji Goto. Group additive contributions to the alcohol-induced α-helix formation of melittin: Implication for the mechanism of the alcohol effects on proteins. *Journal of Molecular Biology*, 275(2):365–378, 1998. ISSN 00222836. doi: 10.1006/jmbi.1997.1468.

[341] Alex Kentsis and Tobin R. Sosnick. Trifluoroethanol promotes helix formation by destabilizing backbone exposure: Desolvation rather than native hydrogen bonding defines the kinetic pathway of dimeric coiled coil folding. *Biochemistry*, 37(41):14613–14622, 1998. ISSN 00062960. doi: 10.1021/bi981641y.

[342] Stefan Grudzielanek, Ralf Jansen, and Roland Winter. Solvational tuning of the unfolding, aggregation and amyloidogenesis of insulin. *Journal of Molecular Biology*, 351(4): 879–894, 2005. ISSN 00222836. doi: 10.1016/j.jmb.2005.06.046.

[343] Wojciech Dzwolak, Stefan Grudzielanek, Vytautas Smirnovas, Revanur Ravindra, Chiara Nicolini, Ralf Jansen, Anna Loksztejn, Sylwester Porowski, and Roland Winter. Ethanol-perturbed amyloidogenic self-assembly of insulin: Looking for origins of amyloid strains. *Biochemistry*, 44(25):8948–8958, 2005. ISSN 00062960. doi: 10.1021/bi050281t.

[344] William M Haynes. *CRC handbook of chemistry and physics*. CRC press, 2014.

[345] Tadato Ban, Daizo Hamada, Kazuhiro Hasegawa, Hironobu Naiki, and Yuji Goto. Direct Observation of Amyloid Fibril Growth Monitored by Thioflavin T Fluorescence. *The Journal of Biological Chemistry*, 278(19), 2003. doi: 10.1074/jbc.C300049200.

[346] Jesper Søndergaard Pedersen, Dantcho Dikov, James L. Flink, Hans Aage Hjuler, Gunna Christiansen, and Daniel Erik Otzen. The changing face of glucagon fibrillation: Structural polymorphism and conformational imprinting. *Journal of Molecular Biology*, 355 (3):501–523, 2006. ISSN 00222836. doi: 10.1016/j.jmb.2005.09.100.

[347] Jesper Søndergaard Pedersen, James M. Flink, Dantcho Dikov, and Daniel Erik Otzen. Sulfates dramatically stabilize a salt-dependent type of glucagon fibrils. *Biophysical Journal*, 90(11):4181–4194, 2006. ISSN 00063495. doi: 10.1529/biophysj.105.070912.

[348] Yrjö Roos and Marcus Karel. Phase transitions of mixtures of amorphous polysaccharides and sugars. *Biotechnology Progress*, 7(1):49–53, 1991.

[349] C Hennigs, T K Kockel, and T A G Langrish. New measurements of the sticky behavior of skim milk powder. *Drying technology*, 19(3-4):471–484, 2001.

[350] Kylie D. Foster, John E. Bronlund, and A. H.J.(Tony) Paterson. Glass transition related cohesion of amorphous sugar powders. *Journal of Food Engineering*, 77(4):997–1006, 2006. ISSN 02608774. doi: 10.1016/j.jfoodeng.2005.08.028.

[351] Manfred Gordon and James S. Taylor. Ideal Copolymers and the Second-Order Transitions of Synthetic Rubbers. I. Noncrystalline Copolymers. *Journal of Applied Chemistry*, 2(9):493–500, 1952. ISSN 0035-9475. doi: 10.5254/1.3539818.

[352] Tani Chen, Alex Fowler, and Mehmet Toner. Literature review: Supplemented phase diagram of the trehalose-water binary mixture. *Cryobiology*, 40(3):277–282, 2000. ISSN 00112240. doi: 10.1006/cryo.2000.2244.

[353] Lois M Crowe, David S Reid, and John H Crowe. Is trehalose special for preserving dry biomaterials. *Biophysical Journal*, 71(October):2087–2093, 1996.

[354] Héctor A. Iglesias, Jorge Chirife, and María P. Buera. Adsorption isotherm of amorphous trehalose. *Journal of the Science of Food and Agriculture*, 75(2):183–186, 1997. ISSN

00225142. doi: 10.1002/(SICI)1097-0010(199710)75:2<183::AID-JSFA860>3.0.CO;2-T.

[355] Silvia Cardona, Carolina Schebor, María P. Buera, Marcus Karel, and Jorge Chirife. Thermal stability of invertase in reduced-moisture amorphous matrices in relation to glassy state and trehalose crystallization. *Journal of Food Science*, 62(1):105–112, 1997. ISSN 00221147. doi: 10.1111/j.1365-2621.1997.tb04378.x.

[356] Osamu Haida, Hiroshi Suga, and Syûzô Seki. Calorimetric study of the glassy state XII. Plural glass-transition phenomena of ethanol. *The Journal of Chemical Thermodynamics*, 9(12):1133–1148, 1977.

[357] W Barth. Design and layout of the cyclone separator on the basis of new investigations. *Brenn. Warme Kraft*, 8(1):9, 1956.

[358] Nishant Kumar Jain and Ipsita Roy. Effect of trehalose on protein structure. *Protein Science*, (September 2008):24–36, 2009. doi: 10.1002/pro.3.

[359] Maarten A Mensink, Henderik W Frijlink, Kees Van Der Voort, and Wouter L J Hinrichs. European Journal of Pharmaceutics and Biopharmaceutics How sugars protect proteins in the solid state and during drying (review): Mechanisms of stabilization in relation to stress conditions. *European Journal of Pharmaceutics and Biopharmaceutics*, 114: 288–295, 2017. ISSN 0939-6411. doi: 10.1016/j.ejpb.2017.01.024.

[360] Arthur H Lefebvre and Vincent G McDonell. *Atomization and sprays*. CRC press, 2017.

[361] B. Adhikari, T. Howes, B. R. Bhandari, and T. a G Langrish. Effect of addition of proteins on the production of amorphous sucrose powder through spray drying. *Journal of Food Engineering*, 94(2):144–153, 2009. ISSN 0260-8774. doi: 10.1016/j.jfoodeng.2009.01.029.

[362] Md Imtiaz-Ul Islam, Mona Edrisi, and Timothy Langrish. Improving Process Yield by Adding WPI to Lactose During Crystallization and Spray Drying Under High-Humidity Conditions. *Drying Technology*, 31(4):393–404, 2013. ISSN 0737-3937. doi: 10.1080/07373937.2012.737396.

[363] Bruno C Hancock and George Zografi. The relationship between the glass transition temperature and the water content of amorphous pharmaceutical solids. *Pharmaceutical research*, 11(4):471–477, 1994.

[364] Satoshi Ohtake and Y. John Wang. Trehalose: Current use and future applications. *Journal of Pharmaceutical Sciences*, 100(6):2020–2053, 2011. ISSN 15206017. doi: 10.1002/jps.22458.

[365] Ramesh K. Sharma, W. Geoffrey Chan, Jia Wang, Bruce E. Waymack, Jan B. Wooten, Jeffrey I. Seeman, and Mohammad R. Hajaligol. On the role of peptides in the pyrolysis of amino acids. *Journal of Analytical and Applied Pyrolysis*, 72(1):153–163, 2004. ISSN 01652370. doi: 10.1016/j.jaap.2004.03.009.

[366] Ingrid M. Weiss, Christina Muth, Robert Drumm, and Helmut O.K. Kirchner. Thermal decomposition of the amino acids glycine, cysteine, aspartic acid, asparagine, glutamic acid, glutamine, arginine and histidine. *BMC Biophysics*, 11(1):1–15, 2018. ISSN 20461682. doi: 10.1186/s13628-018-0042-4.

[367] Sangita Seshadri, Ritu Khurana, and Anthony L. Fink. Fourier transform infrared spectroscopy in analysis of protein deposits. *Methods in Enzymology*, 309:559–576, 1999. ISSN 00766879. doi: 10.1016/S0076-6879(99)09038-2.

[368] Heather D. Couture, Lindsay A. Williams, Joseph Geradts, Sarah J. Nyante, Ebonee N. Butler, J. S. Marron, Charles M. Perou, Melissa A. Troester, and Marc Niethammer. Image analysis with deep learning to predict breast cancer grade, ER status, histologic subtype, and intrinsic subtype. *npj Breast Cancer*, 4(1), 2018. ISSN 23744677. doi: 10.1038/s41523-018-0079-1.

[369] Erick Moen, Dylan Bannon, Takamasa Kudo, William Graf, Markus Covert, and David Van Valen. Deep learning for cellular image analysis. *Nature Methods*, 2019. ISSN 1548-7091. doi: 10.1038/s41592-019-0403-1.

[370] Dimitris Karampalis, Hui Cao, Joel Caragay, Yulong Ding, and Serafim Bakalis. Understanding dissolution phenomena of spray dried powders using a single particle approach. *Chemical Engineering Science*, 196:25–36, 2018. ISSN 00092509. doi: 10.1016/j.ces.2018.11.046.

[371] T. T.H. Tran, M. Jaskulski, J. G. Avila-Acevedo, and E. Tsotsas. Model parameters for single-droplet drying of skim milk and its constituents at moderate and elevated temperatures. *Drying Technology*, 35(4):444–464, 2017. ISSN 15322300. doi: 10.1080/07373937.2016.1182548.

[372] Mo Jiang and Richard D. Braatz. Low-Cost Noninvasive Real-Time Imaging for Tubular Continuous-Flow Crystallization. *Chemical Engineering and Technology*, 41(1):143–148, 2018. ISSN 15214125. doi: 10.1002/ceat.201600276.

[373] Aymeric Ousset, Rosanna Chirico, Florent Robin, Martin Alexander Schubert, Pascal Somville, and Kalliopi Dodou. A novel protocol using small-scale spray-drying for the efficient screening of solid dispersions in early drug development and formulation, as a straight pathway from screening to manufacturing stages. *Pharmaceuticals*, 11(3), 2018. ISSN 14248247. doi: 10.3390/ph11030081.

[374] Ashland. Ashland — from matrix to film coating, your full-service pharmaceutical technology resource, 2013.

[375] Lingjuan Wang-Li, Calvin B. Parnell, and Bryan W. Shaw. Analysis of Cyclone Collection Efficiency. *ASAE Meeting Presentation Analysis*, 2003. doi: 10.13031/2013.15040.

[376] Philip Chi, Lip Kwok, Adam Grabarek, Michael Y T Chow, Yun Lan, Johnny C W Li, Luca Casettari, A James Mason, and Jenny K W Lam. Inhalable spray-dried formulation of D-LAK antimicrobial peptides targeting tuberculosis. *International Journal of Pharmaceutics*, 491(1-2):367–374, 2015. ISSN 0378-5173. doi: 10.1016/j.ijpharm.2015.07.001.

[377] Andrew C Drake, Youngjoo Lee, Emma M Burgess, Jens O M Karlsson, Ali Eroglu, and Adam Z Higgins. Effect of water content on the glass transition temperature of mixtures of sugars , polymers , and penetrating cryoprotectants in physiological buffer. pages 1–15, 2018.

[378] Tiina Lipiäinen. *Stability and Analysis of Solid-State Forms in Pharmaceutical Powders*. 2018. ISBN 9789515142825.

[379] Nicole E. Hunter, Christopher S. Frampton, Duncan Q.M. Craig, and Peter S. Belton. The use of dynamic vapour sorption methods for the characterisation of water uptake in amorphous trehalose. *Carbohydrate Research*, 345(13):1938–1944, 2010. ISSN 00086215. doi: 10.1016/j.carres.2010.06.011.

9 Appendix

A1 Appendix - XRT Characterisation of Pharmaceutical Solid Products (Chapter 4)

A1.1 Micro-XRT Data Acquisition Details

Table A1: Data acquisition settings for scanned pharmaceutical micro-XRT samples. Focus mode: MF - micro-focus (beam spot size 2.0 μm) and NF - nano-focus (beam spot size 0.9 / 0.5 μm).

Sample	Source Voltage / Current	Image Pixelsize	Frame Averaging / Step Size	Scan Time
XRT Pharma Products (Chapter 4)				
TR0	40 kV/ 370 μA	1.20 μm (MF)	4 / 0.2°	01h:16min
TR1	40 kV/ 370 μA	1.20 μm (MF)	2 / 0.2°	00h:22min
TR2	40 kV/ 370 μA	1.20 μm (MF)	1 / 0.8°	00h:07min
TR3	40 kV/ 370 μA	1.20 μm (MF)	1 / 2.0°	00h:03min
Tblt20	40 kV/ 420 μA	4.00 μm (MF)	6 / 0.2°	03h:19min
Tblt50	40 kV/ 375 μA	4.00 μm (MF)	6 / 0.2°	03h:28min
Tblt80	40 kV/ 375 μA	4.00 μm (MF)	6 / 0.2°	03h:27min
Tblt100	40 kV/ 375 μA	4.00 μm (MF)	6 / 0.2°	03h:20min
MET- PVP PhyMix	40 kV/ 480 μA	0.60 μm (NF)	8 / 0.2°	10h:41min
GLY_P01	40 kV/ 360 μA	0.80 μm (MF)	8 / 0.1°	07h:16min
GLY_P02	40 kV/ 440 μA	0.60 μm (NF)	8 / 0.2°	04h:52min
CBZ_P	40 kV/ 500 μA	0.50 μm (NF)	6 / 0.2°	03h:20min
TRE_P	40 kV/ 600 μA	0.80 μm (MF)	8 / 0.2°	06h:04min
LAC_P	40 kV/ 400 μA	0.80 μm (MF)	8 / 0.1°	08h:02min
MAN_P	40 kV/ 390 μA	0.80 μm (MF)	8 / 0.2°	07h:27min
PVP_P	40 kV/ 400 μA	0.90 μm (MF)	8 / 0.1°	07h:40min
PVP-GLY_P	40 kV/ 400 μA	0.80 μm (MF)	6 / 0.4°	01h:40min

PVP-INA_P	40 kV/ 420 μA	0.80 μm (MF)	4 / 0.8°	00h:35min

A1.2 ToF-SIMS Characterisation

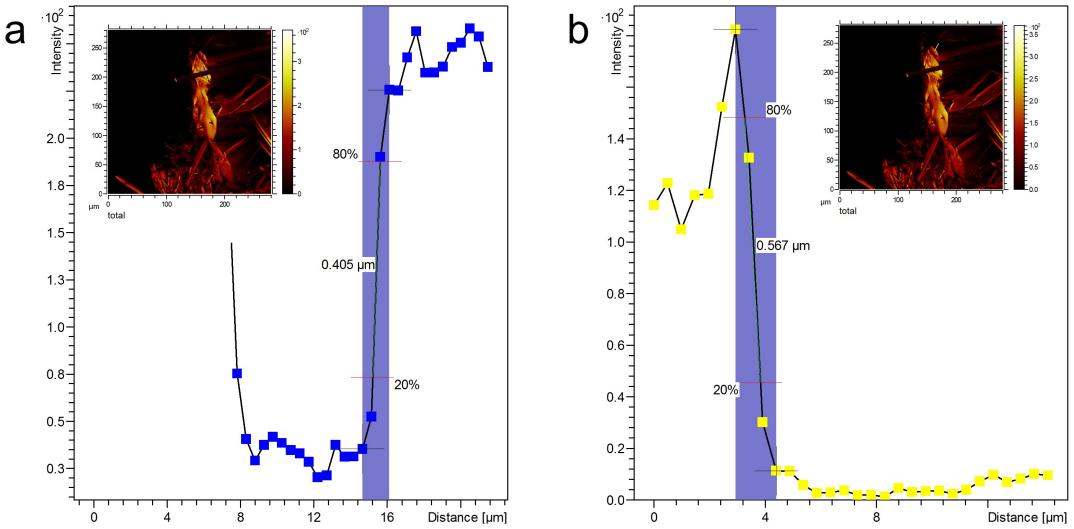

Figure A1: Determination of ToF-SIMS spatial resolution using a 20/80 edge-resolution analysis. The analysis on the total ion image yielded a spatial resolution between 400 - 600 nm ([a] 405 nm / [b] 567 nm) using a linescan method.

A2 Appendix - XRT Image Analysis and Machine Learning for the Characterisation of Multi-Particulates (Chapter 5)

A2.1 Micro-XRT Data Acquisition Details

Table A2: Micro-XRT data acquisition settings for scanned ibuprofen capsules. C0 and C3 were collected aiming for high image data quality. C1, C2, C4 and C5 were collected with accelerated scanning settings for fast image acquisition.

Sample	Source Voltage / Current	Image Pixelsize	Frame Averaging / Step Size	Scan Time
C0	40 kV/380 μA	2.5 μm	3/0.2°	12h:08min
C1	40 kV/400 μA	5.0 μm	3/0.2°	01h:57min
C2	40 kV/400 μA	6.0 μm	3/0.2°	02h:00m
C3	40 kV/360 μA	2.5 μm	3/0.2°	16h:24min
C4	40 kV/400 μA	5.0 μm	3/0.2°	02h:01min
C5	40 kV/400 μA	5.0 μm	3/0.2°	01h:58min

A2.2 Voxel-based arithmetic Operations

The internal capsule volume (V_CS_InV) was calculated from the capsule shell (V_CS) and its ROI (V_CS_ROI, Equation A1). To differentiate between inter- and intra-object background volumes a pellet ROI was defined (V_CP_ROI) as previously described for single particles [7]. V_CP_ROI was subsequently subtracted from V_CS_InV to yield the capsule void space (V_CS_Poros, Equation A2). The total pellet porosity (V_CP_Poros) is given after a subtraction of the pellets' solid phase (V_CP) from V_CP_ROI using Equation A3. The distribution of both can be quantified for the full sample and locally within the capsule image space.

$$\text{V\_CS\_InV} = \text{V\_CS\_ROI} - \text{V\_CS} \tag{A1}$$

$$\text{V\_CS\_Poros} = \text{V\_CS\_InV} - \text{V\_CP\_ROI} \tag{A2}$$

$$\text{V\_CP\_Poros} = \text{V\_CP\_ROI} - \text{V\_CP} \tag{A3}$$

A2.3 Micro-XRT Sensitivity Analysis Details

The impact of changing micro-XRT image quality and image processing parameters on the quantified structural features was investigated during a sensitivity analysis. Sampled conditions of changing micro-XRT image quality and image processing parameters are described in Table A3 (ESI, page A4). The results are presented qualitatively and quantitatively in Fig. A3 (ESI, page A7) and Fig. A2 (ESI, page A6), respectively. Features with the highest variability are related to the particle porosity, which further impacts features describing the object's volume and orientation. The changes in the pellet porosity were further assessed using an approach for structural thickness calculation (CTAn v 1.16.4.1, Bruker). The local thickness of the pellet porosity (V_P_Poros) is compared in Table A4 as volume density distributions normalised to the user defined ground truth (SA_01). The total porosity volumes change significantly with up to 92.44% difference between SA_06 and SA_03. The smaller porosity fractions between 5 μm and 25 μm are particularly sensitive to changing micro-XRT image qualities and image processing parameters indicating a size dependent sensitivity. For SA_01 (user optimised parameters), 99.07% of the total porosity volume are part of the 5 μm and 25 μm size range emphasising the overall impact of these two size fractions to the total porosity volume.

Table A3: Overview of sampling points for a sensitivity analysis systematically assessing the impact of changes in the micro-XRT image quality and image processing parameters.

ID	Info
SA_01	*Optimised parameter (ground truth, user validated)*
SA_02	Reduced micro-XRT image quality (gaussian filter, $\sigma = 0.8$)
SA_03	Reduced micro-XRT image quality (gaussian filter, $\sigma = 1.2$)
SA_04	Ridler-Calvard (alternative image thresholding method)
SA_05	Image threshold value -1.6% of SA_01
SA_06	Image threshold value +1.6% of SA_01
SA_07	No V_ROI noise reduction
SA_08	High V_ROI noise reduction
SA_09	Medium V noise reduction
SA_10	High V noise reduction

Table A4: Relative changes in the porosity volume distribution for selected samples during a sensitivity analysis and the contribution related to the local thickness. The smallest porosity fraction between 5.0 - < 15.0 μm is particularly affected by changes in the micro-XRT image quality and image processing parameters.

Range [μm]	SA_01	SA_02	SA_03	SA_06	SA_09
5.0 - < 15.0	90.12%	30.57%	5.22%	110.42%	31.91%
15.0 - < 25.0	8.95%	3.62%	1.48%	18.40%	8.66%
25.0 - < 35.0	0.53%	0.40%	0.47%	0.61%	0.59%
35.0 - < 45.0	0.24%	0.15%	0.23%	0.27%	0.24%
45.0 - < 55.0	0.12%	0.09%	0.12%	0.13%	0.13%
55.0 - < 65.0	0.02%	0.03%	0.05%	0.01%	0.02%
65.0 - < 75.0	0.02%	0.00%	0.00%	0.03%	0.02%
Sum	**100.00%**	**34.86%**	**7.56%**	**129.86%**	**41.57%**

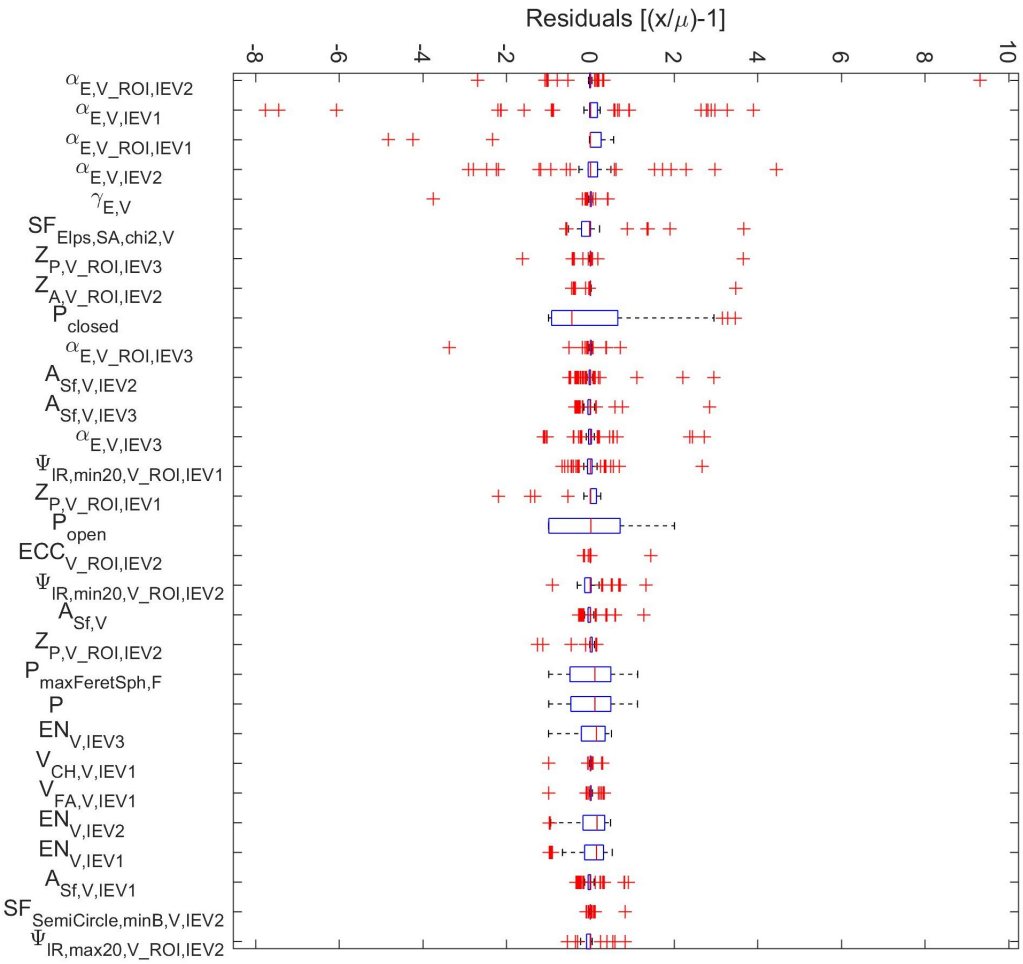

Figure A2: Box plots of the top 30 features with the highest variability during a quantitative sensitivity analysis of micro-XRT image quality and critical image processing parameters on the extracted object features (x = observation, μ = feature mean). The sensitivity analysis identified features linked to the pellet porosity and orientation with the largest dependency on collected data quality and selected processing parameters.

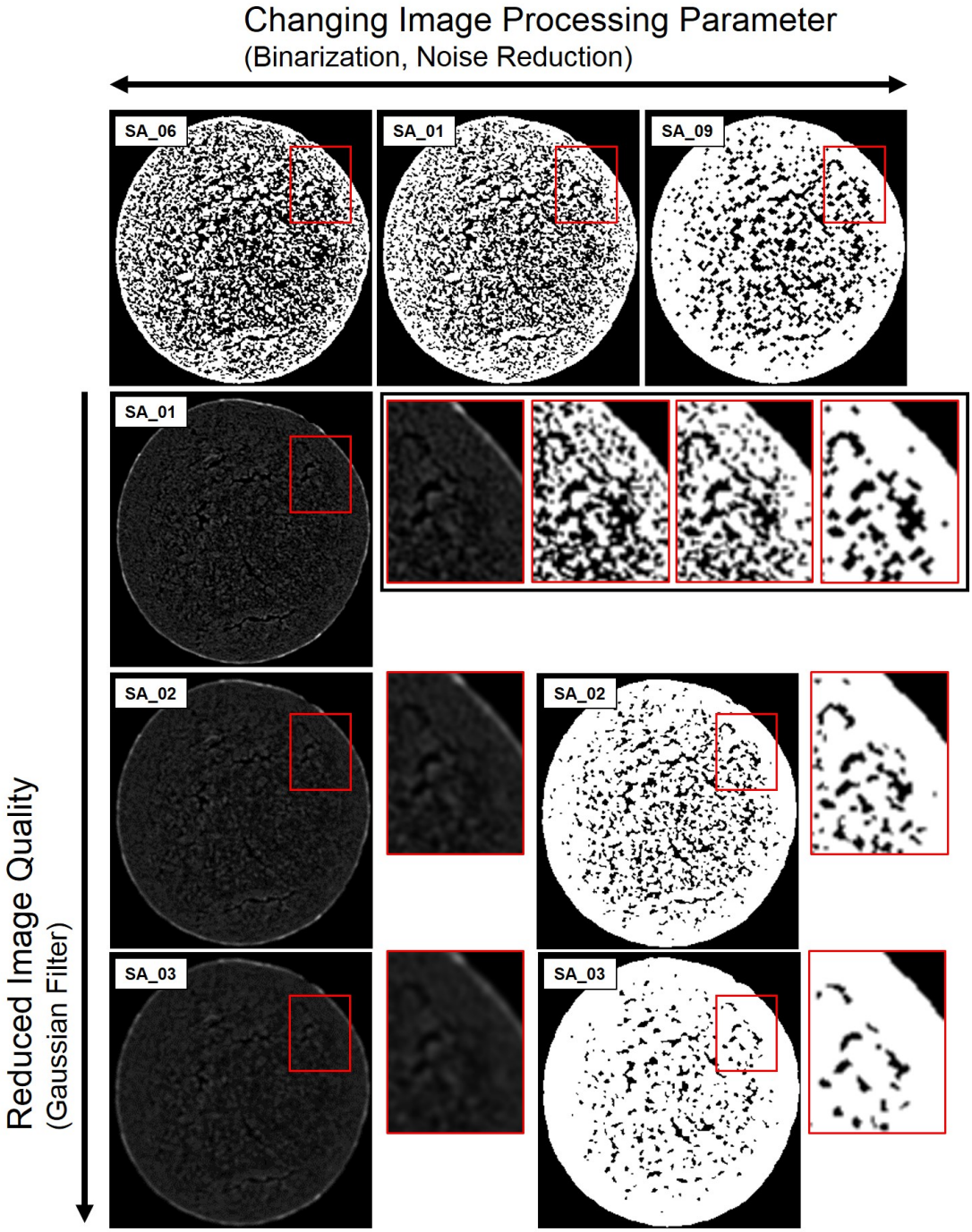

Figure A3: Qualitative visualisation of the impact of the collected micro-XRT image quality and critical image processing parameters on the binarized object volume. The images suggest a strong correlation between the detected internal object porosity and the collected micro-XRT image data quality as well as selected processing parameters.

Table A5: Sensitivity analysis ranking of 132 structural features exhibiting values above a 10% variability threshold comparing the feature residuals of individual sampling points to the user defined ground truth. These features were excluded from the feature selection approach for pellet classification.

Feature	Rank	Residuals (X/μ-1)			Category
		Median	Max	Min	
$\alpha_{E,V\_ROI,IEV2}$	1	0	9.309	-2.7	Orientation
$\alpha_{E,V,IEV1}$	2	0.006	3.895	-7.761	Orientation
$\alpha_{E,V\_ROI,IEV1}$	3	0	0.556	-4.827	Orientation
$\alpha_{E,V,IEV2}$	4	0.004	4.442	-2.912	Orientation
$\gamma_{E,V}$	5	0.001	0.426	-3.76	Orientation
$SF_{Elps,SA,chi2,V}$	6	-0.018	3.665	-0.59	Shape
$Z_{P,V\_ROI,IEV3}$	7	0	3.648	-1.625	Orientation
$Z_{A,V\_ROI,IEV2}$	8	0	3.482	-0.449	Size
P_{closed}	9	-0.443	3.46	-1	Poros
$\alpha_{E,V\_ROI,IEV3}$	10	0.001	0.714	-3.373	Orientation
$A_{Sf,V,IEV2}$	11	-0.001	2.954	-0.508	Surface
$A_{Sf,V,IEV3}$	12	-0.005	2.85	-0.375	Surface
$\alpha_{E,V,IEV3}$	13	0.002	2.72	-1.125	Orientation
$\Psi_{lR,min20,V\_ROI,IEV1}$	14	0.002	2.673	-0.678	Shape
$Z_{P,V\_ROI,IEV1}$	15	0.007	0.248	-2.196	Orientation
P_{open}	16	0.013	2.01	-1	Poros
$ECC_{V\_ROI,IEV2}$	17	0.001	1.441	-0.166	Shape
$\Psi_{lR,min20,V\_ROI,IEV2}$	18	-0.003	1.332	-0.911	Shape
$A_{Sf,V}$	19	-0.001	1.276	-0.278	Surface
$Z_{P,V\_ROI,IEV2}$	20	0.001	0.148	-1.263	Orientation
$P_{maxFeretSph,F}$	21	0.107	1.131	-0.996	Poros
P	22	0.107	1.128	-0.996	Poros
$EN_{V,IEV3}$	23	0.144	0.503	-1	Poros
$V_{CH,V,IEV1}$	24	-0.001	0.299	-1	Shape
$V_{FA,V,IEV1}$	25	-0.001	0.334	-1	Poros

$EN_{V,IEV2}$	26	0.159	0.481	-0.99	Poros
$EN_{V,IEV1}$	27	0.147	0.523	-0.989	Poros
$A_{Sf,V,IEV1}$	28	-0.005	0.906	-0.344	Surface
$SF_{SemiSph,minB,V,IEV2}$	29	-0.003	0.829	-0.108	Shape
$\Psi_{lR,max20,V\_ROI,IEV2}$	30	-0.002	0.827	-0.545	Shape
$\Psi_{lR,max20,V\_ROI,IEV1}$	31	0	0.813	-0.473	Shape
$V_{V,IEV2}$	32	-0.052	0.774	-0.271	Size
$\alpha_{E,V}$	33	0.001	0.497	-0.744	Orientation
$\Psi_{lR,V\_ROI,IEV2}$	34	0.001	0.092	-0.654	Shape
$ECC_{V,IEV2}$	35	0.003	0.118	-0.63	Shape
$\Psi_{lR,min20,V\_ROI,IEV3}$	36	0	0.626	-0.367	Shape
$d_{breadth,V\_ROI}$	37	0.001	0.128	-0.567	Size
$\Psi_{lR,V\_ROI,IEV1}$	38	0.001	0.557	-0.284	Shape
$EX_{V,IEV2}$	39	-0.021	0.544	-0.365	Shape
$SF_{Tri,minB,V,IEV2}$	40	-0.002	0.524	-0.071	Shape
$SF_{SemiSph,minB,V\_ROI,IEV1}$	41	-0.002	0.506	-0.061	Shape
$SF_{SemiSph,minB,V\_ROI,IEV2}$	42	-0.002	0.062	-0.49	Shape
$SF_{Sph,minB,F,V,IEV2}$	43	0.001	0.477	-0.323	Shape
$SF_{PolyArea,V,IEV2}$	44	-0.001	0.463	-0.327	Shape
$V_{FA,V,IEV2}$	45	-0.001	0.448	-0.269	Poros
$SF_{Sph,minB,r,V}$	46	0.004	0.08	-0.44	Size
$EX_{V,IEV3}$	47	-0.031	0.379	-0.359	Shape
$SV_{V,IEV2}$	48	-0.027	0.376	-0.334	Poros
$SF_{Elps,IM,dMin,V,IEV2}$	49	0.001	0.375	-0.054	Size
$\Psi_{lR,V\_ROI,IEV3}$	50	0.001	0.246	-0.373	Shape
$SV_{V,IEV3}$	51	-0.03	0.336	-0.36	Poros
$SF_{Tri,minB,V\_ROI,IEV2}$	52	-0.002	0.049	-0.359	Shape
$SF_{PolyArea,V,IEV3}$	53	0	0.058	-0.347	Shape
$SF_{Sph,minB,F,V,IEV3}$	54	0.001	0.05	-0.346	Shape
$SF_{SemiSph,minB,F,V,IEV2}$	55	0.001	0.079	-0.346	Shape

$SF_{Rect,minB,F,V,IEV3}$	56	0.001	0.05	-0.346	Shape
$d_{eqSph,V,IEV2}$	57	-0.018	0.346	-0.183	Size
$\Psi_{lR,max20,V\_ROI,IEV3}$	58	0.001	0.168	-0.345	Shape
$SF_{Tri,minB,F,V,IEV3}$	59	0.001	0.044	-0.344	Shape
$SF_{Tri,minB,V\_ROI,IEV1}$	60	-0.002	0.341	-0.041	Shape
$SF_{SemiSph,minB,F,V,IEV3}$	61	0.002	0.057	-0.341	Shape
$EX_{V,IEV1}$	62	-0.008	0.336	-0.333	Shape
AR_{V}	63	0	0.336	-0.095	Shape
$SV_{V,IEV1}$	64	-0.028	0.323	-0.335	Poros
$SF_{Rect,minB,V,IEV2}$	65	-0.002	0.334	-0.058	Shape
$SF_{SemiSph,minB,F,V\_ROI,IEV2}$	66	0.001	0.332	-0.04	Shape
$SF_{Tri,minB,F,V,IEV2}$	67	0	0.071	-0.33	Shape
$V_{V,IEV3}$	68	-0.026	0.326	-0.307	Size
$SF_{Rect,minB,F,V,IEV2}$	69	0.001	0.101	-0.323	Shape
$SF_{Sph,minB,F,V\_ROI,IEV2}$	70	0	0.039	-0.32	Shape
$SF_{SemiSph,minB,V,IEV1}$	71	-0.001	0.067	-0.318	Shape
$V_{V,IEV1}$	72	-0.021	0.315	-0.316	Size
$V_{CH,V,IEV2}$	73	-0.002	0.312	-0.043	Shape
$ECC_{V,IEV1}$	74	-0.002	0.212	-0.311	Shape
$Z_{A,V\_ROI,IEV3}$	75	-0.002	0.309	-0.106	Size
$SF_{PolyArea,V\_ROI,IEV2}$	76	-0.002	0.04	-0.309	Shape
$V_{V\_ROI,IEV2}$	77	-0.002	0.04	-0.306	Size
$SF_{Elps,IM,dMin,V\_ROI,IEV2}$	78	-0.001	0.036	-0.3	Size
EX_{V}	79	-0.03	0.298	-0.261	Shape
SV	80	-0.028	0.292	-0.259	Poros
$V_{maxFeretSph,F,V}$	81	-0.02	0.291	-0.26	Shape
V_{V}	82	-0.031	0.286	-0.263	Size
$V_{FA,V,IEV3}$	83	0	0.054	-0.281	Poros
$SF_{Elps,SA,r3,V}$	84	-0.001	0.078	-0.275	Size
$SF_{Sph,minB,F,V\_ROI,IEV1}$	85	0	0.274	-0.05	Shape

$SF_{PolyArea,V\_ROI,IEV1}$	86	-0.002	0.269	-0.036	Shape
$V_{V\_ROI,IEV1}$	87	-0.002	0.266	-0.035	Size
$SF_{Rect,minB,V\_ROI,IEV2}$	88	-0.002	0.037	-0.264	Shape
$V_{CH,V\_ROI,IEV2}$	89	-0.002	0.035	-0.248	Shape
$SF_{Tri,minB,V,IEV1}$	90	-0.001	0.081	-0.238	Shape
$V_{CH,V\_ROI,IEV1}$	91	-0.002	0.235	-0.032	Shape
$EX_{V\_ROI,IEV1}$	92	0	0.228	-0.048	Shape
$\beta_{E,V}$	93	0.002	0.191	-0.228	Orientation
$SF_{Rect,minB,V\_ROI,IEV1}$	94	-0.002	0.225	-0.029	Shape
$SF_{Elps,IM,dMin,V\_ROI,IEV1}$	95	-0.001	0.221	-0.028	Size
$SF_{SemiSph,minB,F,V,IEV1}$	96	0	0.205	-0.129	Shape
$l_{BB,2,V\_ROI,IEV3}$	97	-0.002	0.059	-0.202	Size
$EX_{V\_ROI,IEV2}$	98	0	0.025	-0.202	Shape
$l_{BB,1,V\_ROI,IEV3}$	99	-0.001	0.199	-0.055	Size
$d_{eqSph,V,IEV3}$	100	-0.009	0.16	-0.198	Size
$ECC_{V,IEV3}$	101	0	0.181	-0.196	Shape
$l_{BB,1,V\_ROI,IEV2}$	102	-0.001	0.188	-0.054	Size
$d_{eqSph,V,IEV1}$	103	-0.013	0.154	-0.187	Size
$SF_{Sph,minB,F,V,IEV1}$	104	0.001	0.121	-0.187	Shape
$l_{BB,2,V,IEV3}$	105	-0.002	0.184	-0.064	Size
$SF_{Sph,minB,r,V\_ROI}$	106	0.007	0.081	-0.183	Size
$Z_{A,V\_ROI,IEV1}$	107	-0.002	0.097	-0.181	Shape
$SF_{Elps,IM,dMin,V,IEV1}$	108	0.003	0.07	-0.178	Size
$SF_{PolyArea,V,IEV1}$	109	-0.001	0.067	-0.172	Shape
$l_{BB,1,V\_ROI,IEV1}$	110	-0.001	0.165	-0.036	Size
$d_{eqSph,V\_ROI,IEV2}$	111	-0.001	0.021	-0.165	Size
$SF_{SemiSph,minB,F,V\_ROI,IEV1}$	112	0	0.026	-0.165	Shape
$SF_{Elps,SA,chi2,V\_ROI}$	113	-0.004	0.165	-0.085	Shape
$SF_{Rect,minB,V,IEV1}$	114	0	0.091	-0.161	Shape
$ECC_{V\_ROI,IEV3}$	115	-0.001	0.154	-0.036	Shape

$l_{BB,1,V,IEV2}$	116	0.001	0.057	-0.151	Size
$l_{BB,2,V,IEV1}$	117	0.001	0.149	-0.111	Size
$SF_{SemiSph,minB,V,IEV3}$	118	-0.002	0.146	-0.147	Shape
$ECC_{V\_ROI,IEV1}$	119	0	0.037	-0.142	Shape
γ_{E,V_ROI}	120	0	0.029	-0.138	Orientation
$SF_{Sph,minB,V,IEV1}$	121	-0.001	0.1	-0.136	Shape
$SF_{Elps,IM,dMin,V,IEV3}$	122	0.001	0.054	-0.128	Size
$SF_{Elps,IM,dMax,V,IEV1}$	123	0.002	0.051	-0.127	Size
$d_{eqSph,V\_ROI,IEV1}$	124	-0.001	0.126	-0.017	Size
$SF_{Rect,minB,F,V,IEV1}$	125	0.001	0.1	-0.126	Shape
Ψ_{gl,V_ROI}	126	0.002	0.056	-0.118	Shape
$SF_{SemiSph,minB,F,V\_ROI,IEV3}$	127	-0.001	0.11	-0.025	Shape
$l_{BB,1,V,IEV3}$	128	-0.001	0.055	-0.106	Size
$l_{BB,2,V,IEV2}$	129	0	0.048	-0.103	Size
$V_{CH,V,IEV3}$	130	-0.002	0.06	-0.102	Shape
$EX_{V\_ROI,IEV3}$	131	0	0.034	-0.101	Shape
$A_{Sf,V\_ROI,IEV3}$	132	-0.002	0.101	-0.033	Surface

A2.4 ReliefF Feature Selection Results

Table A6: ReliefF feature ranking of 74 extracted structural features linked to pellet size, shape, surface and orientation attributes. The importance of individual features is expressed by the calculated ReliefF weights which range from -1 to 1 for low and high importance, respectively. Further, the list includes p-values from a two-sample t-test (H_0 of equal means) and F-scores to indicate class separation for individual features, but failing to address important feature-feature dependencies

Feature	Rank	Weight	p-Value	F-Score	Category
$V_{maxFeretSph,F,V\_ROI}$	**1**	**0.536**	**0**	**21.524**	**Shape**
$V_{maxFeretSph,F,V\_ROI,CH}$	2	0.509	0	18.418	Shape

EX_{V_ROI}	3	0.454	0	122.604	Shape
$SF_{Sph,minB,F,V\_ROI,IEV3}$	4	0.45	0	36.905	Shape
AR_{V_ROI}	5	0.382	0	74.827	Shape
$SF_{Elps,SA,r3,V\_ROI}$	**6**	**0.361**	**0**	**69.653**	**Size**
$SV_{CH,V\_ROI,IEV1}$	**7**	**0.306**	**0**	**77.498**	**Surface**
$SF_{Tri,minB,F,V\_ROI,IEV1}$	8	0.305	0	22.544	Shape
$SF_{Rect,minB,F,V\_ROI,IEV1}$	9	0.299	0	75.071	Shape
$SV_{CH,V\_ROI,IEV3}$	10	0.296	0	69.095	Surface
$SV_{CH,V\_ROI,IEV2}$	11	0.283	0	61.428	Surface
$SF_{Tri,minB,F,V\_ROI,IEV3}$	12	0.254	0	22.412	Shape
$SF_{Elps,IM,dMin,V\_ROI,IEV3}$	13	0.25	0	20.187	Size
$SF_{Tri,minB,F,V\_ROI,IEV2}$	14	0.247	0	14.864	Shape
$SF_{Rect,minB,F,V\_ROI,IEV3}$	15	0.246	0	43.947	Shape
$SF_{SemiSph,minB,V\_ROI,IEV3}$	16	0.223	0	28.755	Shape
$SF_{Tri,minB,F,V,IEV1}$	17	0.218	0.003	9.712	Shape
$SF_{Rect,minB,F,V\_ROI,IEV2}$	18	0.205	0.001	16.479	Shape
d_{eqSph,V_ROI}	19	0.19	0	28.666	Size
$d_{eqSph,V}$	20	0.182	0	21.317	Size
$d_{eqSph,V\_ROI,IEV3}$	21	0.175	0	12.443	Size
$SF_{Tri,minB,V,IEV3}$	22	0.173	0	19.858	Shape
$SF_{Tri,minB,V\_ROI,IEV3}$	23	0.172	0	19.62	Shape
$l_{BB,min,V}$	24	0.167	0	30.148	Size
l_{BB,min,V_ROI}	25	0.167	0	30.148	Size
$SF_{PolyArea,V\_ROI,IEV3}$	26	0.164	0	18.712	Shape
V_{V_ROI}	27	0.149	0	14.165	Size
$V_{V\_ROI,IEV3}$	28	0.148	0	7.965	Size
$SF_{Rect,minB,V,IEV3}$	29	0.146	0	17.231	Shape
$SF_{Rect,minB,V\_ROI,IEV3}$	30	0.145	0	17.019	Shape
$V_{CH,V\_ROI,IEV3}$	31	0.137	0	7.57	Shape
V_{CH,V_ROI}	32	0.132	0	13.305	Size

$SF_{Elps,SA,r2,V}$	33	0.129	0	22.872	Size
SV_{CH,V_ROI}	34	0.126	0.7	0.132	Surface
$SF_{Elps,SA,r1,V}$	35	0.122	0	3.298	Size
$SF_{Elps,SA,r2,V\_ROI}$	36	0.121	0	21.183	Size
$A_{Sf,V\_ROI,IEV1}$	37	0.112	0	8.916	Surface
A_{Sf,V_ROI}	38	0.111	0	14.598	Surface
$SF_{Elps,SA,r1,V\_ROI}$	39	0.109	0	3.712	Size
$l_{IB,y}$	40	0.106	0	15.145	Size
$A_{Sf,V\_ROI,IEV2}$	41	0.104	0	6.45	Surface
$l_{BB,2,V\_ROI,IEV1}$	42	0.099	0.044	0.428	Size
$l_{IB,z}$	43	0.097	0	11.666	Size
$l_{BB,2,V\_ROI,IEV2}$	44	0.093	0.027	0.464	Size
$l_{IB,x}$	45	0.092	0	13.497	Size
$l_{BB,1,V,IEV1}$	46	0.089	0.034	0.314	Size
$d_{maxFeret,V}$	47	0.083	0	5.021	Size
$V_{IB,V}$	48	0.078	0	10.256	Size
$SF_{Elps,IM,dMax,V\_ROI,IEV1}$	49	0.072	0	5.468	Size
l_{BB,max,V_ROI}	50	0.07	0	8.199	Size
$l_{BB,max,V}$	51	0.07	0	8.199	Size
$SF_{Elps,IM,dMax,V,IEV3}$	52	0.069	0	4.028	Size
$SF_{Elps,IM,dMax,V\_ROI,IEV3}$	53	0.064	0	4.169	Size
$x_{c,V,IEV1}$	54	0.06	0	2.651	Shape
$y_{c,V,IEV2}$	55	0.059	0	2.692	Shape
$x_{c,V\_ROI,IEV3}$	56	0.059	0	2.771	Shape
$x_{c,V\_ROI,IEV2}$	57	0.058	0	2.608	Shape
$y_{c,V\_ROI,IEV3}$	58	0.057	0	2.639	Shape
$x_{c,V,IEV2}$	59	0.057	0	2.644	Shape
$x_{c,V\_ROI,IEV1}$	60	0.057	0	2.698	Shape
$y_{c,V\_ROI,IEV2}$	61	0.056	0	2.75	Shape
$y_{c,V,IEV1}$	62	0.056	0	2.709	Shape

$x_{c,V,IEV3}$	63	0.056	0	2.79	Shape
$SF_{Sph,minB,V\_ROI,IEV3}$	64	0.056	0	5.271	Shape
$SF_{Sph,minB,V,IEV3}$	65	0.056	0	5.315	Shape
$SF_{Elps,IM,dMax,V,IEV2}$	66	0.054	0	4.164	Size
$y_{c,V,IEV3}$	67	0.054	0	2.691	Shape
$y_{c,V\_ROI,IEV1}$	68	0.053	0	2.779	Shape
$SF_{Sph,minB,V\_ROI,IEV1}$	69	0.051	0	7.13	Shape
$SF_{Elps,IM,dMax,V\_ROI,IEV2}$	70	0.047	0	4.515	Size
$SF_{Sph,minB,V\_ROI,IEV2}$	71	0.043	0	5.474	Shape
$SF_{Sph,minB,V,IEV2}$	72	0.041	0	5.654	Shape
α_{E,V_ROI}	73	0.037	0.861	0.001	Orientation
β_{E,V_ROI}	74	0.033	0.732	0.007	Orientation

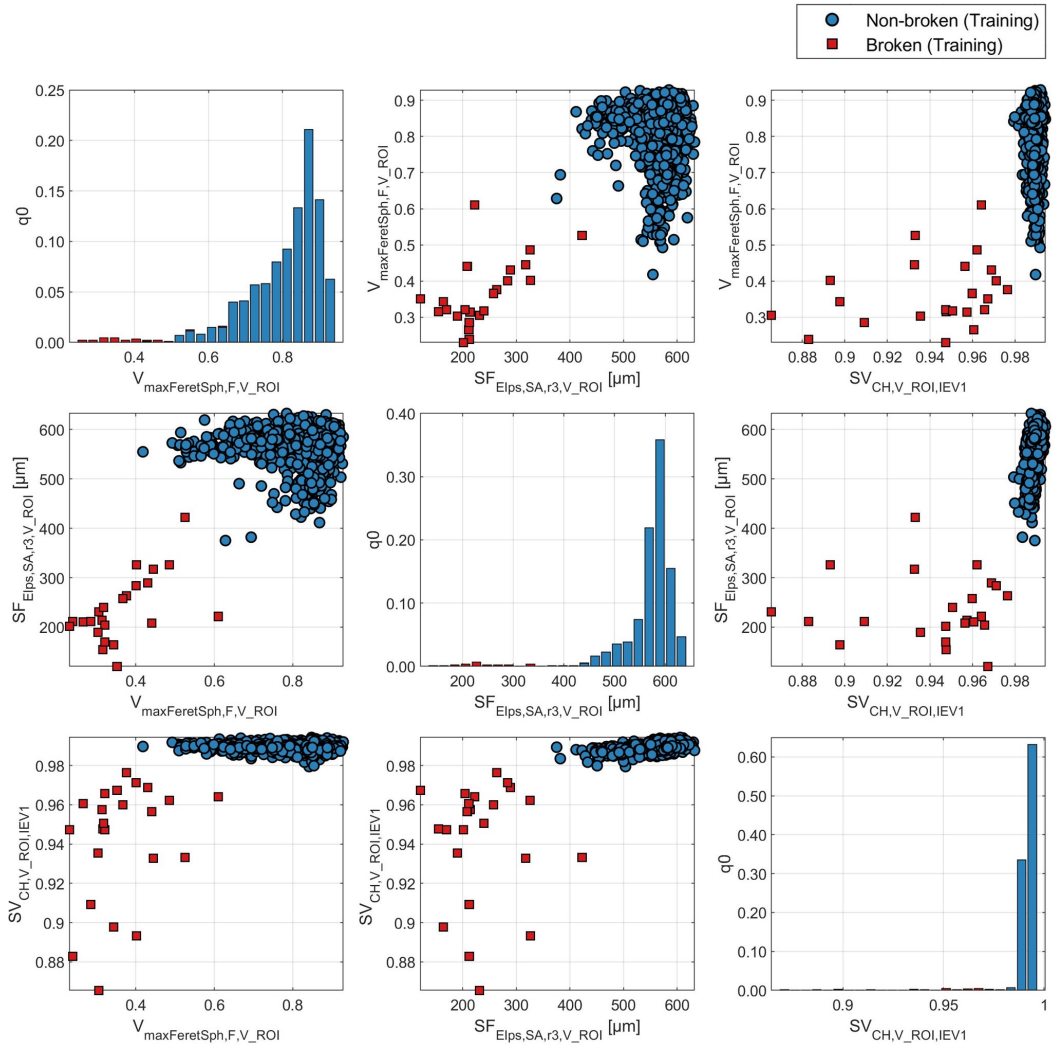

Figure A4: Plotmatrix of the training dataset (DTR) with feature combinations of $SF_{maxFeretSph,F,V\_ROI}$, $SF_{Elps,SA,r3,V\_ROI}$ and $SV_{CH,V\_ROI,IEV1}$.

A2.5 Data Analysis

A2.5.1 ReliefF

The ReliefF algorithm is a filter-method approach which can be used in conjungtion with a labeled training dataset for the selection of features in categorical multi-dimensioanl classification problems [270, 271, 272, 273]. ReliefF calculates a score / weight (W, initialization $W_j = 0$) for each feature (F_j) using the k nearest neighbors method following Equation A4 (ESI, page A17) for nearest neighbor observations from the same class and in Equation A6 (ESI, page A17) for nearest neighbor observations from the different classes. The specified number of updates (m) was equal to the number of observations.

For observations (x_r, x_q) from the same class:

$$W_j^i = W_j^{i-1} - \frac{\Delta_j(x_r, x_q)}{m} \cdot d_{rq} \tag{A4}$$

For observations (x_r, x_q) from different classes with the prior probabilities of the class (p_{y_q}, p_{y_r}):

$$W_j^i = W_j^{i-1} + \frac{p_{y_q}}{1 - p_{y_r}} \cdot \frac{\Delta_j(x_r, x_q)}{m} \cdot d_{rq} \tag{A5}$$

with (for continuous F_j)

$$\Delta_j(x_r, x_q) = \frac{|x_{rj} - x_{qj}|}{\max(F_j) - \min(F_j)}$$

and a distance function (d_{rq}) which is subject to scaling ($\tilde{d}_{rq}$)

$$d_{rq} = \frac{\tilde{d}_{rq}}{\sum_{l=1}^{k} \tilde{d}_{rl}}, \; \tilde{d}_{rq} = exp^{-(\text{rank}(r,q)/\sigma)^2}$$

A2.5.2 F-Score

$$F(i) = \frac{(\bar{x_i}^+ - \bar{x_i})^2 + (\bar{x_i}^- - \bar{x_i})^2}{\frac{1}{n_+ - 1} \sum_{k=1}^{n+} (x_{k,i}^+ - \bar{x_i}^+)^2 + \frac{1}{n_- - 1} \sum_{k=1}^{n-} (x_{k,i}^- - \bar{x_i}^-)^2} \tag{A6}$$

with $\bar{x_i}$, $\bar{x_i}^+$ and $\bar{x_i}^-$, which are the average of the ith feature of the whole, the positive and the negative data set, respectively.

A2.5.3 Support Vector Machines

SVM establish an Optimally Separating Hyperplane (OSH) as a decision surface in the multidimensional feature space between both classes. The n-dimensional training data ($x_i \in R^n$) is used along with their assigned categories ($y_i = \pm 1$) to find the OSH defined by Equation A7 defined by its orthogonal vector $w \in R^n$ and constant $b \in R$. The margin for the OSH is maximised transforming the optimisation problem to a dual quadratic programming problem solved using the Lagrangian multipler method shown in Equation A8. Re-substituting w yields Equation A10. The used features were standardized to avoid scale effects on the classification

outcome (Equation A13). SVMs are kernel methods, where the input data is transformed to a high-dimensional feature space (*kernel trick*). Two of the most popular kernel functions for this transformation are linear (Equation A11) or radial basis functions (rbf, Equation A12).

$$f(x) = x \cdot \ w + b = 0 \tag{A7}$$

$$L_P = \frac{1}{2}\|w\|^2 - \sum_i \alpha_i [y_i(x_i \cdot \ w + b) - 1] \tag{A8}$$

with the partial derivatives at $L_P = 0$

$$\frac{\partial L_P}{\partial w} = w - \sum_i \alpha_i y_i x_i, \frac{\partial L_P}{\partial b} = -\sum_i \alpha_i y_i$$

$$w = \sum_i \alpha_i y_i x_i, \sum_i \alpha_i y_i = 0$$

$$L_D = \sum_i \alpha_i - \frac{1}{2} \sum_i \sum_j \alpha_i \alpha_j y_i y_j K(x_1, x_2) \tag{A9}$$

$$\max_\alpha \sum_i \alpha_i - \frac{1}{2} \sum_i \sum_j \alpha_i \alpha_j y_i y_j K(x_1, x_2) \tag{A10}$$

Kernel functions ($K(x_i, x_j)$) can be used for feature data transformation.

Linear kernel:

$$K(x_i, x_j) = x_i \cdot \ x_j \tag{A11}$$

Radial-Basis-Function kernel (RBF):

$$K(x_i, x_j) = exp(-\frac{\|x_i - x_j\|^2}{2\sigma^2}) \tag{A12}$$

The feature data is standardized to compensate changing measuring scales:

$$x_j^* = \frac{x_j - \mu_j^*}{\sigma_j^*} \text{ with } \mu_j^* = \frac{1}{\sum_k W_k^*} \sum_k W_k^* x_{jk} \tag{A13}$$

A3 Appendix - Investigation of the Particle Design Space of Novel Pharmaceutical Formulations (Chapter 6)

Table A7: Thermal emissivity correction factors for solid phase of HPMC K100LV (HPMC_10) and formulations of MET with MAN and HPMC K100LV (MS_0 - MS_4).

	ε
HPMC_10	0.988 ± 0.006
MS_0	0.942 ± 0.012
MS_1	0.929 ± 0.011
MS_2	0.936 ± 0.002
MS_3	0.949 ± 0.013
MS_4	0.932 ± 0.005

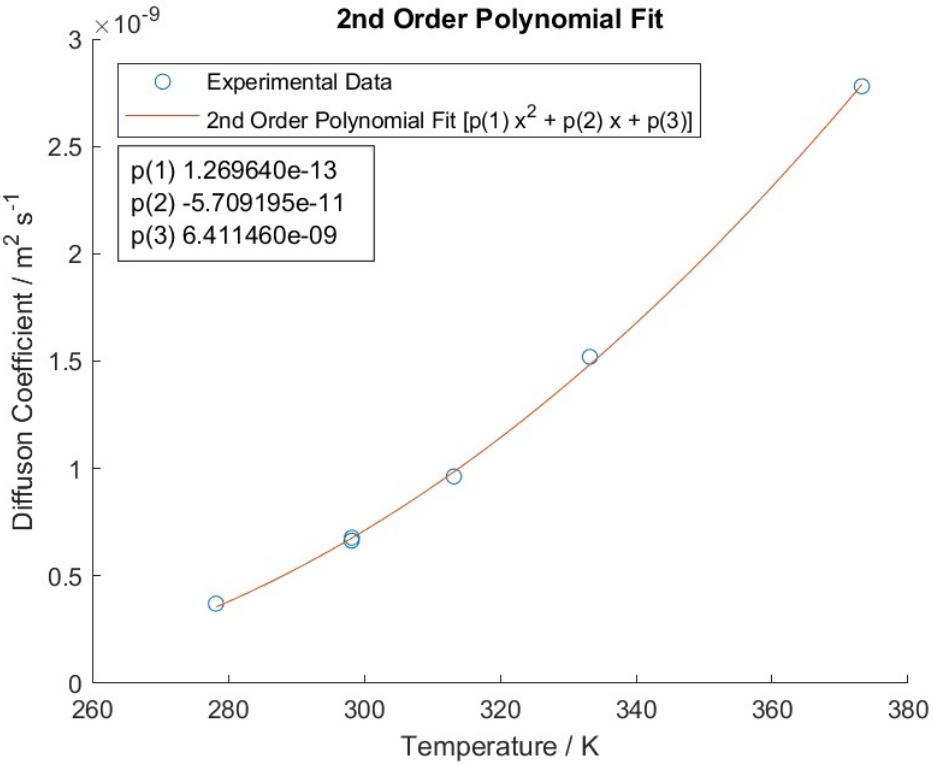

Figure A5: 2^{nd} order polynomial fit to calculate the diffusion coefficient of MAN in water. Reported experimental data from literature.[302, 303]

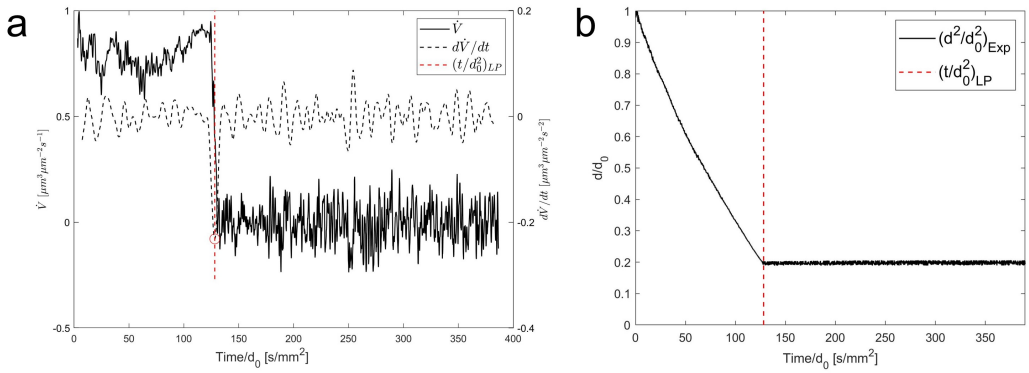

Figure A6: Lock-point (LP) detection during SDD experiments: (a) the evaporation volume flux ($\dot{V} = \Delta V/(A \cdot \Delta t) \propto \dot{m}$) of the solvent from the droplet to the gas phase is calculated iteratively from the changing droplet volume. LP ($(t/d_0^2)_{\mathrm{LP}}$) is detected where $\dot{V}$ undergoes a discontinuous change with $d\dot{V}(t_{LP})/dt = min(d\dot{V}/dt)$. (b) After LP, the particle reaches a final size and further evaporation of residual moisture cannot be quantified through the collected SDD images.

A3.1 Estimation of polymer diffusion coefficient using Stokes-Einstein equation

The viscosity of water can be calculated as a function of the temperature (T) using Equation A14 with A = 0.02939 mPa·s, B = 507.88 K and C = 149.3 K.

$$\eta_{\mathrm{WAT}} = A \cdot e^{\frac{B}{T-C}} \tag{A14}$$

The viscosity of HPMC solutions follows Equation A15 with a constant scaling factor K and the solid mass ratio of HPMC ($x = m_{\mathrm{HPMC}}/(m_{\mathrm{HPMC}} + m_{\mathrm{WAT}})$). For HPMC K100LV, K was determined to be 38.91 solving Equation A15 with $x = 0.02$ w/w and $\eta_{\mathrm{HPMC}} = 100$ mPa·s [374].

$$\eta_{\mathrm{HPMC}} = (1 + K \cdot x)^8 \tag{A15}$$

The radius of the hydrated polymer molecules (R_h) was calculated using Equation A15 which is derived from the Einstein viscosity relation for solid spherical particles with equal effect on the intrinsic solution viscosity ($[\eta]$) [301].

$$R_h = \left(\frac{3 \cdot [\eta] \cdot M_w}{10 \cdot \pi \cdot N_{Av}} \right)^{1/3} \tag{A16}$$

with intrinsic viscosity ($[\eta] = \lim_{c \to 0}(\eta_{sp}/c)$, for HPMC K100LV $[\eta] = 24.49$ mL/g), specific viscosity ($\eta_{sp} = (\eta - \eta_0)/\eta_0$), viscosity of the pure solvent ($\eta_0 = \eta_{\mathrm{WAT}}$), the polymer molecular

weight (M_w) and the Avogadro's constant (N_{Av}). For HPMC K100LV, R_h was calculated to be 1.85 nm. Other macromolecules with similar molecular weights have calculated R_h of 7.82 - 11.46 nm for Dextran or 5.56 - 18.95 for PVP [301].

The solute diffusion coefficient ($D_{s,SE}$) can be estimated as a function of the solution viscosity (η) and the temperature (T) using the Boltzmann constant (k_B) and R_h. The dynamic change of η and $D_{s,SE}$ over the course of the HPMC K100LV SDD experiments is shown in Fig. A7.

$$D_{s,SE} = \frac{k_B \cdot T}{6 \cdot \pi \cdot \eta \cdot R_h} \tag{A17}$$

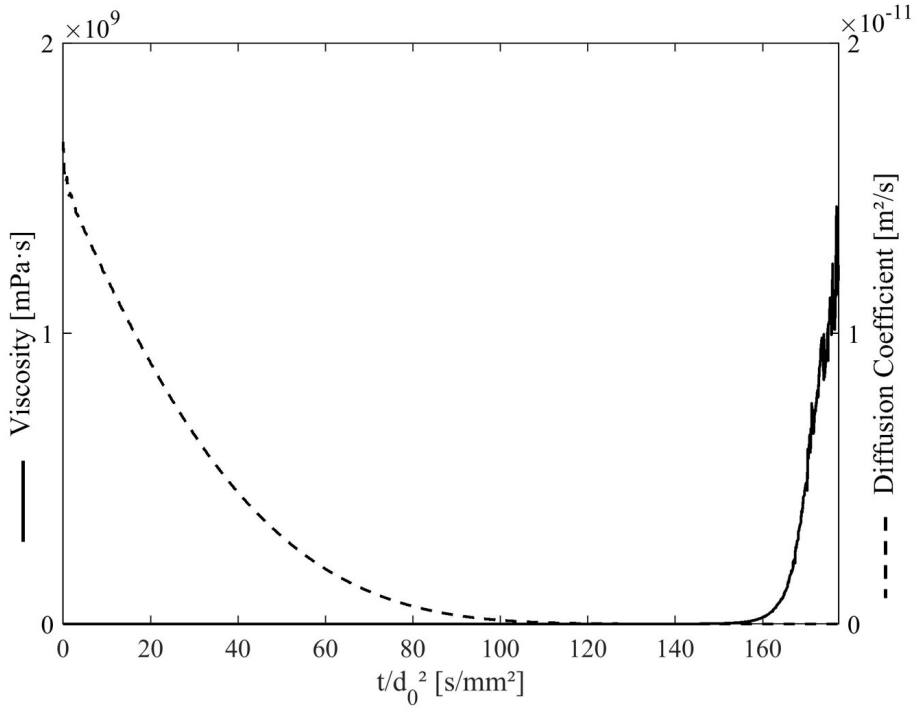

Figure A7: Changes in the calculated solution viscosity (η) and diffusion coefficient (D_s) of HPMC K100LV during liquid evaporation until LP. $\eta_{\text{HPMC K100LV}}$ and $D_{s,\text{HPMC K100LV}}$ are calculated using Equation A15 and Equation A17, respectively.

A4 Appendix - Peptide Isolation via Spray Drying (Chapter 7)

A4.1 Formulas

Spray dryer heat- and mass-balance: Antoine equation to calculate the saturation vapour pressure at P5 ($p_{S,Sat,P5}$) and P9 ($p_{S,Sat,P9}$) as a function of measured local temperature (T_K [K]). For water between 0 °C - 100 °C: A = 10.20, B = 1730.63 and C = -39.72 [DDBST (http://ddbonline.ddbst.com)].

$$p_{S,Sat} = 10^{A-B/(T_K+C)} \tag{A18}$$

Relative Humidity ($RH_{P9,R}$) is defined as the solvent vapour pressure ($p_{S,P9}$) in relation to the saturation vapour pressure ($p_{S,Sat,P9}$).

$$RH_{P9,R} = \frac{p_{S,P9}}{p_{S,Sat,P9}} \tag{A19}$$

Dalton's Rule at constant mole fractions of all inert gases for changes in the absolute pressure between local positions in the spray dryer (i = P3 - P5, $p_{P3} = p_{P4} = p_{P5} \backsimeq 1$ atm $= 1.013 \cdot 10^5$ Pa) and P9 ($p_{P9,R}$).

$$p_{S,i} = p_{S,P9}\frac{p_i}{p_{P9,R}} \tag{A20}$$

$$RH_{i,C} = RH_{P9,R} \cdot \frac{p_i}{p_{P9,R}} \cdot \frac{p_{S,Sat,P9}}{p_{S,Sat,i}} \tag{A21}$$

Cyclone Separation: The solid-gas separation in a cyclone can be described using Barth's classical model [357]. The critical cut-off size of the cyclone ($\bar{d}_{50}$, Equation A22) is a function of air viscosity (η), radial air velocity (v_{r_i}), radius of the exit duct (r_i), tangential particle velocity (v_t), and particle density (ρ_p). Additional information on the volume flow rate (Q), the internal radius of the cyclone (r_a) and the vortex height (h) are needed to estimate v_{r_i} and v_t [375].

$$\bar{d}_{50} = \sqrt{\frac{18 \cdot \eta \cdot v_{r_i} \cdot r_i}{v_t^2 \cdot \rho_p}} \tag{A22}$$

with radial air velocity:

$$v_{r_i} = \frac{Q}{2\pi r_i h}$$

and tangential particle velocity:

$$v_t = v_{in}\sqrt{\frac{r_a}{r_i}}$$

The volume flow rate (Q) was estimated according to Equation A23 using information on the specific humidity change between P3 and P5 ($SH_{P5\text{-}P3}$) and the recorded feed rate ($|FR_{P11,R}|$).

$$Q = \frac{|FR_{P11,R}|}{\Delta SH_{P5\text{-}P3}} \frac{R \cdot T}{p} \tag{A23}$$

with the ideal gas constant (R), local temperature (T in K) and local absolute pressure ($p_{P9} \simeq 1.013 \cdot 10^5$ Pa).

Used values to solve Equation A22 are listed in Table A8.

Table A8: Values for the calculation of the cyclone's cut-off size ($\bar{d}_{50}$) to evaluate the cyclone separation.

Z_0 [m]	r_i [m]	r_a [m]	η [Pa s]	ρ_p [kg/m^3]	Q [m^3/s]	$\bar{d}_{50}$ [m]
$140 \cdot 10^{-3}$	$7 \cdot 10^{-3}$	$19.4 \cdot 10^{-3}$	$1.82 \cdot 10^{-5}$	1470	$4.3 \cdot 10^{-3}$	$9.81 \cdot 10^{-7}$

Table A9: Reported published spray drying conditions for the production of peptide- or protein-based powders on lab-scale [non-conclusive].

Application	**Solvent**	**Concentration**	**Spray Drying Conditions**			**Reference**
			System	$T_{P3,S}$	$FR_{P11,S}$	
D-LAK peptides	Aqueous	10 mg/mL	Büchi B-290	75 °C	3.6 mL/min	Chi et al. [376]
Influenza vaccine	Aqueous	100 - 150 mg/mL	Büchi B-290	110 - 160 °C	1.0 - 4.5 mL/min	Kanojia et al. [132]
Hydrolysed fish collagen	Aqueous	60 mg/mL	Büchi B-290	130 - 150 °C	6 - 8%	Latip et al. [320]
L. acidophilus	Aqueous	200 mg/mL	Büchi B-290	120 - 160 °C	6 - 9 mL/min	Behboudi-J et al. [313]
Trypsin	Aqueous / Organic	3 - 16.1 mg/mL	Büchi B-290	100 °C	30%	Ní Ógáin et al. [112]
Immunoglobulin G	Aqueous	50 - 165 mg/mL	Büchi B-190	130 - 190 °C	3 mL/min	Maury et al. [113]
Insulin	Aqueous	5 - 60 mg/mL	Büchi B-290	75 – 220 °C	1.8 – 5.25 mL/min	Maltesen et al. [111]
Influenza Vaccine	Aqueous	100 - 140 mg/mL	Büchi B-190	60 °C	1 mL/min	Lovalenti et al. [332]
Trypsin	Aqueous / Organic	50 mg/mL	Büchi B-290	130 °C	3 mL/min	Saß and Lee [147]
Insulin	Aqueous	5 mg/mL	Büchi B-191	100 - 220 °C	2 - 5 mL/min	Ståhl et al. [131]

Table A11: Overview of all spray drying experiments performed as part of a study for platform characterisation and process implementation. The experimental approach can be divided in *pure solvent*-runs for a system characterisation (SP_000_XX) and the investigation of spray drying for product isolation with solutions of TRE and GLUC (TRE-h = D-(+)-Trehalose dihydrate, SPT1 - SPT6, GLUC = s-glucagon, SPG1 - SPG5).

Experiment	**Compound**	**Solvent**	**Ethanol[v/v]**	**$T_{P3,S}$** [°C]	***m*** [mg]	***V*** [mL]	***c*** **[mg/mL]**
SDD Experiments							
SDD_TRE	TRE	DI-Water	0.00	-	30	1	30.00
SDD_GLUC	TRE	0.05 M HCl	0.00	-	5	1	5.00
SDD_GLUCF	GLUC:TRE, 1:6 w/w	0.05 M HCl	0.00	-	5/30	1	35.00
Spray Dryer - System Characterisation							
SP_000_07		DI-Water-Ethanol	0.00	Various	Temperature Gradient		
SP_000_10		DI-Water-Ethanol	0.00	Various	Feed Rate		
SP_000_11		DI-Water-Ethanol	0.00	Various	Feed Rate		
SP_000_12		DI-Water-Ethanol	0.00	Various	Spray Gas		
SP_000_13		DI-Water-Ethanol	0.00	Various	Dry Air (Heat Loss System)		
Trehalose							
SPT1	TRE	DI-Water	0.00	70	3315.6	100	30.00
SPT2	TRE	DI-Water	0.00	130	3317.5	100	30.02
SPT3	TRE	DI-Water-Ethanol	0.01	70	3316.8	100	30.01
SPT4	TRE	DI-Water-Ethanol	0.01	130	3315.0	100	29.99
SPT5	TRE	DI-Water-Ethanol	0.50	70	3315.0	100	29.99
SPT6	TRE	DI-Water-Ethanol	0.50	130	3315.0	100	29.99
s-Glucagon							
SPG1	GLUC	0.05 M HCl	0.00	130	500.8	100	5.01
SPG2	GLUC	0.05 M HCl -Ethanol	0.01	130	250.5	50	5.01
SPG3	GLUC	0.05 M HCl -Ethanol	0.50	130	250.07	50	5.00
SPG4	GLUC	0.05 M HCl	0.00	70	501.1	100	5.01
SPG5	GLUC:TRE, 1:6 w/w	0.05 M HCl	0.00	130	250.17 / 1658.3	50	35.01

Table A12: Spray drying experiments of TRE and GLUC: Overview of collected sensor data. Exp_BME data were readily available from a pre-calibrated environmental sensor. $RH_{P5,C}$ was calculated assuming atmospheric pressure at P5 (see Fig. 7.4).

Experiment	c_{Solute} [mg/mL]	**Ethanol** [v/v]	**Exp_B290 Data**			**Exp_BME Data**			
			$T_{P3,S}$ [°C]	$T_{P3,R}$ [°C]	$T_{P5,R}$ [°C]	$RH_{P5,C}$ [%]	$T_{P9,R}$ [°C]	$RH_{P9,R}$ [%]	$p_{P9,R}$ [Pa]
Trehalose									
Data_SPT1	30	0.00	70	70.00 ± 0.00	46.71 ± 0.49	20.54 ± 0.52	34.04 ± 0.03	36.88 ± 0.28	91677.26 ± 28.79
Data_SPT2	30	0.00	130	129.71 ± 0.49	80.00 ± 0.00	5.35 ± 0.00	53.62 ± 0.06	15.77 ± 0.15	92273.36 ± 24.69
Data_SPT3	30	0.01	70	70.00 ± 0.00	48.00 ± 0.00	19.09 ± 0.00	33.40 ± 0.04	37.49 ± 0.20	91112.00 ± 28.16
Data_SPT4	30	0.01	130	130.29 ± 1.38	73.71 ± 1.80	6.51 ± 0.52	52.13 ± 0.03	15.71 ± 0.06	91636.45 ± 24.94
Data_SPT5	30	0.50	70	70.14 ± 0.38	48.00 ± 0.00	12.77 ± 0.00	35.79 ± 0.01	22.16 ± 0.03	92451.49 ± 24.00
Data_SPT6	30	0.50	130	129.86 ± 0.90	76.86 ± 0.69	4.43 ± 0.13	50.86 ± 0.38	12.92 ± 0.21	92501.45 ± 17.61
s-Glucagon									
Data_SPG1	5	0.00	130	129.43 ± 0.53	83.00 ± 0.00	3.83 ± 0.00	56.20 ± 0.01	11.47 ± 0.02	94571.32 ± 10.17
Data_SPG2	5	0.01	130	129.57 ± 0.53	83.00 ± 0.00	3.86 ± 0.00	56.39 ± 0.19	11.18 ± 0.07	92905.55 ± 10.85
Data_SPG3	5	0.50	130	130.00 ± 0.00	83.57 ± 0.53	2.96 ± 0.06	56.32 ± 0.22	8.89 ± 0.15	94149.15 ± 10.76
Data_SPG4	5	0.00	70	69.43 ± 0.53	49.00 ± 0.00	15.50 ± 0.00	35.81 ± 0.01	28.21 ± 0.03	92482.85 ± 6.77
Data_SPG5	35	0.00	130	130.00 ± 0.00	83.00 ± 0.00	3.93 ± 0.00	56.70 ± 0.04	11.29 ± 0.03	92880.98 ± 8.57

Table A13: Spray Drying TRE: Evaluation of BME sensor data.

Experiment	$c_{\mathbf{Solute}}$ [mg/mL]	**Ethanol** [v/v]	$\mathbf{T_{P3,S}}$ [°C]	**Exp_BME Pressure**		
				m_{LinReg} [Pa/min]	t_{LinReg} [Pa]	$\mid \Delta p_{max} \mid$ [Pa]
Trehalose						
SPT1	30	0.00	70	-7.54	9.26E+04	285
SPT2	30	0.00	130	-1.60	9.25E+04	169
SPT3	30	0.01	70	-2.32	9.14E+04	145
SPT4	30	0.01	130	-1.13	9.19E+04	193
SPT5	30	0.50	70	0.16	9.24E+04	197
SPT6	30	0.50	130	-3.37	9.30E+04	243
s-Glucagon						
SPG1	5	0.00	130	-1.36	9.50E+04	141
SPG2	5	0.01	130	0.96	9.26E+04	69
SPG3	5	0.50	130	-5.50	9.53E+04	174
SPG4	5	0.00	70	-1.67	9.31E+04	187
SPG5	35	0.00	130	1.36	9.25E+04	67

A4.3 Figures

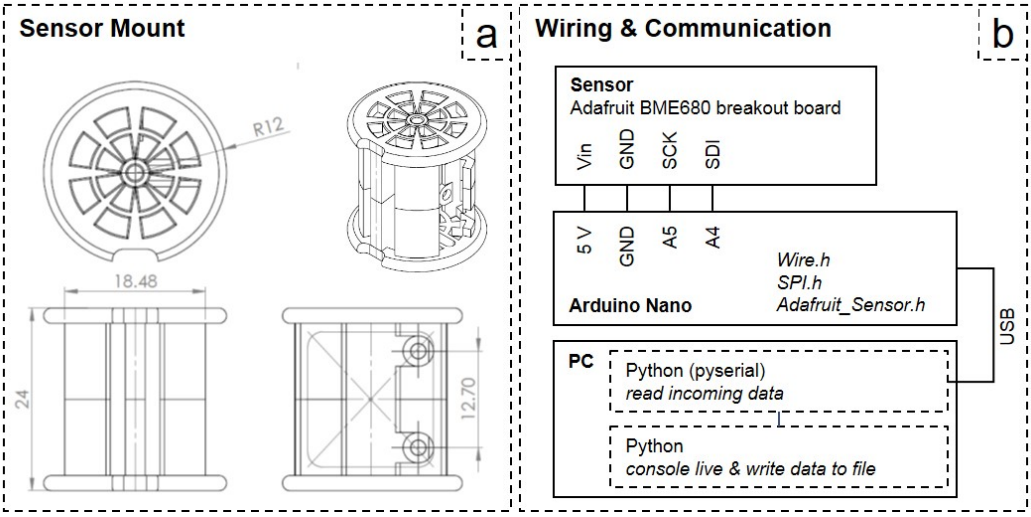

Figure A8: Implementation of the BME680 sensor recording temperature ($T_{P9,R}$), pressure ($p_{P9,R}$) and relative humidity ($RH_{P9,R}$) of the exhaust gas at P9 (see Fig. 7.4). a) 3D printed sensor mount with key dimensions and b) wiring of the BME680 breakout board. [STL-print files and code included in [ThesisDOI StrathData REF]]

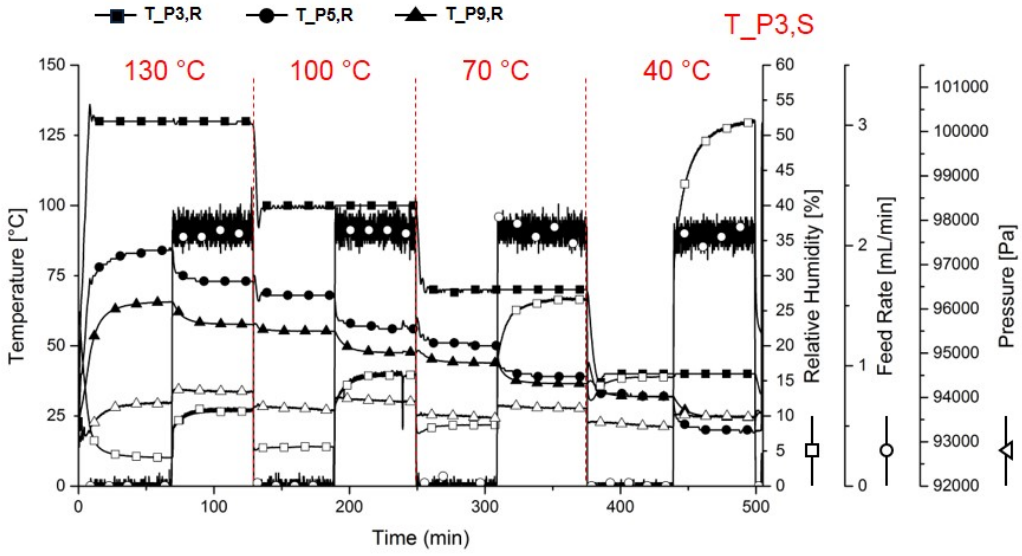

Figure A9: Example for the B290 system characterisation (experiment SP_000_07) assessing impact of selected inlet temperature ($T_{P3,S}$) and feed rate ($FR_{P11,R}$) on measured levels of temperature ($T_{P3,R}$, $T_{P5,R}$ and $T_{P9,R}$), pressure ($p_{P9,R}$) and relative humidity ($RH_{P9,R}$).

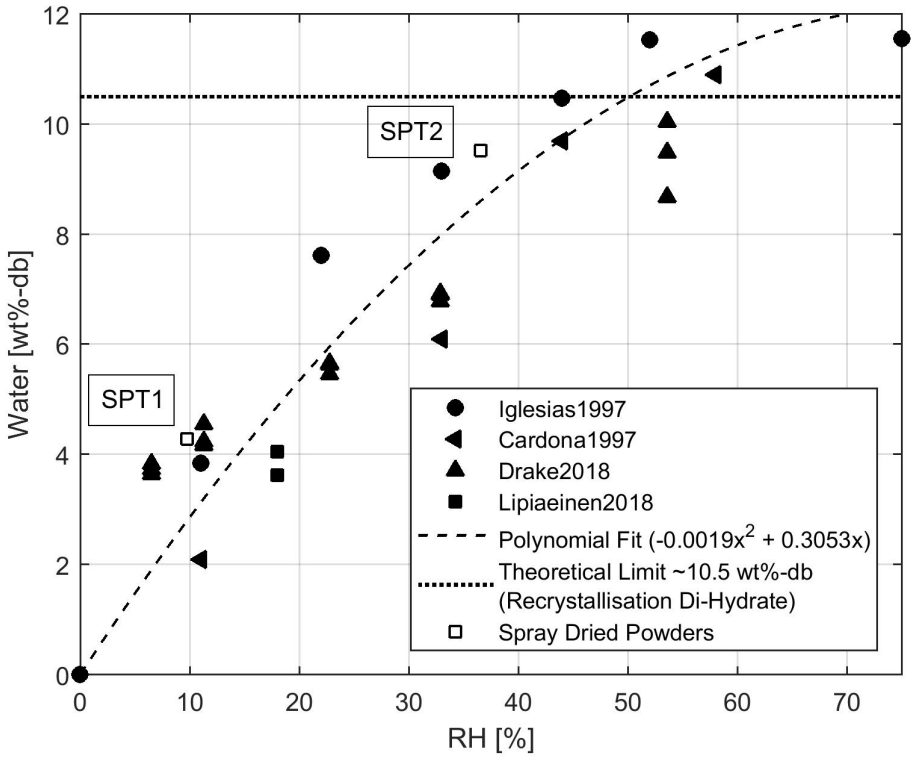

Figure A10: Water adsorption isotherm of amorphous TRE at 25 °C from published data [354, 355, 377, 378] and measured moisture content for experimental spray dried samples (SPT1, SPT2). The published data was used to correlate relative humidity levels ($RH_{P5,C}$) measured during the system characterisation with expected residual water content in the spray dried material. Deviations in reported T_g values might be due to a adsorption/desorption hysteresis.

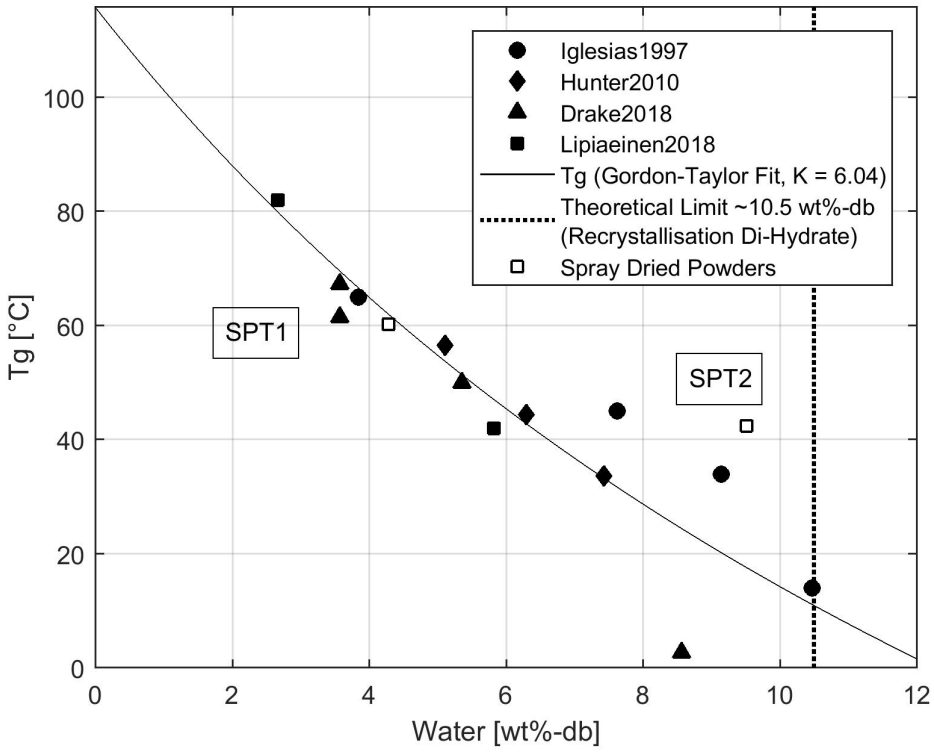

Figure A11: Reported glass transition temperature (T_g) values of TRE samples with changing moisture content [354, 379, 377, 378].

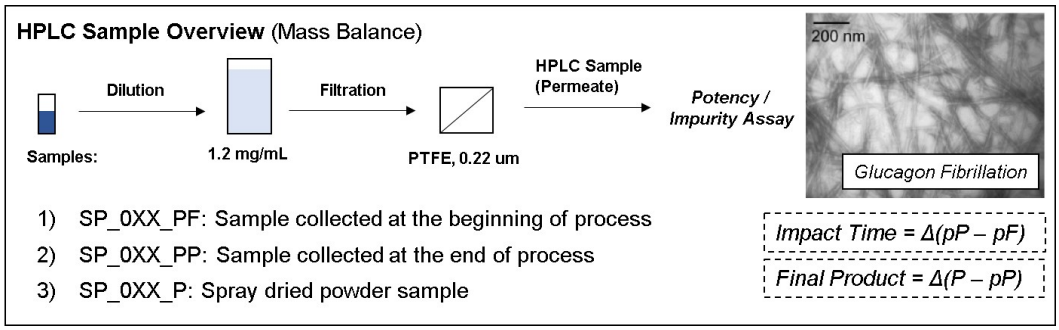

Figure A12: HPLC analysis with sample pre-filtration was used in order to allow a semi-quantitative assessment of the peptide fibrillation. Large mature GLUC fibrils are usually highly elongated. The samples were selected to evaluate relative changes as an indicator for feed stability (pF vs pP) and drying (pP vs P). GLUC fibrils are thin, elongated fibres (image adapted from Pedersen et al. [346])

OPERATING PARAMETERS

PARAMETER	SETTING		
Flow rate	0.75 mL/min		
Gradient profile	Time (minutes)	% Mobile Phase A (80/20 Buffer/ACN)	% Mobile Phase B (60/40 Buffer/ACN)
	0.0*	54.0	46.0
	3.0*	54.0	46.0
	8.0	30.0	70.0
	9.0	30.0	70.0
	9.01*	54.0	46.0
	12.0*	54.0	46.0
	*The ratio of mobile phase A and B may be adjusted to obtain a retention time of approximately 5.4 minutes.		
Autosampler temperature	5°C		
Detection wavelength	214 nm		
Column temperature	45°C		
Injection volume	20.0 µL		
Approximate total run time	12 minutes		
Note(s): After use, it is recommended to flush the column with 80/20 H2O/ACN to remove the high concentration phosphate buffer salt!			

Figure A13: Details of the HPLC potency assay as described in Section 7.2.4.3.

OPERATING PARAMETERS

PARAMETER	SETTING		
Flow rate	0.5 mL/min		
Gradient profile	Time (minutes)	% Mobile Phase A (80/20 Buffer/ACN)	% Mobile Phase B (60/40 H2O/ACN)
	0.0	62.0	38.0
	26.0	62.0	38.0
	30.0	12.0	88.0
	33.0	12.0	88.0
	34.0	62.0	38.0
	44.0	62.0	38.0
	*The ratio of mobile phase A and B may be adjusted to obtain a retention time of approximately 19.5 minutes.		
Auto-sampler temperature	5°C		
Detection wavelength	214 nm		
Column temperature	45°C		
Injection volume	15.0 µL		
Approximate total run time	44 minutes		
Note(s): After use, it is recommended to flush the column with 80/20 H2O/ACN to remove the high concentration phosphate buffer salt!			

Figure A14: Details of the HPLC impurity assay as described in Section 7.2.4.3.

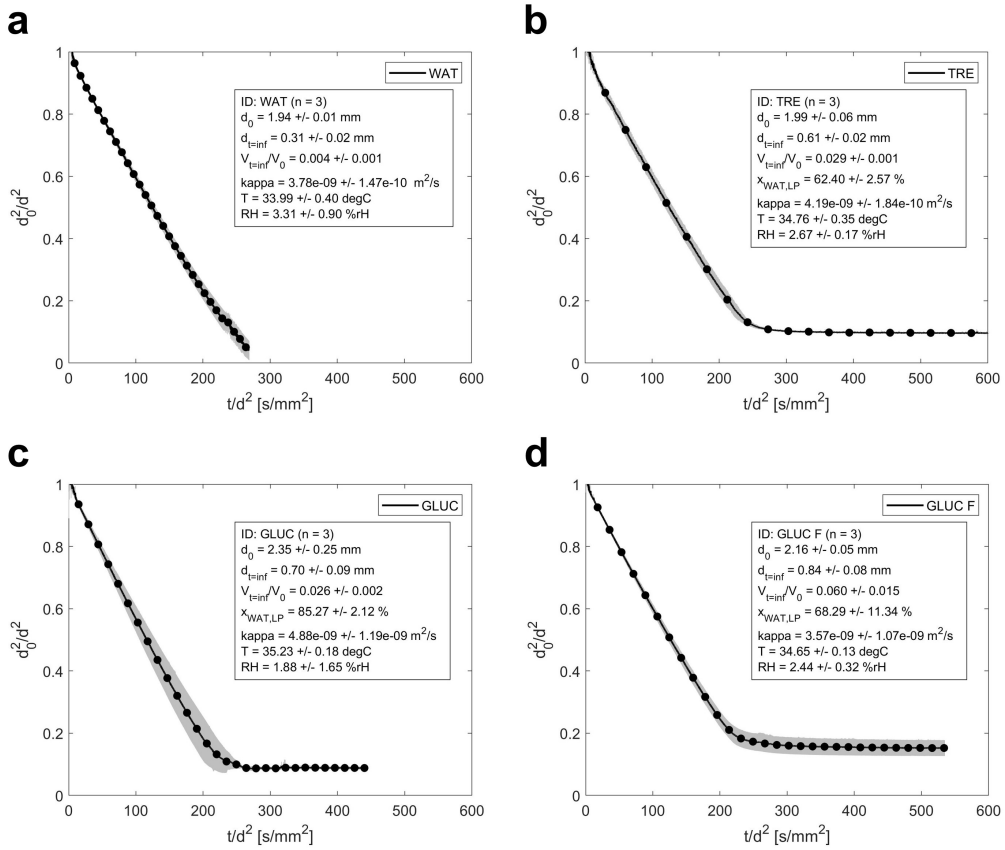

Figure A15: Drying curves of TRE, GLUC and a formulation of GLUC:TRE recorded during SDD experiments on the MSAL. (a) pure water (WAT), (b) TRE c_0 30 mg/mL, (c) GLUC c_0 5 mg/mL and (d) GLUC c_0 5 mg/mL formulation with TRE c_0 30 mg/mL. Annotations: n = number of experiments, d_0/V_0 = starting droplet diameter/volume, $d_{t=inf}/V_{t=inf}$ = final droplet or particle diameter/volume, $x_{WAT,LP}$ = WAT mass fraction at LP, kappa = evaporation rate, T = MSAL ambient temperature and RH = MSAL ambient relative humidity.

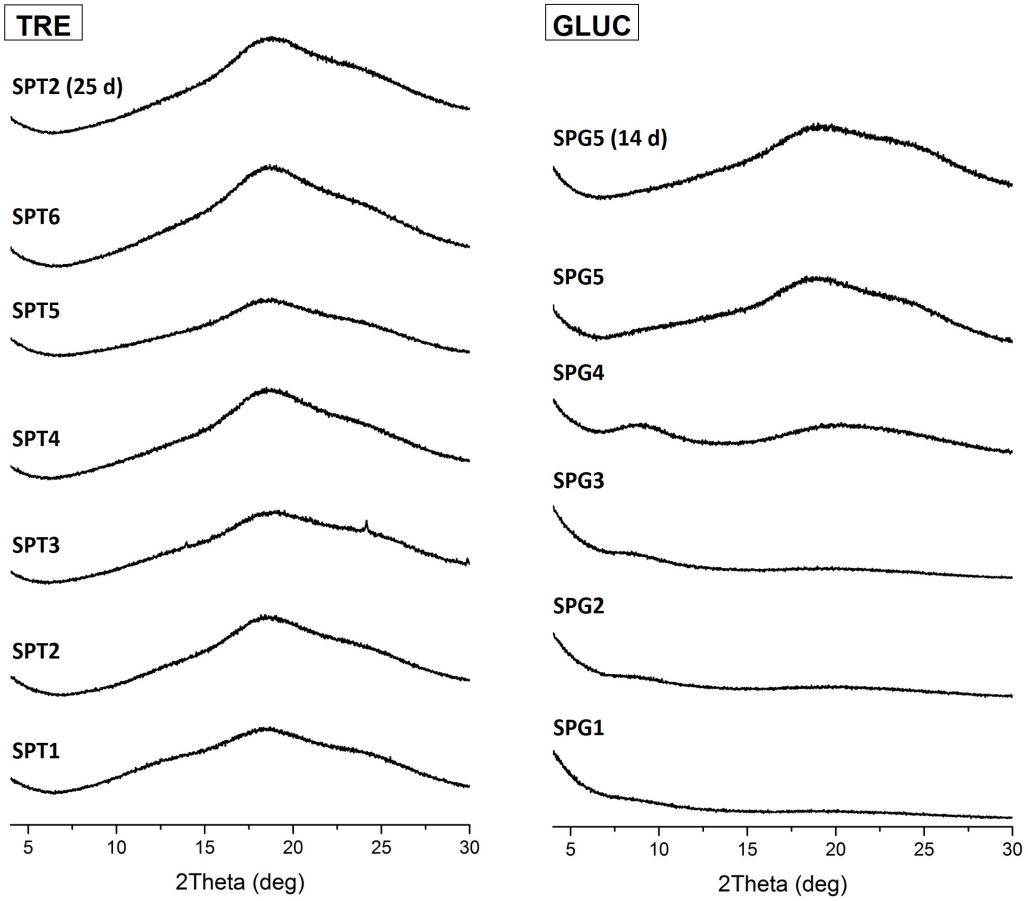

Figure A16: XRPD data of (left) spray dried TRE and (right) GLUC powders suggest an amorphous solid state structure of the produced solids below the XRPD detection limit, except for SPT3. The amorphous solid phase of the TRE matrix aims to protect the peptide against denaturation (water replacement theory [358, 359]).

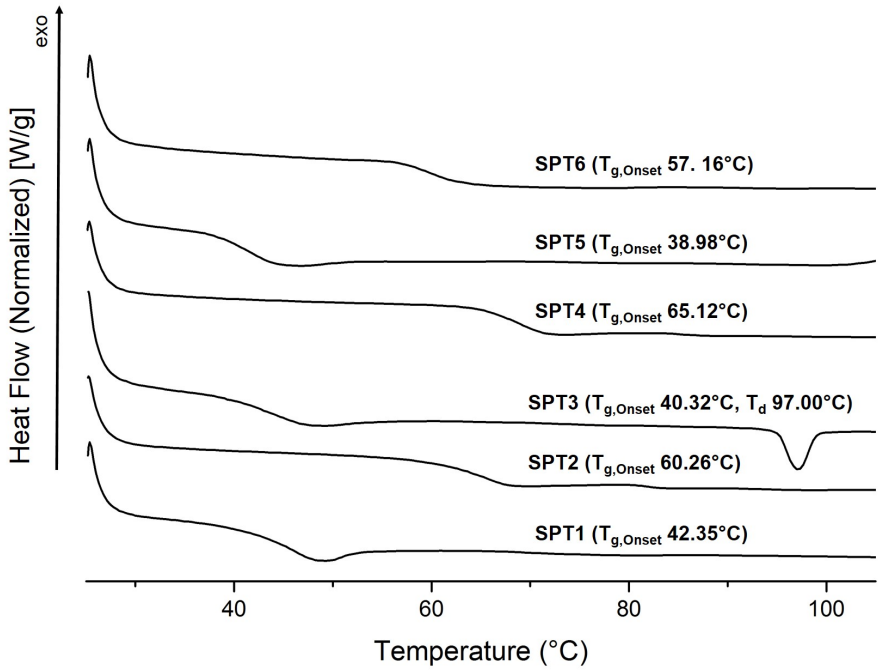

Figure A17: DSC data of spray dried TRE powders suggest an amorphous solid state structure of the produced solids, except for SPT3 with a dehydration peak (T_d) at 97.00 °C. The glass transition temperatures (T_g) of the TRE powders are between 38.98 °C (SPT5) and 60.26 °C (SPT2).

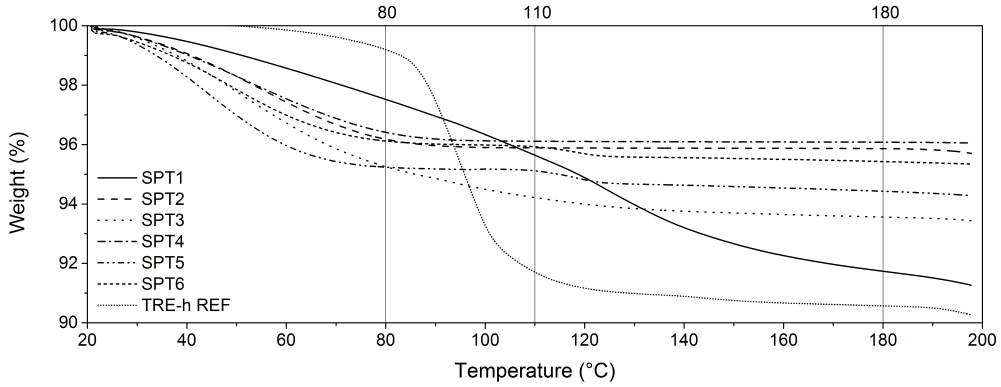

Figure A18: TG-MS data of spray dried TRE powders. Weight loss was subdivided in three steps: ΔRM_{80} (20 - 80 °C) indicating residual unbound moisture, ΔRM_{110} (80 - 110 °C) indicating TRE-h as observed for the TRE-h reference material and ΔRM_{180} (110 - 180 °C) above $T_{g,TRE}$ of 115 °C.

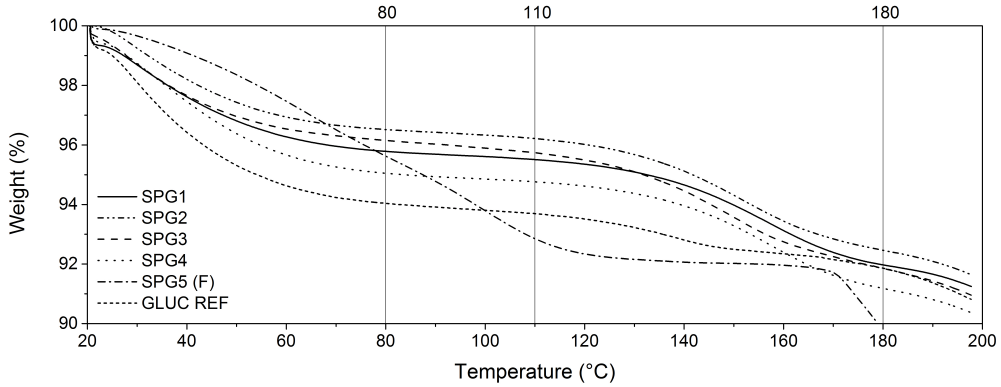

Figure A19: TG-MS data of spray dried GLUC powders. Most of the weight loss occurs in two steps between at ΔRM_{80} (20 - 80 °C) and ΔRM_{180} (110 - 180 °C). ΔRM_{80} relates to unbound residual moisture. ΔRM_{180} might indicate the amount of bound residual moisture, which has an average value of 3.69 $\pm$ 0.14 wt% for all spray dried GLUC samples (except SPG5 (F)) and is unaffected by the conditions of the spray drying process. SPG5 exhibits rapid weight losses above 170 °C and extensive browning indicating a Maillard reaction at these temperatures.

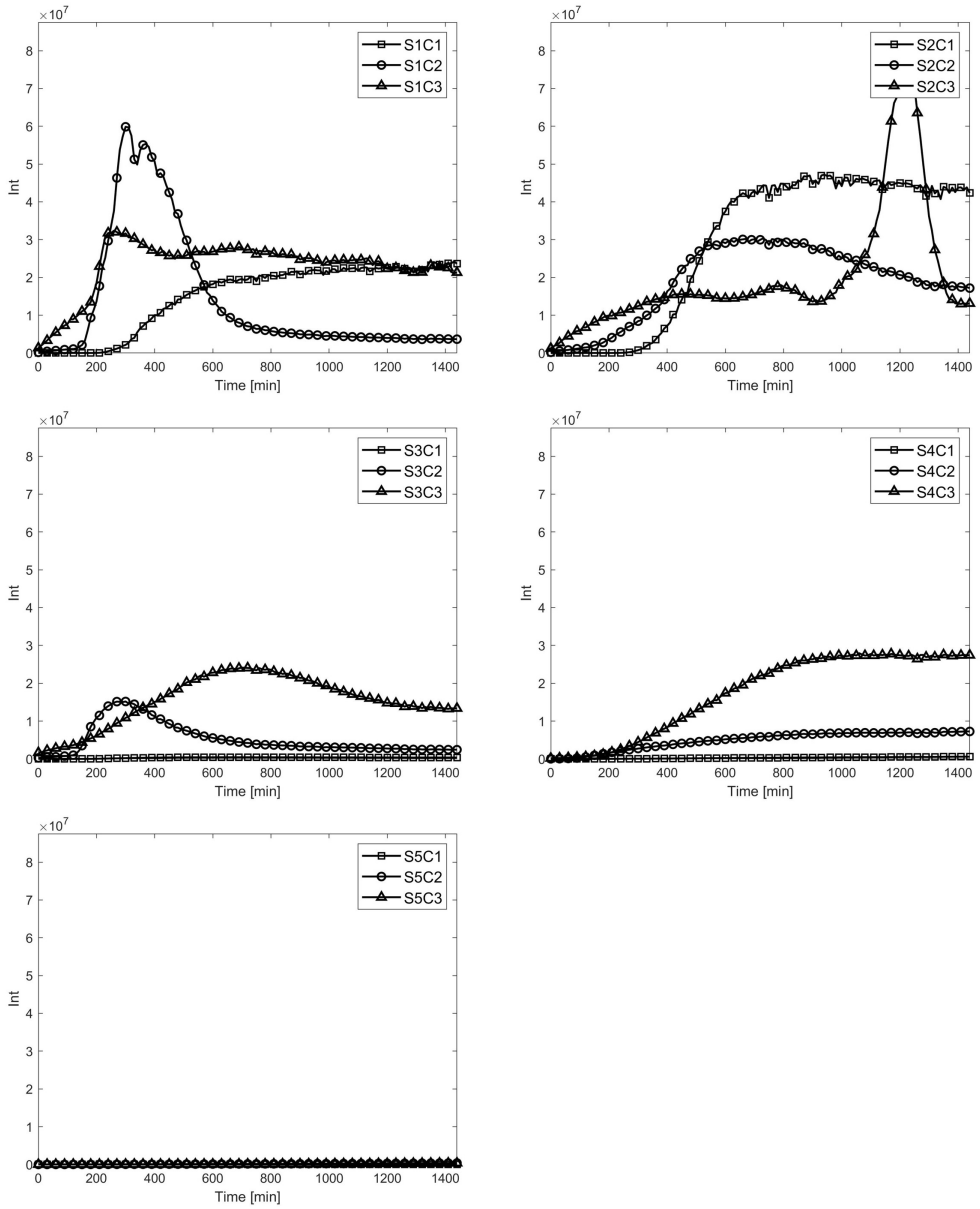

Figure A20: ThT assay for kinetic assessment of freeze-dried GLUC reference powder regarding feed stability (onset of fibrillation) and fibrils growth kinetics at changing ethanol solvent ratios (S1 = 0 v/v%, S2 = 1 v/v%, S3 = 10 v/v%, S4 = 25 v/v%, S5 = 50 v/v%) and changing GLUC concentrations (C1 = 1 mg/mL, C2 = 5 mg/mL, C3 = 15 mg/mL). The collected data suggest a change in the fibrillation kinetics leading to changes in the ThT fluorescence. At a ethanol solvent ratio of 50 v/v%, the ThT fluorescence is completely suppressed. Details of the ThT assay are described in Section 7.2.4.3. All values are calculated means from sample triplicates. The signal of solvent blanks was subtracted to adjust the baseline.

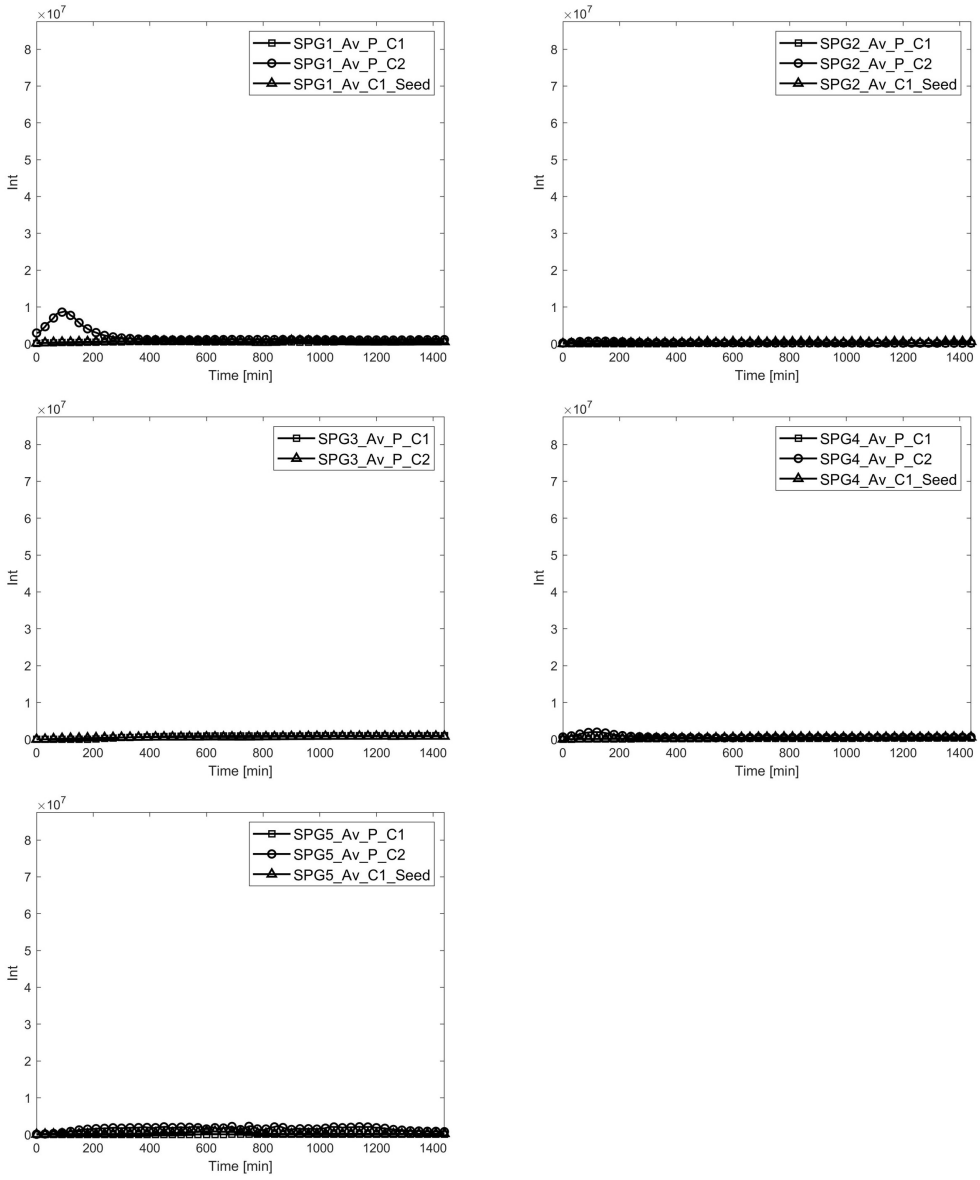

Figure A21: Tht Assay of spray dried GLUC powders in 0.05M HCl at two concentrations (C1 = 1 mg/mL, C2 = 5 mg/mL) and seeded with 5 μl of a suspension of a previously aggregated GLUC sample. The data suggest that the fibrillation kinetics or the fibrillation pathway of the spray dried GLUC powders are significantly altered in direct comparison to data collected for the freeze dried reference material presented in Fig. A20 (Appendix, page A36). Details of the ThT assay are described in Section 7.2.4.3. All values are calculated means from sample triplicates. The signal of solvent blanks was subtracted to adjust the baseline.

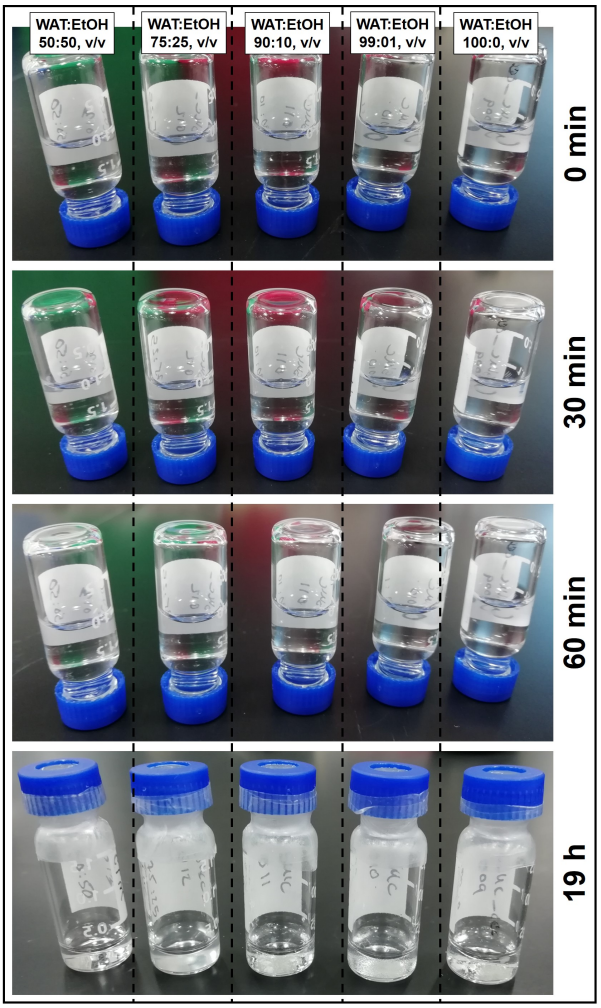

Figure A22: Small scale GLUC samples of 5 mg/mL with increasing ethanol solvent ratios (0 - 50 v/v%). All samples remained stable without visible gelling/aggregation within a one hour time window. After 19 hours all samples showed strong fibrillation except solution prepared in 50:50 v/v% water:ethanol (WAT:EtOH).

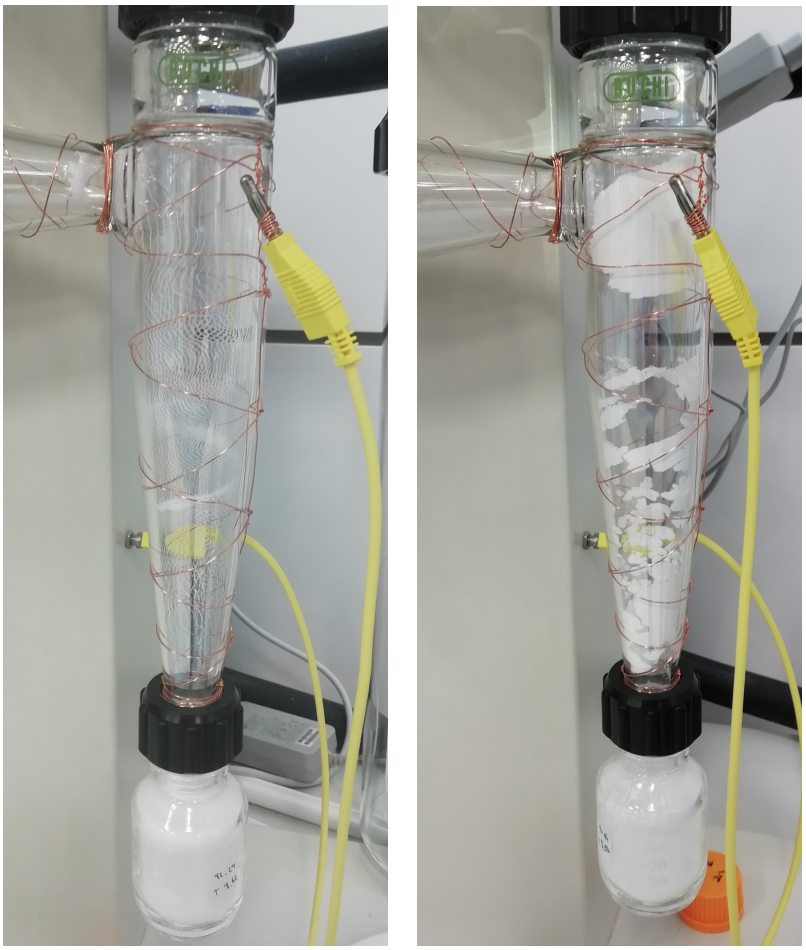

Figure A23: *High performance* cyclones after spray drying experiments (left) SPT2 ($T_{P3,S}$ 130 °C, ethanol 0 v/v%) and (right) SPT6 ($T_{P3,S}$ 130 °C, ethanol 50 v/v%) showing significant differences in the local particle adhesion leading to wall-depositing of material in the cyclone.

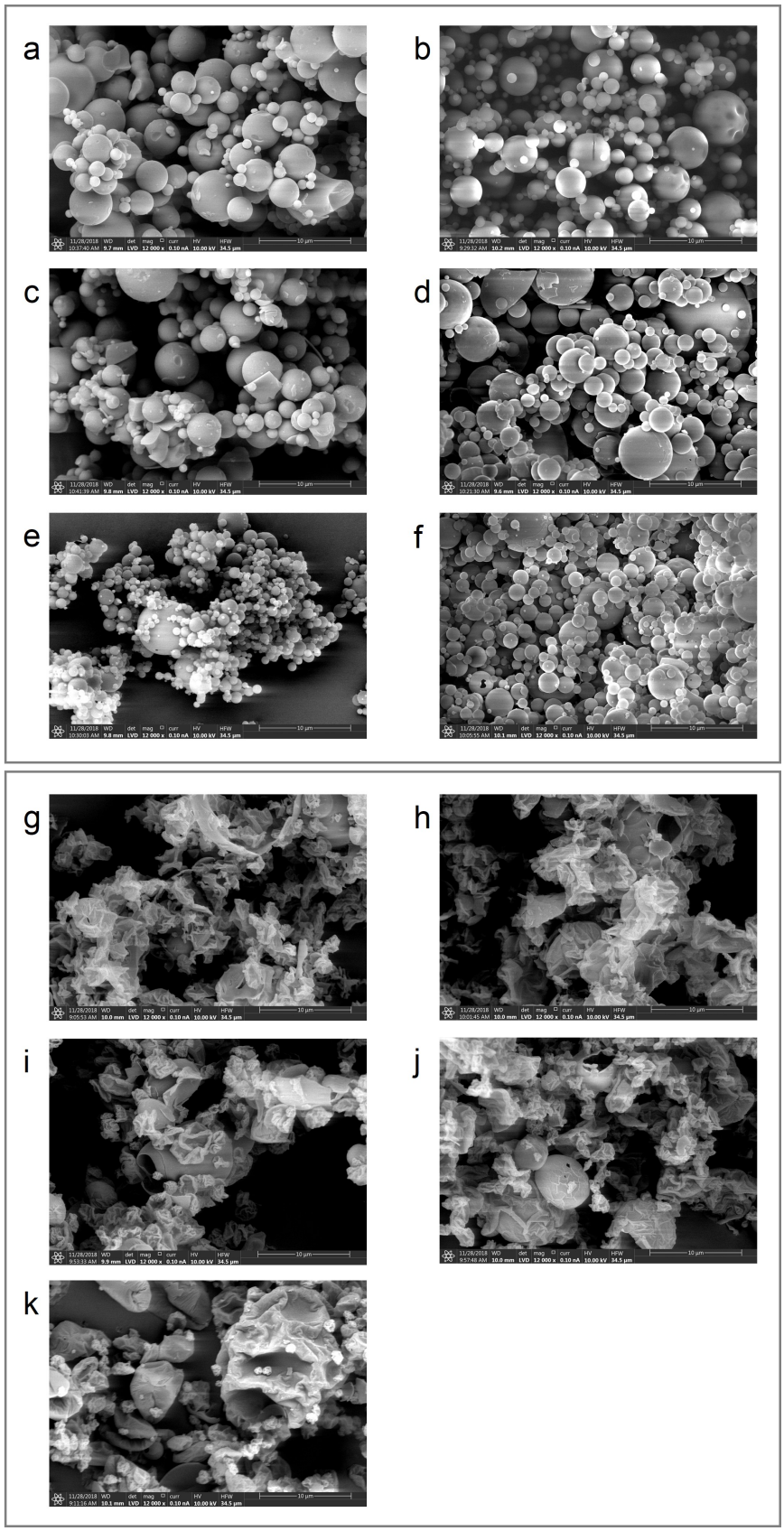

Figure A24: SEM images of spray dried TRE and GLUC samples. TRE samples: (a) SPT1, (b) SPT2, (c) SPT3, (d) SPT4, (e) SPT5, and (f) SPT6. GLUC samples: (g) SPG1, (h) SPG2, (i) SPG3, (j) SPG4, and (k) SPG5.